UNIVERSITÀ DEGLI STUDI DI MILANO

DOTTORATO DI RICERCA IN SCIENZE DELLA TERRA

Geologia Strutturale

Ciclo XXXII

DIPARTIMENTO DI SCIENZE DELLA TERRA

MULTISCALE STRUCTURAL ANALYSIS OF ULTRAMAFIC ROCKS IN DIFFERENT STRUCTURAL DOMAINS OF THE ALPS, INTEGRATED WITH PETROLOGY AND GEOCHEMISTRY: A KEY TO REFINE GEODYNAMIC INTERPRETATIONS OF COLLISIONAL BELTS

GEO/03

PIETRO LUONI

TUTORS
DR. DAVIDE ZANONI
DR. GISELLA REBAY
PROF. MARIA IOLE SPALLA

COORDINATORE DEL DOTTORATO
PROF. FERNANDO CAMARA ARTIGAS

Index

Chapter 1
Introduction

Ophiolites are fragments of oceanic upper mantle and crust that have been incorporated into orogenic belts by different tectonic processes such as obduction or subduction/exhumation (e.g.; Bearth, 1967; Martin et al., 1994; Guillot et al., 2004; Turco and Tartarotti, 2006; Dilek and Furnes, 2011; Balestro et al., 2019 and refs. therein). The first occurrence of ophiolites in Earth evolution is estimated at 3.8 billion-year in the Isua Supracrustal Belt (Furnes et al., 2007) representing the very first trace of plate tectonic activity and beginning of the Wilson cycle whose continuous repetition caused the present-day configuration of oceans and continents. In mountain belts, ophiolites can preserve plentiful structural, textural and compositional information about the oceanic lithosphere (e.g Bearth, 1967; Hoogerduijn Strating, 1991; Dilek and Furnes, 2014), suggesting features such as the degree of development of the ocean basins and their spreading rate. Their presence allow to speculate about pre-collisional configuration of continents and oceans throughout paleogeographic reconstructions (e.g. Schettino and Turco, 2011).

Since the very first definition of ophiolite of Brongniart (1813), ultramafic rocks are considered a fundamental lithotype to study ophiolitic complexes and are used as tracers of oceanic sutures in collisional belts (Guillot et al., 2004; von Raumer and Stampfli, 2008; Arenas and Sanchez, 2015). In particular, serpentinite is a key lithotype for all the tectonic processes that lead the to the opening and closure of oceanic basins because of their ductile rheological properties and the large PT field of stability of their forming minerals (Guillot et al., 2015). Nevertheless, the petrostructural record of ultramafic rocks that formed during convergence, subduction and exhumation histories deserves detailed studies in most of the suture zones of collisional mountain belts; refinement of PT paths and structural history of the oceanic lithosphere can be actually accomplished in spite of the extremely ductile rheology of the highly serpentinised ultramafics. This PhD thesis gives a contribution in unravelling the tectono-metamorphic evolution of the Alpine and Variscan belts by multiscale structural analysis of ultramafic and metasomatised mafic rocks within the Piemonte Zone of the Western Alps or preserved as boudins in the HT Variscan continental rocks of the Argentera Crystalline Massif (upper Valle Gesso). The chosen areas allowed to study ultramafics of Jurassic and Palaeozoic ages that experimented HP-LT and HP-LT to HT-LP conditions, comparing the features of ultramafic rocks that experienced such contrasted thermal evolutions in different orogenic cycles.

The present work applies a well consolidated method, traditionally used for studying continental polydeformed and polymetamorphic terrains (e.g Passchier et al., 1990; Gosso et al., 2015 and refs. therein), to polyphase deformed and metamorphosed oceanic rocks. The first step is performing a detailed structural mapping of selected areas to define the geometrical relationships among the different lithotypes and the superposed structures. The field-work is supported and followed by microstructural and minero-chemical analysis of selected microsites to define the mineral assemblages, and their compositional variations, developed during the structural history. The investigations are

implemented by radiometric dating and whole rock and in-situ trace element analyses, in order to define the petrogenetic environments of the protoliths.

The thesis is organised as a collection of three published paper, and unpublished data, description and discussion that are not yet organised into publication style. There are two main sections. The first section is focused on Alpine ophiolites of the Piemonte Zone and the second section deals with the Variscan mafic/ultramafic rocks of the Argentera Massif.

The first section of the thesis is dedicated to Zermatt-Saas Zone serpentinite from Valtournenche (AO) outcropping in Créton, a locality between Valtournenche and Cervinia. Following a detailed mesostructural analyses of some key-outcrops of Créton serpentinite (1:20 scale), published in Luoni et al. (2019), the microstructural study has been focused on the relict domains that escaped the development of the HP foliation already described by Rebay et al. (2012) and dated in Rebay et al. (2018). The petrological modelling of Ti-humite rich domains was used to infer a new UHP peak in Valtournenche serpentinite (Luoni et al., 2018). The resulting metamorphic evolution has been compared with predictions from the numerical model of Regorda et al. (2017) to decipher the vertical paleogeography of these UHP ophiolites now exposed in Valtournanche. Geochemistry of pyroxenite in serpentinite has been interpreted and relic of basaltic melts have been recognized. Furthermore, the significance of diopsidite layers is discussed. This first section includes three published papers and unpublished data in preparation for submission.

In the same section, a detailed microstructural and petrological study of the Piemonte Zone serpentinite from Valle del Tesso (Lanzo Valley, west of Turin) is presented, with preliminary results on their metamorphic evolution, allowing the construction of a PTdt path in this portion of the Piemonte Zone at the boundary with the Ultramafic Lanzo Massif and the southern termination of Sesia-Lanzo Zone.

The second section explores boudins of diopsidite and serpentinite embedded in the Argentera migmatites (Helvetic Domain), from Valle Gesso (south of Cuneo). A detailed map of the area was produced to define the relationship between ultramafic boudins and migmatites. Microstructures and minero-chemical variations marking the recognised fabrics are described and their metamorphic evolution and significance are discussed.

The Créton serpentinite map is reported as attachment. Mineral abbreviations are from Whitney and Evans (2010).

Chapter 2
Geological setting

The Alps (Fig. 1.1) are part of the Alpine-Himalayan orogenic belt and extends from the Gulf of Genova in the Western Mediterranean to the Vienna basin and represent the morphotectonic result of the convergence between Adria plate and the European passive margin that was accommodated by the closure of the Mesozoic Thetis (Argand, 1911; Argand, 1916; Alvarez, 1976; Dal Piaz, 2001; Spalla et al., 2014; Marotta et al., 2016 and ref therein).
As shown in the Structural Model of Italy (Bigi et al., 1990), the Alpine belt consists in a double verging crustal structure: the northern sector shows a W- to N- verging nappe structure while the southern sector consists of a S-verging thrust and fold belt. The northern and the southern sectors are juxtaposed by the Periadriatic Lineament (Schmid et al., 1989; Dal Piaz, 2010 and references therein). The axial zone of the Alps is part of the north-verging belt and is made of interdigitated portions of subducted oceanic and continental materials (Dal Piaz, 2001).
The main tectonic domains of the Alps are (Fig. 1.1):

- Southern Alps

The Southern Alps are the tectonic domain located to the south of the Periadriatic tectonic line; it is a hinterland-verging thick-skinned fold and thrust belt of Alpine age; it involves a thick Permo-Mesozoic volcano-sedimentary cover at the top of the Variscan crystalline basement. The sedimentary sequences are particularly thick to the east, in the Dolomites and in the Carnic Alps, but gradually diminish towards the west (Doglioni, 1987, 2007 and references therein). In the eastern, central, and western sector different basement units continuously outcrop (Spalla and Gosso, 1999; Zanoni et al., 2010; Spalla et al., 2014). Along the Periadriatic Lineament, both of the Southern Alps and the Penninic and Austroalpine margins are intruded by the magmatic Oligocene stocks of Traversella, Biella, Adamello, Masino-Bregaglia, Bergell and Vedrette di Ries (Bigi et al., 1990; Zanoni et al., 2010 and references therein).

- Helvetic-Dauphinois-Provençal Domain

Different sedimentary and basement units are part of these domains. Some important Variscan basement massifs locally preserve older relics, the so-called *External Crystalline Massifs*, as the Argentera-Mercantour, the Pelvoux, the Belledonne-Grandes Rousses, the Aiguilles Rouges-Mont Blanc, and the Aar-Gottardo massif (von Raumer et al., 1999; Guillot and Ménot, 2009; Schulz and von Raumer, 2011).

- Austroalpine Domain

Austroalpine units constitute the axial zone of the belt together with the Penninic Domain, occupying the shallowest portions in the nappe pile, and are made of subducted rocks deriving from the

continental margin of Adria (Schmid et al., 2004). The Eastern Austroalpine units are more widespread than those of the western part of the Austroalpine, and registered eclogitic to Barrovian metamorphism (Handy and Oberhänsli, 2004); the Western Austroalpine is constituted by the Sesia-Lanzo Zone (Compagnoni et al., 1977; Spalla et al., 1991), the Dent-Blanche nappe (Manzotti et al., 2014 and references therein), and minor klippes such as the Mt. Mary, Pillonet, Etirol-Levaz, Tour Ponton, Acque Rosse, Chatillon, Glacier-Rafray, Grun, and Santanel. They registered amphibolite to eclogite facies metamorphism at younger ages than the Eastern Austroalpine (e.g. Spalla et al., 1996; Rubatto et al., 1999).

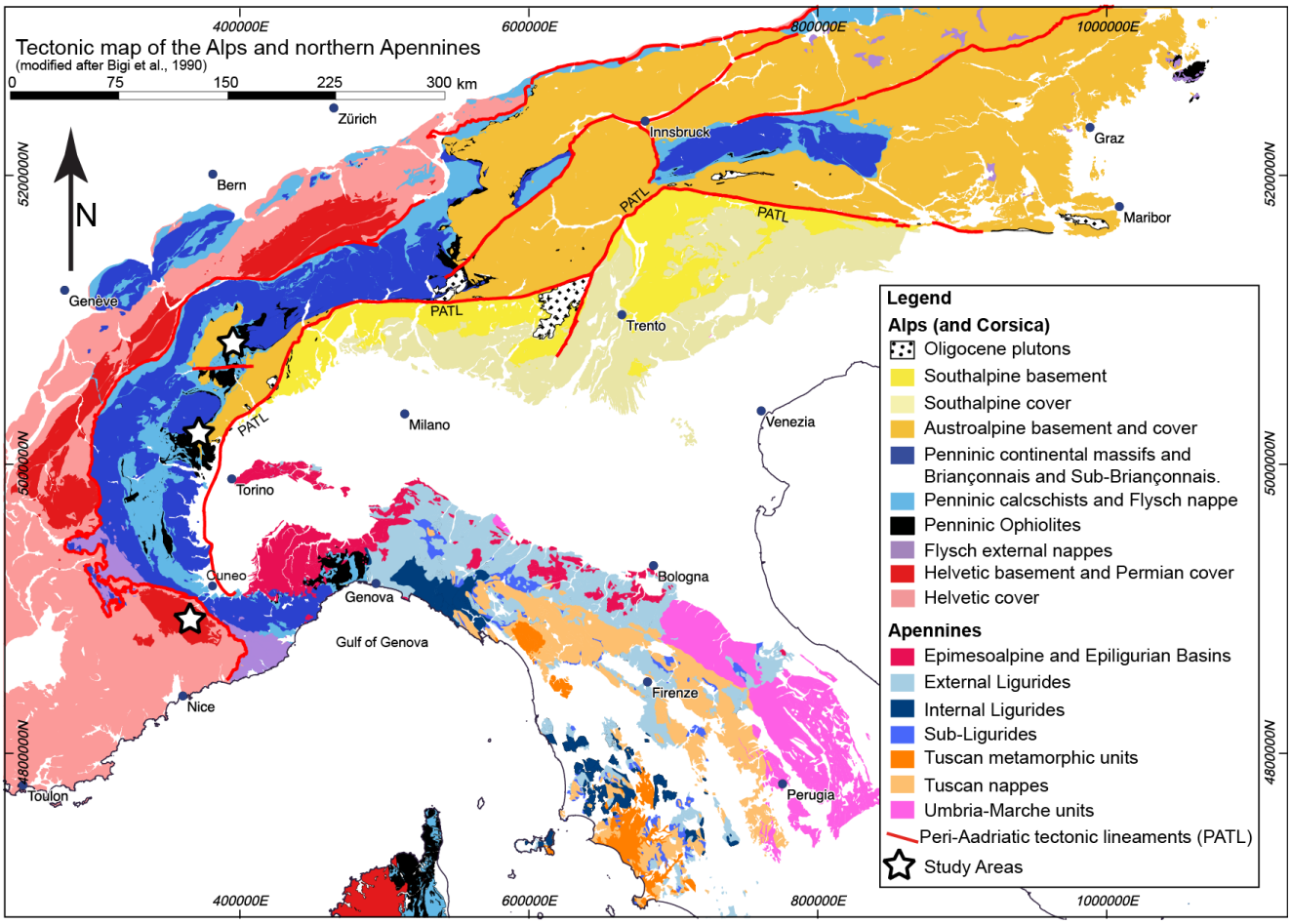

Fig. 1.1. - Tectonic map of the Alps, northern Corsica, and northern Apennines, (Bigi et al., 1990; Gosso et al., 2019). Reference system: WGS 84 / UTM zone 32N. Stars localize the studied mafic and ultramafic rocks.

- Penninic Domain

The structural units of this Domain are both oceanic, such as the Mesozoic ophiolites, and continental, such as the *Internal Crystalline Massifs* (e.g. Gran Paradiso, Monte Rosa, Dora Maira; Bigi et al., 1990) and they are comprised between the Penninic Front and the Austroalpine Domain. The Penninic rocks is areally exposed in the Western Alps while in the Eastern and Central Alps the Austroalpine domains is dominant and Penninic rocks are exposed only in the Engadin, Tauris, and Rechnitz tectonic windows. The paleogeographic provenance of the Penninic continental rocks is nowadays matter of wide scientific debate on logics of subduction-exhumation and collisional mechanics (Polino et al., 1990; Spalla et al., 1996; Dal Piaz, 2010). Rocks registered an HP-LT metamorphism at different depth during the Alpine convergence as they were part of the subducted plate.

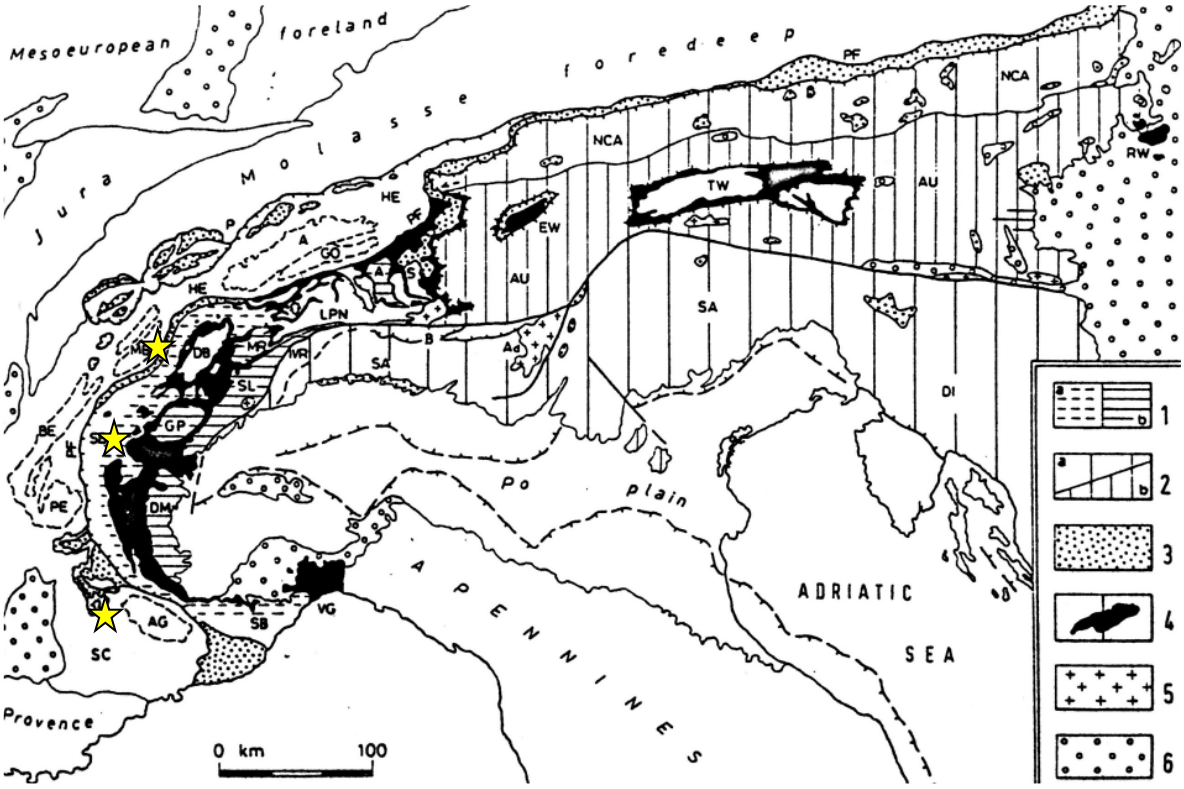

Fig. 1.2. - Tectonic scheme of the Alps. 1a) Eolpine Blueschist facies metamorphism (Briançonnais and Adula); 1b) Eolpine eclogitic facies metamorphism (Continental Central and Western Alps units); 2) Eastern Austroalpine low grade metamorphism from greenschist (a) to Amphibole facies (b); 3) Cretaceous to Eocene flysch nappes; 4) Mesozoic HP-LT units (VG Voltri Group); 5) Tertiary Periadriatic plutons (B Bergell; Ad Adamello); 6) Oligocene and Miocene basins. Main tectonic units: i) External Crystalline Massifs: (P) PreAlpine klippen; (HE) Helvetic-Dauphines; (A-GO) Aar-Gotthard; (MB) Mont Blanc, (BE) Belledonne); (PE) Pelvoux; (AG) Argentera. ii) (SA) Southern Alps; (DI) Dinarides; (IVR) Ivrea Zone; ; iii) Penninic Domain: (FP) Penninic Front; (LPN) Lower Penninic Units, (A) Adula e (SB) Gran San Bernardo; (MR) Monte Rosa; (GP) Gran Paradiso; (DM) Dora Maira; (S) Suretta; Tectonic windows: (EW) Engadin; (TW) Tauern; (RW) Rechnitz; iv) Austroalpine: (SL) Sesia-Lanzo Zone ; (DB) Dent Blanche; (AU) Eastern Austroalpine; (NCA) Northern Calcareous Alps (Polino et al., 1990). Stars localize the studied mafic and ultramafic rocks.

This thesis addresses the ultramafic rocks occurring into three areas located in two of the main domains of the Western Alps: the first section explores rocks from the Piemonte Zone in Valtournanche (Aosta) and Valle del Tesso (Torino); the second section analyses ultramafic rocks enclosed in the Argentera External Crystalline Massif, outcropping in the upper Valle Gesso (Cuneo).

2.1 The Piemonte Zone in the Western Alps

The Mesozoic ophiolites of the Alps are included by definition into the Penninic tectonic domain (Fig. 1.1 and 1.2) and are the remnants of the Alpine Thetis, outcropping along the Alpine belt as metamorphosed tectonic units at different structural levels as shown in Fig. 1.3. A number of paleogeographic models have proposed to recover the pre-Alpine configuration of Penninic continental and oceanic units by means of an extensional relocation of a simple thrust and fold belt; such backward resolution of the paleogeography operates upon a present nappe stack configuration that does not consider the metamorphic, deformational and volumetric changes that must have taken place from rift to collisional plate tectonic events (e.g. Schmid et al., 1990).

In the Western Alps traditionally, two different type of ophiolites are distinguished on the basis of the lithological association and metamorphic assemblages (Martin et al., 1994):

- The *Combin-type ophiolite sequence* is made mostly of carbonate to terrigenous flysch-type metasediments, commonly including interleaves of tabular metabasites and minor metaserpentinites slices (Dal Piaz, 1988). Usually the top of the ophiolitic sequence is dominated by manganiferous quartzites and other oceanic sediments (Dal Piaz et al., 1979; Vannay and Alleman, 1990). The dominant metamorphic imprint is due to greenschist facies metamorphism dated at 38-43 Ma (e.g. Martin and Cortiana, 2001). Rare relics of epidote-blueschist facies have been recognized (Kienast, 1983; Dal Piaz, 1988; Vannay and Alleman, 1990).
- The *Zermatt-Saas-type ophiolite sequence* consists of huge ultramafic and mafic bodies and minor metasedimentary cover. A large part of the ophiolites is constituted by metaserpentinites often enclosing small rodingites bodies (Rahn and Bucher, 1998; Li et al., 2004; Groppo and Compagnoni, 2007; Fontana et al., 2008, 2014; Rebay et al., 2012; Zanoni et al., 2016). Mafic rocks are Mg- and Fe-gabbros and metabasalts, locally preserving primary textures as pillow lavas (Bearth, 1956, 1967; Dal Piaz and Ernst, 1978; Bucher et al., 2005; Bucher and Grapes, 2009), and with a normal-MORB signature (see refernces in Rebay et al., 2018). The metasedimentary cover comprises metaquarzites, calcschists, and subduction mélanges (e.g. Riffelberg-Garten; Dal Piaz et al., 1979; Bearth and Schwandler, 1981; Barnicoat and Fry, 1986; Reinecke, 1991; Mahlen et al., 2005). Eclogite facies metamorphism imprint is dominant in all the lithotypes and widely documented (Barnicoat and Fry, 1986; Bucher and Grapes, 2009; Weber and Bucher, 2015 and references therein) and UHP assemblages have been recognized both in metaophiolites and associated metasediments (e.g. Cignana and Créton; Reinecke, 1991; Frezzotti et al., 2011; Luoni et al., 2018). The eclogitic assemblages are overprinted by greenschist facies metamorphism. The ages of the protoliths are Jurassic and the HP metamorphism is dated between 70 and 40 Ma (see Martin et al., 1994; Rebay et al., 2018 and refs. therein).

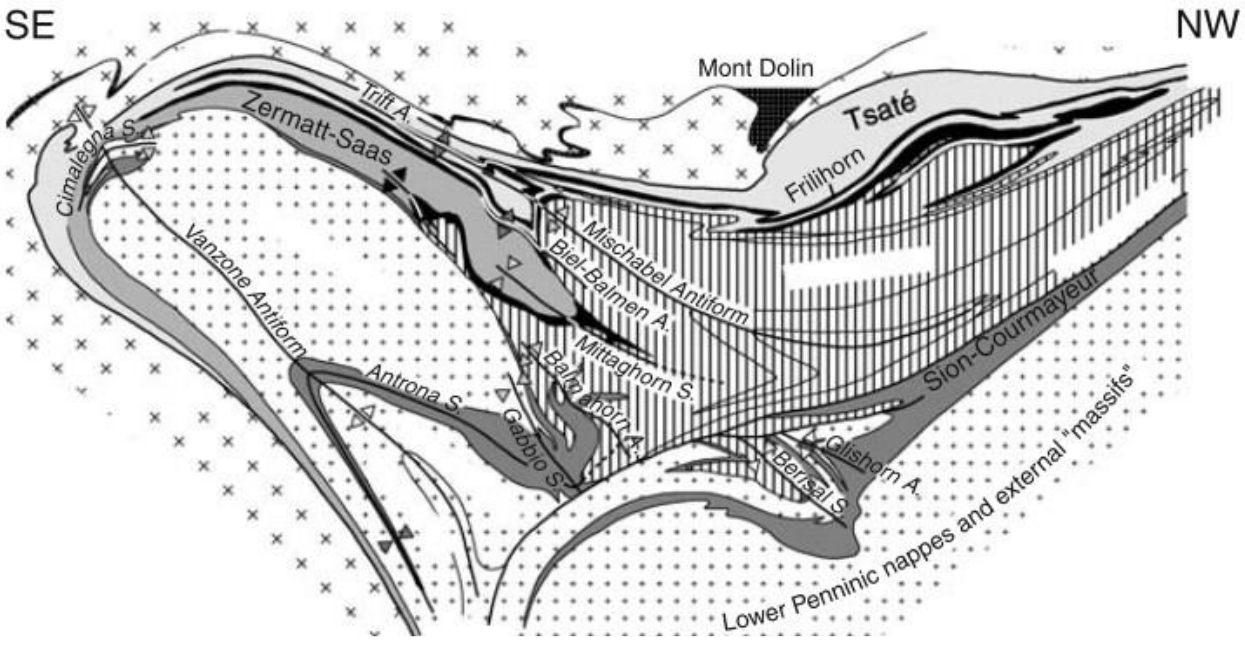

Fig. 1.3. - Part of the classic Besançon - Biella tectonic cross section of the Western Alps, revisited (Pleuger et al., 2007).

Furthermore, *Antrona ophiolite* displays lithological and metamorphic affinities with the Zermatt-Saas-type ophiolite sequence, although it occurs at a lower structural level since it is structurally below the Monte Rosa Nappe (Fig. 1.3). Dominant metabasites and minor rodingite-bearing metaserpentinites, and metasediments are described (Liati et al., 2005; Turco and Tartarotti, 2006; Tartarotti et al., 2011 and references therein). These rocks registered eclogite facies conditions, overprinted by greenschist facies metamorphism.

2.2 External Crystalline Massifs of the Alps

In the Western and Central Alps external margin, External Crystalline Massifs (EMCs) of Argentera, Pelvoux, Belledonne, Mont-Blanc – Aiguilles Rouges and Aar – Gothard are tectonic windows surrounded by Mesozoic cover units (Fig. 1.4). EMCs represent fragment of Variscan basement that was partially involved in the Alpine orogeny and that preserves a long lasting geological pre-Alpine evolution (von Raumer et al., 1999; Guillot et al., 2009). Most of the Variscan area consists of variously migmatized lithotypes that record amphibolite-granulite facies metamorphism in which a number of relics of earlier HP metamorphism are preserved (von Raumer et al., 2009). During the Alpine cycle EMCs recorded a green schist metamorphic imprint localized along thrusts and strike-slip faults. According to Guillot and Ménot (2009), three different sectors have been distinguished on the base of lithostratigraphic, chronologic and metamorphic affinities: the eastern sector includes the NE portion of the Belledonne massif, the internal zone of the Oisans, Aiguilles Rouges, and Argentera massifs. The central sector corresponds to the NW part of the Belledonne massif, Grand Rousses massif and the internal portion of the Oisans massif. The western sector is represented by the external portion of Belledonne. The eastern sector has been interpreted as an oceanic suture zone because MORB-like eclogites occur, while the Central sector is thought to represent the retro-arc domain of the Saxo-Thuringian ocean for the occurrence of Chamrousse ophiolite and associated plagiogranites and volcanoclastic sediments (Guillot and Ménot, 2009). The eastern sector comprises an alternation of meta-flysch and mafic layers (Neoproterozoic-Lower Palaeozoic).

The Palaeozoic tectonic evolution is characterized by the opening of the Rheic ocean between the northern passive margin of Gondwana and Armorica (von Raumer and Stampfli, 2008) as testified by the occurrence of the Chamrousse ophiolitic complex in the Belledonne massif, interpreted as retro-arc basin lithosphere (Guillot and Ménot, 2009). The Variscan subduction was active between the Devonian and the Silurian and subduction relics are represented by eclogites in Belledonne, Aiguilles Rouges and Argentera (Paquette et al., 1989; Rubatto et al., 2001; Spalla et al., 2014). The continental collision occurred in the middle Devonian, as the obduction of Chamrousse ophiolite and the pervasive migmatisation under amphibolite facies metamorphism. As a consequence of the thermal anomaly caused by the slab break-off, EMCs were intruded by magnesian to ferric granites (von Raumer et al., 2014). During the Alpine convergence, EMCs were not involved in the subduction but exclusively involved in the collision, at present occupying the external portion of the Alpine belt and affected by syn-tectonic green-schist facies metamorphism. Alpine structures and assemblages only occur along main tectonic lineaments, preserving the Variscan basement (Corsini et al., 2004; Sanchez et al., 2011; Carosi et al., 2016; Filippi et al., 2019).

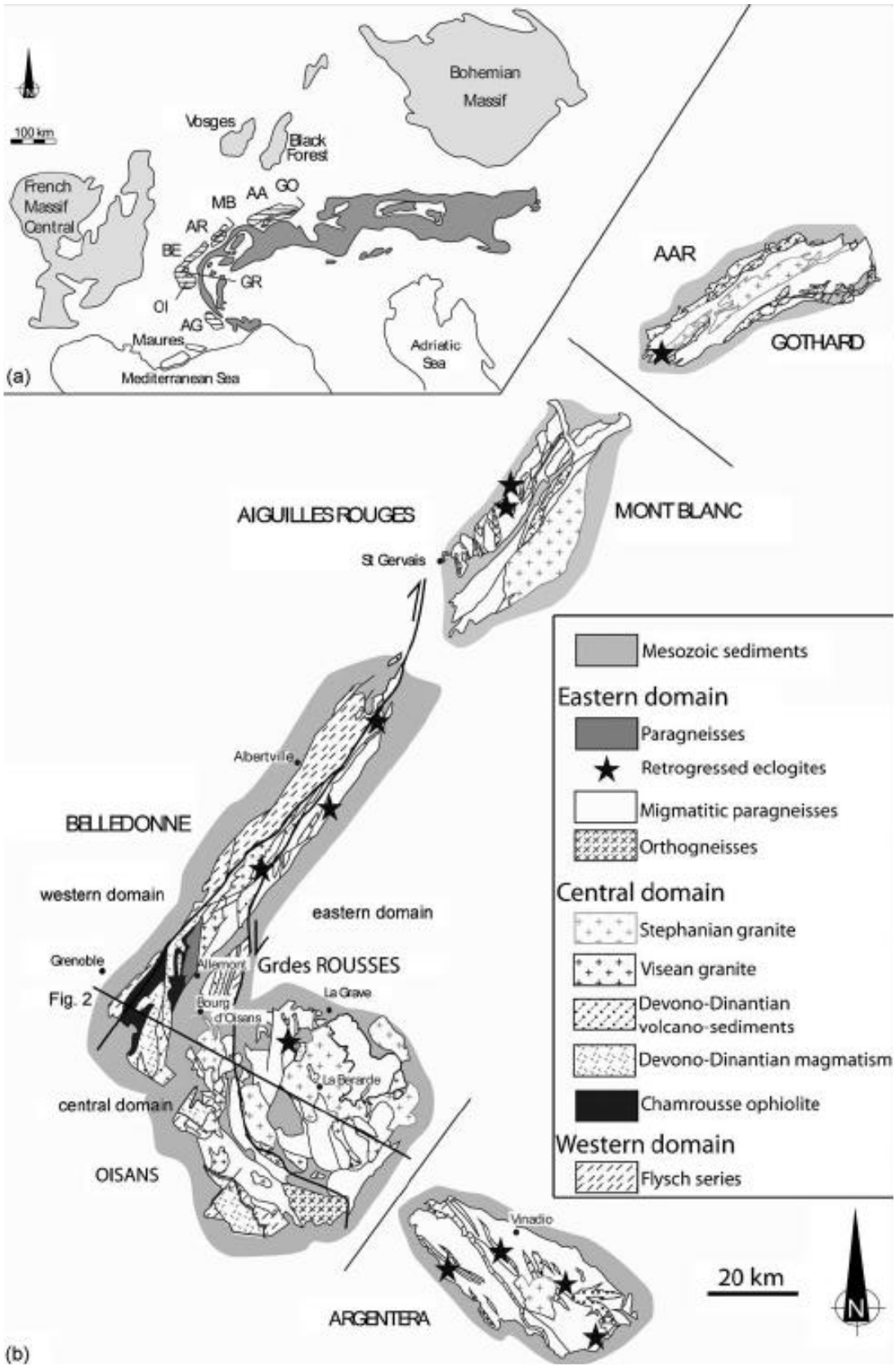

Fig. 1.4. - a) Simplified geologic sketch of the Alps and the European Variscan Massifs: AA = Aar; AG= Argentera; AR: Aiguilles Rouges; BE = Belledonne; GO = Gotthard; GR = Grandes Rousses; MB = Mont Blanc; OI = Oisans. b) Simplified geologic map of the External Crystalline Massifs (EMC) with legend (after Guillot et al., 2009).

Chapter 3
Piemonte Zone HP-LT ultramafic rocks

3.1 – Serpentinite and associated rocks in Valtournenche (Zermatt-Saas Zone, Western Alps)

In this subchapter, the published papers and unpublished data about Zermatt-Saas Zone serpentinite of Valtournanche are presented and organised in different sections. Contents are arranged according to the workflow of the multiscale structural analysis method. The chapter starts with the meso-and micro-scale structural analysis of UHP serpentinite (Luoni et al., 2019), followed by a contribution about the radiometric dating of assemblages marking the dominant HP S2 fabric, and the protoliths (Rebay et al., 2018). Finally, one published contribution on the first individuation of UHP assemblages in Alpine serpentinites (Luoni et al., 2018; American Mineralogist Noted Paper) is presented. A further submitted contribution (Luoni et al., submitted, subchapter 3.1.4), integrates microstructural analysis, metamorphic evolution, with quantitative geodynamic modelling. The final sections describe unpublished geochemical data and a focus on diopsidite enclosed in Valtournanche serpentinite. All the references of the published and submitted papers are integrated in the References chapter.

3.1.1 - Deformation history of ultra high-pressure ophiolitic serpentinites in the Zermatt-Saas zone, Créton, upper Valtournanche (Aosta valley, Western Alps)

Ofioliti, 2019, 44 (2), 111-123. https://doi.org/10.4454/ofioliti.v44i2.468
Pietro Luoni, Davide Zanoni, Gisella Rebay and Maria Iole Spalla

Abstract - Detailed multiscale structural analyses and mapping (1:20 scale) integrated with petrological investigation were used to study a portion of the Zermatt-Saas serpentinites that crop out in upper Valtournanche (north-western Italy). Results are synthesized in a foliation trajectory map that displays the transposed original lithostratigraphy of a serpentinite body exposed at Créton. The serpentinite body comprises magnetite sheets and rare, decimetre-thick, diopsidite layers and lenses. Moreover, veins and aggregates of Ti-chondrodite and Ti-clinohumite, olivine-rich layers and lenses, veinlets of olivine, and layers of dark pyroxenite are embedded in the serpentinites. Serpentinites and associated rocks record three relative age groups of ductile structures: D1 consists of rare folds and S1 foliation; D2 is a group of isoclinal folds and a very pervasive foliation (S2), which is the dominant structure; D3 includes a crenulation and shear zones affecting S2. The detailed meso-structural and microstructural analyses allowed individuating the metamorphic environment of successive deformation stages and correlating the resulting tectono-metamorphic investigation with those already inferred in surrounding areas. In addition, metre- to submillimetre-sized pre-D2 structural, mineralogical, and textural relics have been clearly identified in spite of the strong transposition imposed during the development of S2 high pressure - ultra-high pressure foliation.

3.1.1.1 Introduction

Serpentinites are ever more considered as key players in processes that involve lithosphere subduction and exhumation. Their structural and metamorphic evolutions are poorly explored with respect to those of crustal rocks due to their extreme plasticity and generally high compositional homogeneity (e.g. Scambelluri et al., 1995; Li et al., 2004; Grigull et al., 2012; Rebay et al., 2012, 2012b). Because of their low viscosity, the structural overprinting relationships in Alpine serpentinites are often very rich and therefore well-exposed key-outcrops preserving a long tectonic record, such as primary lithological heterogeneities, deserve extreme analytical care. In localities close to Créton, detailed petrostructural analysis (Zanoni et al., 2012, 2016) reconstruct the deformation history of serpentinites and rodingites and allow recognizing primary and metamorphic relic assemblages, often just preserved as single porphyroclasts. Generally during field mapping in the axial portion of orogenic belts, lithostratigraphic, structural and petrological observations are integrated into a modern structural map that reports foliation trajectories over the finite lithostratigraphic framework (Gosso et al., 1983; Passchier, 1990; Johnson and Duncan, 1992; Connors and Lister, 1995; Zucali et al., 2002; Gosso and Spalla, 2009; Baletti et al., 2012; Zanoni et al., 2012). The goal is therefore to collect the full assemblage of details on relative structural chronology, textural types reflecting fabric gradients (Gosso et al., 2010, 2015), and mineral assemblages marking successive foliations. The representation techniques can reveal the sequence of superposed textural and metamorphic imprints and allow following the lateral continuity of information that is the key for evaluating the significance of structural and mineral relics distribution at the regional scale. The integrated interpretation of

structural and petrologic data is basic for the reconstruction of the tectonic evolution (e.g. Spalla et al., 2005) and therefore this type of maps permits the recognition of geodynamic settings in which mantle and crust portions of orogenic scars have been forged during mountain building processes.
This approach is here applied to enclose the structures and lithologies within the tectonic framework of the Zermatt-Saas serpentinites in the upper Valtournanche and to separate the Alpine structures and fabrics from pre-Alpine oceanic relics. Finally, mineral assemblages associated with successive foliations are used to constrain the P-T-d-t evolution of the Créton serpentinites adding a new tile to the Zermatt-Saas Zone (ZSZ) tectono-metamorphic puzzle (Luoni et al., 2018).

3.1.1.2 Geological setting

The ZSZ is part of the Piemonte Zone, in the Penninic domain of Western Alps (Fig. 3.1.1.1a, b) (Bigi et al., 1990; Dal Piaz, 1992; Martin et al., 1994 and reference therein), comprising carbonatic and terrigenous metasediments, minor quartzites, metabasites, metagabbros, eclogites, rodingites, serpentinites, and minor ophicalcites. ZSZ is interpreted as a wreckage of the Alpine Tethys that is constituted by an ophiolitic suite typical of a slow-spreading setting (Boudier and Nicolas, 1985; Nicolas and Boudier, 2003) buried at mantle-depths, transposed during Alpine subduction-collision, and at present marking the oceanic scar in the axial zone of Western Alps. ZSZ includes serpentinized peridotites (Li et al., 2004; Rebay et al., 2012, 2012b), metagabbros and metarodingites (Li et al., 2004; Rebay et al., 2012, 2012b; Zanoni et al., 2016), N-MORB metabasites (Bucher et al., 2005 and reference therein), and minor metasediments as calcschists and quartzites (Bearth, 1967; Ernst and Dal Piaz, 1978; Tartarotti et al., 2017). The serpentinisation of ZSZ ultramafites was interpreted as mainly due to ocean floor metasomatism responsible also for the rodingitisation of the associated gabbroic dykes (Li et al., 2004; Rebay et al., 2012; 2012b; Zanoni et al., 2012; Zanoni et al., 2016). The ophiolitic complex locally hosts continental rock slices (Dal Piaz et al., 1983; Kienast, 1983; Weber and Bucher, 2015). The ZSZ rocks are widely deformed under eclogite-facies conditions and successively re-equilibrated under blueschist- to greenschist-facies conditions (Bearth, 1967; Ernst and Dal Piaz, 1978; Cartwrigth and Barnicoat, 2002). ZSZ rocks are tectonically coupled and sandwiched with those of the Combin Zone (CZ) between the Monte Rosa and Dent Blanche nappes (Fig. 3.1.1.1b) (Dal Piaz, 1988; Polino et al., 1990; Zingg et al., 1990). The Pancherot-Cime Bianche Unit (PCB) discontinuously marks the boundary between ZSZ and CZ. CZ has been interpreted as derived from an ocean-continent transition zone and is affected by a dominant metamorphic imprint under greenschist-facies conditions, with poorly preserved blueschist facies relics (Dal Piaz, 1974; Dal Piaz and Ernst, 1978; Ring, 1995; Cartwrigth and Barnicoat, 2002). PCB has been described as a continental affinity unit and consists of Permian to Cretaceous sedimentary protoliths (Dal Piaz, 1988, 1999). The tectonic contact between ZSZ and CZ has been repeatedly reworked during the Alpine convergence (Ballèvre and Merle, 1993; Pleuger et al., 2007). Radiometric data assign an age to ZSZ protoliths of oceanic metagabbros and metabasites between 164 and 153 Ma in the Swiss portion (Rubatto et al., 1998) and MORB percolations in serpentinites between 168 and 162 Ma in the Italian upper Valtournanche (Rebay et al., 2018). High pressure - ultra-high pressure peak conditions have been inferred in different localities of the ZSZ. Metabasites of Saas-Fee experienced peak conditions spanning from 1.9-2.2 GPa and 530-600 °C (Dale et al., 2009) and 2.3-2.5 GPa and 530-555 °C

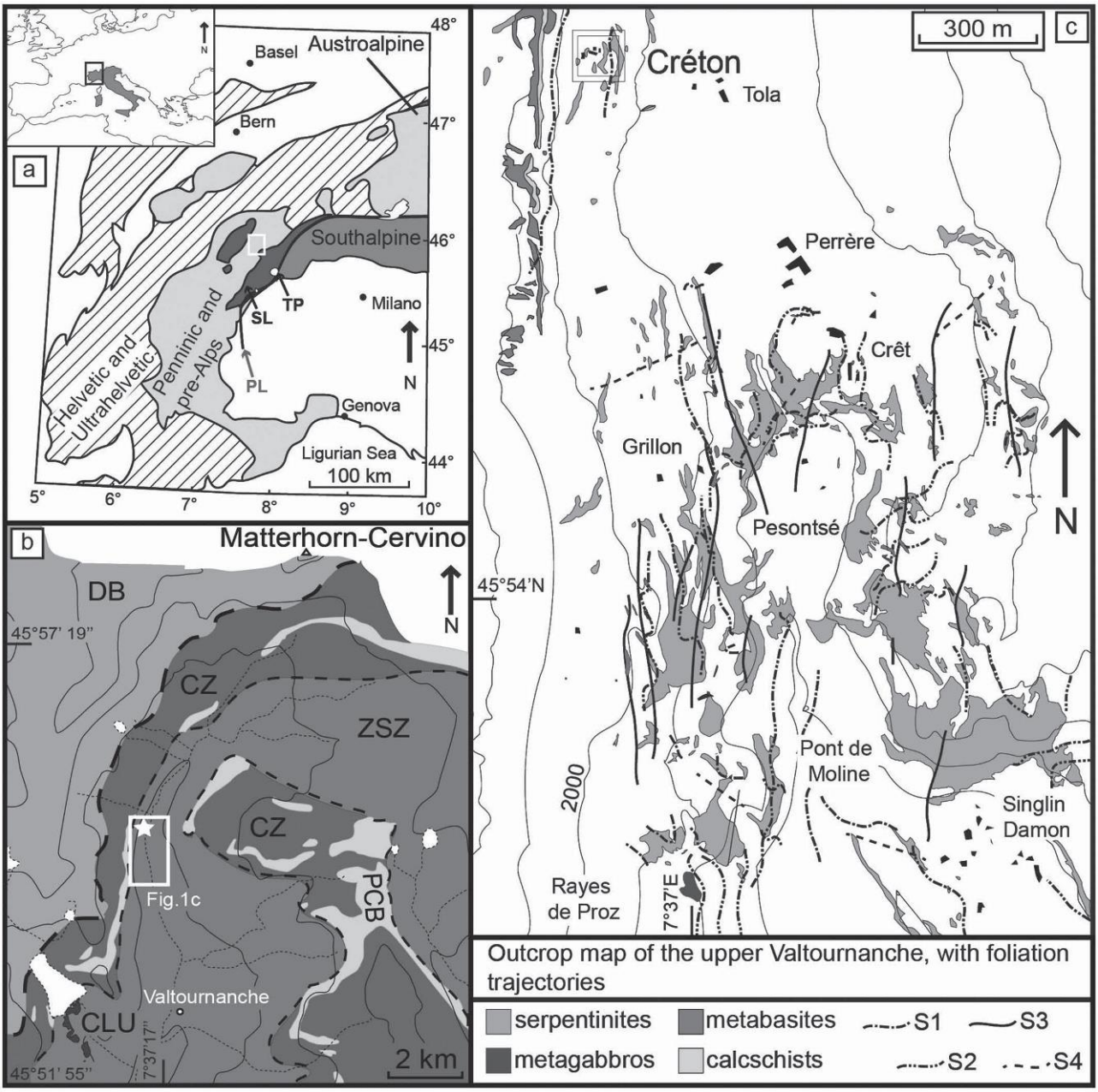

Fig. 3.1.1.1 - a) Simplified tectonic sketch of the Western Alps with the location of the studied area (in the white square). TP- Tertiary plutons; PL- Periadriatic Line; SL- Sesia-Lanzo Zone. b) interpretative tectonic map of the upper Valtournanche (modified after De Giusti et al., 2003). The white star localises Créton, the white rectangle circumscribes Fig. 3.1.1.1c. ZSZ- Zermatt-Saas Zone; CLU- Cignana Lake Unit (redrawn after Forster et al., 2004); PCB- Pancherot-Cime Bianche Unit; CZ- Combin Zone; DB- Dent Blanche nappe; c) outcrop structural map, modified after Rebay et al. (2018) and by Zanoni (unpublished: original mapping at 1:5000 scale) with the foliation trajectories in the meta-ophiolites of the upper Valtournanche (ZSZ). The double square localises Créton outcrops. Relative chronology of successive foliation trajectories and rock types are specified in the legend. Topography redrawn from the technical map of the Val d'Aosta Regional Administration, without hydrography.

(Angiboust et al., 2009) to 2.5-3.0 GPa and 550-600 °C (Bucher et al., 2005). Metagabbros in the ZSZ Swiss portion registered peak conditions at 1.75-2.0 GPa and 550-600 °C (Barnicoat and Fry, 1986), 2.5 GPa and 650 °C (Meyer, 1983) and 2.5 GPa and 610 °C (Bucher and Grapes, 2009). Reinecke (1991) deduced an ultra-high pressure peak of 3.0 GPa and 550-600 °C for quartzites at Lago di Cignana (Cignana Lake Unit = CLU). More recent estimates in CLU indicated conditions from 2.7 to

over 3.2 GPa for temperatures between 590 and 630 °C (van der Klauw et al., 1997; Reinecke, 1998; Groppo et al., 2009) and microdiamonds have been discovered in CLU oceanic meta-sediments (Frezzotti et al., 2011) shifting the peak-conditions at P ≥ 3.2 GPa and T = 600 °C. High pressure at the limit with ultra-high pressure peak conditions are also reported in few studies on serpentinites in the Swiss portion of ZSZ, up to 2.0-2.5 GPa and 600-650 °C (Li et al., 2004), and in Valtournanche, where serpentinites experienced 2.2-2.8 GPa and 580-620 °C (Rebay et al., 2012, 2012b) similarly to the associated rodingites that re-equilibrated at 2.3-2.8 GPa and 580-660 °C (Zanoni et al., 2016). Peak conditions of 2.2-2.3 GPa and 515-645 °C were estimated in a continental slice tectonically embedded in ZSZ ophiolitic rocks at Trockener Steg, in the upper Zermatt valley (Weber and Bucher 2015). In the Créton serpentinites (upper Valtournenche) mapped in this study, Ti-chondrodite relic assemblages allowed to infer 2.8-3.5 GPa and 600-670 °C, indicating that ultra-high pressure assemblages are definitely recorded also in serpentinites (Luoni et al., 2018). Although these Ti-humites bearing assemblages indicate UHP conditions, according to isotopic compositions Gilio et al. (2019) infer a gabbroic origin for their protolith, which was successively metasomatized and recrystallized during subduction. High pressure peak in ZSZ was dated between 70 and 38 Ma, but ages for prograde metamorphic imprints are assessed at least at 80 Ma (Bowtell et al., 1994; Rubatto et al., 1998; Dal Piaz et al., 2001; Skora et al., 2009, 2015; Springer et al., 2009; de Meyer et al., 2014; Weber et al., 2015; Rebay et al., 2018). Syn-D2 mineral associations in serpentinites from upper Valtournanche post-date the ultra-high pressure humite-bearing assemblage and have been dated at 65.5 ± 5.6 Ma (Rebay et al., 2018). This wide range of ages and metamorphic conditions is consistent with a heterogeneous tectonic evolution of different portions of the ZSZ meta-ophiolites that recorded diachronic pressure peaks under different P-T conditions.

3.1.1.3 Structural map

Heterogeneously deformed metamorphic terrains can provide high quality material for laboratory studies after field structural analyses that infer the chronological sequence of structural and metamorphic imprints (e.g. Hobbs et al., 1976; Passchier, 1990; Spalla and Zucali, 2004; Gosso et al., 2015). Indeed, the studied rocks consist of serpentinites that enclose diopsidite and olivine-rich layers and lenses, issued from thoroughly evolved rheological environments. Our structural map reports the grid of superposed foliations and the related transposition of the lithostratigraphy in adjacent outcrops, integrating also the micro-scale results in the definition of grain-scale layering. To show the reworking of lithostratigraphy in detail, a mapping scale of 1:20 was chosen. The recognition of relic structures and textures and the identification of the oceanic lithostratigraphy was possible despite the strong transposition imposed during the pervasive mylonitization. In the map plate a synthetic scheme (1:200 scale) is reported to locate the outcrops mapped at 1:20 scale. This map was drawn using aerial photos from the Geo-Portal of Valle d'Aosta regional administration (http://geoportale.partout.it/). The legend reports lithotypes and fabric elements. Structural orientation data are shown in equal area Schmidt projections (lower hemisphere) separated according to relative chronology. Detailed outcrop maps are georeferenced and the related data are stored into a geodatabase set within a Geographic Information System (GIS) platform. Interpreted 1 m-spaced contour lines have been added on the detailed maps to show the intersection of structures and topography and render the three-dimensional polydeformed lithostratigraphy. The map plate is attached to the thesis as Appendix 1.

3.1.1.4 Lithostratigraphy

In upper Valtournanche, serpentinites are dominant and host hectometre-sized metagabbro bodies and metre-sized rodingite dykes and boudins; a pervasive S2 foliation dominates in serpentinites (Rebay et al., 2012, 2012b, 2018). Créton alpages are located on a ledge over the western slope of Valtournanche. Here outcrops show whaleback surfaces, which, after a patient iron brushing of mosses and lichens, display a great wealth of structures. Créton serpentinites are located in the structurally uppermost part of ZSZ, close to the tectonic contact with the overlying CZ calcschists and metabasites (Fig. 3.1.1.1c). Two types of serpentinites were distinguished on the basis of textural and mineral features: white porphyroclasts serpentinites and olivine-rich serpentinites. Both serpentinite types contain Ti-chondrodite + Ti-clinohumite veins and olivine. Furthermore, all the serpentinites enclose olivine-rich layers, diopsidites, and pyroxenites. Primary relationships between different rocks are synthesized in Table 3.1.1.1 (row "lithostratigraphy"). Modal amounts were quantitatively evaluated using optical microscope.

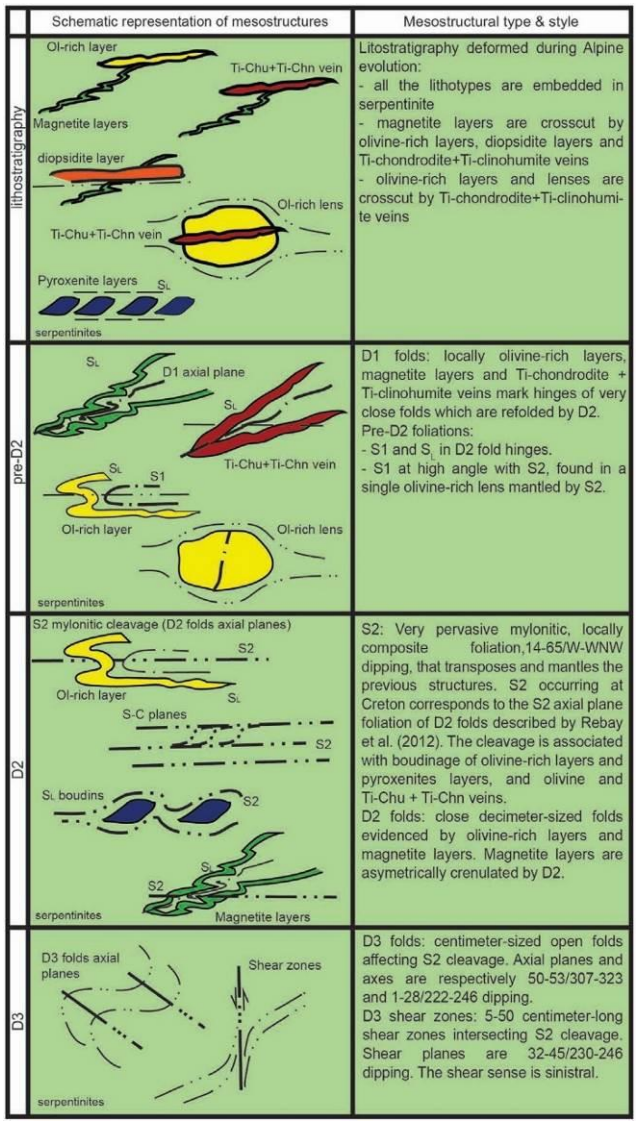

Table 3.1.1.1 - Schematic representation of meso-structures detected in serpentinites and associated rocks. The structural setting of rock assemblages in each field reflects the present-day arrangement, whereas bold traces indicate structures related to the described stage (pre-D2, D2, D3).

The *white porphyroclasts serpentinites* (Fig. 3.1.1.2a, b; outcrop 1 and 2, on the map plate) consist of antigorite (60-90%), magnetite (10-15%), olivine/clinopyroxene (5-10%), calcite + dolomite (< 5%), and locally Ti-clinohumite, chlorite and apatite (<5%). Generally, an altered surface with white and pale grey oval (up to) centimetre domains in an aqua-green matrix, characterizes this very fine- to fine-grained rock, which is affected by a pervasive mylonitic foliation.

Olivine-rich serpentinites (Fig. 3.1.1.2c, d; outcrop 1, on the map plate) appear as ochre, yellow to brownish rocks at the altered surfaces. They contain fine-grained antigorite (50-80%), olivine (20-30%), magnetite (5-15%), chlorite (< 5%), and are rich in millimetre- to submillimetre-thick olivine veins. Also in the olivine veins a mylonitic foliation is the dominant fabric (Fig. 3.1.1.2d).

Both serpentinite types are rich in magnetite layers (Fig. 3.1.1.2a, c; outcrop 1, on the map plate) constituted by magnetite (50-90%), antigorite (10-30%), and locally olivine (10-20%). Layer boundaries are fuzzy due to the transposition produced during the development of the dominant S2 foliation. The metre to decimetre alternation of these two serpentinite types, streaked by magnetite layers, could represent an original compositional layering, transposed during Alpine tectonics.

Fine- to coarse-grained *Ti-Chondrodite + Ti-Clinohumite veins*, with Ti-chondrodite + Ti-clinohumite reddish in colour (Fig. 3.1.1.2b, d, e; outcrop 2, on the map plate), occur in almost all the mapped outcrops and are often rimmed by a centimetre whitish antigorite aggregate. They are composed by Ti-chondrodite + Ti-clinohumite (70-80%), olivine (10-20%), antigorite (5-10%), magnetite ± ilmenite (5-10%),

chlorite (< 5%).

Diopsidites (Fig. 3.1.1.3a, b; outcrop 1 and 6, on the map plate) are constituted by diopside (whitish crystals) (70-80%), antigorite ± chlorite (10-20%), tremolite + actinolite (5-20%), ilmenite ± titanite (5%) and locally contain magnetite, calcite, and apatite (< 5%). They are fine- to coarse-grained and form grey and ochre layers to lenses parallelized into the dominant foliation. Diopsidites preserve more than one mineral-scale foliation, their boundaries with serpentinites are sharp, and often are rimmed by chlorite schists.

Chlorite schists, constituting 1 to 10 cm thick rims between serpentinites and diopsidites (Fig. 3.1.1.3a, outcrop 1, on the map plate), are made of chlorite (60%), clinopyroxene (augite + diopside) (20%), antigorite (10-15%), ilmenite (10%), tremolite and magnetite (2-3%). Locally Ti-clinohumite occurs within these layers.

In serpentinites, boudins and layers of dark *pyroxenites* occur (Fig. 3.1.1.3c, d; outcrop 3 and 5, on the map plate) and are constituted by clinopyroxene (augite + diopside) (70- 80%), antigorite ± chlorite (10-20%), ilmenite ± magnetite (5%), Ti-chondrodite + Ti-clinohumite (5%), tremolite (< 2%). Grain size varies from centimetre clinopyroxene porphyroclasts to the submillimetre grains of diopside, chlorite, and antigorite in the matrix. Locally (outcrop 5, on the map plate), pyroxenite layers or lenses are rimmed by Ti-chondrodite + Ti-clinohumite aggregates with minor oxides.

Yellow very fine- to coarse-grained *Olivine rich-layers* are well exposed in outcrops 2, 3, and 5 (map plate) and occur in 1 to 20 centimetres thick layers and decimetre-sized lenses. They are rich in olivine (60-90%) and contain antigorite (10-20%), magnetite ± Cr-magnetite (10%), chlorite (< 5%), Ti-chondrodite + Ti-clinohumite (< 5%), dolomite (< 2%) and diopside (< 1%).

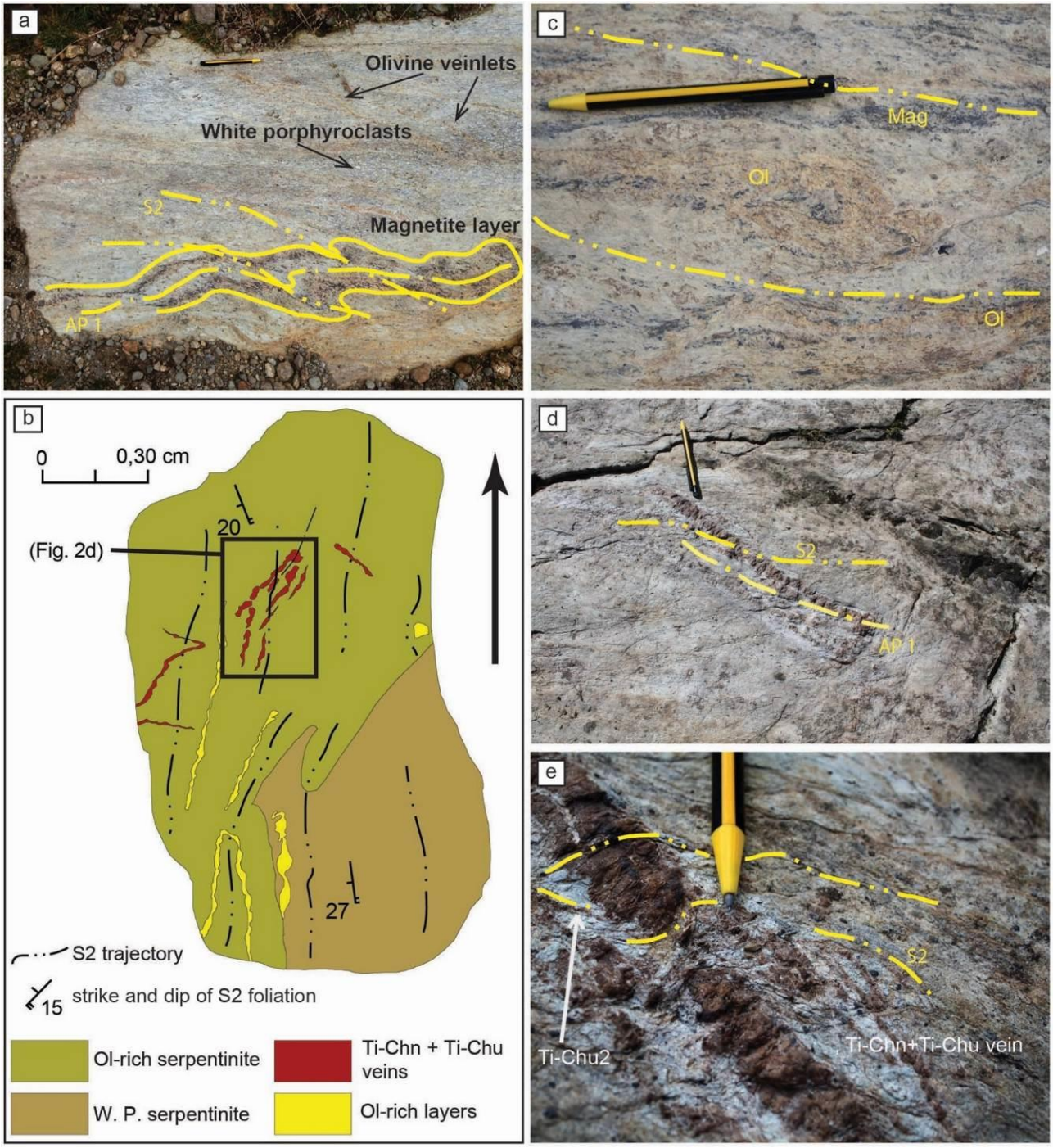

Fig. 3.1.1.2 - Créton area meso-structures: a) Magnetite layer in serpentinites. The magnetite layer is isoclinally folded during D1 and crenulated and foliated during D2. S2 mantles pale, lenticular porphyroclasts. In the upper part of the outcrop olivine-bearing veins are parallel to S2 (outcrop 1); b) detail of outcrop 2a: the contact between white porphyroclasts serpentinites (W.P. serpentinites) and olivine-rich serpentinites is folded by D2. Furthermore, Ti-chondrodite + Ti-clinohumite veins are folded by D1 and transposed, crenulated, and foliated by D2; c) relationships between S2 and mineral layering in olivine-rich serpentinites; d) Ti-chondrodite + Ti-clinohumite vein that marks a D1 fold hinge and is transposed during D2 (outcrop 2 in the map); this structure is included in Fig. 3.1.1.2b; e) Close-up on Ti-chondrodite + Ti-clinohumite lenses (Fig. 3.1.1.2d) intersected by S2 with Ti-clinohumite2 in the pressure shadows.

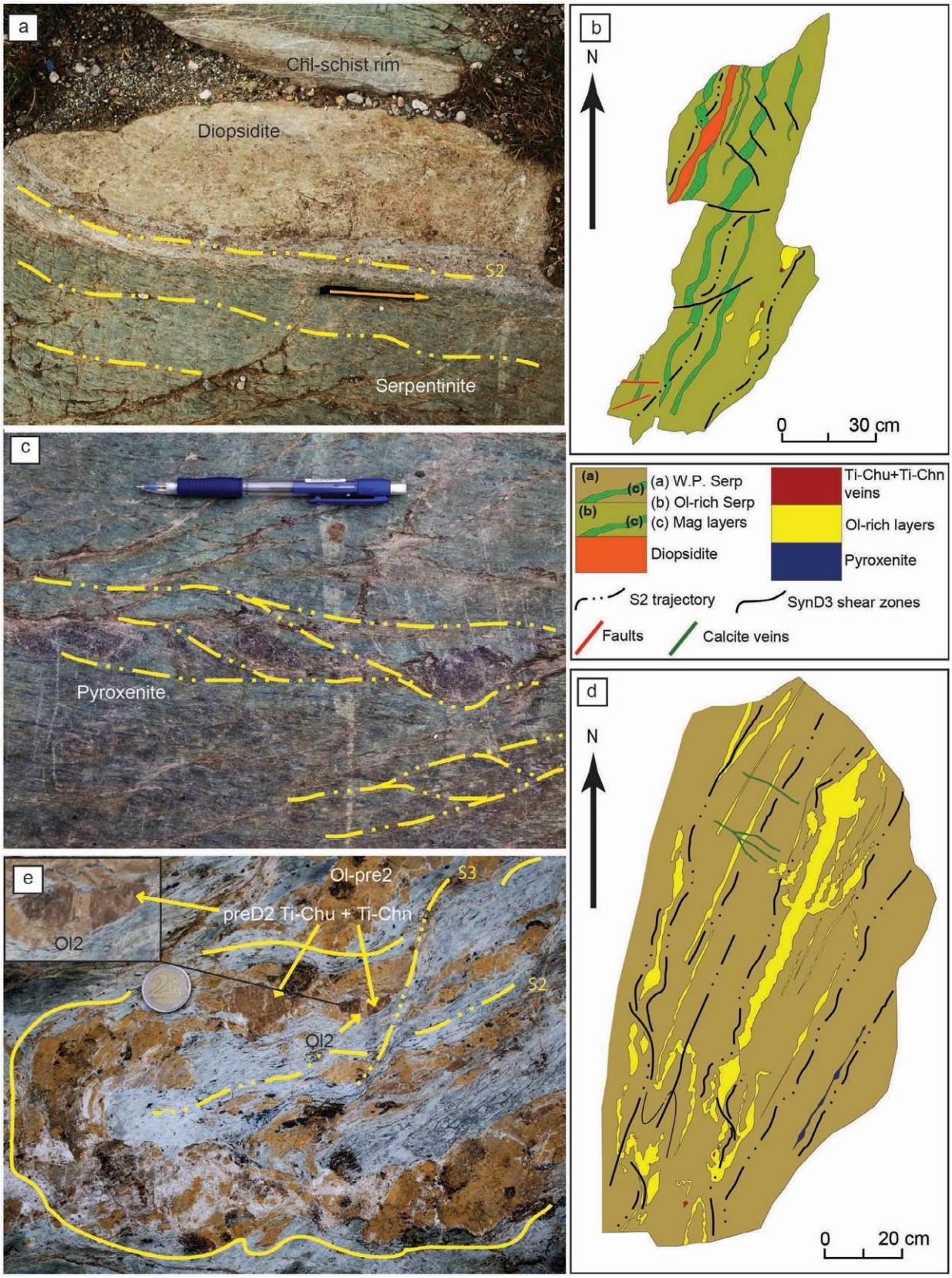

Fig, 3.1.3 - Créton area meso-structures: a) decimetre-thick layer of diopsidite with rims of chlorite schists parallel to S2 (outcrop 1 in the map); b) detail of outcrop 6a: magnetite layers, olivine-rich layers and a layer of diopsidite, embedded in olivine-rich serpentinites, are transposed and parallelised into S2. A magnetite layer is crosscut by the diopsidite and some of the magnetite layers are crosscut by D3 shear zones (legend between Fig. 3.1.1.3b and d); c) layer of aligned lenses of

dark pyroxenite intersected by the composite S-C D2 fabric (outcrop 1 in the map); d) detail map of outcrop 5, olivine-rich layers, enclosed in white porphyroclasts serpentinite (W.P. Serp), mark D2 fold hinges, whose flanks are folded by D3. S2 is the axial plane foliation. A layer of pyroxenite is boudinaged by D2 and parallelized into S2. Calcite veins crosscut S2 foliation (legend between Fig. 3.1.1.b and d); e) olivine-rich layer isoclinally folded and boudinaged during D2 and intersected by S2 foliation; the layer is displaced along a D3 shear zone. Note the porphyroclast of pre-D2 Ti-chondrodite + Ti-clinohumite affected by syn-D2 boudinage with necks filled by olivine2 (outcrop 5 in the map).

A few millimetre-thick ochre-yellow *olivine veinlets* are composed by coarse- to fine-grained olivine (90-95%), antigorite (10-15%), and magnetite (5%). Veins show different lengths, from few centimetres to more than 1 metre and are wrapped, parallelized, and boudinaged by the dominant foliation (Fig. 3.1.1.2a; outcrop 1, on the map plate).
Calcite-bearing veins are undeformed, usually at a high angle with respect to the dominant foliation and constituted by calcite (90%) and minor oxides (10%).

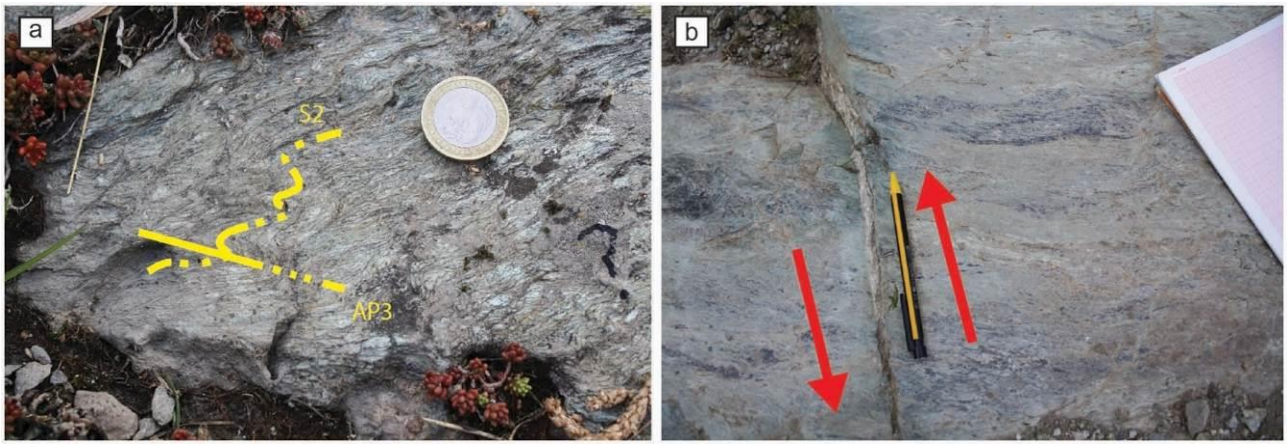

Fig. 3.1.1.4 - Créton area meso-structures: a) D3 crenulation affecting S2 foliation in serpentinites (outcrop 2 in the map); b) sinistral fault, mineralized by antigorite fibres (outcrop 6 in the map), displacing a magnetite layer.

3.1.1.5 Structural relationships

Three groups of superimposed ductile structures, indicated as pre-D2 (comprising pre-D2 mineral micro-aggregates and rare D1 mesoscopic fabric elements) D2, and D3, and a fourth group of brittle structures affect serpentinites and the interlayered rocks. In Table 3.1.1.1 the main relationships between structures and rocks are schematically reported. All the rocks exposed at Créton record a dominant foliation that according to structural features, orientation, and mineral composition is identified as the same regional S2 recognized by Rebay et al. (2012a, 2012b), Zanoni et al. (2012, 2016). Like in Valtournanche, at Créton S2 is the structure that mostly affects the lithostratigraphic boundaries. In places, primary mineralogical layering and boundaries between the different serpentinite types and between serpentinites and the embedded lithotypes (e.g. Fig. 3.1.1.3d: serpentinite - olivine-rich layers' contact) escaped the transposition during successive deformation stages. Primary foliations (SL) corresponding to lithological boundaries between white porphyroclasts serpentinites and olivine-rich serpentinites are locally blurred. Where sharp, SL is folded by or parallel to the dominant foliation.
The two types of serpentinite constitute alternating and tectonically interlayered metre-thick bands. Millimetre- to centimetre-thick and centimetre- to metre-long magnetite layers in serpentinites are

strongly transposed (see for examples outcrop 1 in which all the variably sized-layers exist). Diopsidite lenses and layers are parallel to the dominant foliation of serpentinites. Diopsidite layers locally crosscut magnetite thin layers (Fig. 3.1.1.3b; outcrop 6a). Also the dark pyroxenite layers (outcrops 1, 3, 5 and 6) are parallelized and boudinaged into the dominant foliation. Boudins are normally oblate. Locally, isolated centimetre-sized lenses of pyroxenites occur (outcrop 2c). Olivine-rich layers and lenses are mainly parallelized into and wrapped by the dominant foliation (outcrop 2 and 3).

Ti-chondrodite + Ti-clinohumite veins are wrapped and boudinaged within the S2 foliation and locally veins at high angle with S2 are variably transposed. Olivine veins are mostly parallel to S2 (see outcrop 1) whereas Ti-chondrodite + Ti-clinohumite vein orientations are more variable with respect to the same foliation.

D1 stage affected serpentinites, magnetite layers, olivine-rich layers, a diopsidite layer, and Ti-chondrodite + Ti-clinohumite veins, as shown by the D1 fold hinges and S1 foliation recorded in localized layers and lenses of diopsidite and olivine-rich layers. In outcrop 1 (see map plate), magnetite layers are often isoclinally folded during D1 (Fig. 3.1.1.2a), whereas an olivine-rich layer marks a D1 isoclinal fold in outcrop 5. Rare S1 foliation marked by antigorite and magnetite constitutes D2 fold hinges in serpentinites. In outcrop 2a (see map plate), a Ti-chondrodite + Ti-clinohumite vein materializes an isoclinal D1 fold hinge (Fig. 3.1.1.2d): the axial plane is sub-vertical and forms an angle of 10° with S2 (outcrop 2a in map plate). The olivine-rich boudinaged layers in outcrop 2b (see map plate) preserve a very rare pre-D2 (S1) foliation marked by layers of granoblastic olivine aggregates. In outcrop 6a, also diopsidite preserves a pre-D2 (S1) foliation, which is marked by the SPO of diopside porphyroclasts, at high angle with respect to S2 in serpentinites.

D2 structures consist of folds and S2 foliation. S2 is a mylonitic, locally composite, foliation and is the dominant fabric element in the Créton outcrops. S2 dips W-WNW/14°- 65° in all the lithotypes.

D2 folds deform the contact between the white porphyroclasts and the olivine-rich serpentinites (outcrops 1 and 2a; see map plate) with isoclinal decimetre folds associated with S2 axial plane foliation. In both serpentinite types, S2 is mylonitic, pervasive, and affects all the embedded lithotypes. Locally S-C foliations occur (outcrop 1, Fig. 3.1.1.3c), with millimetre- to centimetre-spaced C planes. In magnetite layers, S2 is marked by films of magnetite and antigorite. D2 is evidenced also by an asymmetric crenulation (outcrop 1; see map plate). Generally, in these levels S2 is marked by trails of magnetite grains (S2 thin films). D1 fold limbs are parallel to and intersected by S2 (Fig. 3.1.1.2a). Because of its pervasiveness, S2 obliterated S1 axial plane foliation.

Diopsidite layers and lenses are parallel to S2 that wraps also around them. The diopsidite layer and the associated chlorite schist rims in outcrop 1 (see map plate and Fig. 3.1.1.3) are pervasively foliated by S2, which is mylonitic in the rim. Olivine-rich layers and lenses are enveloped by S2 and the same layers are affected by isoclinal to open D2 folds with centimetre to decimetre hinges (Fig. 3.1.1.3d, e; outcrop 5 in map plate). Syn-D2 boudins of olivine-rich layers occur. Locally, also Ti-chondrodite + Ti-clinohumite lenses in olivine-rich layers are boudinaged during D2 development and their necks are filled with olivine.

Dark pyroxenite layers are transposed, parallelized, and boudinaged into S2 foliation (Fig. 3.1.1.3c; outcrops 3 and 5; map plate). Where S2 is an S-C composite fabric, pyroxenite lenses are often aligned along S-planes. Ti-chondrodite + Ti-clinohumite veins are parallelized into S2 mineral layering of the serpentinites, and are locally boudinaged and wrapped by S2 (outcrops 2 and 4; map plate). Veins at a

high angle with S2 are foliated and crenulated. Isolated aggregates of Ti-chondrodite + Ti-clinohumite grains are elongated into S2 and display pressure shadows bounded by thin anastomosed layers of Ti-clinohumite (Fig. 3.1.1.3e) marking S2 (outcrop 2a; map plate).

Rare D3 centimetre-wide crenulation affects S2 in serpentinites. D3 fold axial surfaces dip at medium angle towards WNW and fold axes dip at a low angle towards WSW (Fig. 3.1.1.4a). Locally, olivine-rich layers parallel to S2 and S2 are deviated by syn-D3 decimetre-long sinistral shear zones (see outcrop 5 in map plate; Fig. 3.1.1.3d, e).

The Créton serpentinites are finally affected by *D4* sub- vertical E-W dilatant fractures, mostly filled by calcite (outcrop 5) or by perpendicular to oblique serpentine fibres. Where fibres are oblique, fractures are actually small sinistral strike-slip faults with an offset of 5-10 cm (outcrops 1and 6 in map plate; Fig. 3.1.1.4b).

3.1.1.5 Microstructures and metamorphic evolution

In the following, we describe the main microstructural features used to infer the mineral assemblages marking the superposed fabrics, and therefore the timing of the successive metamorphic and deformation events affecting them. Pre-D2 relicts include D1 structures and mineral and textural domains. D1 structural relics are scarce, with surfaces never exceeding one metre. Their marked re-orientation by transposition and discontinuity inhibits direct correlation of D1 structures even in the same outcrop. Due to D2 intense transposition, mineral relics occurring as porphyroclasts or polygonal lenticular aggregates, wrapped by S2, are described as part of pre-D2 assemblages, not being univocally relatable as D1 fabrics as is the case for S1 relic foliation.

In the *white porphyroclasts serpentinites*, S2 is mylonitic, locally characterized by S-C planes and is marked by antigorite + magnetite and locally by diopside/olivine + Ti-clinohumite + chlorite. S2 wraps millimetre-sized porphyroclasts of magnetite, olivine/clinopyroxene, Ti-clinohumite, lenses of antigorite flakes, often rimmed by a thin magnetite corona (Fig. 3.1.1.5a), either iso- or randomly-oriented. Locally, porphyroclasts of pre-D2 dolomite, with dolomite2 rims, and apatite are enveloped by S2. Calcite veins occur at high angle with respect to S2. Occasionally, D3 folding is associated with an incipient S3 axial plane foliation marked by antigorite + magnetite.

In the very fine-grained *olivine-rich serpentinites* olivine2 and antigorite2 mark the S2 continuous and mylonitic pervasive foliation, wrapping pre-D2 magnetite + olivine porphyroclasts (Fig. 3.1.1.5b). Locally, micro-layers of magnetite mark D2 microfold hinges and scattered aggregates of Ti-clinohumite2 occur in the matrix. In both serpentinite types, D3 shear zones and S3 axial plane foliation are marked by antigorite3 + magnetite3 ± tremolite3.

The millimetre-thick *magnetite layers* within the hosting serpentinites comprise pre-D2 magnetite porphyroclasts and submillimetre grains of magnetite2 parallel to S2. These layers may have recorded a strong transposition during D2 development.

The *Ti-chondrodite + Ti-clinohumite veins* preserve porphyroclasts of red-orange twinned pre-D2 Ti-chondrodite (Fig. 3.1.1.5c), olivine, and spinel (currently replaced by ilmenite + magnetite) that are mantled by polygonal aggregates of Ti-chondrodite + Ti-clinohumite + ilmenite + magnetite
+ olivine + chlorite (related to the pre-D2 to early D2 stage, Luoni et al., 2018). In the veins these core-mantle structures are wrapped by S2 underlined by Ti-clinohumite2 + olivine2 + antigorite2 + magnetite2 + chlorite2 (Fig. 3.1.1.5d).

In *diopsidites* pre-D2 diopside porphyroclasts are parallel to S2 and often rimmed by a corona of polygonal diopside2 (Fig. 3.1.1.5e). They include single grains of magnetite, antigorite, and chlorite. Porphyroclasts of pre-D2 ilmenite, rimmed by titanite2, and apatite also occur. S2 is marked by diopside + antigorite + chlorite ± ilmenite. Calcite2 is locally interstitial between diopside porphyroclasts. Randomly oriented needles of tremolite3 and actinolite3 overgrew S2 foliation.
In *chlorite schists*, continuous and mylonitic S2 foliation is marked by SPO of chlorite, diopside, and antigorite and wraps porphyroclasts of clinopyroxene, chlorite, ilmenite, and magnetite. Locally relic Ti-clinohumite grains occur. Chlorite3 and tremolite3 locally overgrew S2.
In *pyroxenites* pre-D2 clinopyroxene porphyroclasts are deformed, often kinked and rich in inclusions of antigorite, ilmenite, magnetite, chlorite, Ti-clinohumite, and Ti-chondrodite. Occasionally they preserve inclusion-free augitic cores. Some clinopyroxene porphyroclasts are extensively to completely re-crystallized in sub-grains or new grains of diopside2 or replaced by chlorite2. Diopside2 inclusion-free rims also occur around some pre-D2 clinopyroxene porphyroclasts. Locally, spinel (currently ilmenite + magnetite) occurs in aggregates within Ti-clinohumite and Ti-chondrodite polygonal aggregates. Ilmenite + magnetite + Ti-chondrodite+ Ti-clinohumite polygonal aggregates rim pre-D2 clinopyroxene and spinel (Fig. 3.1.1.5f). Pre-D2 clinopyroxene is wrapped by a S2 foliation that is marked by diopside + antigorite + Ti-clinohumite + magnetite + chlorite.
In *olivine-rich layers* (Fig. 3.1.1.5g), millimetre-sized porphyroclasts of pre-D2 olivine (with magnetite, antigorite, and rare diopside inclusions) and Cr-magnetite, rimmed by magnetite2, are mantled by sub-millimetre pre-D2 to early D2 polygonal aggregates of olivine + antigorite + magnetite (Luoni et al., 2018), locally with dolomite and Ti-clinohumite. Rare pre-D2 millimetre Ti-chondrodite twinned crystals, surrounded by Ti-chondrodite + Ti-clinohumite polygonal aggregates, have been observed. S2 is marked by olivine + antigorite + magnetite ± Ti-clinohumite.
The *olivine veinlets* consist of rows of pre-D2 millimetre-sized olivine porphyroclasts (Fig. 3.1.1.5h) that are wrapped by antigorite2 aligned within S2 foliation. Olivine porphyroclasts contain antigorite + magnetite inclusions, Ti-clinohumite tapering lamellae, and are rimmed by olivine2. Towards the veins, sub-millimetre grains of olivine2 occur in the antigorite + magnetite matrix and an olivine2 SPO marks S2 foliation.
In Table 3.1.1.2, a summary of the mineral assemblages marking the successive fabric elements is shown for each rock type.

Rock type	Mineral modes	Mineral assemblages synkinematic with successive deformation stages			
		pre-D2	pre-D2 to early D2	D2	D3 and post D2
Serpentinite	Srp (60-90%), Ol (5-30%)/Cpx (5-10%), Mag (5-15%), Ti-Chu (5%), Cal + Dol (<5%). Locally Chl, Ap (<5%)	Srp + Mag + Cpx/Ol + Ti-Chu + Dol + Ap		Srp + Mag + Cpx/Ol + Ti-Chu ± Chl ± Cal ± Dol	Srp + Mag + Chl + Cal
Ti-Chn + Ti-Chu veins	Ti-Chn + Ti-Chu (70-80%), Ol (10-20%), Atg (5-10%), Mag ± Ilm (5-10%), Chl (<5%)	Ti-Chn + Ex-Spl + Ol ± Chl + Srp	Ti-Chn + Ti-Chu + Ol + Ilm + Mag + Chl + Srp	Ti-Chu + Srp + Ol + Chl + Mag	
Pyroxenite	Cpx (70-80%), Atg ± Chl (10-20%), Ilm ± Mag (5%), Ti-Chn + Ti-Chn (5%), Amph (<2%)	Cpx (augitic core) + Spl + Srp + Chl (+ Ti-Chn)	Cpx + Srp + Chl + Ti-Chn + Ti-Chu + Ilm + Mag	Cpx + Srp + Ti-Chu + Chl + Mag	Srp + Chl + Mag + Amph
Olivine-rich layers and lenses	Ol (60-90%), Atg (10-20%), Mag ± Cr-Mag (10%), Chl (<5%), Ti-Chn + Ti-Chn (<5%), Dol (<2%) Cpx (<1%)	Ol + Srp + Mag + Cr-Mag + Cpx ± Ti-Chn + Chl	Ol + Srp + Mag + Ti-Chu + Dol	Ol + Srp + Mag + Ti-Chu	Srp + Cal

Table 3.1.1.2 - Mineral modes and assemblages marking superposed fabrics for the different rock types.

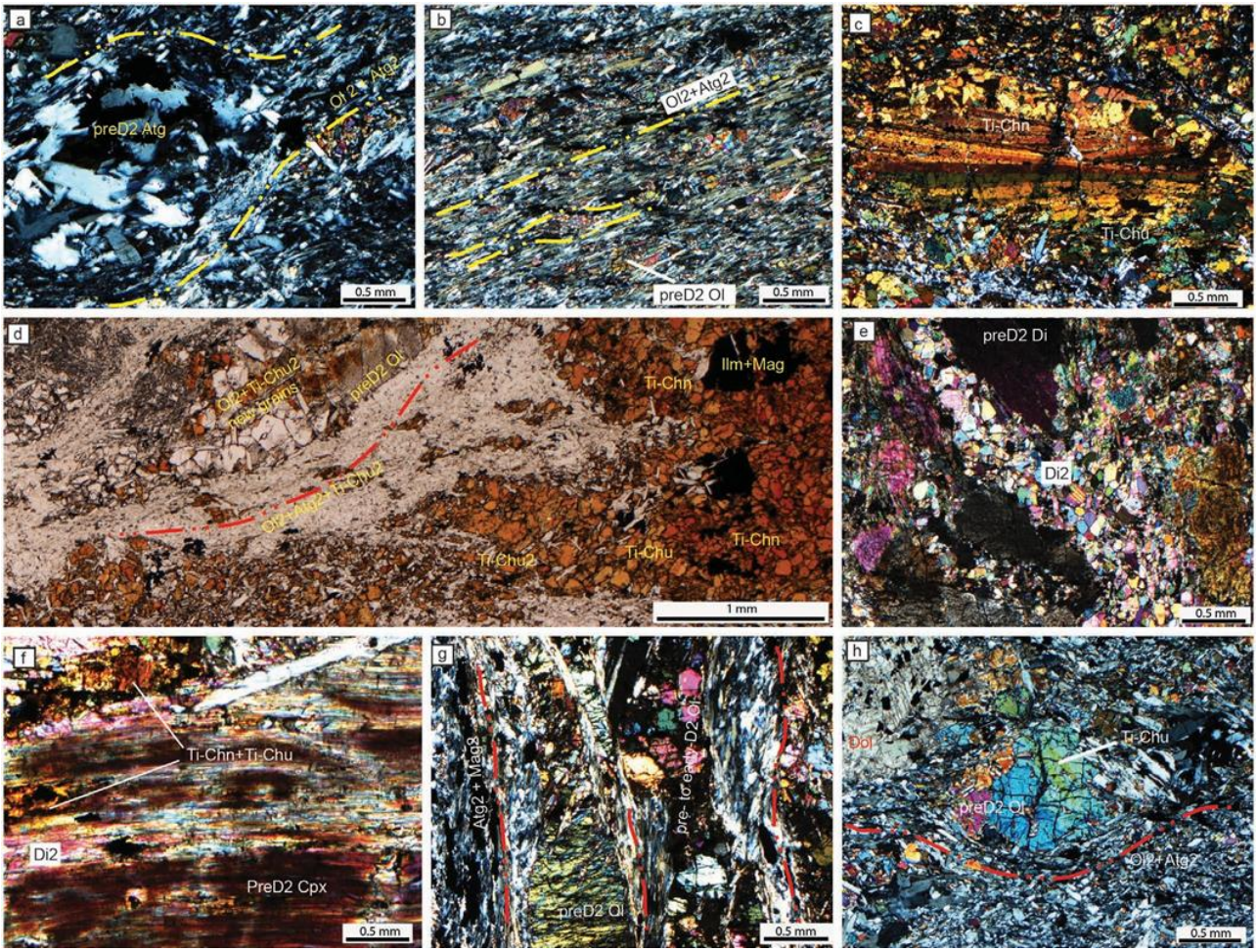

Fig. 3.1.1.5 - Créton area microstructures: a) completely serpentinized white lenticular domain wrapped by S2, made of antigorite2 and olivine2 (crossed polars) from outcrop 1; b) olivine-rich serpentinites with S2 marked by antigorite2, olivine2, and magnetite2 from outcrop 1; S2 wraps around pre-D2 olivine porphyroclasts (crossed polars) partly recrystallized, as evidenced by sub-grains and new grains; c) a porphyroclast of Ti-chondrodite mantled by Ti-clinohumite (core mantle structure) from a Ti-chondrodite + Ti-clinohumite vein in outcrop 2a (crossed polars); d) pre-D2 to early D2 Ti-chondrodite + Ti-clinohumite + ex-spinel occupying lenticular domains and pre-D2 olivine porphyroclasts wrapped by olivine2 + antigorite2 + Ti-clinohumite2, and magnetite2 along S2 (outcrop 2a in map plate); e) Diopsidite from outcrop 1. Pre-D2 diopside porphyroclast mantled by polygonal new grains of diopside2; f) Ti-chondrodite + Ti-clinohumite filling fractures and cleavages of a pre-D2 clinopyroxene porphyroclast (crossed polars; outcrop 2c); g) olivine-rich layers with S2 at the contact with serpentinites (layers rich in antigorite, outcrop 4); S2 wraps around porphyroclasts of pre-D2 olivine and polygonal olivine grains and is marked by antigorite2 and magnetite2; crossed polars; h) olivine porphyroclast, from a boudinaged olivine veinlet, with Ti-clinohumite tapering lamellae, mantled by S2 (from outcrop 1), crossed polars.

The inferred parageneses, coupled with chemical analyses of selected microstructural domains (Rebay et al., 2012, 2012b; Luoni et al., 2018), allowed constraining PT conditions under which pre-D2, D2 and D3 fabrics developed. Results are synthesized in Fig. 3.1.1.6. Luoni et al. (2018) constrained pre-D2 development conditions at 2.8-3.5 GPa and 600-670 °C (Ti-chondrodite + antigorite + chlorite + spinel + olivine) and the conditions for the transition from pre-D2 to early D2 at 2.1-3.0 GPa and 570-670 °C. Rebay et al. (2012) proposed that mineralogical foliation S2, marked by clinopyroxene + olivine + antigorite + chlorite (± Ti-clinohumite + magnetite and ilmenite) developed at 2.2-2.8 GPa and 580-660 °C at 65 ± 5.6 Ma (Rebay et al., 2018) and successively was overprinted by the D3 metamorphic assemblages (antigorite + tremolite) developed at 0.6-1.4 GPa and 500-600 °C.

Protoliths are dated in the same area at 165±3.2 Ma (Rebay et al., 2018). These results highlight the occurrence of an ultra-high pressure peak recorded in the ZSZ earlier than 65±5.6 Ma.

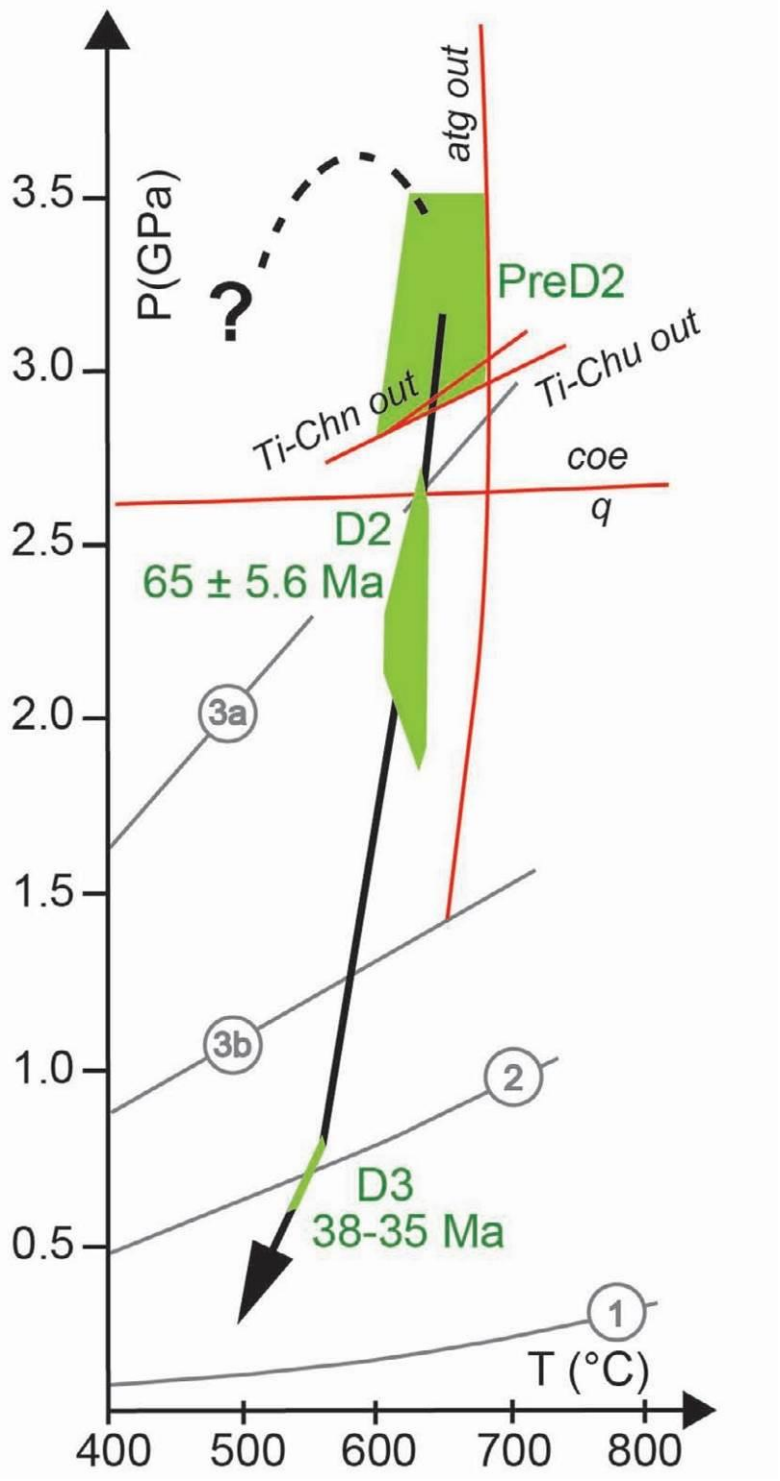

Fig. 3.1.1.6 - P-T-d-t evolution of the Valtournanche serpentinites integrating the physical conditions of metamorphism as estimated by Rebay et al. (2012) and Luoni et al. (2018) and age data from Rebay et al. (2018). Ti-chondrodite out, Ti-clinohumite out, antigorite out curves are from Shen et al. (2015) (modified after Luoni et al., 2018). Grey geotherms are after Cloos et al. (1993): (1) near spreading ridge or volcanic arc; (2) normal gradient of old plate interior; (3a) cold subduction zones; (3b) warm subduction zones.

3.1.1.6 Discussion

The structural observations of the Créton outcrops are summarized in a geological map showing the superposed successive Alpine structures overprinting the primary lithostratigraphic sequence.

Ti-chondrodite + Ti-clinohumite veins crosscut both magnetite layers and olivine-rich layers and lenses, while no intersection has been observed between the olivine veins and the other rocks. As the olivine veins are crosscut by S2, they predate the transition from UHP to HP exhumation. Diopsidite, pyroxenite, and olivine-rich layers locally crosscut magnetite layers, indicating that magnetite layering predates their development. No structural relationships indicate a relative chronology between olivine-rich layers and pyroxenite. In particular, the locally preserved porphyroclastic texture in olivine-rich layers, with millimetre-sized olivine porphyroclasts and new grains, is similar to that described by Mercier and Nicolas (1975) in deformed lherzolite xenoliths, and could suggest that olivine-rich layers may have formed before the Alpine subduction, even if we cannot exclude that they may also be related to brucite (and serpentine) breakdown during prograde evolution. In the serpentinite outcrops adjacent to those of Créton, Rebay et al. (2018) obtained Jurassic ages (165±3.2 Ma) on zircons associated with augitic clinopyroxene derived from percolation of evolved gabbro melt, as suggested by trace element composition. These data suggest us a magmatic origin of pyroxenites in an oceanic environment (Luoni et al., 2018) and allow to exclude other possible interpretations for the origin of pyroxenite layers (see Borghini et al., 2016 for a discussion). The most ancient feature at Créton is the association of white porphyroclasts serpentinite, olivine-rich serpentinite, and magnetite layers. This layering was successively affected by magmatic or metasomatic processes as testified by discordant diopsidites and olivine-rich layers.

Three phases of ductile deformation, affecting the lithostratigraphy, have been recognized at the meso-scale: D1, D2, and D3, with S2 representing the dominant foliation. Pre-D2 relics display up to metric surfaces and consist of rootless fold hinges and lenticular crystal aggregates. S2 is mylonitic and decimetre- to metre-sized D2 folds are mostly isoclinal. D3 is testified by the crenulation of S2, rarely associated with a differentiated axial plan S3 foliation. During the last brittle D4 stage serpentine or calcite filled fracture sets, locally display a centimetre-scale dislocation.

The kinematic, orientation and style compatibility, coupled with the marking assemblages, allow the correlation of D2 Créton stage with the D2 syn-high pressure stage proposed for the adjacent serpentinites, which is dated at 65±5.6 Ma (Rebay et al., 2012; 2012b; 2018). PT conditions inferred for D2 development suggest a T/depth ratio of 7-11°Ckm^{-1}. The ultra-high pressure assemblage marking pre-D2 fabric (Ti-chondrodite + antigorite + chlorite + spinel + olivine for estimated T of 600-670 °C and P of 2.8-3.5 GPa after Luoni et al., 2018) indicate a T/depth ratio of 6-8 °Ckm^{-1}. Also D3 structures can be related to the D3 described by Rebay et al. (2012a; 2012b), contemporaneous to amphibole-epidote facies conditions; here physical conditions of metamorphism during D3 indicate a T/depth ratio comprised between 21 and 26 °Ckm^{-1}. D4 developed at shallow structural level at the end of the exhumation history. Moreover, structural and metamorphic evolution and radiometric ages obtained for D2 development indicate that ultra-high pressure conditions where reached before at least 60 Ma. As shown in Fig. 3.1.1.6, pre-D2 and D2 conditions are close to those of cold subduction zones (Cloos, 1993), with a P-climax characterized by a considerably lower thermal state with respect to the earlier stages of ZSZ serpentinite exhumation (D2). Latest stages of decompression occurred under

higher temperatures, close to the intraplate normal thermal state (Cloos, 1993), compatible with continental collision.

The detection of ultra-high pressure rocks at Créton individuates another UHP unit that must be added to that of Cignana Lake Unit (Reinecke, 1991; Groppo et al., 2009; Frezzotti et al., 2011). Both these oceanic lithosphere crustal slices occur close to the tectonic contact between CZ and ZSZ. Since UHP Ti-Chn-bearing assemblages in serpentinites, have been exclusively detected in upper Valtournanche (Créton and Cignana: Luoni et al., 2018; Gilio et al., 2019), they are not sufficient to infer UHP conditions to the serpentinites of the whole ZSZ. Indeed, the detection of UHP rocks at Créton individualizes another UHP unit that must be added to that of Cignana Lake Unit, already identified on the basis of coesite- and diamond-bearing assemblages in oceanic metasediments (Reinecke, 1991; Groppo et al., 2009; Frezzotti et al., 2011). Both these oceanic slices occur close to the tectonic contact between CZ and ZSZ. In addition, the heterogeneous and diachronic tectono-metamorphic evolutions recorded in different portions of the ZSZ (see Rebay et al., 2018 and references therein) suggest that this domain can be considered a tectono-metamorphic puzzle rather than a homogeneous subducted and exhumed coherent slab.

3.1.1.7 Conclusion

In conclusion, the type of multiscale structural analyses (from 1:200 to 1:20 to microscale) here used may open possibilities of describing and deciphering more complex evolutions in apparently monotonous rocks such as serpentinites, which are usually considered to display weak variations in mineral assemblages. Créton serpentinites represent a heterogeneous oceanic peridotite slice with magnetite layers, in which layers and lenses of scarcely preserved pyroxenites and olivine-rich layers, and completely re-equilibrated diopsidites are embedded. These rocks reached and heterogeneously recorded ultra-high pressure peak conditions, testified by Ti-chondrodite and Ti-clinohumite bearing pre-D2 assemblages (Shen et al., 2015; González-Jiménez et al., 2017; Luoni et al., 2018) under highly depressed thermal regime before Palaeocene, and were exhumed up to D2 PT conditions (Rebay et al., 2012, 2012b) still in a depressed thermal state, typical of cold subduction zones. On the contrary, the last stages of exhumation (D3-D4) occurred under considerably higher thermal state suggesting the contemporaneity with the Alpine continental collision.

3.1.1.8 Acknowledgements

Insightful reviews by Vicente López Sánchez-Vizcaíno and Marco Scambelluri greatly improved the first version of the manuscript and are acknowledged. G. Gosso gave useful advice during field-work and C. Malinverno made the thin sections. PL thanks Paolo Papone and Ugo Zuretti for their kind hospitality during field work. PL is grateful to Studio Ciocca. Funding by University of Milano PSR2018_DZANONI “Analisi strutturale delle catene collisionali”. Results here presented have been developed in the frame of the MIUR Project “Dipartimenti di Eccellenza 2017-Le geoscienze per la società: risorse e loro evoluzione (Work-package 3, Tasks 3.3-3.4)”.

3.1.2 - Dating of ultramafic rocks from the Western Alps ophiolites discloses Late Cretaceous subduction ages in the Zermatt-Saas Zone

Geological Magazine, 2018, 155 (2), 298–315. https://doi.org/10.1017/S0016756817000334
Gisella Rebay, Davide Zanoni, Antonio Langone, Pietro Luoni, Massimo Tiepolo and Maria Iole Spalla

Abstract - The Zermatt-Saas Zone was part of the Middle to Late Jurassic Tethyan lithosphere that underwent oceanic metamorphism during Mesozoic time and subduction during Eocene time (HP to UHP metamorphism). In upper Valtournanche, serpentinite, metarodingite and eclogite record a dominant S2 foliation that developed under 2.5 ± 0.3 GPa and 600 ± 20 °C during Alpine subduction. Serpentinites contain clinopyroxene and rare zircon porphyroclasts. Clinopyroxene porphyroclasts show fringes within S2 with similar compositions to that of grains defining S2. Zircon cores show zoning typical of magmatic growth and thin fringes parallel to the S2 foliation. These features indicate crystallization of clinopyroxene and zircon fringes during HP syn-D2 metamorphism, related to the Alpine subduction. The U–Pb zircon dates for cores and fringes reveal crystallization at 165 ± 3.2 Ma and 65.5 ± 5.6 Ma, respectively. The Middle Jurassic dates are in agreement with the known ages for the oceanic accretion of the Tethyan lithosphere. The Late Cretaceous - Palaeocene dates suggest that the Zermatt-Saas Zone experienced high-pressure to ultra-high-pressure (HP–UHP) metamorphism at c. 16 Ma earlier than previously reported. This result is in agreement with the evidence that in the Western Alps the continental Sesia-Lanzo Zone reached the subduction climax at least from 70 Ma and was exhumed during ongoing oceanic subduction. Our results are further evidence that the Zermatt-Saas ophiolites diachronically recorded heterogeneous HP–UHP metamorphism.

3.1.2.1 Introduction

Ophiolites represent oceanic remnants in mountain chains and their tracking, together with the reconstruction of their structural and metamorphic history, is still one of the basic tools for understanding the dynamics of collisional chain development. In the Alps, the key significance of ophiolites in geodynamics was long understood before the birth of plate tectonics (e.g. Brongniart, 1813; Argand, 1911; Steinmann, 1927). Since the first geological research within the Alps ophiolites from the Piedmont zone have been a favourable investigation object (Dal Piaz, 2010), especially in the exploration of deformation and mineral transformation histories of high-pressure (HP) and ultra-high-pressure (UHP) units of the Zermatt-Saas Zone (ZSZ). In the last years a debate developed on this portion of the Piedmont zone, regarding whether the pressure–temperature (P–T) conditions registered by ZSZ rocks are largely uniform or if different portions of ZSZ recorded different P–T-peak conditions and underwent different exhumation paths over different time spans (e.g. Lapen et al., 2003; Li et al., 2004; Angiboust et al., 2009; Groppo et al., 2009; Angiboust and Agard, 2010; de Meyer et al., 2014; Skora et al., 2015; Weber and Bucher, 2015; Weber et al., 2015). This last view has been recently reinforced by multiscalar structural and petrological analysis supported by detailed field mapping (Rebay et al., 2012; Weber and Bucher, 2015; Zanoni et al., 2016). The multiscalar analytical approach could be deeply reinforced by careful geochronological work, and becomes important in understanding the critical size of oceanic units able to record a homogeneous structural and

metamorphic evolution during burial and exhumation paths in a subduction system. This means identifying volumes that have completed, remaining intact, their tectonic trajectory during a given time span. In addition, this allows light to be shed on how the coupling and decoupling of tectonic units can occur in the subduction mantle wedge or in the orogenic wedge during continental collision (e.g. Cloos, 1982; Chemenda et al., 1995; Stoeckhert and Gerya, 2005; Baumann et al., 2010; Roda et al., 2010; Gerya, 2011; Malatesta et al., 2012, 2016; Roda et al., 2012). Different subduction dynamics can result in the formation of tectonic units with different sizes and different ages, sharing a coherent structural and metamorphic evolution. The main goal of this contribution is to present new age data on microstructural sites selected on the basis of a well-defined chronology of superimposed structures and metamorphic imprints at the regional scale, and to implement the chronological outline of eclogitized ZSZ ophiolites from the upper Valtournanche serpentinites in order to take some steps towards a better constrained regional framework.

3.1.2.2 Geological setting

The ZSZ, together with the Combin Zone (CZ), represents a Tethyan ocean relict that comprises rocks variously affected by oceanic and subduction-related metamorphism, which now are transposed along the axial belt of the Western Alps (Caron et al., 1984; Reddy et al., 1999; Dal Piaz, 2010; Spalla et al., 2010). These two zones are tectonically sandwiched between the continental Monte Rosa (beneath) and Dent Blanche - Sesia Lanzo nappes (above) that belong to the Penninic and Austroalpine domains, respectively (e.g. Bearth, 1967; Polino et al., 1990). The ZSZ (Fig. 3.1.2.1a, b) underlies the CZ and, due to their different lithostratigraphic and metamorphic features, these two units have been interpreted as deriving from the oceanic lithosphere and from the ocean–continent transition zone, respectively (e.g. Dal Piaz and Ernst, 1978; Dal Piaz et al., 1981). In the upper Valtournanche, ZSZ and CZ are separated by slices of pre-Alpine continental rocks and schists deriving from Permian-Cretaceous sediments (Dal Piaz, 1999, 2010). The main difference between ZSZ and CZ is the dominant metamorphic imprint: eclogite facies in the first and greenschist facies in the second. Despite the pervasive greenschist re-equilibration, CZ rocks preserve blueschist facies relicts, whereas remnants of eclogite facies assemblages have never been detected, even in the less-deformed rocks (Cartwright and Barnicoat, 2002; Dal Piaz, 1974; Dal Piaz and Ernst, 1978; Ring, 1995). The greenschist facies assemblages are extremely localized in the mostly eclogitized rocks of ZSZ and are mainly interpreted as exhumation-related metamorphic imprints (e.g. Cartwright and Barnicoat, 2002; Ernst and Dal Piaz, 1978); scattered relics predating the eclogite facies peak preserve blueschist facies mineral assemblages (e.g. Chinner and Dixon, 1973; Ernst and Dal Piaz, 1978). Metabasic rocks are the most explored to determine the Alpine metamorphic evolution of this portion of the Tethys ocean and results give a wide span of P–T values in different portions of ZSZ: 2.5–3.0 GPa and 550–600 °C (Bucher et al., 2005); 1.9–2.2 GPa and 530–600 °C (Dale et al., 2009); and, south of the Aosta-Ranzola fault (St Marcel valley), 2.1 ± 0.3 GPa and 550 ± 60 °C (Martin et al., 2008). The metagabbros of the Swiss portion of the ZSZ record peak conditions of 2.5–2.8 GPa and 600-610 °C (Bucher and Grapes, 2009) or alternatively 1.9–2.2 GPa and 500–580 °C (Dale et al., 2009). Pressures from 2.7 to >3.2 GPa and temperatures of 590–630 °C are estimated at Lago di Cignana (e.g.

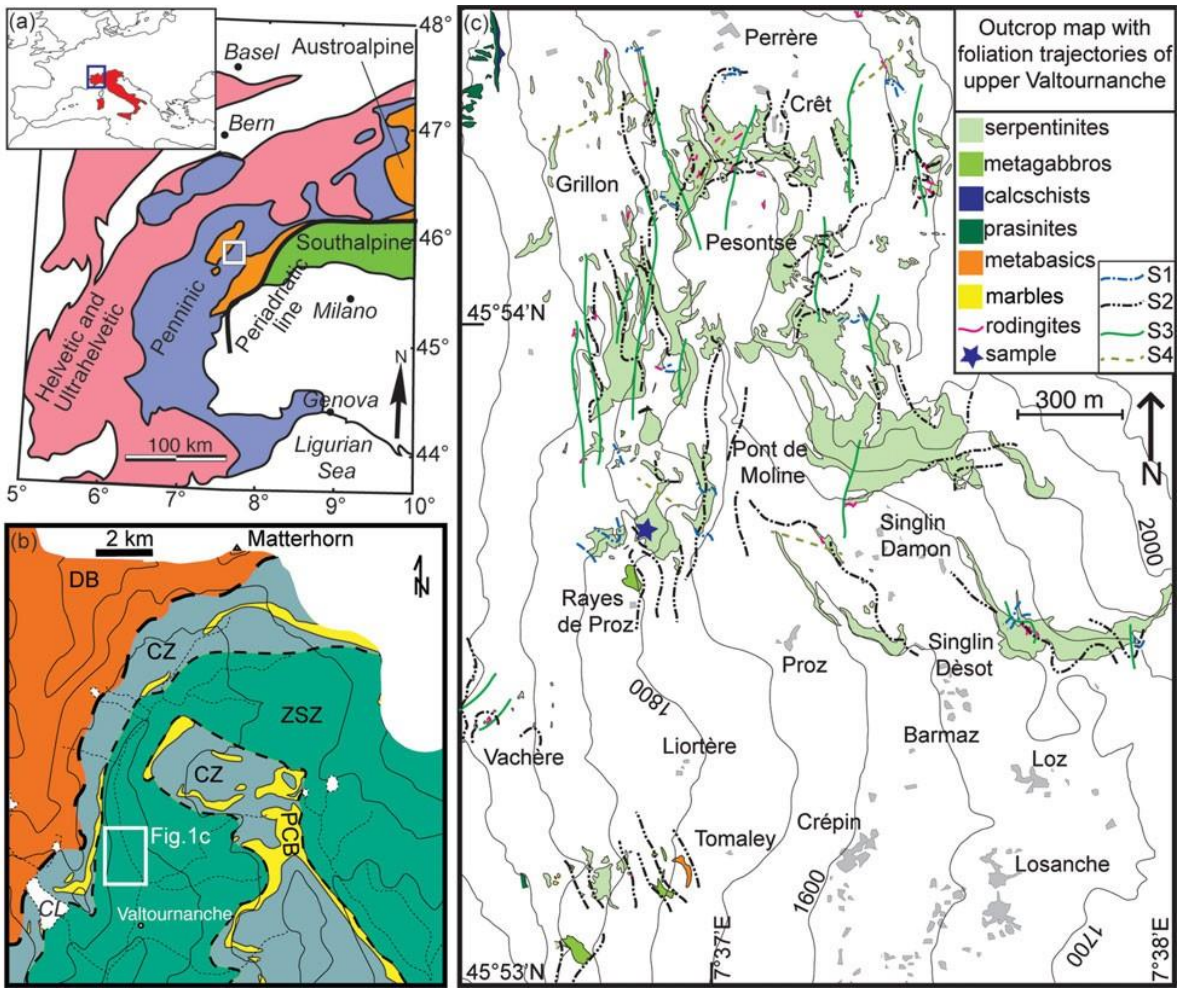

Fig. 3.1.2.1 - Geological and structural outline of the upper Valtournanche. (a) Tectonic sketch map of the Western Alps and its location within Europe and the Mediterranean region. (b) Interpretative tectonic sketch of the upper Valtournanche redrawn from the geotectonic map of the Aosta Valley (De Giusti et al., 2003); area indicated by the thick white square in (a). ZSZ – Zermatt-Saas Zone; PCB – Pancherot-Cime Bianche-Bettaforca unit; CZ – Combin Zone; DB – Dent Blanche nappe; CL – Cignana Lake. (c) Outcrop map with the foliation trajectories of the metaophiolites of the upper Valtournanche (ZSZ), synthesized from an original mapping (unpublished) at 1:5000 scale. Relative chronology of superimposed foliation is shown in the legend. Topography redrawn from the technical map of the Val d'Aosta Regional Administration without hydrography.

Reinecke, 1991, 1998; van der Klauw et al., 1997; Groppo et al., 2009), where microdiamonds have also been found in oceanic metasedimentary rocks (Frezzotti et al., 2011). Peak P–T estimates from serpentinites of the Swiss side are at 2.0–2.5 GPa and 600–650 °C (Li et al., 2004), whereas in the Italian side they are at 2.2–2.8 GPa and 580–620 °C (Rebay et al., 2012). The latter estimates have recently been supported by P–T peak conditions determined by thermodynamic modelling of the hosted eclogitized rodingites (2.3–2.8 GPa and 580–660 °C; Zanoni et al., 2016). All these P–T estimates led to the inference of trajectories indicating the occurrence of heterogeneous metamorphic evolutions in different portions of ZSZ. In contrast, different authors have suggested a homogeneous evolution for the entire ZSZ based on the assemblages from metabasites and calcschists, with peak conditions at 2.3 ± 0.1 GPa and 540 ± 40 °C (Angiboust et al., 2009; Angiboust and Agard, 2010). In

Key	Locality	Rock	Dating method; mineral	Age (Ma)	Peak *P–T* conditions	Event	Reference
Zermatt-Saas Zone							
	Allalin glacier	Metagabbro	U–Th–Pb; zircon	164.0 ± 2.7		Emplacement	Rubatto, Gebauer & Fanning, 1998
	Mellichen	Leucogabbro	U–Th–Pb; zircon	163.5 + 1.8		Emplacement	Rubatto, Gebauer & Fanning, 1998
	Tasch Valley	Metasediment	U–Th–Pb; zircon	153–173		Deposition	Rubatto, Gebauer & Fanning, 1998
	Cignana	Metasediment	U–Th–Pb; zircon	161 ± 11		Deposition	Rubatto, Gebauer & Fanning, 1998
3	Triftji	Metapelite	Rb–Sr; garnet phengite inclusion	44.86 ± 0.49 to 43.6 ± 1.8		Prograde	de Meyer *et al.* 2014
3	Triftji	Metapelite	Rb–Sr; phengite (matrix)	40.01 ± 0.51 to 39.5 ± 1.1		Prograde	de Meyer *et al.* 2014
5	Pfulwe	Eclogite	Lu–Hf; garnet	48.9 ± 2.8		Prograde	Skora *et al.* 2015
12	Chamois	Eclogite	Lu–Hf; garnet	52.6 ± 1.7		Prograde	Skora *et al.* 2015
8	Trockener Steg	Eclogite (continental)	Lu–Hf; garnet-whole-rock	56.5 ± 2.7 to 58.2 ± 1.4		Prograde	Weber *et al.* 2015
11	Cignana	Eclogite	Lu–Hf; garnet-omphacite-whole-rock	48.8 ± 2.1		Prograde	Lapen *et al.* 2003
11	Cignana	Eclogite	REE; garnet	70–80		Prograde	Skora *et al.* 2009
9	Breuil	Metabasalts and metagabbros			0.8–1.2 GPa, 420–520 °C	HP	Ernst & Dal Piaz, 1978
2	Allalinhorn	Metagabbro			1.5 GPa, 570–700 °C	HP	Chinner & Dixon, 1973
2	Allalinhorn	Metagabbro			2.5 GPa, 610 °C	HP	Bucher & Grapes, 2009
2	Allalinhorn	Metabasalts			2.3–2.5 GPa, 530–555 °C	HP	Angiboust *et al.* 2009
6	Zermatt	Metabasites			1.4 GPa, 600 °C	HP	Oberhänsli 1980
6	Zermatt	Metabasites			1.75–2.0 GPa, 550–600 °C	HP	Barnicoat 1988
8	Trockener Steg	Eclogite (continental)			2.2–2.3 GPa, 515–645 °C	HP	Weber & Bucher, 2015
8	Trockener Steg	Eclogite			2.2–2.3 GPa, 450–550 °C	HP	Weber & Bucher, 2015
7	Lichenbrettier	Serpentinites			2.0–2.5 GPa, 600–650 °C	HP	Li, Rahn & Bucher, 2004
7	Riffelhorn-Gornergrat	Serpentinites			2.0–2.5 GPa, 600–650 °C	HP	Li, Rahn & Bucher, 2004
13	St Jacques	Eclogite	Lu–Hf; garnet	39.2 ± 1.6	0.8–1.2 GPa, 420–520 °C	HP	Skora *et al.* 2015; Ernst & Dal Piaz, 1978
5	Pfulwe	Eclogite	Lu–Hf; garnet-whole- rock	48.9 ± 4.8	1.75–2.0 GPa, 550–600 °C	HP	Mahlen *et al.* 2006; Barnicoat & Fry 1986
1	Saas Fee	Eclogite	Lu–Hf; garnet	38.1 ± 2.7 to 40.7 ± 1.8		HP	Skora *et al.* 2015
1	Saas Fee	Metagabbro			2.5 GPa, 650 °C	HP	Meyer 1983
1	Saas Fee	Metabasites			2.5 GPa, 650 °C	HP	Bucher & Frey 1994
10	Valtournenche	Serpentinites			2.2–2.8 GPa, 600 °C	HP–UHP	Rebay, Spalla & Zanoni, 2012
10	Valtournenche	Rodingites			2.3–2.8 GPa, 580–660 °C	HP–UHP	Zanoni, Rebay & Spalla, 2016
5	Pfulwe	Metabasalts			2.5–3.0 GPa, 550–600 °C	UHP	Bucher *et al.* 2005
3	Mellichen	Leucogabbro	U–Th–Pb; zircon	48.8 ± 2.9		UHP	Rubatto, Gebauer & Fanning, 1998
3	Mellichen	Leucogabbro	U–Th–Pb; zircon	40.3 ± 9.2		UHP	Rubatto, Gebauer & Fanning, 1998
3	Mellichen	Metabasalts			2.5–3.0 GPa, 550–600 °C	UHP	Bucher *et al.* 2005
11	Cignana	Eclogite	Sm–Nd; garnet	40.6 ± 2.6	2.6–3.0 GPa, c. 600 °C	UHP	Amato *et al.* 1999; van der Klauw, Reinecke & Stöckhert, 1997

Table 3.1.2.1. - Summary of age data for Western Alps ophiolites and peak P–T conditions for Zermatt-Saas Zone

Key	Locality	Rock	Dating method; mineral	Age (Ma)	Peak *P–T* conditions	Event	Reference
11	Cignana	Eclogite	Sm–Nd; garnet	52 ± 18		UHP	Bowtell, Cliff & Barnicoat,1994
11	Cignana	Eclogite	U–Th–Pb; zircon	44.1 ± 0.7		UHP	Rubatto, Gebauer & Fanning, 1998
11	Cignana	Metasediment	U–Th–Pb; zircon	44.1 ± 0.7	2.7–3.0 GPa, 600 °C	UHP	Rubatto, Gebauer & Fanning, 1998; Reinecke 1995, 1998
11	Cignana	Metasediments	Ar–Ar; garnet phengite inclusion	43.2 ± 1.1 44.4 ± 1.5		UHP	Gouzu *et al.* 2006; Reinecke, 1991
11	Cignana	Quarzite	Rb–Sr; phengite	40.7 ± 0.1	2.6–2.8 GPa, 590–630 °C	UHP–retrograde	Skora *et al.* 2015; Reinecke, 1991
1	Saas Fee	Calcshists	Rb–Sr; phengite	39.5 ± 0.1		HP–retrograde	Skora *et al.* 2015
	Cignana	Quarzite	Rb–Sr; whole-rock-phengite	38 ± 2		Retrograde	Amato *et al.* 1999
	Tasch Valley	Metapelite	Rb–Sr; whole-rock-phengite	38 ± 2		Retrograde	Amato *et al.* 1999
	Cignana	Metasediments	Ar–Ar; phengite (matrix)	42–37 (plateaux age)		Retrograde	Gouzu *et al.* 2006
Combin Zone	Cignana (UU)	Metabasite	K–Ar; phengite	38–41		Retrograde	Gouzu *et al.* 2016
	Cignana (UU)	Metasediments	K–Ar; phengite	38–41		Retrograde	Gouzu *et al.* 2016
	Cignana (LU)	Eclogite	K–Ar; paragonite	37–38		Retrograde	Gouzu *et al.* 2016
	Cignana (LU)	Eclogite	K–Ar; phengite	37–38		Retrograde	Gouzu *et al.* 2016
	Cignana (LCU)	Pelitic shist	K–Ar; phengite	39–41		Retrograde	Gouzu *et al.* 2016
	Cignana (LCU)	Piemontite shist	K–Ar; phengite	39–41		Retrograde	Gouzu *et al.* 2016
	Cignana (LCU)	Eclogite	K–Ar; paragonite	39–41		Retrograde	Gouzu *et al.* 2016
	Cignana (LCU)	Mn-rich metasediment	K–Ar; phengite	39–41		Retrograde	Gouzu *et al.* 2016
Antrona	Cignana	Calcshists	K–Ar; phengite	36–40		Retrograde	Gouzu *et al.* 2016
	Gueglihorn	Metabasics	Pb–U; zircon	155 ± 1.6		Emplacement	Liati, Froitzheim & Fanning, 2005
	Passo del Mottone	Metabasics	Pb–U; zircon	158 ± 17		Emplacement	Liati, Froitzheim & Fanning, 2005
	Quarata	Metabasics	Pb–U; zircon	155.6 ± 2.1		Emplacement	Liati, Froitzheim & Fanning, 2005
	Hinterrhein area	Metagabbro	Pb–U; zircon	161 ± 3.9		Emplacement	Liati, Froitzheim & Fanning, 2005
	Passo del Mottone	Amphibolite	Pb–U; zircon	38.5 ± 0.7		HP	Liati, Froitzheim & Fanning, 2005
	Alpe la Balma	Eclogite	Lu–Hf; garnet-whole-rock	42–45.5		HP	Herwartz *et al.* 2008
Monviso	Vernè (Val Varaita)	Meta-plagiogranite	U–Pb; zircon	152 ± 2		Emplacement	Lombardo, Rubatto & Castelli, 2002
	Lago Superiore	Eclogite	U–Pb; zircon	163 ± 2		Emplacement	Rubatto & Hermann, 2003
	Lago Superiore	Eclogite	Lu–Hf; garnet-whole-rock	49.2 ± 1.2		Prograde–HP	Duchêne *et al.* 1997
	Lago Superiore	Metamorphic vein	U–Pb; zircon	45 ± 1		HP	Rubatto & Hermann, 2003
	Lago Superiore	Eclogitic mylonite	Rb–Sr; phengite	41.6 ± 0.4		HP	Cliff, Barnicoat & Inger, 1998
	Lago Superiore	Eclogitic mylonite	Sm–Nd; garnet and clinoyroxene	60 ± 12		HP	Cliff, Barnicoat & Inger, 1998
	Lago Superiore	Eclogitic metagabbros	Ar–Ar; phengite	48–53 Ma		HP	Monié & Philippot, 1989
Voltri Group		Eclogite	Ar–Ar; phengite	49.0 ± 0.4		HP	Federico *et al.* 2005
		Blueschists	Ar–Ar; phengite	43.5 ± 1.7		HP–retrograde	Federico *et al.* 2005
		Metasediments	Ar–Ar; muscovite	32.9 ± 0.8		Retrograde	Federico *et al.* 2005

Table 3.1.2.1 - Summary of age data for Western Alps ophiolites and peak P–T conditions for Zermatt-Saas Zone

addition, part of the Monviso ophiolite has been interpreted as forming a single unit with the ZSZ, which would consist of a continuous slab, recording a coherent metamorphic evolution during the Alpine subduction (Angiboust et al., 2012).

This interpretation differs from that of previous authors, suggesting that the Monviso is a complex of eclogitized ophiolitic slices accreted during the final stages of their exhumation on the basis of contrasted P–T trajectories (Schwartz et al., 2000; Guillot et al., 2004). Consistent with a heterogeneous metamorphic evolution, Alpine ages indicate a wide time interval of re-equilibration during subduction of the ZSZ rocks and associated continental slivers (Table 3.1.2.1) of 80–38 Ma, with ages interpreted as referred to peak conditions as 52–38 Ma (Bowtell et al., 1994; Rubatto, Gebauer and Fanning, 1998; Dal Piaz et al., 2001; Skora et al., 2009, 2015; Springer et al., 2009; de Meyer et al., 2014; Weber et al., 2015). Moreover, considering only U–Pb zircon methods, such ages cluster at c. 48-40 Ma (Table 3.1.2.1). Protolith ages indicate gabbro emplacement at 167–161 Ma and sediment deposition during 170–150 Ma (Table 3.1.2.1; Rubatto et al., 1998).

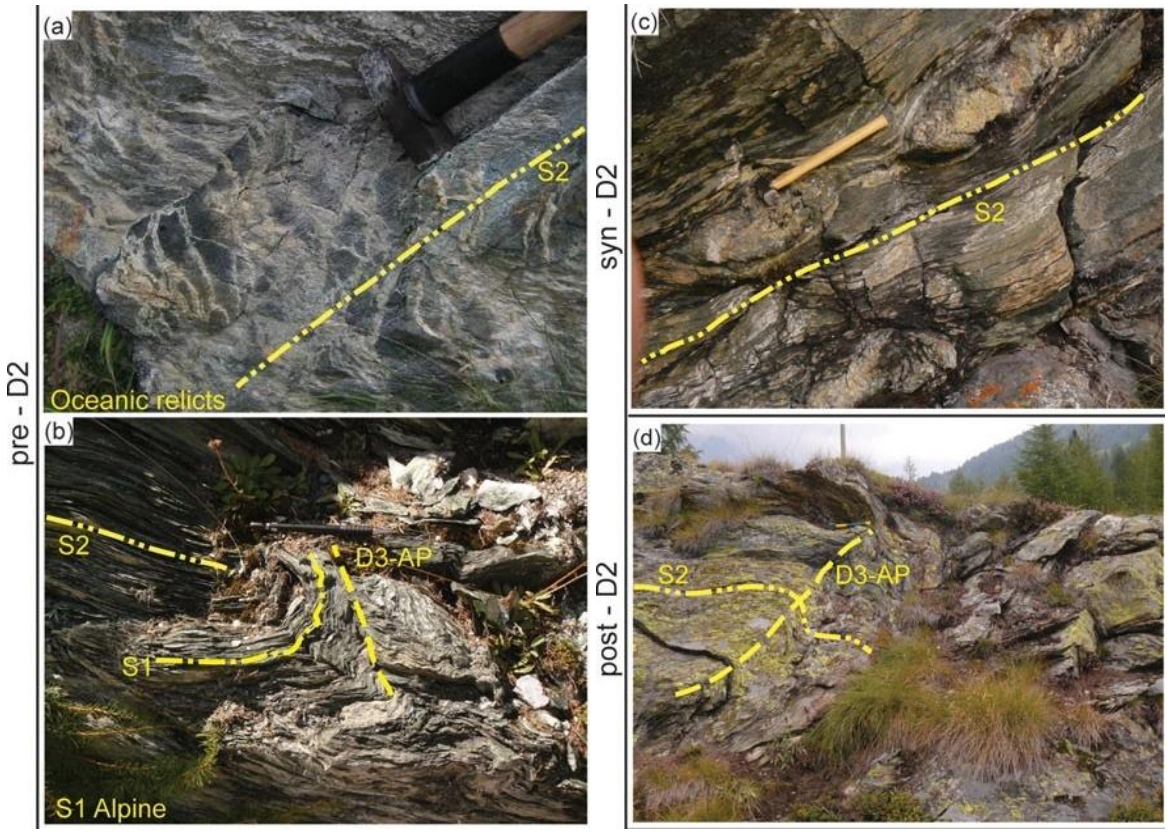

Fig. 3.1.2.2 - (a) Net of whitish amphibole-clinopyroxene-bearing veins intersected by S2 foliation. Hammer for scale. (b) S1 foliation folded during the development of D2 and post-D2 deformation stages. D2 is accompanied by the development of the S2 foliation and D3 produced only a folding (D3-AP D3 axial plane). Pencil for scale. (c) Pervasive S2 foliation that wraps around rodingite boudins. Hammer for scale. (d) Metre-sized D3 fold. Hammer for scale.

3.1.2.3 Mesostructure

Along the upper Valtournanche valley, between Valtournanche village and Perrère hydroelectric plant, serpentinite is the dominant lithotype. Hectometre-sized metagabbro bodies and up to a few metres thick rodingite boudins and dykes are associated with serpentinites, together with marbles and calcschists (Fig. 3.1.2.1c). The dominant fabric in serpentinites, metagabbros and rodingites is the

tectonitic to mylonitic S2 foliation, and less-deformed domains contain textural and structural pre-D2 relicts (Fig. 3.1.2.2a–c). S2 is in turn overprinted by two groups of superimposed ductile structures (D3 and D4); all ductile structures were mapped with spatial continuity (Fig. 3.1.2.1c) by means of multiscale structural analysis (Rebay et al., 2012; Zanoni et al., 2012, 2016). S2 locally is mylonitic and associated with a tight to isoclinal folding that is characterized by a shallow west-dipping axial plane and a NNW–SSE shallow plunging axis. Contacts between serpentinites and metagabbros or rodingites are mainly reworked during the S2 development (see Zanoni et al., 2016). In serpentinite, S2 is marked by Alpine HP–UHP mineral assemblages and is pre-dated by clinopyroxene porphyroclasts and amphibole-clinopyroxene-bearing vein nets (Fig. 3.1.2.2a), ascribable to the oceanic evolution, and by an S1 foliation (Fig. 3.1.2.2b) that represents the oldest detectable Alpine fabric (Rebay et al., 2012; Zanoni et al., 2016). S1 foliation and up to millimetre-sized oceanic relicts are also preserved in rodingites (Zanoni et al., 2016). S2 is post-dated by localized ductile shear zones and by two groups of folds, represented by tight folds with west-dipping axial plane and a N–S shallow plunging axis (D3, Fig. 3.1.2.2d) and by open to gentle upright folds with shallow axis (D4), respectively. Among these latter two folding stages, the first is associated with the development of a differentiated axial plane foliation S3 that in serpentinites is marked by a mineral assemblage indicating low-pressure metamorphic conditions, representing the retrograde metamorphic re-equilibration during uplift (Rebay et al., 2012).

3.1.2.4 Microstructures and mineral chemistry

Serpentinites have been divided into two groups on the basis of D2 parageneses – Ti-clinohumite-bearing and eclogite facies serpentinite – described in detail by Rebay et al. (2012). PreD2 minerals are represented by porphyroclasts of olivine1, clinopyroxene1 and Ti-clinohumite1 that are wrapped by S2 foliation (Fig. 3.1.2.3a). New mineral growths occur at the rims of clinopyroxene, Ti-clinohumite and olivine as fringes elongated parallel to S2 (Fig. 3.1.2.3a, b). The parageneses associated with D2 consist of olivine2, clinopyroxene2, antigorite ± Ti-clinohumite2 ± chlorite ± zircon (Fig. 3.1.2.3a, b), whereas post-D2 foliation is defined by serpentine, chlorite amphibole (Fig. 3.1.2.3c). A sample of eclogite facies serpentinite, collected north of Rayes de Proz (star in Fig. 3.1.2.1c), is characterized by pervasive S2 foliation, wrapping around clinopyroxene porphyroclasts (Fig. 3.1.2.3d–f) and relationships between mineral growth and S2 development are similar to those described above. Two generations of zircon (namely zircon1 and zircon2) are easily recognizable where pre-D2 cores consist of porphyroclasts rimmed by syn-D2 fringe-like overgrowths, aligned along S2 foliation (Fig. 3.1.2.3g). This texture is consistent with that of clinopyroxene, Ti-clinohumite and olivine from all serpentinite types (Fig. 3.1.2.3h). Larger zircon grains are at times boudinaged (Fig. 3.1.2.3i). Compositions of olivine and clinopyroxene associated with pre-D2 and syn-D2 assemblages are different and distinctive, as detailed in Rebay et al. (2012). In summary, olivine cores and rims are very similar in composition, with a slight decrease in Mg towards the rims. Clinopyroxene cores are Al (up to 0.3 apfu), Ti- and Cr-rich and Ca-poor (0.8–0.92 apfu), whereas syn-D2 rims are Ca-rich (0.94–1 apfu) and Ti-, Cr- and Al-poor. Syn-D2 serpentine has higher Mg (up to 11.45 apfu) and lower Fe (up to 0.9 apfu) and Al (up to 0.8 apfu) contents than pre-D2 serpentine. Based on the major-element compositional variations, using classical geothermobarometry and thermodynamic modelling, 2.5 ± 0.3 GPa and 600 ± 20 °C were estimated for the formation of mineral

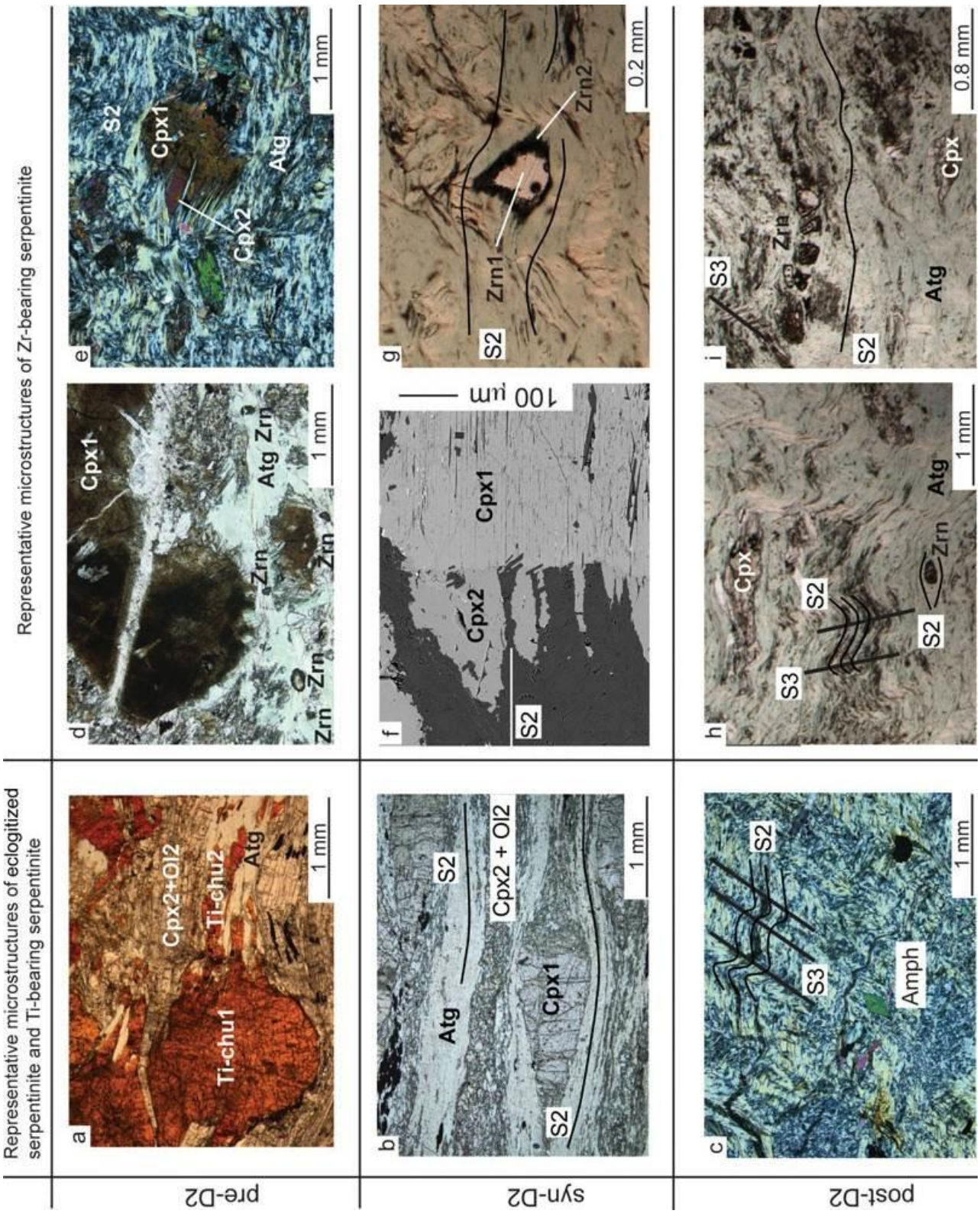

Fig. 3.1.2.3 - Microphotographs of (a–c) eclogitized and Ti-clinohumite-bearing serpentinite, and (d–i) of the zircon bearing eclogitized serpentinite sample. (a) Ti-clinohumite1 porphyroclasts (Ti-chu1) wrapped by S2 defined by Ti-clinohumite2 (Ti-cChu2), olivine2 (Ol2), clinopyroxene2 (Cpx2) and antigorite (Atg); (b) syn-D2 mylonite with a clinopyroxene1 porphyroclast (Cpx1) and banded S2 foliation defined by clinopyroxene2 (Cpx2), olivine2 (Ol2) and antigorite (Atg); (c) S2 defined by antigorite overprinted by an incipient S3 crenulation cleavage; amphibole (Amph) porphyroblasts (note basal sections) show SPO parallel to S3; (d) large field view of the zircon-bearing serpentinite with a large, fractured, clinopyroxene (Cpx1) porphyroclast (dark) wrapped by S2, which is defined by antigorite (Atg), olivine2

and clinopyroxene2 (in the lower part there are five zircon porphyroclasts, Zrn); (e) clinopyroxene1 porphyroclast (Cpx1) with clinopyroxene2 (Cpx2) spikes parallel to S2, here defined by antigorite (Atg); (f) SEM backscattered image of a large clinopyroxene1 (Cpx1) with spikes of clinopyroxene2 (Cpx2) parallel to S2; (g) zircon (Zrn1) wrapped by antigorite defining S2, showing zircon2 (Zrn2) growths parallel to S2 (see zircon shape in CL image in Fig. 3.1.2.4c, h) clinopyroxene (Cpx) and zircon (Zrn) porphyroclasts wrapped by S2 overprinted by S3 crenulation cleavage; and (i) large zircon boudinaged within S2 that wraps a small clinopyroxene1 (Cpx1) porphyroclast, overprinted by S3 crenulation cleavage.

parageneses associated with D2 deformation stage (Rebay et al., 2012). Clinopyroxene and zircon cores were analysed for trace-element composition with laser ablation (LA) ICP-MS (Table 3.1.2.2) at the CNR–IGG UOS of Pavia. The instrument couples a Nd:YAG laser working at 266 nm with a quadrupole ICP-MS (Perkin Elmer DRCe). All analyses were carried out using a 10 μm spot (see appendix 2). The chondrite-normalized rare Earth element (REE) pattern (Fig. 3.1.2.4) of clinopyroxene is characterized by flat heavy REE (at about 100 times CI chondrite), a weak light REE depletion and negative Eu anomaly.

Zr and Y concentrations are relatively high and are in the ranges 93.3–118 ppm and 402–449 ppm. The trace element composition of zircon cores is characterized by low U concentration (9–18 ppm) and a chondrite-normalized REE pattern typical of growth under magmatic conditions, characterized by light REE depletion, positive Ce anomaly and heavy REE (HREE) enrichment (up to 3000 times CI chondrite). Zircon REE patterns parallel that of clinopyroxene for the occurrence of a negative Eu anomaly. Zircon fringe dimensions allowed only a single analysis. Trace-element composition of zircon fringes matches that of magmatic cores, revealing no significant difference in both REE contents and Th/U ratios. The absence of garnet and other mineral phases with high compatibility for REE (and other trace elements) in the HP–UHP mineral paragenesis in these rocks prevents their redistribution during zircon recrystallization, and accounts for the similar concentrations between magmatic cores and metamorphic rims.

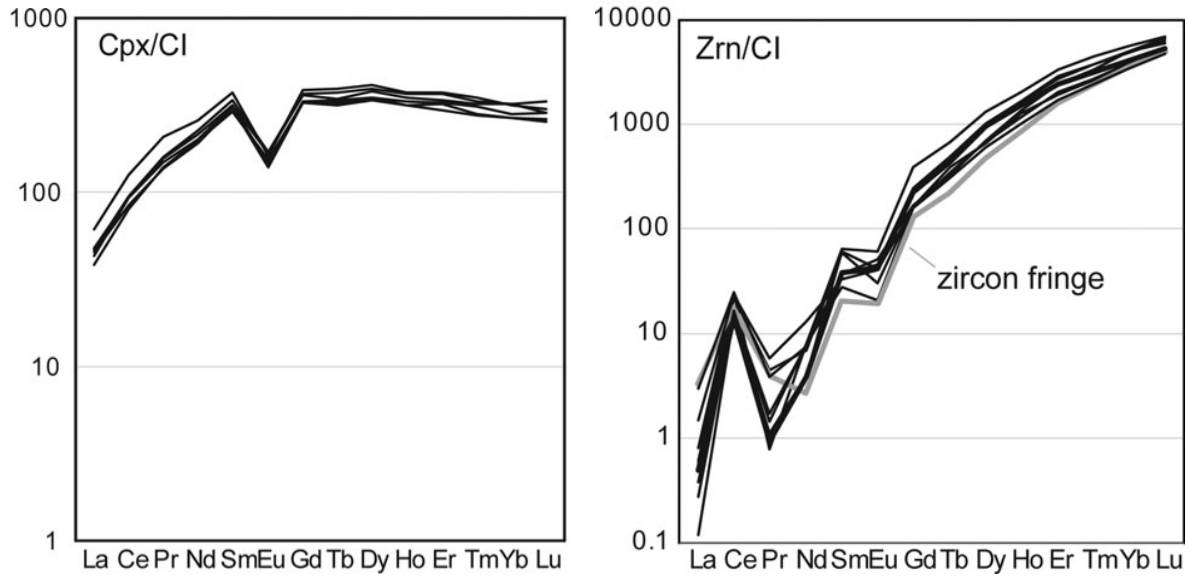

Fig. 3.1.2.4 - REE patterns (chondrite normalized) of clinopyroxene and zircon cores

3.1.2.5 U–Pb zircon geochronology

U–Pb zircon geochronology was carried out with LA- ICP-MS on polished thin-sections at the CNR–IGG UOS of Pavia. The system couples an ArF excimer laser microprobe (type GeoLas102 from MicroLas) with a sector field ICP-MS (type Element from ThermoFinnigan). The signal ^{202}Hg, ^{204}(Pb Hg), ^{206}Pb, ^{207}Pb, ^{208}Pb, ^{232}Th and ^{238}U masses were acquired. ^{202}Hg is acquired to correct the isobaric interference of 204Hg on 204Pb, so that the common Pb in the sample can be monitored. The relatively high background at mass 204, due to trace of Hg in the He gas, prevents small amounts of common Pb being detected, however. Remarkably, in the investigated samples the signal of ^{204}(Pb Hg) was always indistinguishable from the background and therefore no common Pb correction was applied. The ^{235}U signal is calculated from ^{238}U on the basis of the ratio ^{238}U /^{235}U = 137.818 (Hiess et al., 2012).

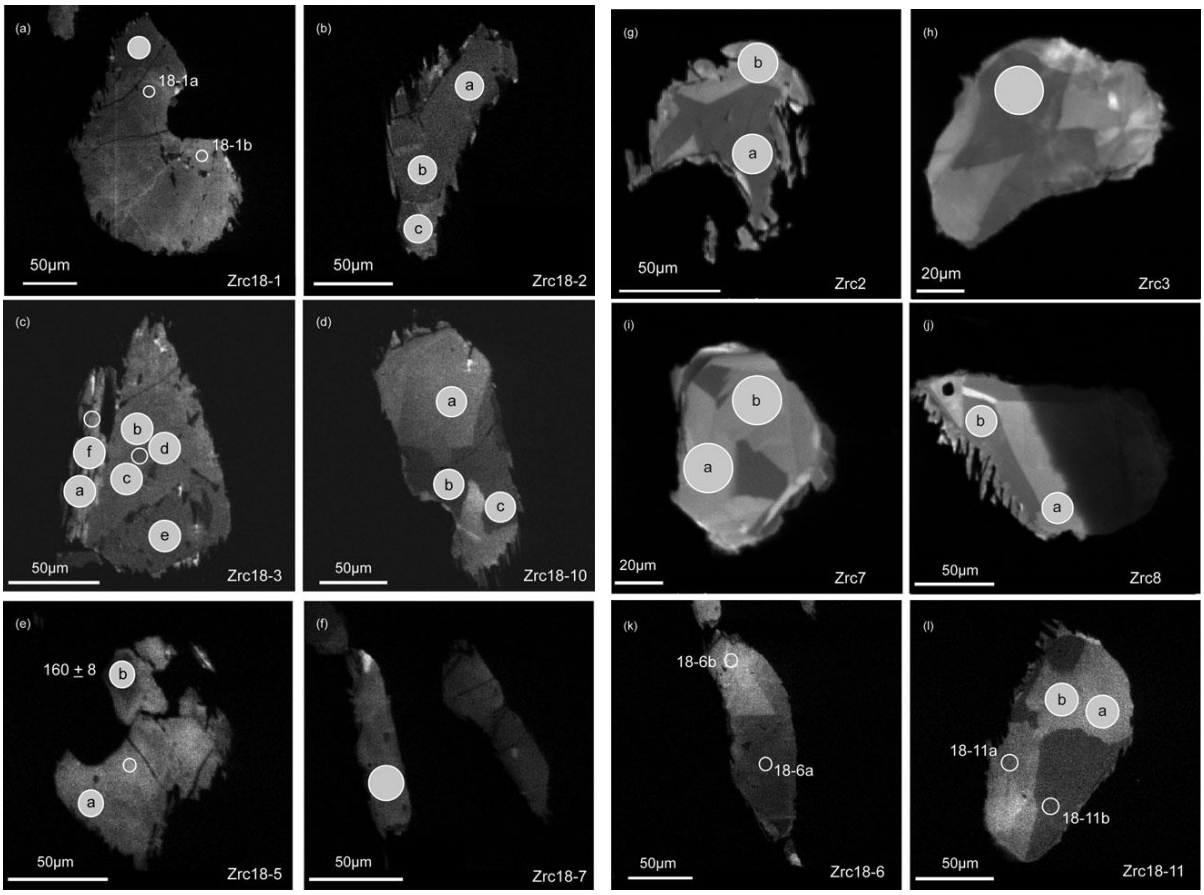

Fig. 3.1.2.5 - SEM images of zircon grains. (a–c) CL image of homogeneous zircon core with fringe-like syn-D2 overgrowth; (d) CL images of zircon grains showing sector and/or broad-banding zoning within cores and narrow rims with fringe-like syn-D2 overgrowth; (e, f) CL image of homogeneous zircon core with very few and tiny syn-S2 overgrowths; and (g–j, k–m) CL images of zircon grains showing sector and/or broad-banding zoning within cores and narrow rims with fringe-like syn-D2 overgrowth. Each image has the name of the zircon indicated and the large shaded circles indicate the spot analysed for U–Th–Pb geochronology, whereas smaller empty circles indicate spots analysed for trace elements. Letters differentiate circles in the same zircon, and correspond to the analyses in Tables 3.2.2 and 3.2.3. The concordant age of 168 ± 8 Ma obtained for zircon 18-5 spot b is also indicated in (e).

Mineral	Cpx						Zrn								
Grain	1	1	1	2	2	3	18_1a	18_1b	18_03	18_03	18_05	18_06a	18_06b	18_11a	18_11b
Position	Core	Core	Rim	Core	Core	Core	Core dark	Core light	Fringe	Core	Core	Core dark	Core light	Core light	Core dark
Li	18.4	15.7	15.4	13.6	14.5	16.6	<1.84	2.32	<1.26	<0.00	3.35	<0.00	<2.07	<1.66	<0.00
Be	1.15	1.48	4.65	2.43	<2.26	2.83	27.1	<0.00	<14.04	<11.40	<12.41	<0.00	<0.00	<12.42	<8.76
B	4.94	3.72	8.98	6.97	3.97	4.27	<8.03	<9.23	16.48	14.18	66.13	14.84	11.73	23.48	35.83
Na	6039	6187	5547	6370	5359	7102	10.8	136.0	22.3	103.6	9.9	15.6	30.3	<2.51	120.8
Sc	138	139	130	166	155	154	492	485	390	448	490	423	432	444	406
Ti	2390	2602	1846	2707	2450	2296	37.9	60.2	14.7	<8.35	<10.67	12.6	46.6	20.1	36.1
V	102	103	107	74.2	74.7	70.7	2.72	<1.50	6.15	5.26	<1.88	<1.39	1.59	<1.29	<1.37
Cr	1470	1830	538	84.0	79.4	85.0	24.7	<15.74	108.0	<13.78	<18.42	<12.24	13.8	<12.46	<13.83
Co	35.7	34.9	31.3	41.3	36.1	37.4	0.67	<0.40	7.69	0.4	2.04	<0.21	1.96	<0.27	0.7
Ni	343	356	325	234	236	254	<1.69	<1.59	131	2.94	7.44	4.06	29.7	<1.16	2.63
Zn	114	119	109	190	144	135	<6.64	32.6	<6.61	5.28	<6.59	<4.99	<3.18	<5.07	<4.57
Rb	0.077	<0.030	0.109	0.126	<0.035	0.059	0.36	0.47	<0.25	0.44	<0.23	0.23	0.7	0.91	0.76
Sr	12.4	12.4	12.5	13.1	15.0	13.4	0.75	1.07	0.42	0.73	0.84	0.44	0.55	0.58	0.88
Y	402	410	483	465	407	449	1919	1828	1474	2381	2155	2693	1687	2651	3245
Zr	118	117	93	137	118	124	—	—	—	—	—	—	—	—	—
Nb	0.273	0.624	0.333	0.392	0.404	0.762	49.8	46.4	36.7	37.5	37.0	31.0	33.7	33.9	28.2
Ba	0.039	<0.00	0.61	<0.064	0.108	0.409	<0.00	<0.243	0.36	<0.00	<0.00	0.2	0.22	0.2	<0.37
La	10.6	11.2	14.5	11.0	9.1	10.2	0.191	0.14	0.78	0.116	0.7	0.065	0.347	0.028	0.088
Ce	50.9	55.8	76.4	57.3	48.2	56.0	14.7	13.4	10.6	8.6	14.9	9.8	14.2	9.2	10.1
Pr	12.2	13.2	18.4	14.2	12.3	14.0	0.07	0.396	0.354	0.083	0.34	0.155	0.516	0.1	0.127
Nd	86.6	90.4	116	102	89.3	97.1	3.63	3.13	1.21	1.76	3.37	3.55	5.97	1.79	3.64
Sm	44.7	45.9	54.6	49.5	43.1	46.6	4.04	8.59	3.03	5.55	5.46	5.52	4.93	9	9.58
Eu	7.74	8.19	9.05	9.5	8.56	9.33	1.16	1.69	1.09	2.33	2.88	2.56	2.27	2.33	3.41
Gd	64.5	65.5	75.4	71.7	64.4	70.5	30.9	32.1	25.5	44.2	33.0	48.2	31.5	48.8	75.5
Tb	11.5	12.3	14.4	13.7	11.8	12.5	12.64	14.2	8.07	15.8	12.05	17.2	11.3	18.1	24.3
Dy	82.5	85.0	100.1	95.5	84.4	92.7	163	161	115	231	167	245	147	243	319
Ho	17.6	17.5	20.9	20.5	18.3	19.4	66.1	70.7	48.0	84.7	74.9	91.4	56.6	92.7	113
Er	47.0	50.8	58.9	58.2	51.5	53.5	321	309	256	386	386	459	273	432	527
Tm	6.66	6.77	8.41	8.01	7.5	7.79	66.0	64.5	57.4	76.6	79.9	91.8	59.1	90.1	108
Yb	43.1	43.5	51.2	51.8	46.0	52.0	621	575	588	670	806	808	562	796	921
Lu	6.16	6.35	7.28	8.04	6.94	6.99	127	114	121	130	145	161	114	154	166
Hf	5.46	5.36	5.39	6.24	5.15	6.78	12546	12504	11558	11337	12349	10941	10415	11184	11229
Ta	0.0145	0.0299	0.0233	0.0075	0.054	0.034	0.510	0.319	2.03	0.162	0.63	0.456	1.1	0.455	0.767
Pb	0.286	0.219	0.331	0.283	0.286	0.329	0.210	0.470	0.430	0.400	0.780	0.231	0.232	0.263	0.310
Th	0.0462	0.053	0.0365	0.082	0.102	0.0324	6.45	4.15	4.16	4.46	12.57	7.77	15.43	7.29	9.22
U	0.0044	<0.0063	0.0116	0.017	0.0077	0.0468	10.4	8.9	12.7	9.1	16.5	14.0	17.6	14.5	15.8
Th/U							0.62	0.46	0.33	0.49	0.76	0.55	0.88	0.50	0.58

Table 3.1.2.2 - Trace element composition (ppm) of clinopyroxene and zircon (zircon grain names refer to Fig. 3.1.2.5)

Identifier	Zrc#	Position		CI	Isotope ratios						Apparent ages			
					$^{207}Pb/^{206}Pb$	2σ	$^{207}Pb/^{235}U$	2σ	$^{206}Pb/^{238}U$	2σ	$^{207}Pb/^{235}U$	2σ	$^{206}Pb/^{238}U$	2σ
Ju24a005	18-5	a	Core	Bright	0.0701	0.0135	0.2570	0.0485	0.0266	0.0013	232	44	169	9
Ju24a006	18-1		Core	Dark	0.1071	0.0226	0.3947	0.0803	0.0267	0.0017	338	69	170	11
Ju24a007	18-2	a	Rim	Dark	0.1526	0.0180	0.5925	0.0669	0.0282	0.0013	472	53	179	8
Ju24a008	18-2	b	Core	Dark	0.0962	0.0300	0.3422	0.1032	0.0258	0.0022	299	90	164	14
Ju24a009	18-2	c	Core	Bright/dark	0.1841	0.0423	0.7581	0.1621	0.0299	0.0028	573	122	190	18
Ju24a010	18-3	a	Rim	Bright	0.4551	0.1359	0.6044	0.1484	0.0096	0.0017	480	118	62	11
Ju24a011	18-3	b	Rim	Bright	0.1695	0.0744	0.2486	0.1020	0.0107	0.0017	225	93	68	11
Ju24a012	18-3	c	Core	Bright/dark	0.1036	0.0161	0.3635	0.0549	0.0255	0.0012	315	48	162	8
Ju24a013	18-3	d	Core	Dark	0.0954	0.0152	0.3461	0.0539	0.0263	0.0013	302	47	167	8
Ju24a014	18-3	e	Rim	Dark	0.1080	0.0248	0.4011	0.0889	0.0269	0.0019	342	76	171	12
Ju24a015	18-10	a	Core	Bright	0.0860	0.0231	0.3300	0.0859	0.0279	0.0022	290	75	177	14
Ju24a016	18-10	b	Core	Dark	0.0523	0.0090	0.1914	0.0326	0.0266	0.0012	178	30	169	8
Ju24a017	18-10	c	Core	Dark	0.1132	0.0251	0.4214	0.0893	0.0270	0.0020	357	76	172	13
Ju24a022	18-11	a	Core	Bright	0.1276	0.0268	0.4782	0.0957	0.0272	0.0020	397	79	173	13
Ju24a023	18-11	b	Core	Bright	0.1099	0.0197	0.4097	0.0709	0.0270	0.0016	349	60	172	10
Ju24a024	8	a	Core	Brigth	0.0881	0.0132	0.3323	0.0486	0.0274	0.0013	291	43	174	8
Ju24a025	8	b	Core	Dark	0.2311	0.0641	0.9054	0.2293	0.0285	0.0035	655	166	181	22
Ju24a026	3		Core	Dark	0.2431	0.0328	1.0193	0.1259	0.0304	0.0020	714	88	193	13
Ju24a027	2	a	Core	Dark	0.2108	0.0398	0.3116	0.0544	0.0107	0.0009	275	48	69	6
Ju24a028	7	a	Core	Bright	0.1510	0.0271	0.6015	0.1025	0.0289	0.0019	478	81	184	12
Ju24a029	7	b	Core	Bright	0.0477	0.0180	0.1853	0.0690	0.0282	0.0020	173	64	179	13
Ju24a034	2	b	Rim	Bright	0.0494	0.0591	0.0679	0.0808	0.0100	0.0013	64	79	67	9
Ju24a035	18-3	f	Rim	Bright	0.0460	0.0597	0.0657	0.0851	0.0104	0.0012	67	84	65	8
Ju24a036	18-5	b	Rim	Dark	0.0489	0.0105	0.1707	0.0361	0.0253	0.0013	161	34	160	8
Ju24a037	18-7		Rim	Dark	0.0540	0.0279	0.1860	0.0956	0.0250	0.0015	159	89	173	9

Table 3.1.2.3 - Zircon isotopic data and apparent ages (zircon numbers refer to Fig. 3.1.2.5)

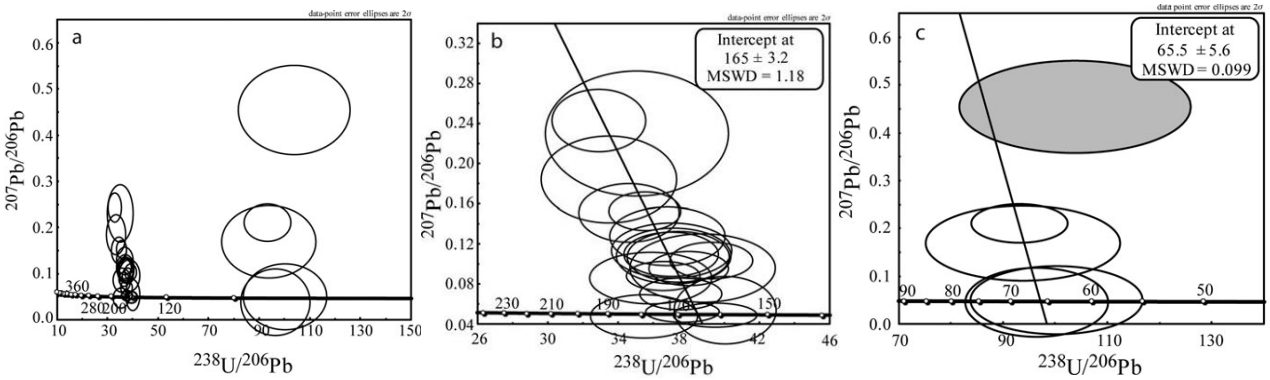

Fig. 3.1.2.6 - Tera-Wasserburg diagrams of isotopic ratios obtained from (a) all analysed zircon, (b) zircon cores and (c) syn-D2 overgrowths.

Laser-induced U–Pb fractionation and mass discrimination effects were simultaneously corrected using a matrix-matched external standard and considering the same integration intervals on the standard and the unknowns. Analyses were carried out using a spot size of 20 μm and a laser fluence of 8 J cm–2. The reference zircon GJ–1 (Jackson et al., 2004) was adopted as external standard and the reference zircons91500 (Wiedenbeck et al., 1995) and 02123 (Ketchum et al., 2001) were selected as validation standards. Data reduction was carried out with the software package GLITTER® (van Achterbergh et al., 2001). Individual uncertainties given by the software for the isotope ratios were propagated relative to the respective reproducibility of the standard. This procedure was carried out for each analytical run as reported in Horstwood et al. (2003). ISOPLOT/Ex 3.00 software package by Ludwig (2003) was used for U–Pb apparent age calculations and representations. Data for external standards and validation standards are reported in Appendix 2.

3.1.2.6 Pressure-temperature-deformation-time (P-T-d-t) evolution and discussion

Textural features, mineral compositions and U–Pb geochronology allow additional constrains to be imposed on the two evolution steps witnessed by the ZSZ serpentinites and detailed in Rebay et al. (2012). Cores of the clinopyroxene and zircon porphyroclasts yield information on the protolith and more in general on the magmatic stage. The primary mineralogy of the rock is not preserved, so the identification of the rock type is not straightforward. Nonetheless, the negative Eu anomaly in both clinopyroxene and zircon (Fig. 3.1.2.4) suggests that the equilibrium melt already crystallized plagioclase. The abundant zircon and the relatively high concentrations of incompatible elements, such as Zr and Y, also suggest that the equilibrium melt was relatively evolved and not basaltic. Support for this conclusion is provided by the similar trace-element composition of analysed clinopyroxene as those from evolved lithologies of the Alpine Tethys such as the Fe–Ti oxide diorites (Tiepolo et al., 1997). Textural and chemical features of zircon and clinopyroxene coupled to the overall mineralogy of the rock (olivine/serpentine-dominated) suggest that the evolved melt likely percolated/intruded the lithospheric mantle. The occurrence of gabbro bodies and rodingite dykes nearby support this conclusion. Processes of melt percolation and melt-rock reaction between the oceanic lithospheric mantle and melts with MORB affinity are well documented in both the Lanzo Massif (Piccardo et al., 2007a; Piccardo et al., 2007b) and the Ligurian ophiolites (Sanfilippo et al., 2014). U–Pb geochronology yields a date of 165 3.2 Ma for the zircon cores. Regarding mantle rocks, this date can either constrain the age of injection of the MORB-type melt into the mantle or the age of cooling of the

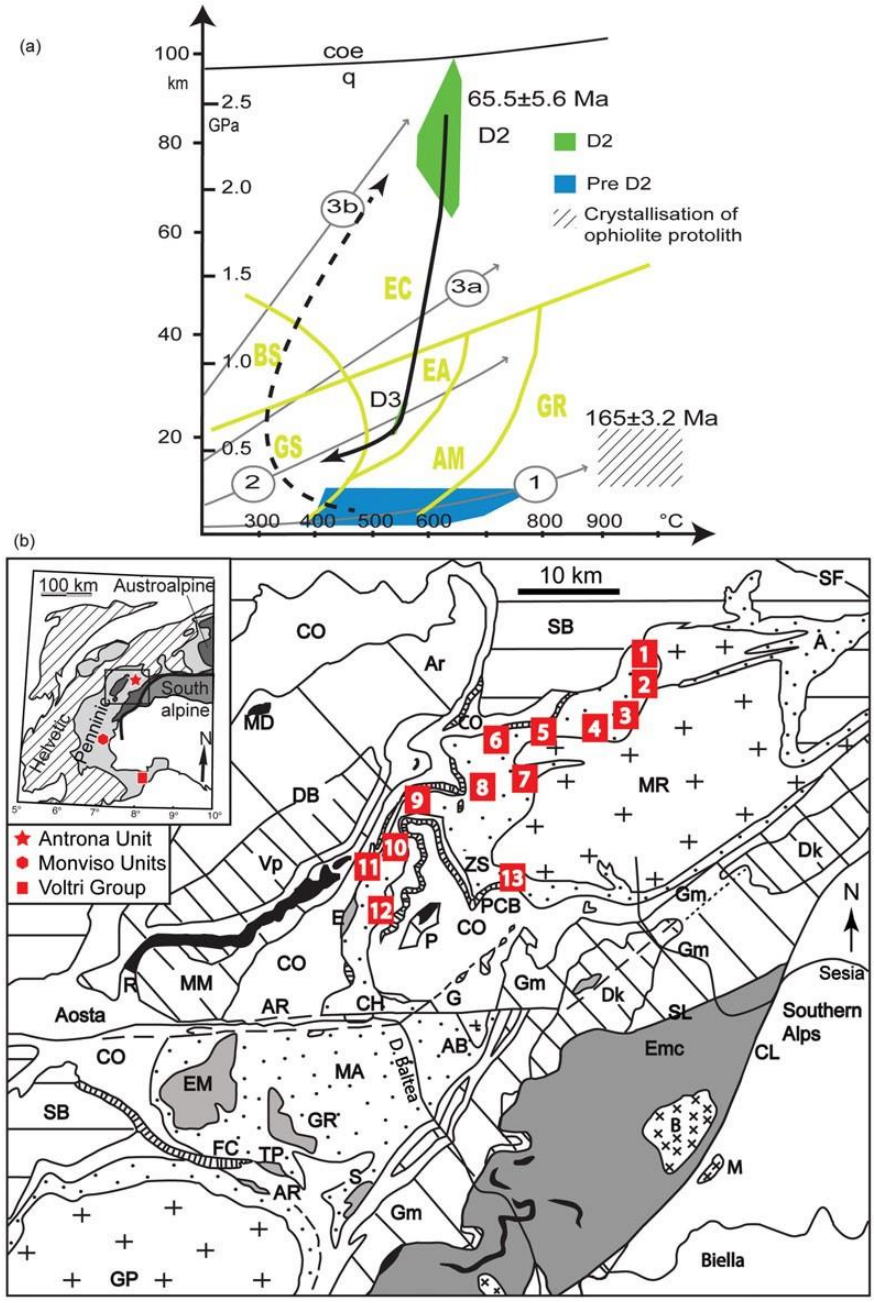

Fig. 3.1.2.7 - (a) P–T–d–t evolution of the studied ZSZ rocks synthesized from Rebay, Spalla and Zanoni (2012) and Zanoni, Rebay and Spalla (2016). Metamorphic facies are after Spear (1993). GS – greenschist; BS – blueschist; EC – eclogite; EA – epidote-amphibolite; AM – amphibolite; GR – granulite. Geotherms after Cloos (1993): (1) near spreading ridge or volcanic arc; (2) normal gradient of old plate interior; (3a) warm subduction zones; and (3b) cold subduction zones. (b) Tectonic sketch map of the north-western Alps with the location of dated samples in the ZSZ. The inset shows the Western Alps with location of dated samples at Monviso. Nappe systems: Penninic continental nappe (MR – Monte Rosa; AB – Arcesa-Brusson; GP – Gran Paradiso; SB – Gran St Bernard); Austroalpine nappe (DB – Dent Blanche; MM – Mont Mary; P – Pillonet; AR – Acque Rosse; CH – Chatillon-St Vincent; E – Etirol-Levaz; G – Grun; EM – Mt Emilius; GR – Glacier-Refray; S – Santanel; TP – Tour Ponton; SL – Sesia-Lanzo Zone; Vp – Valpelline series; Dk – Diorite-kinzigitic series, Ar – Arolla series; Gm1 – Gneiss Minuti Complex, non-eclogitic; Gm2 – Gneiss Minuti Complex, with eclogitic relicts; Emc – Eclogitic Micashist Complex; Mesozoic metasedimentary cover (black): R – Roisan Zone); and Ophiolite Piedmont Zone (CO – Combin Zone; PCB – Pancherot-Cime Bianche; FC – Faisceau de Cogne; ZS – Zermatt-Saas; MA – Mt Avic; A – Antrona ophiolite). Tectonic lines: CL – Canavese tectonic line; AR – Aosta-Ranzola fault system; SF – Simplon normal fault; MD – Mont Dolent; B – Biella; M – Miagliano; SC – Redrawn after Dal Piaz (1999).

oceanic lithosphere as a consequence of exhumation. Notwithstanding, the Middle Jurassic age is in perfect agreement with current knowledge on the age of formation of the Tethyan oceanic lithosphere in the Alps and Apennines (Rubatto et al., 1998; Marotta et al., 2016; Tribuzio et al., 2016). Both clinopyroxene and zircon porphyroclasts have rims and fringes parallel to the S2 foliation at the strain cap and shadow, respectively, which crystallized at P–T conditions of 2.2–2.8 GPa and 580–620 °C (Rebay et al., 2012). The new U–Pb data reveal that this HP–UHP event, registered by the re-crystallization of zircon rims and fringes at these P–T conditions, likely occurred at 65.5 5.6 Ma and was followed by syn-D3 re-equilibration under epidote- amphibolite facies conditions (Fig. 3.1.2.7a; Rebay et al., 2012; Zanoni et al., 2016). Radiometric ages obtained in this work extend the range 35–52 Ma reported in the literature for the Alpine HP–UHP re-equilibration towards older ages (Fig. 3.1.2.7b; Table 3.1.2.1). Remarkably, most of the literature ages have been obtained from samples that are within 20 km of the investigated area, and some are even nearer (5 km). Such geochronological heterogeneities imply that some sections of the ZSZ have likely experienced HP–UHP metamorphism earlier than previously thought; this supports the interpretation, based on contrasted P–T evolutions, that ZSZ is a complex containing different tectono-metamorphic units (e.g. Rebay et al., 2012; Weber and Bucher, 2015). The new ages are comparable to those already reported for the HP re-equilibration in the subducted continental crust of the Sesia-Lanzo Zone, which records the oldest subduction ages among the tectonic units of the Western Alps (Rubatto et al., 1999; Handy and Oberhänsli, 2004; Meda et al., 2010; Spalla et al., 2010; Cenki-Tok et al., 2011; Rubatto et al., 2011; Roda et al., 2012). Similar ages were also reported for the continental inliers of ZSZ (Beltrando et al., 2010; Weber et al., 2015; Fassmer et al., 2016). Older ages interpreted as dating the P–T prograde evolution (Table 3.1.2.1; Skora et al., 2009, 2015) indicate that the subduction of ZSZ oceanic slices was already active at 80 Ma. Our data are therefore coherent with oceanic lithosphere subduction, necessary to justify the low thermal regime under which Western Alpine continental crust was exhumed (e.g. Zucali et al., 2002; Roda et al., 2012). Scattered peak ages (41–72 Ma; Cliff et al., 1998; Table 3.1.2.1) are also observed in the Monviso Massif, supporting the interpretation that it represents a complex of ophiolitic HP slices accreted during the final stages of their exhumation (Schwartz et al., 2000; Guillot et al., 2004). The detection of contrasted petrologic and chronologic histories in both the ZSZ and Monviso Massif confirms that the HP metaophiolites of Piedmont zone is a highly heterogeneous domain composed of slices of variable size, from one to tens of kilometres3 (e.g. Guillot et al., 2004).

3.1.2.7 Conclusions

In summary, our results allow us to demonstrate that multiscale structural analysis assisted by detailed thermodynamic modelling is a fundamental tool for dating single deformation stages and associated mineral transformations. The results confirm a Middle Jurassic age for oceanic crust accretion, which is in agreement with that observed in the ophiolitic complexes from the Alps and Apennines. Finally, our results allow us to widen the time span under which rocks of ZSZ recorded HP–UHP conditions during 70–38 Ma and to infer that syn-D2 eclogite facies metamorphic imprint developed at 65.5 ± 5.6 Ma under a very low thermal regime, as suggested by the relationships with geotherm inferred by Cloos (1993) for cold subduction zones (Fig. 3.1.2.7). These findings go along with the cold thermal regime under which the Sesia-Lanzo Zone was exhumed, before intrusion of the Periadriatic magmas, which is compatible with ongoing oceanic subduction (e.g. Zucali et al., 2002; Zanoni et al., 2010;

Roda et al., 2012; Roda and Zanoni, 2016). Heterogeneous HP–UHP ages and contrasted P–T–d–t evolution within ZSZ can be explained either by: considering slices of ophiolites within a hydrated mantle wedge that follow the same path at different times in a subduction system, where they can be tectonically sampled at different depths; or considering that they can follow different paths. These ophiolite slices can be coupled and/or decoupled at different times in a relatively long-lasting subduction system where oceanic and continental lithosphere are involved, as is the case for the Western Alps.

3.1.2.8 Acknowledgement

G.R., D.Z. and M.I.S. acknowledge funding from MIUR (Ministero dell'Istruzione, dell'Università e della Ricerca) PRIN 2010–2011 (grant number 2010AZR98L) 'Birth and death of oceanic basins: geodynamic processes from rifting to continental collision in Mediterranean and circum-Mediterranean orogens' and G. Gosso, A.M. Marotta and M. Zucali for fruitful discussions on Alpine dynamics. D.Z. and P.L. acknowledge funding from the projects 'Deformazione e metamorfismo delle ofioliti di alta pressione nelle Alpi Occidentali', Università di Pavia and 'Analisi delle impronte strutturali e metamorfiche delle rocce femiche e ultrafemiche della Zona Zermatt-Saas (alta Valtournanche) per la ricostruzione della loro evoluzione geodinamica', Università di Milano, respectively. We wish to thank Gaetano Ortolano, Giovanni Capponi and an anonymous reviewer for useful suggestions and discussions that improved the manuscript.

3.1.2.9 Supplementary materials

Appendix 1. Trace Elements Acquisition methods

Selected masses were acquired in peak hopping mode and each analysis consisted in the acquisition of 1minute of background and 1minute of ablation signal. Further details on the analytical method have been reported by Tiepolo et al. (2003). The laser was operated at 10Hz with a pulse energy on the sample of 0.01-0.03 mJ. The spot size was set to 20 µm and 50 µm for zircon and clinopyroxene respectively. Data reduction was performed with the 'GLITTER' software package (van Achtenbergh et al., 2001) using NIST SRM 612 as the external standard and 44Ca and 29Si as the internal standard for clinopyroxene and zircon, respectively. Precision and accuracy, assessed during each analytical run on the BCR-2 USGS reference glass, are better than 6% relative.

Appendix 2. External standards and validation standards for geochronology

			$^{207}Pb/^{206}Pb$		$^{207}Pb/^{235}U$		$^{206}Pb/^{238}U$		Apparent ages			
Identifier	Zircon name	Run position	Ratio	2σ	Ratio	2σ	Ratio	2σ	$^{207}Pb/^{235}U$	2σ	$^{206}Pb/^{238}U$	2σ
External standard												
Ju24a002	GJ-1	n.2	0.0602	0.0014	0.8106	0.0210	0.0977	0.0024	603	23	601	16
Ju24a003	GJ-1	n.3	0.0597	0.0014	0.8011	0.0208	0.0973	0.0024	597	23	599	16
Ju24a004	GJ-1	n.4	0.0609	0.0014	0.8194	0.0214	0.0976	0.0024	608	23	600	16
Ju24a018	GJ-1	n.18	0.0601	0.0014	0.8115	0.0212	0.0980	0.0024	603	23	603	16
Ju24a019	GJ-1	n.19	0.0598	0.0014	0.8051	0.0211	0.0977	0.0024	600	23	601	16
Ju24a030	GJ-1	n.30	0.0590	0.0014	0.7976	0.0211	0.0981	0.0025	595	23	603	16
Ju24a031	GJ-1	n.31	0.0596	0.0014	0.8010	0.0212	0.0975	0.0024	597	23	600	16
Ju24a032	GJ-1	n.32	0.0616	0.0014	0.8342	0.0220	0.0983	0.0025	616	24	604	16
Ju24a033	GJ-1	n.33	0.0606	0.0014	0.8075	0.0213	0.0966	0.0024	601	23	594	16
Quality control												
Ju24a020	02123	n.20	0.0530	0.0014	0.3441	0.0212	0.0471	0.0024	300	23	297	10
Ju24a021	91500	n.21	0.0753	0.0014	1.8708	0.0211	0.1802	0.0024	1071	48	1068	30

3.1.3 - UHP Ti-chondrodite in the Zermatt-Saas serpentinite: Constraints on a new tectonic scenario

American Mineralogist, 2018, 103, 1002–1005. http://doi.org/10.2138/am-2018-6460
Pietro Luoni, Gisella Rebay, Maria Iole Spalla and Davide Zanoni

Abstract - We focus on the key role of different Ti-humite minerals in subducted serpentinites as possible indicators of extreme pressure conditions. The occurrence of Ti-chondrodite and/or Ti-clinohumite assemblages in the eclogitized serpentinites of the Zermatt-Saas Zone (ZSZ) of the Western Alps allows the recrystallization of such rocks at UHP conditions (P = 2.8–3.5 GPa, T = 600–670 °C) to be determined. Such conditions are similar to those registered by the nearby Cignana unit, a main Alpine area for UHP metamorphism, where coesite and microdiamond have been found. In ZSZ serpentinites, the new UHP assemblage predates the previously recognized HP-UHP paragenesis, which was recently dated at 65 Ma. This finding opens up a new interpretation for the petrologically and structurally well-constrained HP/UHP records, especially because all other ages for HP-UHP metamorphism in the ZSZ are much younger, and for the size of UHP units. Our findings suggest that ophiolites in the axial zone of collisional belts are a mosaic of oceanic lithosphere slices that recorded contrasted thermal and mechanical evolutions during their physical trajectories in the subduction wedge.

3.1.3.1 Introduction

HP-UHP mineral assemblages are the trademark of subduction zones. The most widely known are metamorphic coesite and diamond inclusions in host grains in eclogite-facies crust of the Western Alps, Norway, Central Europe, China, and Kazakhstan and majoritic garnet and Si-bearing spinel in garnet peridotite (e.g., Ernst and Liou, 2008; Frezzotti et al., 2011). Recognized as upper mantle minerals from Colorado Plateau kimberlites (Aoki et al., 1976; Smith, 1977), Ti-clinohumite and Ti-chondrodite are also part of HP-UHP assemblages in ultramafites from China and the Western Alps (Scambelluri and Rampone, 1999; Shen et al., 2015). Shen et al. (2015) proposed conditions of 2.7 GPa and 550–660 °C for the assemblage Ti-chondrodite (Ti-Chn) + Ti-clinohumite (Ti-Chu) + Atg + Chl + Ol + Spl, demonstrating that Ti-Chn + Ti-Chu assemblages are indicators of UHP conditions in serpentinized Ti-rich ultramafites (mineral abbreviations after Whitney and Evans, 2010). The experimental demonstration of Ti-humite minerals defining HP-UHP conditions encouraged us to examine in detail fabrics and mineral assemblages in Valtournanche (Rebay et al., 2018 and references therein), to determine the microstructural relationships of Ti-Chu and/or Ti-Chn relics with the dominant HP/ UHP foliation (S2) in these rocks. The occurrence of UHP rocks in the axial zones of orogenic belts has fuelled debates on geodynamic environment (i.e., subduction, collision, late orogenic extension), exhumation mechanisms, and the timing of exhumation, which strongly influence the preservation of UHP assemblages (Ernst and Liou, 2008). In the Alps, findings of UHP phases have led to the identification of hectometre to kilometre UHP tectonic units within HP nappes. Coesite (Reinecke, 1991) and microdiamond (Frezzotti et al., 2011) relics occur in the Cignana Lake Unit (CLU) at the tectonic contact between the Zermatt-Saas Zone (ZSZ) and the Combin Zone (CZ). The shape, size, and exhumation environment of these UHP tectonic units are discussed. The occurrence of Ti-humites makes serpentinites a new key target for identification of UHP units.

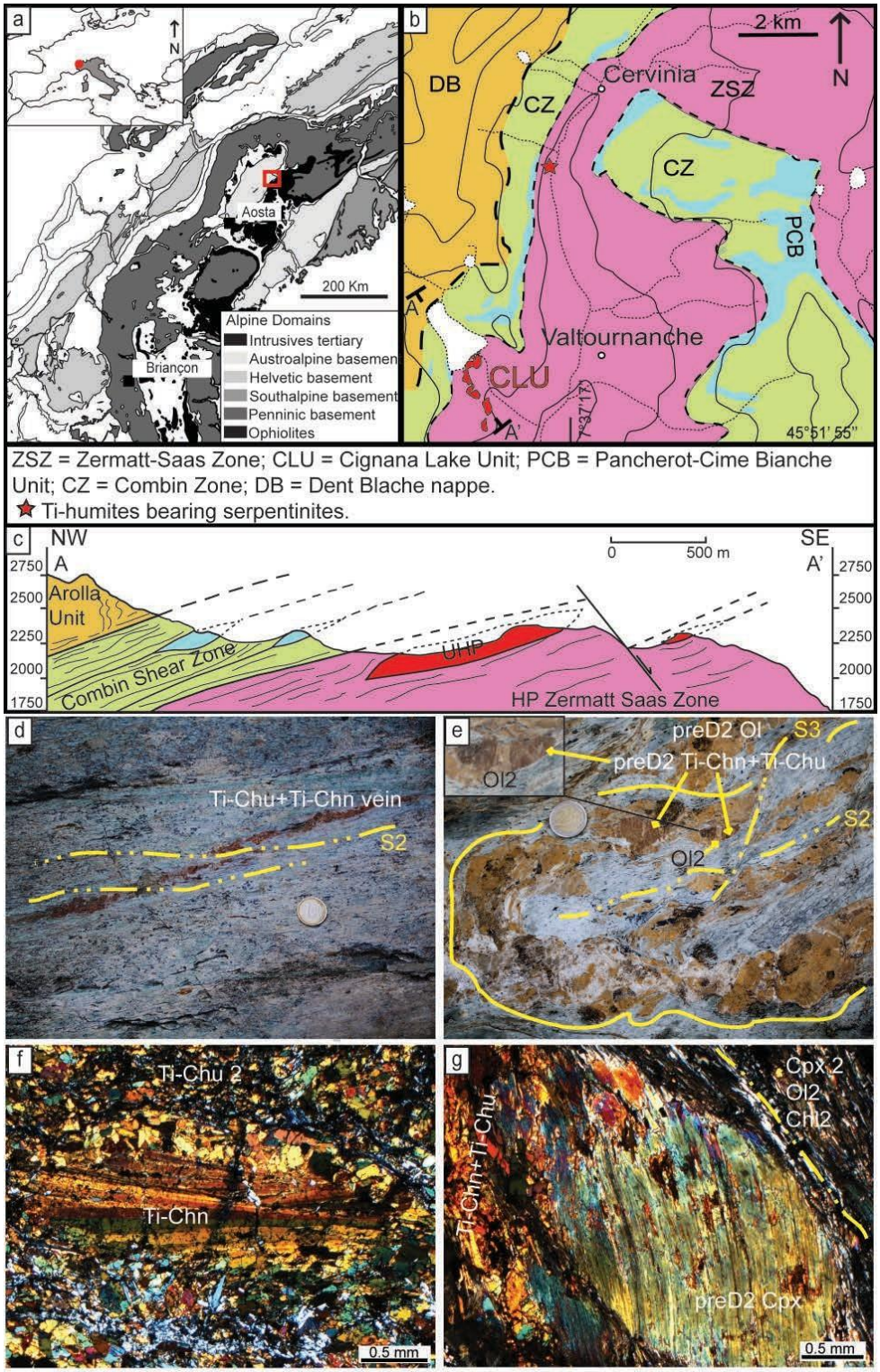

Fig. 3.1.3.1. (a) Location of the studied area and simplified tectonic scheme of Western Alps. (b) Interpretative tectonic sketch of the upper Valtournanche (modified after Groppo et al., 2009; Zanoni et al., 2016); A–A′ = cross-section trace in c. (c) Cross section (see b for location) on the western slope of Valtournanche (modified after Groppo et al., 2009).
(d) Transposed Ti-Chn + Ti-Chu veins at low angle to S2. (e) Ol-rich layer folded by D2. (f) Ti-Chn porphyroclast mantled by Ti-Chu2 aggregate; crossed polars. (g) Pre-D2 Cpx porphyroclast, with Ti-Chn + Ti-Chu exsolutions and Ti-Chn + Ti-Chu bearing fractures, wrapped by S2 foliation; crossed polars

The ZSZ (Figs. 3.1.3.1a and b) was derived from the internal portion of the Piedmont oceanic realm. It was trapped in the suture zone of the Western Alps during Alpine convergence. It comprises serpentinite, meta-gabbro, meta-rodingite, meta-basalt, and various metasediments. The metamorphism of the ZSZ is typical for eclogite facies conditions, locally overprinted by greenschist-facies mineral assemblages (commonly interpreted as exhumation-related). Peak P-T estimates range from 1.9–2.2 GPa and 500–600 °C to 2.3–2.8 GPa and 580–660 °C in different portions of the ZSZ (Bucher et al., 2005; Bucher and Grapes, 2009; Zanoni et al., 2016). Such a wide P-T span suggests that different portions of the ZSZ underwent different tectono-metamorphic evolutions. In contrast, a common, and consequently uniform, evolution of the entire ZSZ was proposed by Angiboust and Agard (2010), with metamorphism peaking at 2.3 ± 0.1 GPa and 540 ± 40 °C. UHP conditions of 2.7 to >3.2 GPa and 590–630 °C have been recorded in small slices of oceanic rocks at the boundary between the ZSZ and CZ, at Lago di Cignana (Fig. 3.1.3.1c) (Groppo et al., 2009 and references therein). Protholith U/Pb ages range from 153–164 Ma (metabasites) to 162–168 Ma (serpentinites, Rebay et al., 2018 and references therein). Peak metamorphic ages are 71–38 Ma so that subduction might have been active already at 80 Ma (Table 3.1.2.1), indicating a wide time interval of re-equilibration during subduction and supporting a heterogeneous evolution of ZSZ. In particular, the dominant HP/UHP foliation (S2) of upper Valtournanche has been dated at 65.5 ± 5.6 Ma (Rebay et al., 2018).

3.1.3.2 Mesostructures and rock types

In ZSZ serpentinites from upper Valtournanche, continuous structural mapping of superposed fabric elements allows the recognition of four groups of ductile structures, where D1–D3 are synmetamorphic, and D4 consists of open folds and local disjunctive cleavage (Zanoni et al., 2016). South of Cervinia (Fig. 3.1.3.1b), serpentinites contain Mag-rich layers alternating with decimetre-thick Cpx- and Ol-rich layers and lenses, Ti-Chu and Ol veins (Fig. 3.1.3.1d), and rare rodingite dikes. As observed at the regional scale, here serpentinites record the dominant S2 composite foliation that wraps centimetre-sized oval Cpx porphyroclasts and transposes Ol veins. S2 intersects Mag-, Cpx-, and Ol-rich layers that are locally rimmed by Ti-Chu aggregates. Different pre-D2 relics are preserved: a foliation in the centimetre-sized D2 lithons; humite-bearing veins marking centimetre-sized tight fold hinges or disrupted into lenticular aggregates mantled by S2; millimetre- to centimetre-thick Mag-rich and up to 10 cm thick Ol-rich layers (Fig. 3.1.3.1e) marking relic folded foliations. These relics are scattered and their dispersion inhibits any walking-correlation between them. For this reason, they will be hereafter labelled as pre-D2 (see also appendix 3).

3.1.3.3 Microstructures and paragenesis

The S2 foliation in serpentinite is marked by shape preferred orientation (SPO) of Ti-Chu2+Atg2 ± Ol2+Chl2+Mag2 ± Cpx2 (numbers denote the relative age of associated fabrics; Rebay et al., 2018) and intersects or wraps around pre-D2 humite-bearing veins and lenses in which Ti-Chn ± Ti-Chu occur. Pre-D2 relics are Mag, Ti-Chn, Ol, or Cpx porphyroclasts, and veins or lenticular micro-aggregates containing Ti-Chn, Ti-Chu, Ol, and Spl [currently not preserved (ex-Spl) and replaced by Ilm with Mag exsolutions], variably transposed and recrystallized during S2 development. Cpx and Cr-rich Ol porphyroclasts, wrapped by S2 and containing exsolutions of Ti-humites, are pre-subduction mantle or ocean floor relics (e.g., Zanoni et al., 2016). Lenses of Ti-Chu + Ol polygonal aggregates are elongated parallel to S2.

Well-preserved pre-D2 Alpine fabrics and Ti-rich assemblages have been found in serpentinite and in veins. Within the veins, red-orange twinned Ti-Chn porphyroclasts, reaching 4 mm (Fig. 3.1.3.1f), enclose randomly oriented Atg and Ilm with lobate grain boundaries, which can be interpreted as relics. Ti-Chn porphyroclasts are cut by fractures filled by Atg2 + Ti-Chu2 and rimmed by polygonal Ti-Chu. Twins are simple or tapering lamellae. In the veins, porphyroclasts of Spl ± Ti-Chn are rimmed by aggregates of small, equigranular polygonal Ti-Chn + Ti-Chu + Ilm + Mag, forming a core-mantle structure. Ol-porphyroclasts (up to 5 mm) with tapering Ti-Chu exsolution lamellae show rims with Atg and Ti-Chu inclusions. The veins are variably transposed by S2 (Ti-Chu2 + Ol2 + Atg2 + Mag2 + Chl2).

In serpentinite, scattered pre-D2 Mag porphyroclasts, up to 5 mm and wrapped by S2, are locally zoned, preserve Cr-rich cores, and are cut by pre-D2 fractures filled by Ti-Chn + Atg +Mag. Polygonal Ol2+Ti-Chu2 occur in pressure shadows of Ol porphyroclasts and show SPO gradually parallelized into S2. Moreover, lenticular micro-aggregates of Ti-Chu + Ilm ± Ti-Chn with minor Atg and Chl, with SPO parallel to S2, replace Ti-Chn porphyroclasts. Ti-Chn occurs in elongated crystals kinked by D2. Pre-D2 Cpx porphyroclasts, with lamellae of Ilm + Mag +Chl + Ti-Chu or Ti-Chn, reach 15 mm and are deformed and kinked. Rarely, they preserve inclusion-free augitic cores. Cpx has Cpx2 rims or pressure shadows of Cpx2 + Atg2+ Chl2. The pre-D2 Cpx grains are cut, at high angle with S2, by conjugate veins of Ti-Chu (polygonal aggregates in Fig. 3.1.3.1g). In Ol-rich layers, S2 (Atg2 + Ol2 + Mag2) wraps pre-D2 Ol and Cr-magnetite porphyroclasts (<5 mm). Ol porphyroclasts, with Cpx, Atg, and Mag inclusions, are locally rimmed by a corona and have pressure shadows of polygonal Ol + Atg + Mag. In summary, the microstructural relationships (see also appendix 3) demonstrate the following sequence of assemblages and fabrics: (1) a pre-D2 mineral assemblage consisting of Cpx or Ol + Ti-Chn + Spl porphyroclasts + Atg ± Chl. The rare relics of Ol, Cpx, and Cr-rich Mag porphyroclasts are yet earlier, and we interpret them as pre-Alpine minerals (e.g. Zanoni et al., 2016). (2) Ti-Chn +Ti-Chu polygonal aggregates (with minor Chl + Ilm + Mag + Atg + Cpx or Ol) can be interpreted as either predating S2 or being synkinematic with the early stages of S2 development (hereafter, pre-D2 to early D2). (3) D2 mylonitic assemblage is Ti-Chu2 + Atg2 + Chl2 + Mag2 ± Ol2 ± Cpx2. A similar sequence of fabrics has been observed in olivine-rich layers. With respect to experimental data, this sequence of successive assemblages indicates that the transition from pre-D2 to D2 reflects the transition from UHP to HP conditions (Figs. 15 and 17 in Shen et al., 2015).

3.1.3.4 Mineral compositions and metamorphic evolutions

Minerals were analysed with a JEOL 8200 Super Probe (WDS), at 15 kV accelerating voltage and a beam current of 15 nA. Natural silicates were used as standards and matrix corrections were calculated using the ZAF procedure. Ti-Chn and Ti-Chu were recalculated on the basis of 13 and 7 cations, respectively. Ol trace elements were obtained, from inclusion-free crystals (checked at SEM images), at Pavia CNR-IGG with a LA-ICP-MS system coupling a 266 nm Nd:YAG laser probe with a double focusing magnetic-sector mass spectrometer, using NIST 610, NIST 611, and BCR2 standards, and GLITTER data processing (Rebay et al., 2018 and references therein). Spot size was 40–55 µm, laser frequency 10 Hz, acquisition was for 40–60 s preceded and followed by at least 40 s background counting. Ti-Chn has 0.32–0.41 Ti apfu and M/Si (M = Mg + Fe + Mn + Ni+ Ti) of 2.43–2.62. Polygonal aggregates have higher M/Si and Ti than porphyroclasts (Fig. 3.1.3.2a): for one sample, M/Si is in the range reported by González-Jiménez et al. (2017), whereas others have consistently higher M/Si probably due to bulk composition. X_{Mg} [Mg/(Mg+Fe)] is 0.88–0.92. Mn is <0.04 apfu. Ti-

Chu composition varies slightly with microstructural position: Ti-Chu in polygonal aggregates has lower M/Si and Mg + Fe + Ti + Ni than Ti-Chu2; Ti is 0.32–0.39 apfu, but usually lower in polygonal aggregates (Fig. 3.1.3.2a). The Ti-Chu exsolutions in pre-D2 Ol have lower Ti content than Ti-Chu2; similarly, X_{Mg} is higher in polygonal Ti-Chu aggregates than in Ti-Chu2. Mn is <0.05 apfu and X_{Mg} 0.89–0.95. In serpentinites, Ol in veins is the richest in Mg (X_{Mg} 0.90–0.96); Ol associated with Ti-Chn porphyroclasts is the richest in Fe (X_{Mg} 0.90–0.91). In Ol porphyroclasts within Ol-rich layers X_{Mg} is 0.89–0.96; in polygonal Ol, X_{Mg} has a similar range. Mn is <0.02 apfu. In Ti-Chn + Ti-Chu veins, Atg shows the widest variation in Al, Si, Mg, and Fe content. Pre-D2 Atg is generally Mg, Fe, and Al poor, whereas Atg2 is richer in Si. Chl is always penninite. In serpentinites, Mag in polygonal aggregates and Mag2 have small amounts of Cr; locally Mag2 is pure magnetite. Pre-D2 Mag porphyroclasts have chromite-rich cores (Mg-chromite + chromite <40%). The cores of pre-D2 Cpx porphyroclasts are augite; Cpx2 has Al <0.6 apfu, higher than the diopsidic rims around the porphyroclasts.

In Ol-rich layers, Ol has variable Cr and Al contents (acquired for T-estimation, e.g., De Hoog et al., 2010, all reported values are above detection limits): 2.43–17.90 and 0.33–3.59 ppm in Ol porphyroclasts, and 2.06–5.98 and 0.88–2.05 ppm in polygonal Ol, respectively. Ol with Cr >10 ppm is interpreted as pre-Alpine relic. Pre-D2 P-T conditions (Fig. 3.1.3.2b) are inferred using a combination of methods. Experimental results in Ti-rich bulks (Shen et al., 2015) limit Ti-Chn + Ti-Chu stability field at minimum P-values of 2.6–3.1 GPa at 560–700 °C by the univariant Ti-Chn out (field above the Ti-Chn out in Fig. 3.1.3.2b), which would constrain Pmin for the pre-D2 assemblage Ti-Chn + Ol + Spl + Chl + Atg. Higher Ti contents enlarge the Chn stability field toward lower P and therefore the occurrence of Ti-rich phases (e.g., relic Ilm, Ilm after Spl) in our rocks suggest to refer to the Schreinemaker P-T grid proposed by Shen et al. (2015) to estimate more reliable P conditions for pre-D2 to early D2 (reactions 1 and 2, Fig. 3.1.3.2b). To this purpose, T conditions shall be constrained. In serpentinite, temperatures for the pre-D2 to early D2 polygonal assemblages were calculated with THERMOCALC (Powell et al., 1998) using the Average T method (AvT): Ol or Cpx (Fo-Fa/Di-Hed), Chl (Clin-Daph), Mag (Mt, Usp), Ilm (Ilm-Geik) solid solutions (calculated using Ax program, end-members' names as in Ax instructions) were used with Atg and Chu (with no Ti) end-members. Since Fe-Mg exchange is poorly constrained, the obtained values, of 640 ± 70 °C (2σ), calculated between 2.1 and 3.0 GPa, are affected by high errors. In Ol-rich layers, the Al content of Ol (De Hoog et al., 2010) indicates 645 ± 55 °C for pre-D2 (calculated from 2.7 to 3.5 GPa) (Ol porphyroclasts), and 635 ± 45 °C for pre-D2 to early D2 (calculated from 2.0 to 3.0 GPa) (Ol-polygonal aggregates) (Fig. 3.1.3.2b). The Atg-out curve indicates T < 670 °C for Opx-free assemblages. The stability of Atg varies as a function of bulk composition toward lower T in Ti-free systems (<640–650 °C; Padrón-Navarta et al., 2013 and references therein), but we refer to the T values estimated for Ti-rich systems by Shen et al. (2015), which have more similar composition to the studied rocks. Considering the sequence of the inferred assemblages, i.e., (1) pre-D2 with Ti-Chn (without Ti-Chu and with Spl), (2) pre-D2 to early D2 with Ti-Chu + Ti-Chn, and (3) synD2 with Ti-Chu, we propose for the estimated T interval, a Pmin of 2.8–3.0 GPa and a Pmax of 3.5 GPa for pre-D2 assemblage 1. Assemblage 2 (pre-D2 to early D2) is stable at similar T-interval (570 to 670 °C), for which the coexistence of Ti-Chu and Ti-Chn indicates a P range from 2.1 to 3.0 GPa (see Fig. 3.1.3.2b, reaction 1). Finally, the syn-S2 paragenesis (without Ti-Chn) is stable below the Ti-Chn out reactions in all compositions, at P-T conditions similar to those previously determined for syn-D2 in serpentinite and rodingite (Zanoni et al., 2016; Rebay et al., 2018).

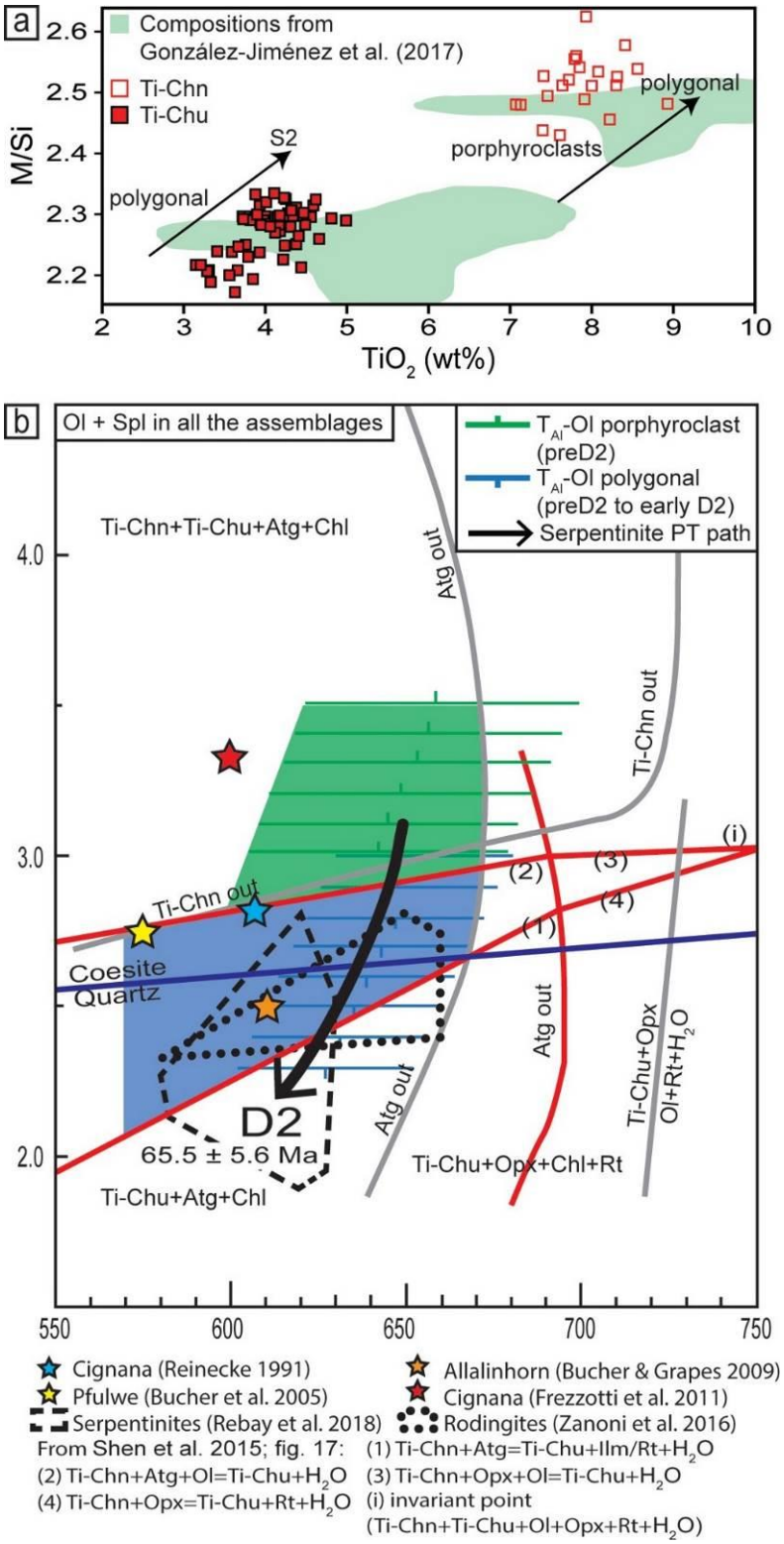

Fig. 3.1.3.2 - (a) M/Si vs. TiO_2 in Ti-Chu and Ti-Chn. (b) Pre-D2 *P-T* conditions (green and blue fields are for pre-D2 and pre-D2 to early D2 assemblages, respectively). Reaction curves and stability fields of mineral assemblages are from Shen et al. (2015); red indicates curves from Ti-richer systems.

3.1.3.5 Discussion and implications

The different chronologically and petrologically framed types of Ti-humites allows UHP conditions in serpentinites to be identified in rocks generally not considered to be diagnostic from a pressure point of view. The diagnostic UHP assemblage (Ti-Chn + Atg + Chl+ Spl + Ol/Cpx) predated the dominant

65 ± 5.6 Ma old foliation (S2 in Rebay et al., 2018) that formed at the limit between HP and UHP and up to now was considered to be at the metamorphic climax conditions. The peak conditions recorded in the ZSZ serpentinites are therefore increased to 2.8–3.5 GPa and 600–670 °C. The rocks were successively re-equilibrated at 2.1–3.0 GPa and 570–670 °C during pre-D2 to early D2. Finally, the rocks were re-equilibrated at 2.2–2.8 GPa and 580–660 °C during S2 development (Zanoni et al., 2016; Rebay et al., 2018). Consequently, the age of the new pressure peak needs to be earlier than the Paleogene-Cretaceous boundary. The implications of this finding are significant (1) for Alpine geology and, more in general, (2) for the interpretation of burial and exhumation processes of UHP/HP meta-ophiolites in collisional belts. In the framework of the Alpine belt, these rocks, together with others preserving UHP assemblages, are distributed along the tectonic contact between ZSZ and CZ and record different and diachronic peak pressures. For example, the nearby LCU underwent UHP (600 °C and P > 3.2 GPa) at 42 ± 2 Ma (Table 3.1.2.1 and references therein), much earlier than the rocks studied in this paper. Consequently, the P-climax was recorded at different depths and times in different portions of ZSZ, which therefore consists of a mosaic of tectonometamorphic units probably accreted at depth. Possibly only a few vestiges of these units preserving UHP signatures survived the main regional foliation development. Others may still be detected. From a more general point of view, the resulting tectonic framework of this key area for the eclogitized oceanic crust points out that ophiolites in the axial zone of collisional belts correspond to a mosaic of slices of oceanic lithosphere recording different thermal and structural evolutions during their burial and exhumation trajectories in the mantle wedge of a subduction system

3.1.3.6 Acknowledgments

Reviewers J.-M. Lardeaux, J.A. Padrón-Navarta, J. Hermann, and Editor I. Swainson provided advice greatly improving the paper. Funding by PSR2015-1716DZANO_M and Studio Ciocca. We thank A. Langone (IGG-CNR Pavia) for his assistance with LA- ICP-MS. This paper is dedicated to the memory of Harry W. Green, who made great improvements on the study and interpretation of UHP ultramafic rocks.

3.1.3.6 Supplementary materials

	Ti-clinohumite		
Texture	in Ol	polygonal	S2
SiO_2	37.13	36.14	37.39
TiO_2	3.43	4.41	3.59
FeO	5.71	7.15	5.44
MnO	0.44	0.58	0.44
MgO	50.47	48.26	50.95
Sum	97.40	96.63	97.94
Si	4.01	3.98	4.01
Ti	0.28	0.37	0.29
Fe^{2+}	0.52	0.66	0.49
Mn	0.04	0.05	0.04
Mg	8.13	7.93	8.16
Cation sum	13.00	13.00	13.00

	Ti-chondrodite	
Texture	porphyroclast	polygonal
SiO_2	32.51	33.38
TiO_2	7.79	8.47
FeO	10.85	8.40
MnO	0.49	0.58
MgO	45.38	46.77
Sum	97.06	97.83
Si	1.97	1.99
Ti	0.35	0.38
Fe^{2+}	0.55	0.42
Mn	0.03	0.03
Mg	4.10	4.16
Cation sum	7.00	7.00

	Olivine	
Texture	porphyroclast	polygona
SiO_2	41.11	40.89
TiO_2	-	-
Al_2O_3	-	-
Cr_2O_3	-	-
FeO	8.20	8.80
MnO	0.35	0.33
MgO	50.17	49.76
NiO	0.11	0.13
Sum	99.94	99.99
Si	1.00	1.00
Ti	-	-
Fe^{2+}	0.17	0.18
Mn	0.01	0.01
Mg	1.82	1.81
Ni	0.00	0.00
Cation sum	3.00	3.00
Al (ppm)	0.42	1.47
Cr (ppm)	7.67	2.11

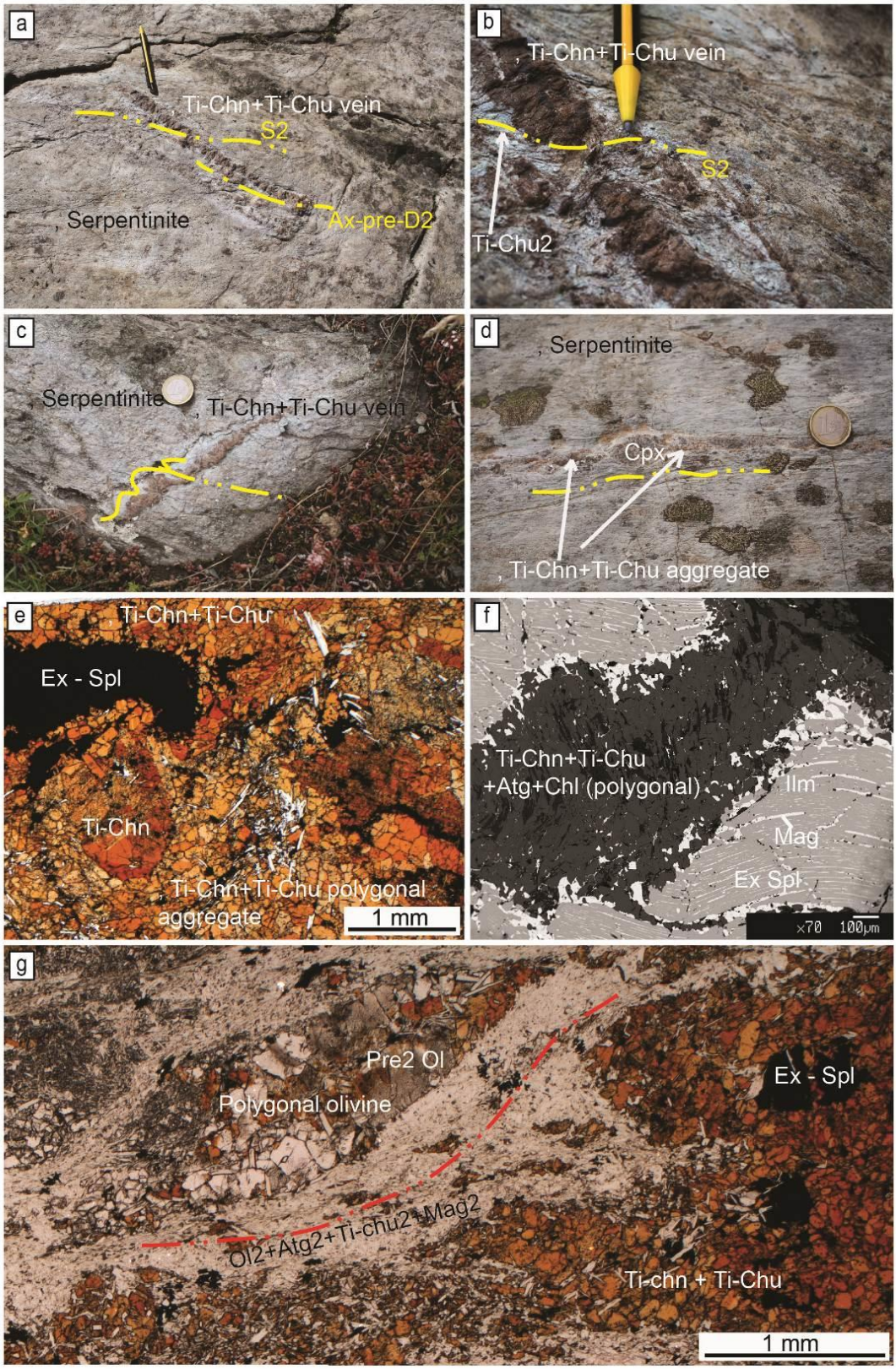

Fig. a - Ti-Chn + Ti-Chu vein in serpentinites transposed by D2 and preserving pre-D2 hinge.
Fig. b - Detail of Ti-Chn + Ti-Chu vein transposed by D2 and foliated by S2.
Fig. c - Ti-Chn + Ti-Chu vein crenulated by D2.
Fig. d - Cpx porphyroclasts wrapped by S2 and locally rimmed by humites.
Fig. e - Ex Spl and Ti-chn porphyroclasts in Ti-Chn + Ti-Chu + Atg polygonal aggregate.
Fig. f - Ex-Spl fracture filled with polygonal Ti-Chn + Ti-Chu + Atg + Chl + Ilm + Mag.
Fig. g - Ol and Ex-Spl porphyroclasts and polygonal Ti-Chu + Ti-Chn aggregate wrapped by S2.

3.1.4 Tectono-metamorphic evolution of UHP Zermatt-Saas serpentinites: a tool for vertical paleogeographic restoration

Submitted to International Geology Review, December 2019

Pietro Luoni, Gisella Rebay, Manuel Roda, Davide Zanoni, and Maria Iole Spalla

Abstract - Within the Zermatt-Saas Zone (ZSZ, northwestern Alps), Ti-chondrodite- and Ti-clinohumite-bearing assemblages in serpentinites indicate UHP conditions. Multiscale structural analysis (1:20 scale mapping) and petrological investigation of serpentinites at Créton (upper Valtournanche) evidenced a polyphasic deformation and metamorphic history. In this locality and at regional scale, S2 is the dominant foliation that developed under HP-UHP conditions. Pre-D2 mineral and textural relicts are preserved despite the pervasiveness of S2. Pre-D2 olivine + Ti-chondrodite + spinel assemblage implies re-equilibration at 2.8–3.3 GPa and 600–630 °C, in agreement with conditions recorded by coesite- and microdiamond-bearing rocks in the Cignana Unit. The P-T conditions inferred for syn-D2 assemblages at Créton are similar to those estimated for D2 in the surrounding serpentinites, which were dated at 65 ± 5.6 Ma. These results suggest that portions of ZSZ were subducted at high depth before 70 Ma and widen the time span under which ZSZ recorded P-T peak conditions. The comparison of these data with results of a numerical model of an ocean-continent subduction system gives insights on coupling stages of this UHP unit with the surrounding ZSZ rocks during the Alpine convergence and vertical paleogeography during different time steps.

3.1.4.1 Introduction

Emplacement of Ultra High Pressure (UHP) rocks in the axial portion of orogenic chains (Chopin 1984; Smith 1984; Kienast et al., 1991; Reinecke 1991; Ernst and Liou 1999) has opened up the need to identify the geodynamic context of their formation and coupling with the surrounding units, apparently free of this metamorphic imprint, and precisely if such formation and/or coupling occurred in a context of subduction, collision or, even, of late orogenic extension. Moreover, the discussion on exhumation mechanisms and timing that are effective for the preservation of UHP assemblages is still open. In the Alps the detection of UHP mineral phases, such as coesite, ellenbergerite, Mg-dumortierite, and microdiamonds, allowed the individuation of hectometre- to kilometre-scale UHP tectonic units enclosed in HP nappes both of oceanic (Zermatt-Saas Zone) and continental (Dora Maira Massif) origin (e.g. Chopin 1984; Chopin et al., 1986; Reinecke 1991; Ferraris et al., 1995; Frezzotti et al., 2011). In the last decades several UHP mineral records have been detected in metabasites and metasediments of the Zermatt-Saas Zone, (Reinecke 1991; Reinecke et al., 1994; van der Klauw et al., 1997; Bucher et al., 2005; Groppo et al., 2009; Frezzotti et al., 2011) and more recently, UHP conditions have been reported also in serpentinites from Créton, in upper Valtournanche (Luoni et al., 2018). In particular, the hectometre-sized Cignana Unit and the UHP Créton serpentinites are localized close to the tectonic contact between Zermatt-Saas and Combin zones (Forster et al., 2004; Luoni et al., 2019 and refs. therein). As evidenced by reviewing the rich-literature (Rebay et al., 2018 and refs. therein) the Pmax conditions are heterogeneous and the proposed metamorphic evolutions are not coherent and often contrasting, as well as the radiometric ages, recently inferred for the peak conditions, which are spread over a time interval from Upper Cretaceous to middle Eocene.

Therefore, a comparison between high-precision structural and metamorphic data, defining the tectono-thermal evolution of these UHP slices, with the predictions from quantitative geodynamic

models becomes a fundamental key to investigate their potential formation and coupling environment during different stages of the convergent Alpine history.
With this aim, the present contribution shows a multiscale structural and petrological analysis that is finalised to define the PTdt evolution of the Créton UHP serpentinites. The results are compared with the prediction of a 2D quantitative geodynamic model of an ocean-continent subduction system.

3.1.4.2 Geological setting

The Zermatt-Saas Zone (ZSZ) is one of the main units of the Piemonte Zone in the Penninic domain of the Western Alps (Fig. 3.1.4.1a; Bigi et al., 1990; Dal Piaz, 1992; Dal Piaz, 2010, Balestro et al., 2019 and references therein). The Piemonte Zone occurs in the axial part of the Western Alps, from the Ligurian Alps to Switzerland (Fig. 3.1.4.1a) and is bordered by the Sesia-Lanzo Zone and the Po Plain to the east, and the Briançonnaise Zone to the west (Beltrando et al., 2010; Dal Piaz, 2010; Spalla et al., 2010; Roda et al., 2019 and references therein). It mostly comprises meta-ophiolites consisting of serpentinites, metagabbros, metabasites, and metasediments with minor continental outliers (Fassmer et al., 2016; Weber and Bucher, 2015 and refs therein).
The ZSZ is interpreted as a remnant of the Alpine Tethys oceanic lithosphere, sutured in the Alpine belt during the Alpine subduction and collision (Dal Piaz, 2001; Reddy et al., 1999; Balestro et al., 2019). Together with the Combin Zone (CZ), ZSZ is sandwiched between the continental nappes of Monte Rosa and Dent Blanche (Fig. 3.1.4.1b). ZSZ and CZ are separated by the Pancherot-Cime Bianche-Bettaforca unit (PCB). The CZ is an ophiolite-bearing unit characterized by mostly metasedimentary rocks and interpreted as derived by an ocean-continent transition zone (e.g. Dal Piaz and Ernst, 1978; Dal Piaz et al., 1981). CZ rocks recorded blueschist facies conditions during the Alpine convergence, recognizable despite the pervasive greenschist facies metamorphism (Reddy et al., 1999; Bousquet et al., 2004 and reference therein). The PCB laying between ZSZ and CZ, is a discontinuous horizon of metasedimentary rocks of Austroalpine affinity, dominated by greenschist facies metamorphic imprint, whose protoliths are thought to be deposited on a thinned continental margin (Dal Piaz, 1988; Dal Piaz, 1999; Passeri et al., 2018).
The ZSZ preserves a complete ophiolitic sequence derived from the internal portion of the oceanic realm (Bearth, 1967; Ernst and Dal Piaz, 1978; Tartarotti et al., 2017). It includes serpentinites (Li et al., 2004a; Rebay et al., 2012), metagabbros and metarodingites (Li et al., 2004b; Zanoni et al., 2016), metabasites (Bucher et al., 2005 and reference therein), and metasedimentary cover, which consists of calcschists, marbles, and quartzites. Ophiolites locally enclose continental slices, such as the Theodul Glacier Unit (TGU) (Weber and Bucher, 2015). The age of protoliths is proposed to be 164-153 Ma for metagabbros and metabasites (Rubatto et al., 1998) in the Swiss portion of ZSZ, and 168-162 Ma for basalt melt-percolated serpentinites in Valtournanche (Rebay et al., 2018). The whole ZSZ is dominated by an eclogite facies metamorphic imprint, registered during the Alpine subduction, and overprinted by epidote amphibolite and greenschist facies metamorphism (Ernst and Dal Piaz, 1978; Spalla et al., 1996; Rebay et al., 2012; Rebay et al., 2018). Since Reinecke (1991) inferred metamorphic PT peak conditions at 3.0 GPa and 550-600 °C for quartzites in the Cignana Lake Unit (CLU; Fig. 3.1.4.1b and Fig. 3.1.4.1c), HP-UHP peak conditions have been estimated in other localities of the ZSZ. Metabasites of Saas-Fee experienced PT conditions from 1.9-2.2 GPa and 530-

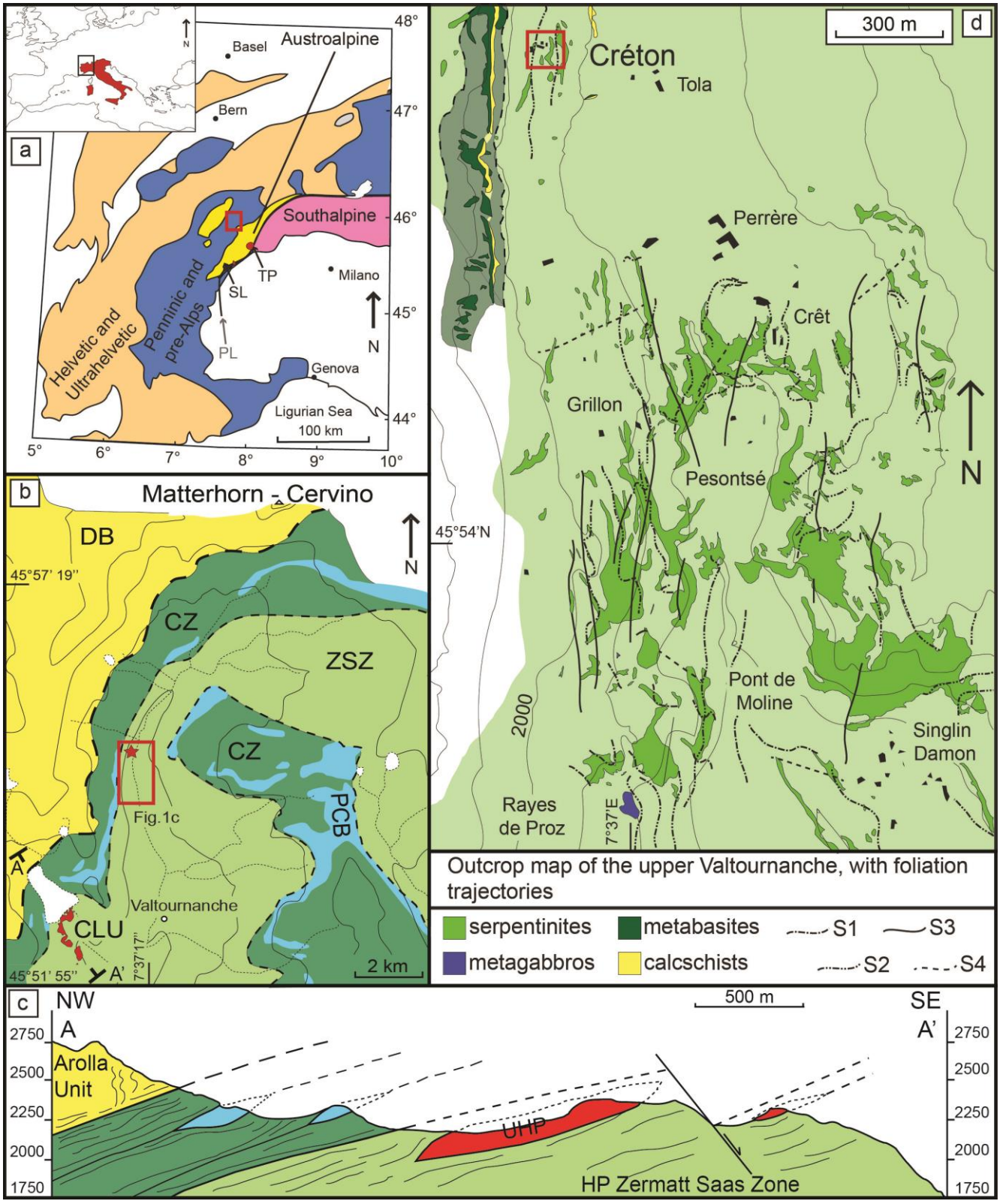

Fig. 3.1.4.1. (a) Location of the studied area in the simplified tectonic framework of the Western Alps; (b) simplified structural setting of the upper Valtournanche (redrawn after De Giusti et al., 2003 and Forster et al., 2004): CLU Cignana Lake Unit; CZ Combin Zone; DB Dent Blanch Nappe; PCB Pancherot-Cime Bianche Unit; ZSZ Zermatt-Saas Zone. AA' cross-section is shown in Fig. 3.1.4.d. The red star is the location of the studied area and the red rectangle is Fig. 3.1.4.1c; (1c) foliation trajectory map with legend of Upper Valtournanche after Luoni et al. (2019) and Zanoni (unpublished: original mapping at 1:5000 scale). Red square locates the Créton outcrops; (d) cross-section of UHP Cignana Lake Unit and Arolla Unit (Dent Blanche Nappe) – Combin Zone – Zermatt-Saas Zone contacts (Forster et al., 2004).

Key	Locality	Age (Ma)	Peak P-T conditions	Reference
1	Saas Fee	38.1 ± 2.7 - 40.7 ± 1.8		Skora *et al.* 2015
	Saas Fee		2.5 GPa 650 °C	Meyer 1983
	Saas Fee		2.5 GPa 650 °C	Bucher and Frey 1994
	Saas Fee	39.5 ± 0.1		Skora *et al.* 2015
2	Allalinhorn		1.5 GPa 570-700 °C	Chinner & Dixon 1973
	Allalinhorn		2.5 GPa 610 °C	Bucher and Grapes 2009
	Allalinhorn		2.3-2.5 GPa 530-555 °C	Angiboust *et al.* 2009
3	Mellichen	48.8 ± 2.9		Rubatto *et al.* 1998
	Mellichen	40.3 ± 9.2		Rubatto *et al.* 1998
	Mellichen		2.5-3.0 GPa 550-600 °C	Bucher *et al.* 2005
5	Pfulwe	48.9 ± 4.8	1.75-2.0 GPa 550-600 °C	Mahlen *et al.* 2006; Barnicoat and Fry 1986
	Pfulwe		2.5-3.0 GPa 550-600 °C	Bucher *et al.* 2005
6	Zermatt		1.4 GPa 600 °C	Oberhänsli 1980
	Zermatt		1.75-2.0 GPa 550-600 °C	Barnicoat 1988
7	Lichenbretter		2.0-2.5 GPa 600-650 °C	Li *et al.* 2004
	Riffelhorn-Gornergrat		2.0-2.5 GPa 600-650 °C	Li *et al.* 2004
8	Trockener Steg		2.2-2.3 GPa 515-645 °C	Weber & Bucher 2015
	Trockener Steg		2.2-2.3 GPa 450-550 °C	Weber & Bucher 2015
9	Breuil		0.8-1.2 GPa 420-520 °C	Ernst & Dal Piaz 1978
10	Valtournenche	65.5 ± 5.6	2.2-2.8 GPa 600 °C	Rebay *et al.* 2012; Rebay et al. 2018
	Valtournenche		2.3–2.8 GPa 580–660 °C	Zanoni *et al.* 2016
11	Cignana	40.6 ± 2.6	2.6-3.0 GPa ca. 600 °C	Amato *et al.* 1999; van der Klauw et al. 1997
	Cignana	52 ± 18 Ma		Bowtell *et al.* 1994
	Cignana	44.1 ± 0.7		Rubatto *et al.* 1998
	Cignana	44.1 ± 0.7	2.7-3.0 GPa 600 °C	Rubatto *et al.* 1998; Reinecke 1995, 1997
	Cignana	43.2 ± 1.1 - 44.4 ± 1.5		Gouzo *et al.* 2006; Reinecke 1991
	Cignana	40.7 ± 0.1	2.6-2.8 GPa 590-630 °C	Skora *et al.* 2015; Reinecke 1991
12	St. Jacques	39.2 ± 1.6	0.8-1.2 GPa 420-520 °C	Skora *et al.* 2015, Ernst & Dal Piaz 1978

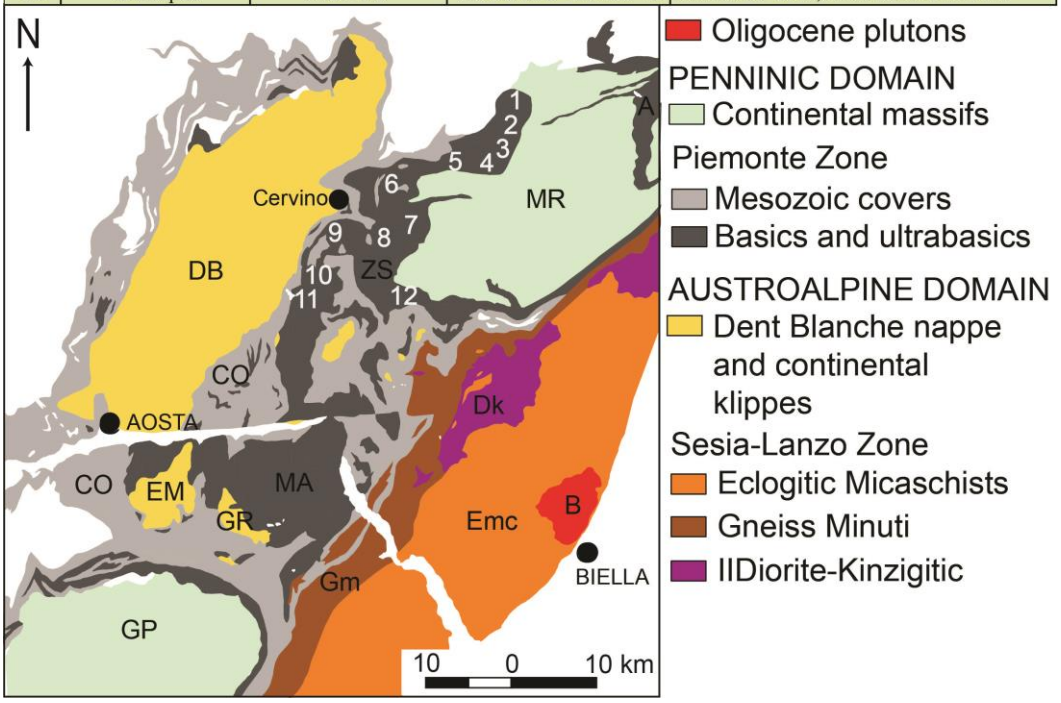

Table 3.1.4.1. Metamorphic conditions and radiometric ages of the HP-UHP peaks of Zermatt-Saas Zone (after Rebay et al., 2018). Data are localised in the underlying tectonic sketch (redrawn after Dal Piaz, 1999): A=Antrona Ophiolite; DB=Dent-Blanche nappe; MR=Monte Rosa; ZS=Zermatt-Saas Zone; CO=Combin Zone; Dk=II Diorite-Kinzigitic Zone; EM=Mont Emilius, GR=Glacier-Refray; MA=Mont Avic; B=Biella pluton; Emc=Eclogitic Micaschists Complex; Gm=Gneiss Minuti Complex; GP=Gran Paradiso.

600 °C (Dale et al., 2009) and 2.3-2.5 GPa and 530-555 °C (Angiboust et al., 2009) to 2.5-3.0 GPa and 550-600 °C (Bucher et al., 2005). Metagabbros in the Swiss portion of ZSZ registered peak conditions of 1.75-2.0 GPa and 550-600 °C (Barnicoat and Fry, 1986), 2.5 GPa and 650 °C (Meyer, 1983) and 2.5 GPa and 610 °C (Bucher and Grapes, 2009). Further estimates in CLU show PT conditions from

2.7 to over 3.2 GPa and temperatures of 590-630°C (van der Klauw et al., 1997; Reinecke, 1998; Groppo et al., 2009), accompanied by the discovery of microdiamonds in oceanic metasediments (Frezzotti et al., 2011). HP-UHP peak conditions are also reported for the mantle rocks of the ZSZ: serpentinites from the Swiss portion of the ZSZ recorded peak conditions at 2.0-2.5 GPa and 600-650°C (Li et al., 2004a) while serpentinites from Valtournanche experienced peak conditions at 2.2-2.8 GPa and 580-620°C (Rebay et al., 2012), together with the associated rodingites at 2.3–2.8 GPa and 580–660°C (Zanoni et al., 2016). In TGU at Trockener Steg (Zermatt area) peak conditions of 2.2-2.3 GPa and 515-645°C are estimated in a continental slice enclosed within ZSZ (Weber and Bucher, 2015).

ZSZ serpentinites have been interpreted to be affected by an ocean floor metasomatism responsible for serpentinisation of the peridotites and rodingitisation of the associated gabbroic dikes (Rahn and Bucher, 1998; Li et al., 2004b; Zanoni et al., 2016). Ti-clinohumite in veins and aggregates has been interpreted as the record of both ocean-floor metasomatism, at conditions of 0.4 GPa and 420 °C (Rahn and Bucher, 1998), and HP-UHP syn-subduction metamorphism, since Ti-clinohumite is in textural equilibrium with HP mineral assemblages (Scambelluri and Rampone, 1999; Groppo and Compagnoni, 2007; Ferrando et al., 2010; Rebay et al., 2012).

Recently at Créton (see Fig. 3.1.4.1d), the finding of Ti-chondrodite and Ti-chondrodite + Ti-clinohumite bearing assemblages allowed inferring UHP conditions predating the HP-UHP regional scale fabrics in the ZSZ serpentinites (Luoni et al., 2018).

Although all these peak PT estimates disclose HP-UHP conditions, differences in P and T values occur (see Rebay et al., 2018), together with a heterogeneous areal distribution of Pmax conditions. Furthermore, peak ages range between 68 and 38 Ma, although evidence of prograde metamorphism dates back at 80 Ma (e.g. Skora et al., 2015). These data (Table 3.1.4.1) are in contrast with ZSZ experiencing a homogeneous evolution during the Alpine convergence (e.g. Angiboust et al., 2009; Angiboust and Agard, 2010), but rather enforce the interpretation of a heterogeneous metamorphic evolution covering a wide time span during the subduction of the ZSZ rocks and associated continental slivers (Spalla et al., 1996; Gerya and Stöckhert 2005; Spalla et al., 2010; Roda et al., 2012).

3.1.4.3 Deformation history

Valtournanche serpentinites and rodingites underwent a common structural evolution of three ductile syn-metamorphic stages (D1, D2, D3) followed by a stage (D4) not associated with new mineral growth (Rebay et al., 2012; Zanoni et al., 2012). During D2 the most pervasive foliation S2 developed under HP conditions (Fig. 3.1.4.1d). D3 structures consist of open folds and the associated S3 foliation, whereas D4 mostly consists of open folds with sub vertical axial planes. Créton outcrops have been the subject of high-precision structural mapping at 1:20 scale to further investigate pre-D2 evolution and to precisely define the rich lithostratigraphy of UHP serpentinites (Fig. 3.1.4.2, Luoni et al., 2019).

Créton serpentinites are close to the boundary with calcschists and metabasites of the CZ (Fig. 3.1.4.1d). They contain layers of magnetite and embed rare decimetre-thick pyroxenite and olivine-rich layers and lenses. Locally Ti-chondrodite and Ti-clinohumite and olivine veins occur. The effects of polyphasic deformation, modelling the original lithostratigraphy, are synthesised in Fig. 3.1.4.3.

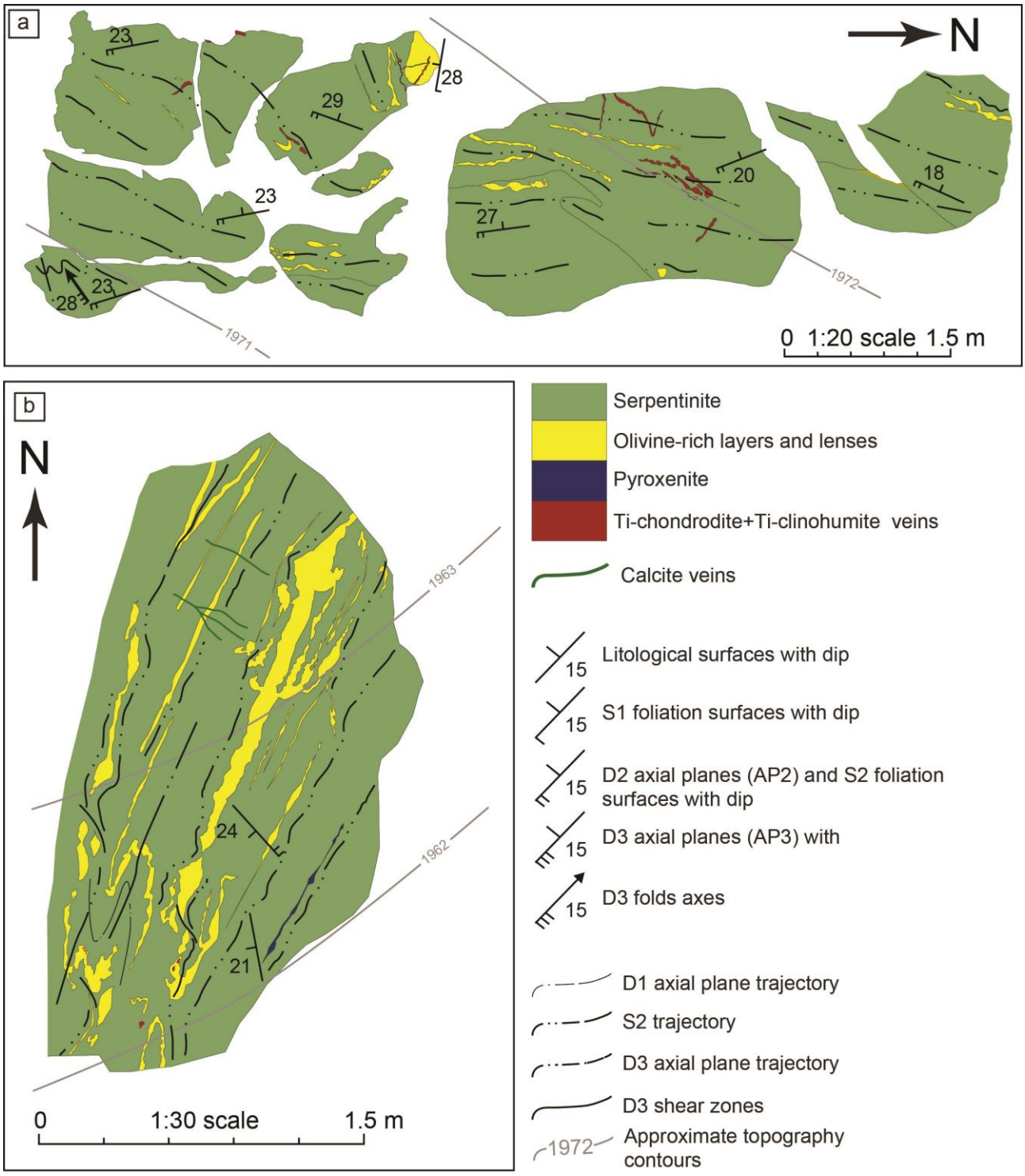

Fig. 3.1.4.2. Form surface maps of two outcrops from Créton, showing a quite complete lithostratigraphy and sequence of superposed fabrics (modified after Luoni et al., 2019).

As described by Luoni et al. (2019), D1 structures are rare D1 rootless fold hinges marked by magnetite layers, olivine-rich layers, Ti-chondrodite + Ti-clinohumite veins (Fig. 3.1.4.3a) and S1 foliation in an olivine-rich lens.

D2 produced tight to isoclinal folds of olivine-rich layers (Fig. 3.1.4.3b), and boudins of olivine-rich layers, pyroxenite, and Ti-chondrodite + Ti-clinohumite veins, locally with a granoblastic texture in which an oriented fabric is lacking. Magnetite layers are often asymmetrically crenulated by D2. S2 is

a mylonitic, locally composite, foliation (Fig. 3.1.4.3b) and represents the dominant structure. S2 shows a dip azimuth at W-WNW/14°- 65° and is observed in all lithotypes intersecting previous structures.

Rare D3 centimetre-wide crenulation affects S2 in serpentinites. D3 fold axial planes dip WNW with medium angle and fold axes dip at a low angle towards WSW (Luoni et al., 2019). S3 axial plane foliation has been recognized only at the microscale. D3 also developed shear zones deflecting S2, magnetite layers (Fig. 3.1.4.3c) and olivine-rich layers.

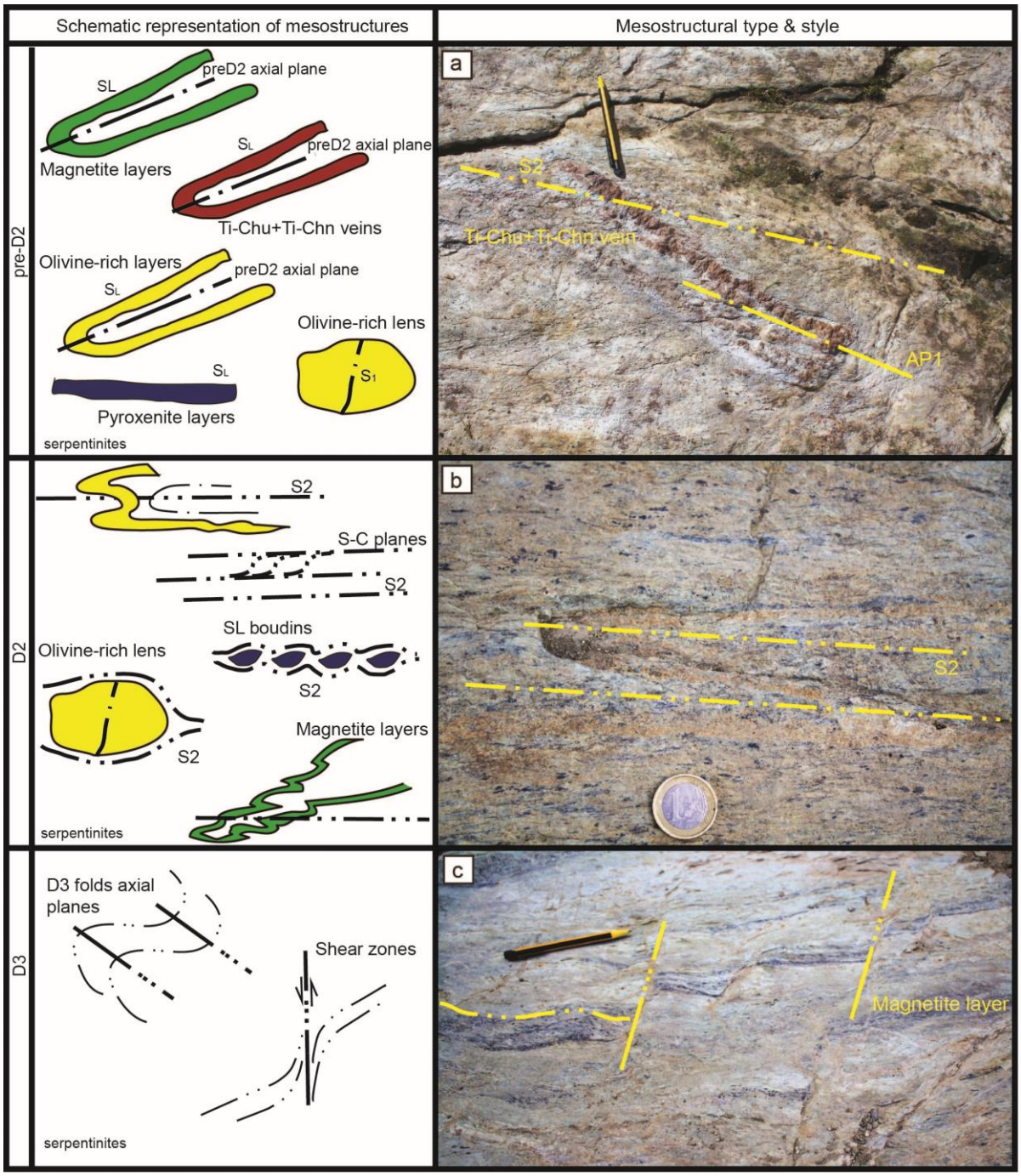

Fig. 3.1.4.3. Mesostructures revealing the tectonic history of Créton serpentinites. (a) Ti-chondrodite + Ti-clinohumite vein marking D1 isoclinal fold and intersected by S2 foliation: AP1 = D1 axial plane; (b) olivine-rich layer underlying D2 tight folds in olivine-rich serpentinite; (c) magnetite layer intersected by S2 and D3 discrete shear zones in serpentinite. Coin and pencil for scale.

3.1.4.4 Syn-metamorphic fabric evolution

Petrographic and structural microanalysis is focused on serpentinites and embedded rocks such as olivine-rich layers and lenses, pyroxenites, Ti-chondrodite + Ti-clinohumite veins. S2 affects serpentinites and all the embedded lithotypes and contains pre-D2 mineral and textural relicts consisting of S1 relics or deformed veins and lenses with granoblastic textures.

Four subsequent mineral assemblages were distinguished (Table 3.1.4.2): pre-D2 relics are porphyroclasts and mineral aggregates wrapped by S2, locally marking S1 foliation; pre-D2 to early-D2 minerals constitute polygonal aggregates, often around pre-D2 porphyroclasts, and are wrapped by S2. D2 assemblages underline S2 foliation and fill syn-D2 boudins necks. Locally syn-D3 minerals overgrew S2 foliation or marked incipient D3 folds axial plane foliation. Mineral abbreviations are from Whitney and Evans (2010).

Serpentinite

Antigorite marks both pre-D2 and syn-D2 domains. SPO (shape preferred orientation) of Atg2 fibres defines S2 mylonitic foliation with Mag2 and Ol2 (Fig. 3.1.4.4a) or Cpx2 (Fig. 3.1.4.4b). Often Cpx2 is parallel to Chl2 SPO and LPO (Fig. 3.1.4.4b). S2 wraps pre-D2 centimetre-sized oval aggregates of antigorite: they can be constituted of oriented fibres of Atg or made of interlobate Atg lamellae in mesh textures. Submillimetre-sized pre-D2 olivine porphyroclasts are wrapped by S2 and often enclose sharp-edged and anhedral to rounded Mag (Fig. 3.1.4.4a). Furthermore, pre-D2 Ol aligned porphyroclasts constitute the remnants of olivine veinlets. Pre-D2 Ol shows undulose extinction, and contains Ti-Chu lamellae, Atg, Mag, and fluid inclusions. Ol2 often rims pre-D2 Ol. Locally, Cpx2 or Ol2 and Atg2 occur in S2 pressure shadows of pre-D2 Ol. Pre-D2 millimetre-sized rounded Cr-Mag and Mag are wrapped by S2 and often rimmed by Mag2. Mag2 grains are aligned in submillimetre layers along S2 (Fig. 3.1.4.4a). Chlorite constitutes lenses and anastomosed layers wrapping Cpx2 aggregates and Ti-chondrodite + Ti-clinohumite veins. Aggregates of chlorite contain Chl2 grains parallel to S2, locally rimmed by Chl3. Locally, in Chl-rich aggregates, S2 is marked by Chl2 ± Atg2 and wraps pre-D2 Chl porphyroclasts as they display different LPO with respect to minerals underlying S2. Pre-D2 Ti-Chu porphyroclasts with undulose extinction are scattered in the serpentinite matrix and are wrapped by S2 foliation marked by Atg2 + Mag2 ± Ti-Chu2. SPO of Atg3 and Mag3 marks the rare S3 foliation and D3 shear zones with Amph3. Rare dolomite porphyroclasts are wrapped by S2 marked by Dol2 + Mag2 + Atg2 + Ol2. Rare apatite porphyroclasts, with undulose extinction are wrapped by S2 defined by Atg2 + Cpx2 + Chl2. Calcite veins are locally parallel to S2 foliations (Cal2) and fill fractures crosscutting S2 (post-D2 Cal).

Olivine-rich layers and lenses

Olivine-rich layers display massive cores with more than 90% of olivine and strongly foliated rims with a higher modal amount of Atg than the cores. The cores of these layers contain millimetre pre-D2 subhedral Ol porphyroclasts (Fig. 3.1.4.4c) with weak undulose extinction and fractures. Locally their SPO is parallel to the S2 foliation wrapping or crosscutting the layers. They are rich in inclusions of micron-sized Mag and Atg. Mag is mostly sharp-edged and rounded while Atg flakes may have both sharp and irregular edges. Ol porphyroclasts are surrounded by polygonal aggregates of submillimetre pre-D2 to early-D2 Ol + Atg + Mag. These aggregates do not show any preferred orientation. Edges between grains are sharp and Mag inclusions are common. Mag is also interstitial among Ol polygonal grains. Micron-sized, rounded and sharp-edged inclusions of clinopyroxene occur both in pre-D2 and in pre-D2-to-early-D2 Ol. In the rims of the layers, where S2 is pervasive, Atg is more abundant than

Ol and wraps pre-D2 Ol porphyroclasts. Polygonal pre-D2 to early-D2 Ol occurs in pressure shadows of pre-D2 Ol whereas Ol2 is very fine grained and shows SPO parallel to

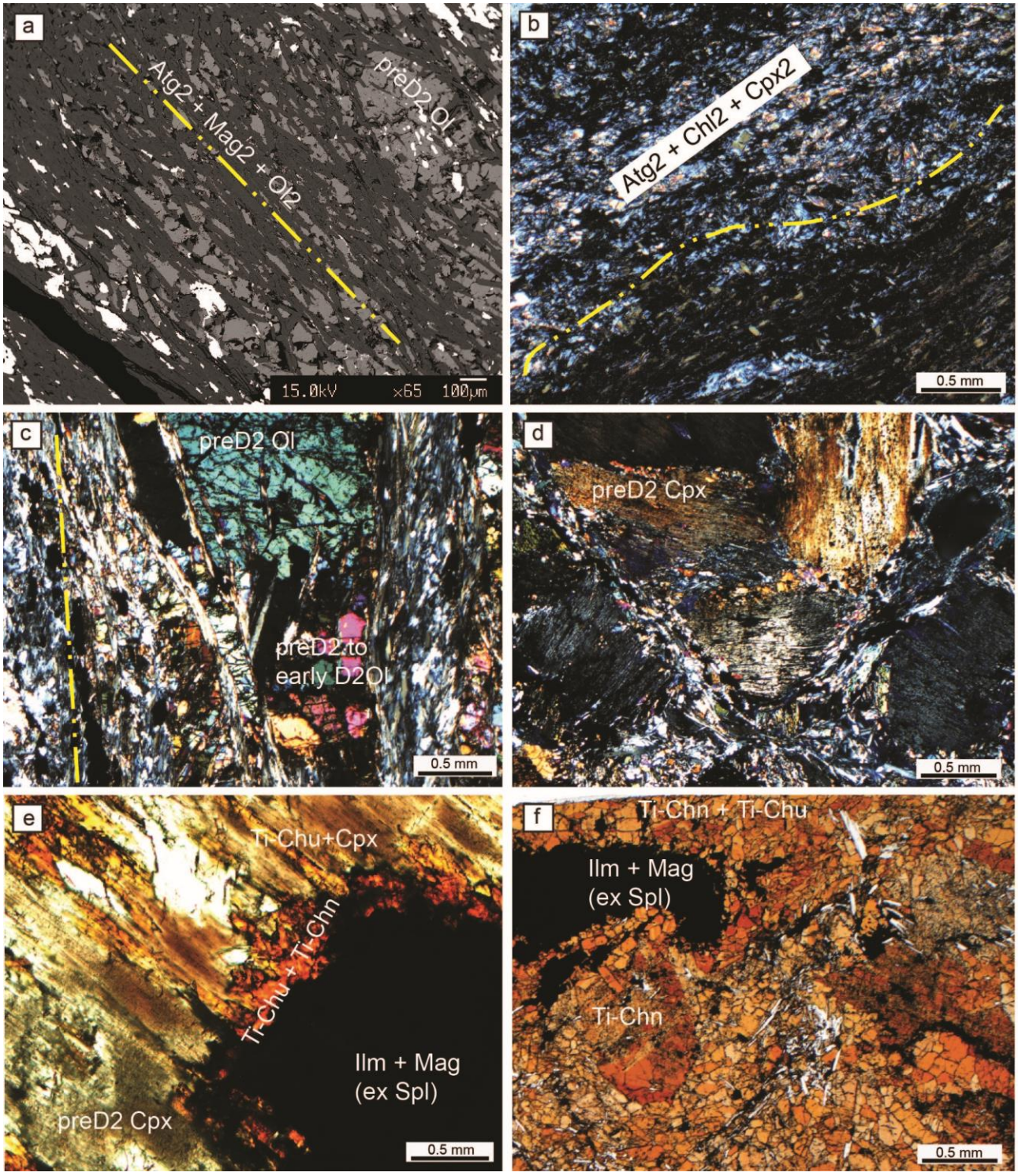

Fig. 3.1.4.4. Microstructures. (a) S2 foliation in serpentinite marked by Atg2 + Mag2 + Ol2, wrapping pre-D2 Ol with Mag inclusions (BSE image); (b) S2 foliation in serpentinite marked by Atg2 + Chl2 + Cpx2 (crossed polars); (c) olivine-rich layer with pre-D2 and pre-D2 to early-D2 Ol wrapped by S2 foliation marked by Ol2 + Atg2 + Mag2 (crossed polars); (d) Cpx porphyroclast in a Atg2 + Chl2 + Cpx2 + Mag2 matrix (crossed polars); (e) Ti-Chu + Ti-Chn rim between Ilm + Mag aggregate and pre-D2 to early-D2 Cpx (plane polarised light); (f) Core-mantle structure with pre-D2 Ti-Chn porphyroclast surrounded by a Ti-Chn +Ti-Chu polygonal aggregate (plane polarized light).

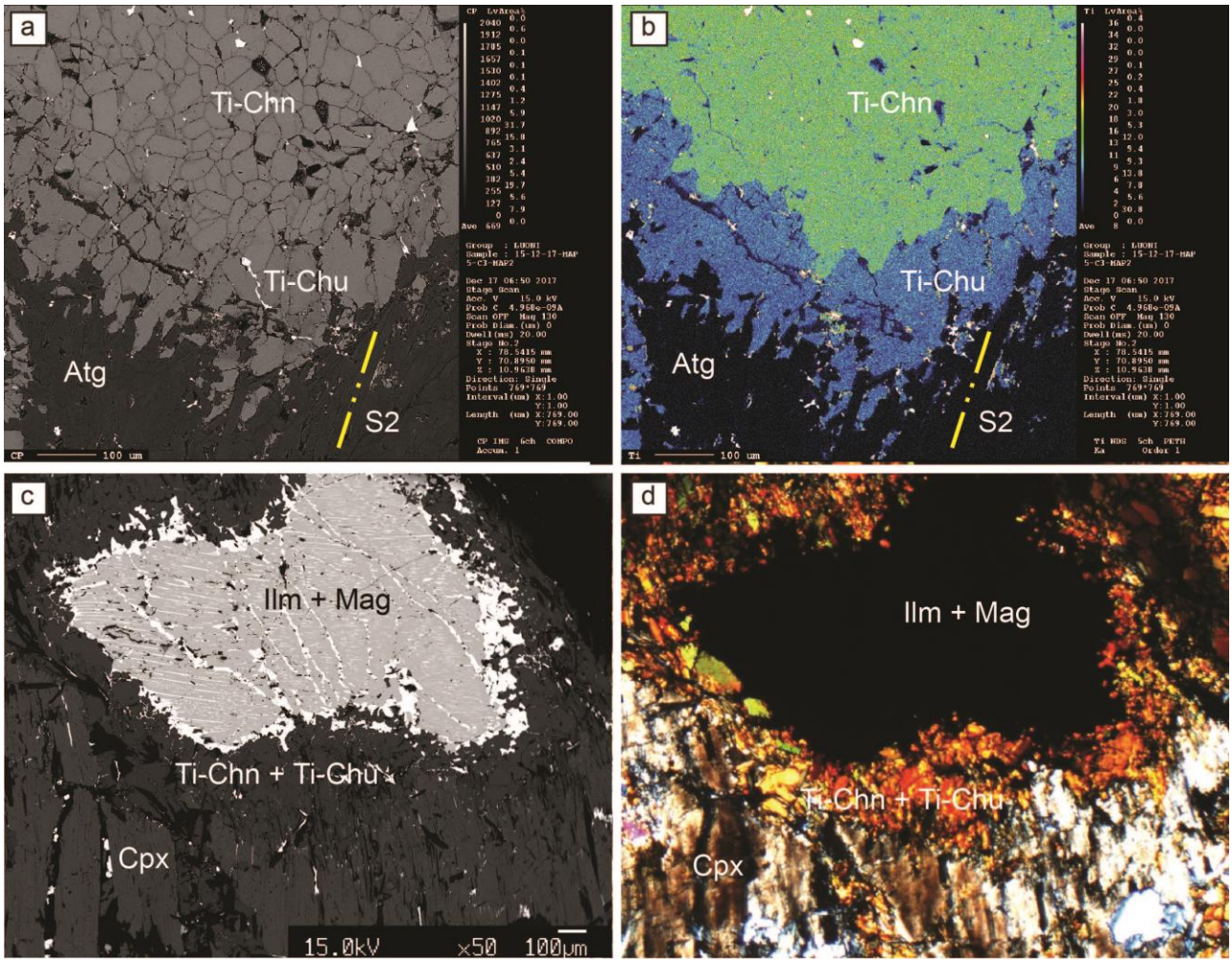

Fig. 3.1.4.5. (a-b-c-d) Grains in Ti-Chu polygonal aggregates at the rim of Ti-Chn aggregates are gradually parallelised into S2 in BSE (a) and Ti maps (b); (c-d) pre-D2-to-early-D2 Cpx, Ti-Chu + Ti-Chn rim, Ilm + Mag aggregate in BSE (c) and crossed polars (d).

the foliation marked by Atg2 + Ol2 + Mag2. Ol2 with Atg2 also fill syn-D2 necks of pre-D2 Ol boudins. Locally, Mag2 and Chl2 rim pre-D2 Cr-Mag porphyroclasts. An olivine-rich lens is foliated and banded with alternating layers respectively richer in Ol and Atg. In the millimetre Ol-rich layers pre-D2 Ol relicts are anhedral, fractured and display slight undulose extinction. They are partially surrounded by polygonal aggregates of submillimetre-sized Ol. Both the porphyroclasts and the polygonal aggregates are contained in a micron-sized matrix of polygonal Atg + Ol + Mag, with Pre-D2 Cr-Mag porphyroclasts rimmed by Mag and Fe-Chl.

Pyroxenite

Anhedral to subhedral centimetre-sized pre-D2 Cpx porphyroclasts are strongly deformed, locally kinked, with exsolution of Ilm + Mag (Fig. 3.1.4.4d) and contain Atg + Chl + Ti-Chn and Ti-Chu along cleavages. Locally rare exsolutions- and strain-free augite cores are preserved in pre-D2 Cpx crystals.

Cpx porphyroclasts are often partially or totally replaced by Cpx2 new grains and Chl2. S2 oriented aggregates of Atg2 + Chl2 + Mag2 + Cpx2 wrap Cpx porphyroclasts where Chl2 and Atg2 SPO is parallel to S2. Locally, between the rim of Cpx porphyroclasts and millimetre globular aggregates of Ilm + Mag (former Spl), aggregates of polygonal pre-D2 to early-D2 Ti-Chn + Ti-Chu occur (Fig. 3.1.4.4e). The edges among Ti-humites grains and Ilm + Mag are sharp. The edges between Ti-

humites and Cpx porphyroclasts are interdigitated and often the Ti-humites occur along Cpx porphyroclasts cleavages.

Ti-Chu + Ti-Chn veins

Millimetre-sized pre-D2 Ti-Chn porphyroclasts are subhedral and twinned, with tapering lamellae, and enclose Atg and Mag (Fig. 3.1.4.4f). Ti-Chn + Ti-Chu submillimetre subhedral grains constitute pre-D2-to-early-D2 assemblage together with Chl, Atg, Ilm, and Mag (Fig. 3.1.4.5a and Fig. 3.1.4.5b). Ol constitutes pre-D2 porphyroclasts locally replaced by pre-D2 to early-D2 almost equigranular, subhedral Ol grains. Locally pre-D2 to early-D2 Ol constitutes ribbon-shaped aggregates parallel to S2. Ol2 also marks S2 with SPO of submillimetre grains. Pre-D2 millimetre-sized and anhedral Spl is replaced by Ilm + Mag exsolutions (similarly to Fig. 3.1.4.5c and Fig. 3.1.4.5d). Pre-D2 to early-D2 Ilm + Mag are often equigranular and with sharp edges in polygonal Ti-Chn + Ti-Chu aggregates.

Rock type	Mineral modes	Mineral assemblages synkinematic with successive deformation stages			
		pre-D2	pre-D2 to early D2	D2	D3 and post D2
Serpentinite	Srp (60-90%), Ol (5-30%)/Cpx (5-10%), Mag (5-15%), Ti-Chu (5%), Cal + Dol (<5%). Locally Chl, Ap (<5%)	Srp + Mag + Cpx/Ol + Ti-Chu + Dol + Ap		Srp + Mag + Cpx/Ol + Ti-Chu ± Chl ± Cal ± Dol	Srp + Mag + Chl + Cal
Ti-Chn + Ti-Chu veins	Ti-Chn + Ti-Chu (70-80%), Ol (10-20%), Atg (5-10%), Mag ± Ilm (5-10%), Chl (<5%)	Ti-Chn + Ex-Spl + Ol ± Chl + Srp	Ti-Chn + Ti-Chu + Ol + Ilm + Mag + Chl + Srp	Ti-Chu + Srp + Ol + Chl + Mag	
Pyroxenite	Cpx (70-80%), Atg ± Chl (10-20%), Ilm ± Mag (5%), Ti-Chn + Ti-Chn (5%), Amph (<2%)	Cpx (augitic core) + Spl + Srp + Chl (+ Ti-Chn)	Cpx + Srp + Chl + Ti-Chn + Ti-Chu + Ilm + Mag	Cpx + Srp + Ti-Chu + Chl + Mag	Srp + Chl + Mag + Amph
Olivine-rich layers and lenses	Ol (60-90%), Atg (10-20%), Mag ± Cr-Mag (10%), Chl (<5%), Ti-Chn + Ti-Chn (<5%), Dol (<2%) Cpx (<1%)	Ol + Srp + Mag + Cr-Mag + Cpx ± Ti-Chn + Chl	Ol + Srp + Mag + Ti-Chu + Dol	Ol + Srp + Mag + Ti-Chu	Srp + Cal

Table 3.1.4.2. Mineral modes and assemblages marking superposed fabrics for the different rock types.

3.1.4.5 Mineral compositional evolution

WDS mineral analyses were acquired from different microstructural sites by using the electron microprobe (JEOL 8200 Super Probe) operating at the "A. Desio" Earth Science Department of Milano University. A 15 keV accelerating voltage and a beam current of 15nA were used. Natural silicates were used as standards and matrix corrections were calculated using the ZAF procedure. Mineral formulae were recalculated on the basis of the following number of oxygen atoms: 4 for olivine, 6 for clinopyroxene, 116 for serpentine, 28 for chlorite, 4 for magnetite, 3 for ilmenite, and 24 for amphibole. Ti-chondrodite and Ti-clinohumite formulae were recalculated on the basis of 7 and 13 cations respectively. Fe3+ in ilmenite was recalculated according to Droop (1987). Diagrams showing the significant compositional variations of the main minerals are shown in Fig. 3.1.4.6 and a synthesis of the mineral compositions is reported in Table 3.1.4.3.

Olivine in serpentinites and olivine-rich layers is fosteritic and its composition is controlled by bulk composition (Fig. 3.1.4.6a): olivine from the olivine-veins in serpentinite is the richest in Mg and olivine within Ti-clinohumite and Ti-chondrodite porphyroclasts is the richest in Fe. Olivine from olivine-rich layers shows the highest variation of Mg and Fe content, with the exception of olivine marking the relic S1, which has intermediate values of Fe. Mn is lower than 0.01 a.p.f.u..

Ti-chondrodite and Ti-clinohumite: Ti-chondrodite is higher in both M/Si and TiO2 than Ti-clinohumite. Ti-clinohumite2 shows higher M/Si and TiO2 than Ti-clinohumite in pre-D2-to-early-D2 polygonal grains. Similarly, pre-D2-to-early-D2 Ti-Chn has higher M/Si and TiO2 than pre-D2 Ti-Chn porphyroclasts (Fig. 3.1.4.6b).

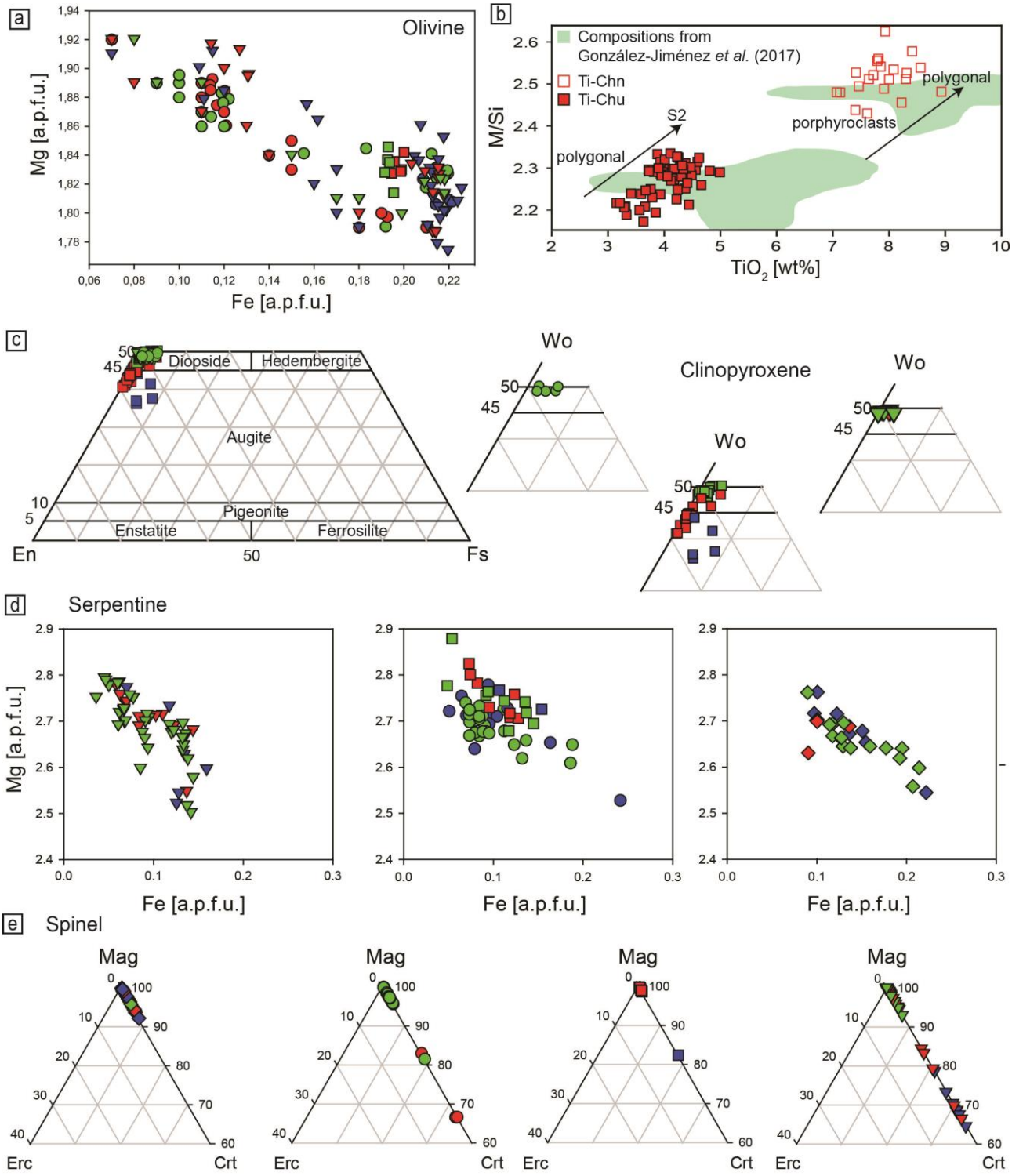

Fig. 3.1.4.6: Mineral chemistry diagrams. (a) olivine; (b) humites; (c) clinopyroxene; (d) serpentine; (e) spinel. Symbols refer to rocks and colours to structural stages: circle = serpentinite; square = Ti-chondrodite + Ti-clinohumite vein; diamonds = pyroxenites; triangles = olivine-rich layers; blue = pre-D2; red = pre-D2 to early-D2; green = syn-D2.

	Serpentinites				Pyroxenites			Olivine-rich layers			Olivine-rich lens
	preD2	preD2 to early D2	D2	D3	preD2	preD2 to early D2	D2	D3	preD2	preD2 to early D2	D2	
Olivine												
Fe tot		0.07-0.22	0.09-0.23	-	-	-	-	-	0.07-0.23	0.07-0.22	0.08-0.22	0.14-0.18
Mg		1.79-1.92	1.81-1.90	-	-	-	-	-	1.77-1.92	1.78-1.92	1.780-1.92	1.81-1.87
Mn		0.01	0.00-0.01	-	-	-	-	-	0.01	0.01	0.01	-
XMg		0.89-0.96	0.89-0.95	-	-	-	-	-	0.89-0.96	0.89-0.96	0.89-0.96	0.90-0.93
Serpentine												
Mg	2.53-2.78	2.76-2.83	2.54-3.16	2.65-2.75	2.54-2.76	2.63-2.75	2.56-2.77	2.66-2.70	2.52-2.78	2.55-2.78	2.50-2.79	2.64-3.39
Fe tot	0.05-0.24	0.07-0.12	0.04-0.39	0.09-0.14	0.09-0.22	0.09-0.14	0.09-0.21	0.10-0.16	0.06-0.16	0.06-0.14	0.05-0.14	0.04-0.20
Al	0.00-0.13	0.0-0.07	0.0-0.15	0.03-0.13	0.05-0.15	0.03-0.13	0.0-0.15	0.10-0.15	0.01-0.11	0.02-0.13	0.0-0.14	0.0-0.13
Clinopyroxene												
Fe2	-	-	0.0-0.05	-	0.02-0.13	0.0-0.7	0.0-0.06	-	0.03	0.03	-	0.03
Fe3	-	-	0.0-0.09	-	0.11-0.14	0.0-0.14	0.0-0.08	-	-	-	-	-
Mg	-	-	0.88-1.00	-	0.91-1.01	0.93-1.06	0.92-1.05	-	0.97-0.98	0.96-0.98	-	0.95
Ca	-	-	0.97-1.00	-	0.73-0.87	083-0.96	0.95-1.02	-	0.97-0.98	0.97-0.98	-	1
Na	-	-	0.00-0.01	-	0.03-0.05	0.01-0.03	0.0-0.01	-	-	-	-	-
Ti	-	-	-	-	0.02-0.03	0.0-0.05	-	-	-	-	-	-
Magnetite												
Fe2	0.70-0.92	0.90-0.99	0.84-0.99	-	0.92-1.01	0.93-0.96	0.91-0.99	-	0.74-0.94	0.73-0.93	0.86-0.94	0.75-0.90
Fe3	1.28-1.98	1.88-1.98	1.-60-1.99	-	1.74-1.98	1.84-1.96	1.91-1.99	-	1.34-1.99	1.29-1.99	1.85-1.99	1.25-1.98
Cr	0.0-0.63	0.0-0.02	0.0-0.06	-	0.0-0.15	0.02-0.11	0.0-0.11	-	0.0-0.62	0.0-0.65	0.0-0.14	0.01-0.68
Chlorite												
Fe tot	0.56-0.68	0.52-0.67	0.55-0.88	-	0.58-0.91	0.57-0.63	0.53-0.94	-	-	-	-	0.47-0.71
Mg	9.74-10.04	9.84-10.04	9.69-10.08	-	9.51-9.91	9.86-9.91	9.57-10.01	-	-	-	-	9.70-10.02
Al	2.43-2.85	2.52-2.99	2.70-3.13	-	2.59-2.99	2.75-2.96	2.53-3.02	-	-	-	-	2.41-2.97
Ilmenite												
Fe2	-	0.59-0.85	0.39-0.67	-	-	0.35-0.61	0.6	-	-	-	-	-
Fe3	-	0.03-0.07	0.03-0.08	-	-	0.01-0.04	0.02-0.03	-	-	-	-	-
Ti	-	0.96-0.98	0.96-0.98	-	-	0.98-0.99	0.98-0.98	-	-	-	-	-

Table 3.1.4.3. Compositional range of olivine, serpentine, clinopyroxene, magnetite, chlorite, amphibole, and ilmenite in atoms per formula unit, in serpentinites, pyroxenite layers, and olivine-rich layers, during different deformation stages. X_{Mg} = Mg/(Mg+ Fe^{2+}); X_{Fe} = Fe^{2+}/(Mg+ Fe^{2+}).

Assemblage	Ol-rich			Cpx-rich			
Mineral	Ol	Srp	Mag	Srp	Chl	Cpx	Mag
Texture	2	2	2	2	2	2	2
SiO2	40.00	42.09	0.04	43.74	34.18	52.89	0.03
TiO2	0.05	0.03	0.07	0.06	0.03	0.00	0.29
Al2O3	0.00	1.26	0.00	1.58	12.63	0.45	0.05
Cr2O3	0.01	0.10	0.59	0.02	0.31	0.03	0.95
Fe2O3	-	-	70.31	-	-	2.28	67.29
FeO	10.25	3.04	29.50	4.79	4.27	0.00	29.92
MnO	0.36	0.03	0.23	0.01	0.05	0.14	0.10
MgO	49.80	36.42	1.26	37.68	34.74	17.66	0.48
CaO	0.03	0.00	0.02	0.03	0.01	24.72	0.01
Na2O	0.02	0.00	0.13	0.02	0.02	0.12	0.05
K2O	0.00	0.00	0.00	0.00	0.00	0.01	0.00
NiO	0.15	0.05	0.00	0.11	0.09	0.01	0.18
Sum	100.67	83.02	102.15	88.04	86.33	100.14	99.35
Ox	4	7	3	7	28	6	3
Si	0.98	2.05	0.00	2.03	6.53	1.95	0.00
Ti	0.00	0.00	0.00	0.00	0.00	0.00	0.01
Al	0.00	0.07	0.00	0.09	2.84	0.02	0.00
Cr	0.00	0.00	0.02	0.00	0.05	0.00	0.03
Fe3	-	-	1.98	-	-	0.06	1.95
Fe2	0.21	0.12	0.92	0.19	0.68	0.00	0.97
Mn	0.01	0.00	0.01	0.00	0.01	0.00	0.00
Mg	1.82	2.65	0.07	2.61	9.89	0.97	0.03
Ca	0.00	0.00	0.00	0.00	0.00	0.98	0.00
Na	0.00	0.00	0.00	0.00	0.01	0.01	0.01
K	0.00	0.00	0.00	0.00	0.00	0.00	0.00
Ni	0.00	0.00	0.00	0.00	0.01	0.00	0.00
cationSUM	3.02	4.91	3.00	4.92	20.03	4.00	3.00

Table 3.1.4.4. Selected EMPA mineral chemical analyses selected for calculating the bulk rock composition used in pseudosections.

Clinopyroxene: in olivine-rich layers and serpentinites, pre-D2 Cpx and Cpx2 have a diopsiditic composition (Morimoto, 1988; Fig. 3.1.4.6c). Ca is generally comprised between 0.88 and 1.02 a.p.f.u., whereas Ti is lower than the detection limit (Table 3.1.4.3). In pyroxenites, Pre-D2 Cpx cores and pre-D2-to-early-D2 Cpx are augite, with pre-D2-to-early-D2 Cpx richer in Ca. Cpx2 is a pure diopside. The Ca increase from pre-D2 to D2 is accompanied by a decrease of Al and Na. Ti is < 0.05 a.p.f.u. in pre-D2 and pre-D2-to-early-D2 Cpx and it is lower than detection limit in Cpx2 (Table 3.1.4.3; Fig. 3.1.4.6c).

Serpentine composition (Fig. 3.1.4.6d) is mostly controlled by the bulk composition. Atg from Ti-Chn + Ti-Chu veins is the richest in Mg, whereas Atg from pyroxenites is the richest in Fe.

Oxides: Spinel composition (Ferracutti et al., 2015) is controlled by microstructure and the bulk rock chemistry (Fig. 3.1.4.6e). In olivine-rich layers and lenses, cores of Mag porphyroclasts are richer in Cr than the rims, and Mag2 (i.e. the rims) is pure magnetite. In serpentinites and Ti-Chn + Ti-Chu veins, both pre-D2 Mag and Mag2 are pure magnetite. Oxide exsolutions in clinopyroxene porphyroclasts consist of magnetite (Fig. 3.1.4.6e).

Chlorite is generally penninite (Zussman et al., 1992) in all rock types and no appreciable differences have been recognized among different generations (Table 3.1.4.3) and lithotypes. Syn-D3 amphibole in serpentinites is tremolite (Locock, 2014).

3.1.4.6 Physical conditions of Metamorphism

The microstructural analysis of Créton serpentinites allowed distinguishing two subsequent parageneses (Table 3.1.4.2) that occur in domains wrapped by S2:

a) pre-D2 Ti-Chn + Atg + Spl ± Chl + Ol/Cpx,

b) pre-D2-to-early-D2 Ti-Chn + Ti-Chu + Atg + Ilm + Mag + Ol/Cpx.

On the contrary S2 is marked by the Ti-Chn-free assemblage:

Ti-Chu + Atg + Mag + Chl + Ol/Cpx.

Metamorphic reaction curves from the literature, for Ti-poor and Ti-rich systems (Shen et al., 2015) and pseudosections allow inferring the PT evolution of Créton rocks (Fig. 3.1.4.7). In the Ti-rich system experiments (Fig. 3.1.4.7a), Ti-Chn-out is at higher Pmin (2.6-3.0 GPa at 550-670 °C) than in the Ti-poor system (Fig. 3.1.4.7b), where Ti-Chn + Ti-Chu are stable together between 1.9 and 2.8 GPa (at 550-670 °C). In both figures, temperatures in our samples are constrained using the Al content in pre-D2 Ol porphyroclasts and pre-D2-to-early-D2 polygonal Ol (De Hoog et al., 2010), represented as green and blue lines considering a 2 σ error, respectively. Tmax is limited by the Atg out curve at 670 °C in both systems.

D2 metamorphic conditions have been modelled in the CFMASHO system with pseudosections using THERMOCALC software (Holland and Powell, 1998; Powell et al., 1998; dataset tc-ds62) for two different samples: in the first sample Cpx does not occur and S2 is marked by Ol + Atg + Mag, in the second sample Ol is not present and S2 is underlined by Cpx + Atg + Chl + Mag. The amphibole and pyroxene activity-composition models are those of Diener et al. (2007) and of Zeh et al. (2005), respectively. The garnet models are from White et al. (2007) (but with the garnet asymmetry involving αgr = 3 instead of 9), and the Fe-Ti oxide and epidote models are from Holland and Powell (1998). Chlorite activity model is from Holland et al. (1998). The other phases are pure end-members: brucite, magnetite and H2O. Rock compositions (Fig. 3.1.4.7c and Fig. 3.1.4.7d) are estimated integrating modal proportions by polarised light microscope analysis with the phase compositions acquired by WDS analysis. Because serpentine is > 40%, the modelling was performed with H2O in excess (Guiraud et al., 2001; Rebay et al., 2010). Although Créton serpentinites are rich in Ti-humite minerals, the modelled samples are the poorest in Ti-phases in order to minimize Ti content in the bulk composition, as reliable a-x models for Ti-rich minerals are not available. In both the pseudosections, magnetite and H2O are in excess. Bulk compositions have been calculated by the mode of the minerals, whose compositions are reported in Table 3.1.4.4.

In Fig. 3.1.4.7c a pseudosection calculated for a sample with Ol - Atg - Mag bearing S2 is presented. All fields are delimited by vertical curves. Bivariant fields are narrow, spanning maximum over a range of 10°C, whereas trivariant and quadrivariant fields are wider, and all fields are stable within the whole range of considered pressures from 1 to 4 GPa. Chlorite is stable at T < 580 °C and ortopyroxene is stable at T > 592 °C. Even if this is a Cpx-free sample, olivine and diopside are predicted to be stable in every field. It is though important to note that in the Ol - Di - Atg field, constrained between 560 and 640 °C by the Chl-out and Opx-in curves, the predicted Cpx mode is negligible <0.1%, and therefore this field represents the assemblage we actually observe in the rock.

The pseudosection of Fig. 3.1.4.7d is calculated for the composition of a rock where clinopyroxene is found in D2 together with Atg - Chl - Mag. Fields are again mostly separated by vertical boundaries as already seen in the olivine-bearing rock, but a horizontal divariant field with Di - Atg - Chl - Mag, separates at lower temperatures (<650°C) a field where actinolite is stable at P < 1.6 -1.8 GPa from a field where Ta is stable with Di - Atg - Chl (and Mag) for P > 1.7 GPa. This latter field represents the

assemblage observed in our sample, once it is realized that the predicted Ta mode in this field is < 2%. D3 assemblage stability conditions are constrained by the predicted coexistence of actinolite and antigorite at P < 1.7 GPa.

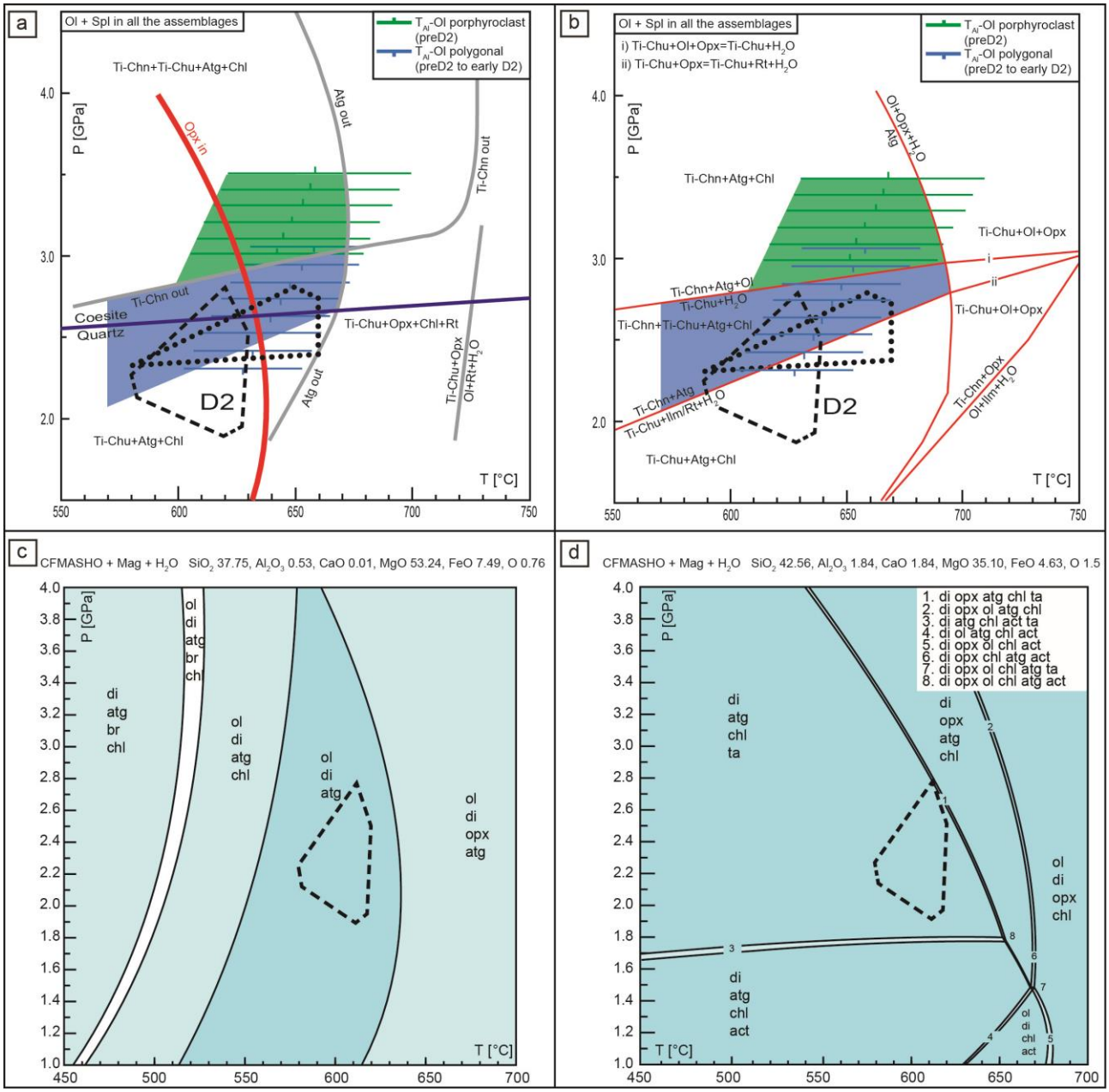

Fig. 3.1.4.7. (a-b) Pre-D2 (green area) and pre-D2-to-early-D2 PT conditions (blue area): (a) experimentally determined fields in Ti-rich systems (grey curves, redrawn from Shen et al., 2015); (b) experimental data combined with Schreinemaker analysis, representing phase relations in systems with less Ti and involving Ti-humites, Atg, Opx, Ol, and Chl (red curves, redrawn from Shen et al., 2015). Green and blue lines represent temperatures calculated from pre-D2 olivine (De Hoog et al., 2010) and with error bars. The red thick curve represents Opx-in from Fig. 3.1.4.7c; (c-d) pseudosections calculated in the CFMASHO system for syn-D2 Ol-bearing (c) and Cpx-bearing (d) mineral assemblages; compositions (mol%) are reported at the top of each pseudosections. Dotted and dashed areas in all panels represent syn-D2 PT conditions for Valtournanche rodingites (Zanoni et al., 2016) and serpentinites (Rebay et al., 2012) respectively.

In this latter case, Cpx and Ol have never been observed in the same assemblage, and it is therefore impossible to further constrain PT conditions by using isopleths of these two phases as done in Rebay

et al., 2012, in samples from nearby outcrops. Rebay et al. (2012) estimated for D2 2.5 ± .3 GPa and 600 ± 20°C, and for D3 1 ± .4 GPa and 550 ± 50°C, as indicated in Fig. 3.1.4.7a and Fig. 3.1.4.7b with dashed and dotted polygons.
On the other hand, the Opx-in curve in Fig. 3.1.4.7c (Ol-rich assemblage), calculated for syn-D2 conditions in serpentinite, can be superposed to the PT fields of the pre-D2 and pre-D2 to early-D2 stages (Fig. 3.1.4.7a), to further constrain their conditions.
In fact, in serpentinite, pre-D2 and D2 assemblages are characterised by the same chemical system, and Opx never occurs neither in pre-D2 nor in D2 assemblage. The Opx-in curve, calculated for D2 assemblage in serpentinite, represents therefore a temperature constrain also for pre-D2 stage. Likely, Ti-Chn + Ti-Chu veins, that formed before D2 stage, and occur in the same serpentinite outcrops of the samples used for the determination of syn-D2 conditions, don't contain Opx. Then, Opx-in curve from Ol-rich assemblage (Fig. 3.1.4.7c) is preferred to Opx-in curve from Cpx-rich assemblage (Fig. 3.1.4.7d) as no Cpx occurs in the fields of Fig. 3.1.4.7a and Fig. 3.1.4.7b.
The superposition of the Opx-in curve from the Ol-rich assemblage pseudosection (red curve in Fig. 3.1.4.7a) let decrease Tmax from 670 to 630 °C and Pmax from 3.5 to 3.3 GPa. Therefore, new pre-D2 PT conditions can be proposed as P = 2.8-3.3 GPa and 600-630 °C. In the same way, pre-D2 to early-D2 conditions can be delimited by Opx-in curve: Tmax is reduced to 630 °C and Pmax to 2.9 GPa.

3.1.4.7 Geodynamic modelling and tectonic history

Setup

We used the 2D finite element method to simulate an ocean-continent subduction (Regorda et al., 2017) in order to compare the tectono-metamorphic history of serpentinites of the ZSZ with the evolution of the oceanic lithosphere within a subduction zone, since in the literature a continental upper plate is proposed for the Alpine subduction system (Dal Piaz et al., 1972; Polino et al., 1990; Roda et al., 2012 and reference therein). The physics of the crust-mantle system is described by coupled equations for continuity, conservation of momentum, and conservation of energy (Marotta et al., 2006). The equations are solved by means of the 2D finite element code Submar (Marotta et al., 2006), which includes erosion and sedimentation processes (Roda et al., 2012), shear heating (Regorda et al., 2017), and oceanic crust dehydration and mantle serpentinisation mechanisms (Meda et al., 2010; Roda et al., 2010; Roda et al., 2012). According to Regorda et al. (2017), a viscous rheology is assumed for the sublithospheric mantle, and a brittle/plastic rheology is assumed for the lithosphere. The material and rheological parameters used in the simulation are listed in Table 3.1.4.5.
An initial continental lithospheric thickness of 80 km, including 30 km of continental crust, is assumed (Fig. 3.1.4.8) to represent the originally thinned passive margin that characterized the former margin of Adria (Dal Piaz, 2001; Roda et al., 2019). An oceanic lithospheric thickness of 80 km is chosen to represent an age of ca. 40 Myr for the Tethys Ocean (Handy et al., 2010; Roda et al., 2012), based on the cooling model of a semi-infinite half-space (Turcotte and Schubert, 2002), and characterized by a slow spreading rate (2.5 cm/yr full spreading). The upper oceanic crust is considered to be composed by 5 km thick layer of porous and fractured basalts and serpentinites (Carlson and Miller, 1997; Juteau and Maury, 1999; Christensen, 2004; Cannat et al., 2013). The lower oceanic crust is represented by a 5 km thick serpentinite-free layer with the rheology of a dry diabase (Carlson and Miller, 1997; Canales et al., 2000; Christensen, 2004; Cannat et al., 2013; Rüpke and Hasenclever, 2017).
To simulate plate convergence, a horizontal velocity of 3 cm/yr is imposed along the bottom of the oceanic crust (Roda et al., 2010; Roda et al., 2012) and the initial slab dip is 45° (Roda et al., 2010).

The model runs for 65 Myr of oceanic subduction, i.e. from 100 to 35 Ma (Dal Piaz et al., 2003; Handy et al., 2010; Roda et al., 2012). Additional details about the model setup are summarized in the caption of Fig. 3.1.4.8.

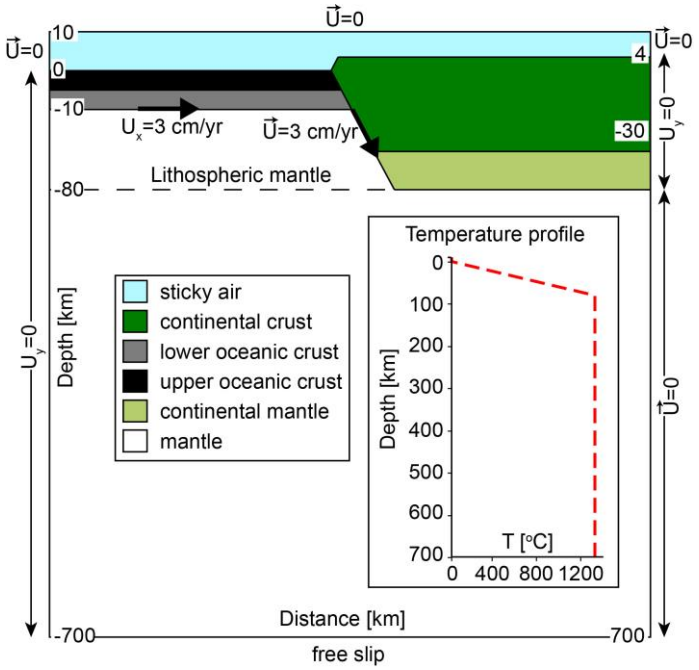

Fig. 3.1.4.8. Setup of the numerical model. The model domain is 1400 km wide and 710 km deep. The initial lithosphere thickness is 80 km and is defined by the 1227°C isotherm. The velocity boundary conditions correspond to a free slip condition along the bottom of the domain and a fixed velocity along the top boundary. The vertical component of the velocity vector (Uy) is fixed at 0 cm/yr on the right boundary along the entire lithospheric thickness (80 km depth) and along the left side from 0 to 700 km depth. No slip conditions are imposed on the right and left sides of the domain from the topographic surface to the upper boundary. Plate convergence is simulated with a horizontal velocity of 3 cm/yr, and it is fixed along the bottom of the oceanic crust and at the nodes of the numerical grid and distributed along a 45°-dipping plane from the trench to a depth of 100 km. The thermal boundary conditions correspond to 0°C at the top of the domain and 1227°C at the bottom. The initial thermal configuration corresponds to a uniform purely conductive upper thermal boundary layer throughout the lithosphere (from 0 to 80 km depth and from 0°C to 1227°C) and a uniform sublithospheric temperature of 1227°C (inset). The temperatures are fixed along the left vertical sidewall, and a zero thermal flux is imposed on the right side. The materials included in the model account for the upper and lower oceanic crust, continental crust, mantle, and sticky air (see Table 3.1.4.5 for material parameters and rheology).

	Continental crust	Upper oceanic crust	Lower oceanic crust	Dry mantle	Serpentinized mantle	Sediments	Sticky air
Rheology	Dry granite		Diabase	Dry dunite	Serpentinite		
μ_0 (Pa s)	3.47E+21	1.61E+19	1.61E+22	5.01E+20	1.00E+19	1.00E+19	1.00E+19
ρ_0 (kg m^{-3})	2640	2961	2961	3200	3000	2640	1000
K (W m^{-1} K^{-1})	3.03	2.1	2.1	4.15	4.15	3.03	0.026
H_r (μW m^{-3})	2.5	0.4	0.4	0.002	0.002	2	-
E (kJ mol^{-1})	38.43	103	103	130			
References	a,d,f,l	b,f,j,k,l	a,b,c,f,l	c,d,e,f,j,l	d,f,g,h,i	g,j	g,j

Table 3.1.4.5. Material and rheological parameters used in the simulation. References: a) Ranalli and Murphy (1987); b) Afonso and Ranalli (2004); c) Kirby (1983); d) Haenel et al. (1988); e) Chopra and Paterson (1981); f) Dubois and Diament (1997); Best and Christiansen (2001); g) Roda et al. (2011); h) Schmidt and Poli (1998); i) Gerya and Stöckhert (2005); j) Roda et al. (2012); k) Gerya and Yuen (2003); l) Meda et al. (2010).

Model results

The subduction of the oceanic lithosphere induces the tectonic erosion of part of the continental crust from the overriding plate due to the strong coupling along the plate boundary. The burial flow carries the oceanic and continental crust, trench sediments and mantle markers toward deep levels of the subduction zone. The hydrated upper oceanic crust progressively releases fluids within the mantle wedge during the burial, and serpentinisation of the overriding mantle occurs. The size of the serpentinized mantle wedge increases with time due to the continuous dehydration of the upper oceanic crust and the progressive cooling of the subduction system. The strong contrast between serpentinites and dry mantle results in an intense counterclockwise convection flow developed in the upper part of the mantle wedge. As a consequence, part of the subducted material is exhumed to shallower structural levels within the mantle wedge and the rest remains in the deeper portion of the mantle wedge or is inhumed in the sublithospheric mantle. The upper oceanic crust is commonly involved in the exhumation process, sometimes coupled with recycled trench sediments. During the exhumation within the mantle wedge, the oceanic crust can also be coupled with dry continental mantle and continental crust coming from the upper plate.

The result of such a tectonic mingling is a subduction-related mélange comprising a mixture of exhumed upper oceanic and continental crustal slices, buried and exhumed trench sediments, and continental lithospheric mantle enclosed within the serpentinized matrix derived from the hydrated mantle wedge. The subducted materials record different PT peak conditions, different P-T-t evolutions and different exhumation trajectories, and the size of a single tectono-metamorphic unit ranges from 2-3 km2 to several tens of km2, which is consistent with the results already discussed by Roda et al. (2012).

Natural data vs model predictions

The inferred PTdt path of Créton serpentinites is compared with the tectonic setting and thermal state predicted by the numerical model of an ocean-continent subduction zone. Since ZSZ serpentinites have been interpreted as affected by ocean floor metasomatism, therefore representing the upper part of the oceanic lithosphere, we focus on the geological setting recorded by the markers that belong to the upper oceanic crust at different timing of the tectono-metamorphic history. The first structural and metamorphic re-equilibration predates D2, and the serpentinites recorded the peak conditions at pressure of 2.8-3.3 GPa and temperature of 600-630°C (Figs 7 and 9). There is no radiometric age associated with this stage, but pre-D2 structures are clearly older than D2 stage, which has been dated 60-70 Ma by Rebay et al. (2018). The oldest age proposed for the prograde path of ZSZ is 80 Ma (Skora et al., 2009). Therefore, we extrapolate two main events of the numerical simulation to be compared with the pre-D2 stage at steps of 80 and 72 Ma (Fig. 3.1.4.9). For the oldest event (80 Ma), the pre-D2 PT conditions occur in the portion of the upper oceanic crust within the serpentinized mantle wedge still close to the slab (Fig. 3.1.4.9a). The lithological mixing is poor and only few markers of trench sediments record the same PT conditions (Fig. 3.1.4.9a). Pre-D2 conditions can be also potentially reached by a portion of the lithospheric oceanic mantle below the Benioff plane (Fig. 3.1.4.9a). However, this portion has been excluded for the comparison because the ocean floor metasomatism, widely testified in the ZSZ oceanic lithosphere of upper Valtournanche, does not occur below the Benioff plane. In the simulated system, pre-D2 conditions occur at a distance of 100-130 km from the trench and at ca. 80-110 km depth (Fig. 3.1.4.9a and Fig. 3.1.4.9b). At 72 Ma, the size of the serpentinized mantle wedge increases, and the pre-D2 PT conditions extend to an innermost portion of the mantle wedge (Fig. 3.1.4.9c). The lithological mixing is still poor and characterized by upper

oceanic crust and few sediment markers. Again, the portion of the lithospheric oceanic mantle below the Benioff plane recording pre-D2 conditions can be excluded from the comparison, for the reasons already pointed out. The fitting of pre-D2 PT conditions in the subduction system is accomplished at a distance of 110-145 km from the trench and at ca. 80-110 km depth (Fig. 3.1.4.9c and Fig. 3.1.4.9d).
The D2 stage represents the first exhumation stage recorded by Créton serpentinites and occurs at P and T conditions of 1.8-2.8 GPa and 580-620°C. The D2 radiometric age varies from 70 to 60 Ma and, therefore, we compare D2 PT conditions with three different time steps of the simulation: 70, 65, and 60 Ma (Fig. 3.1.4.10). In the oldest step (70 Ma), D2 conditions are recorded by markers of upper oceanic crust within the mantle wedge, coupled with rare markers of trench sediments and some markers of continental crust (Fig. 3.1.4.10a). In the successive steps, the amount of trench sediments recording D2 conditions sensibly increases (Fig. 3.1.4.10c and Fig. 3.1.4.10e). With the size increase of the serpentinized mantle wedge with time, the area characterised by PT conditions fitting with those of D2 moves away from the slab (Fig. 3.1.4.10a, Fig. 3.1.4.10c, and Fig. 3.1.4.10e), and the maximum distance from the trench varies from 125 km at 70 Ma to 155 km at 60 Ma (Fig. 3.1.4.10b, Fig. 3.1.4.10d, and Fig. 3.1.4.10f). Starting from the oldest age, depth varies between 85 and 55 km.
The D3 stage occurred under epidote-amphibolite facies conditions (Rebay et al., 2012), under an intermediate PT ratio, compatible with a Barrovian metamorphism. Therefore, D3 PT conditions likely occurred at the end of the oceanic subduction, at the beginning of the continental collision (Regorda et al., 2017).

3.1.4.8 Discussions

Results of this integrated structural, petrological, and modelling approach on Créton serpentinites show that rocks that are generally considered cryptic, preserve a wealth of information to be disclosed, that in this case-study results into the reconstruction of a complex polydeformed and polymetamorphosed lithostratigraphy of a portion of oceanic crust. Serpentinites, with magnetite layers and Ti-chondrodite + Ti-clinohumite veins, embed pyroxenites, diopsidites, and Ol-rich layers. Serpentinites registered the effects of a D1 deformation stage, whose relics are rare rootless fold hinges, a D2 stage that produced isoclinal folds and the dominant fabric, which is the S2 mylonitic foliation, and D3 crenulating S2 and associated with discrete shear zones.
By reconstructing the successive mineral assemblages, and the definition of the PT conditions registered by serpentinites, the correlation of the fabrics of Créton outcrops with those described by Rebay et al. (2012) and Zanoni et al. (2012, 2016) was possible. The pre-D2 (Ti-Chn + Atg + Spl ± Chl + Ol/Cpx) and pre-D2 to early-D2 (Ti-Chn + Ti-Chu + Atg + Ilm + Mag + Ol/Cpx) assemblages in Ti-Chondrodite + Ti-Clinohumite veins indicate pressure and temperature ranges of 2.8-3.3 GPa and 600-630 °C, and 2.1-3.0 GPa and 570-670 °C, respectively (Fig. 3.1.4.7a and Fig. 3.1.4.7b).
The integration of the petrological modelling of syn-D2 PT conditions for Cpx + Atg + Mag + Chl- and Ol + Atg + Mag-bearing S2 in serpentinites suggest in pressures greater than 1.8 GPa and temperatures between 540 and 640 °C. As Ol and Cpx never occur together along S2 foliation, these results represent the best ones obtainable for these assemblages and, at the same time, they confirm those proposed for the S2 assemblage developed in adjacent serpentinites and rodingites (Rebay et al., 2012; Zanoni et al., 2016) at 2.2-2.8 GPa and 580-620 °C, that has been dated at 60-70 Ma (Rebay et al., 2018). Furthermore, although referred to different compositional systems, the calculated curve of Opx-in for syn-D2 assemblages in serpentinites have been used to better constrain pre-D2 and pre-D2-to-early-D2 metamorphic conditions of Ti-Chn + Ti-Chu veins, since these veins formed before the D2

stage. The new proposed conditions are characterised by pressure and temperature ranges of 2.8-3.3 GPa and 600-630 °C for pre-D2 stage, and 2.1-2.9 GPa and 570-630 °C for pre-D2 to early-D2 stage.
The comparison between PT conditions for pre-D2 and D2 stages and the prediction of a numerical model of an ocean-continent subduction allowed inferring a vertical "paleogeography" for the serpentinites during their evolution between 80 and 60 Ma in the subduction system. The model suggests that, between 80 and 72 Ma, markers of upper oceanic crust that represent the Créton serpentinites attained pre-D2 PT conditions at a distance from the trench ranging from 100 km to 145 km, at depths of 80-110 km. D2 PT conditions were attained by markers located at a distance from the trench from 125 km at 70 Ma to 155 km at 60 Ma, for depths between 85 and 55 km.
At pre-D2 PT conditions, the lithological mixing between oceanic markers and trench sediments is poor, and the continental markers are rare or absent. On the other hand, at D2 PT conditions, the lithological mixing between oceanic markers and trench sediments sensibly increases and some continental markers attained the same PT conditions. Therefore, it can be proposed that the coupling between rodingite-bearing serpentinites of ZSZ, metasediments and continental slices (e.g. Weber and Bucher, 2015) is more likely attained during D2, still under eclogite facies conditions (Weber et al., 2015) but during the exhumation of Créton serpentinites that already begins during oceanic subduction, long before the continental collision. This evolution is also consistent with the strong parallelization of Valtournanche lithostratigraphic surfaces with S2 foliation.

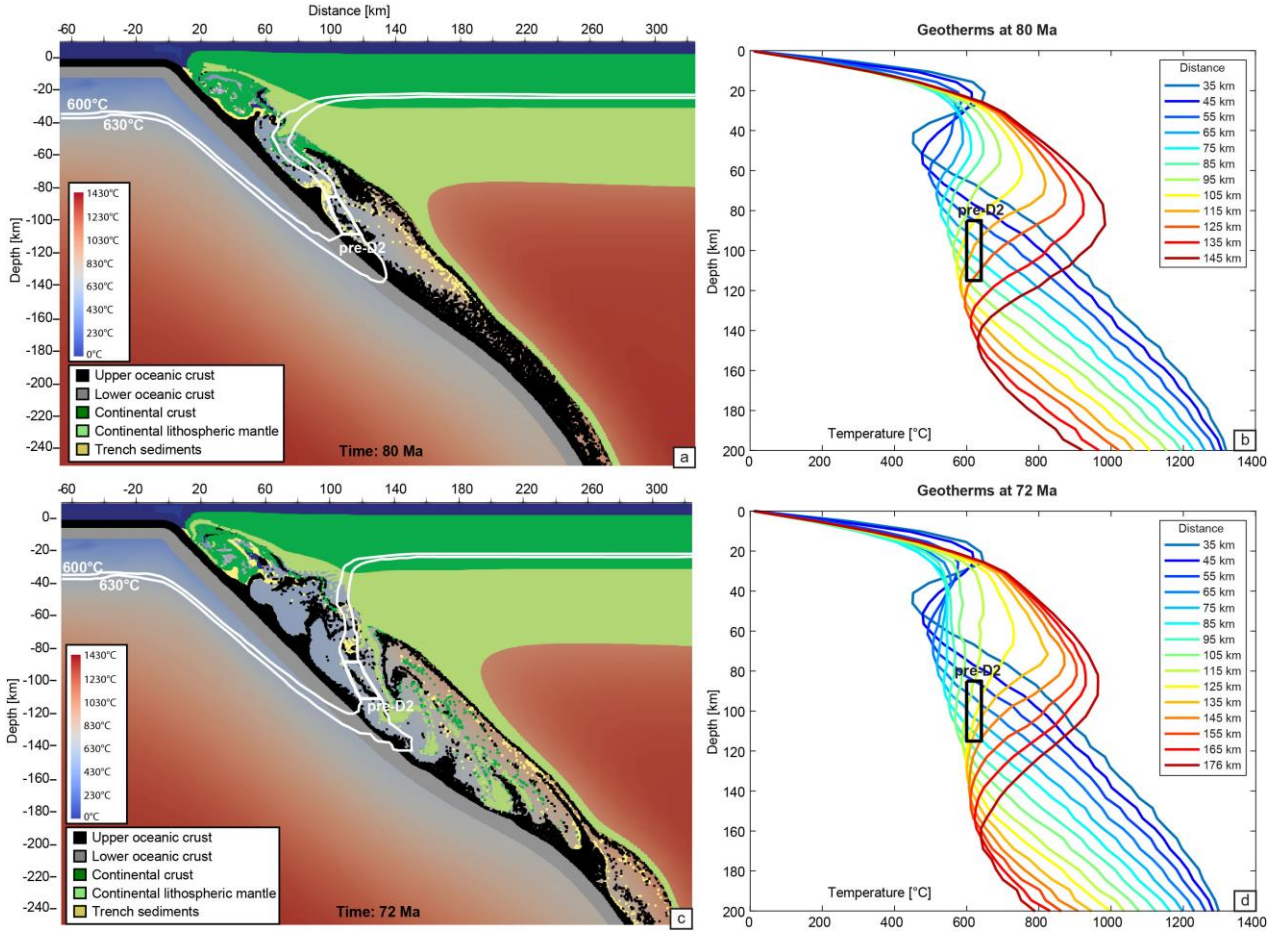

Fig. 3.1.4.9. Results of the simulation represented by geodynamic setting (a-c) and related geotherms (b-d) after 20 (a-b) and 28 Myr (c-d) of oceanic subduction, (corresponding to 80 and 72 Ma absolute ages) and comparison with the pre-D2 PT conditions (white box), defined by isotherms and depths. (a) At 80 Ma, the pre-D2 PT conditions are matched by markers that belong to the upper oceanic crust, located within the serpentinized mantle wedge and close to the slab. (b)

Geotherms extrapolated at different distances from the trench indicate that the pre-D2 PT conditions occur at a distance of 100-130 km from the trench and at ca. 80-110 km depth. (c) At 72 Ma, the pre-D2 PT conditions occur in an inner portion of the mantle wedge. (d) The location of the pre-D2 PT conditions in the subduction system is reached at a distance of 110-145 km from the trench and at ca. 80-110 km depth.

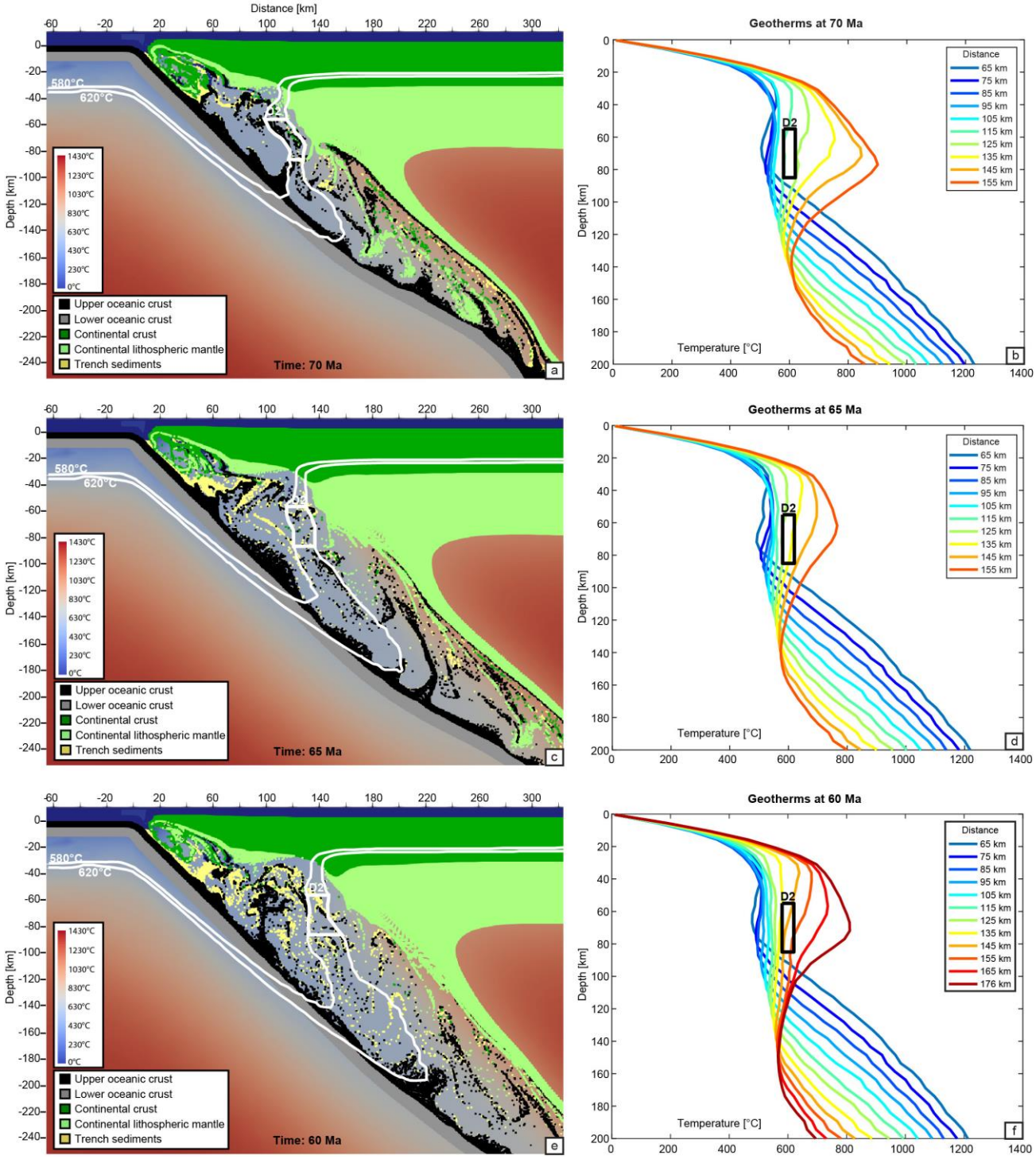

Fig. 3.1.4.10. Results of the simulation represented by geodynamic setting (a-c) and related geotherms (b-d) after 30 (a-b), 35 (c-d) and 40 Myr (e-f) of oceanic subduction, (corresponding to 70, 65 and 60 Ma absolute ages) and comparison with the D2 PT conditions (white box), defined by isotherms and depths. At 70 Ma (a), D2 PT conditions are recorded by markers of upper oceanic crust within the mantle wedge, and they are coupled with rare markers of trench sediments and some markers of continental crust. In the younger steps (c-e), the location of D2 PT conditions moves away from the slab. The maximum distance from the trench (b-d-e) varies from 125 km at 70 Ma to 155 km at 60 Ma.

3.1.4.8 Conclusions

The integration of different approaches in this study adds a new UHP puzzle tile to ZSZ tectonic evolution. The Créton serpentinite reached UHP conditions (2.8-3.3 GPa and 600-630 °C) before the development of the dominant S2 foliation, which has been dated at 60 to 70 Ma and represents an exhumation-related structural and metamorphic imprint. At the regional scale, this new UHP finding reinforces the idea of a heterogeneous nature of ZSZ, that can be therefore interpreted as constituted by different tectono-metamorphic units, which were amalgamated and partly obliterated during the development of the dominant regional foliation S2 under UHP-HP conditions. The vertical restoration of Créton serpentinite during subduction reconstructed by comparing the PTtd path with 2D model predictions suggests that the pre-D2 re-equilibration took place at around 100 km depth, close to the slab, before 70 Ma. Afterwards, these rocks were exhumed and migrated toward the top of the serpentinised wedge where syn-D2 assemblages developed between 60 and 80 km depth: here Ti-humite-bearing serpentinites were tectonically mixed with trench sediments and minor slices of continental crust.

The good agreement of the inferred tectono-metamorphic evolution compared with the predictions of the quantitative geodynamic modelling of an ocean-continent subduction system, together with the heterogeneous and diachronous metamorphic evolutions inferred in different portions of ZSZ, suggests that ophiolites from the axial zone of the Alpine belt can be considered as a tectonic mélange of different oceanic lithospheric slices that recorded different thermal and structural evolutions during their burial and exhumation trajectories in the mantle wedge of the subduction system.

3.1.5 Analysis of pyroxene and olivine trace elements from Créton lithostratigraphic assemblage

This paragraph aims refining the petrogenetic environments and processes responsible for the lithostratigraphy recognizable in Créton serpentinites (see map plate from Luoni et al., 2019) even if strongly transposed during the Alpine subduction. By detailed multiscale structural analysis, relic textural domains were selected to investigate the distribution of trace elements in the most preserved relict cores of clinopyroxene (Cpx) and olivine (Ol) porphyroclasts from pyroxenite and diopsidite, and from olivine-rich layer respectively.

Trace element composition of clinopyroxene and olivine from 3 samples of pyroxenite, 1 sample of diopsidite, and 1 sample of olivine-rich layer were carried out at the CNR-IGG UOS of Pavia University with a LA-ICP-MS system coupling a 266 nm Nd:YAG laser probe with a quadrupole ICP-MS (DRCe from PerkinElmer), using NIST 610, NIST 612, and BCR2 standards, and GLITTER data processing. Spot size was 40–55 mm according to the minerals sizes, laser frequency 10 Hz, acquisition was for 40–60 s preceded and followed by at least 40 s background counting.

3.1.5.1 Pyroxenite

Samples 29 and 18

Samples 18 and 29 consist of pyroxenite from outcrop 2 and 5, respectively. In both samples Cpx1 forms porphyroclasts wrapped by S2 with exsolution of Fe and Ti oxides and Ti-humites; Cpx2 forms recrystallized portion of Cpx1 or rims around Cpx1 and are exsolution-free. Cpx1 is locally rimmed by

polygonal aggregates of Ti-Chn + Ti-Chu + Ilm + Mag. Locally in sample 29, exsolution-free pinkish cores of Cpx1 are called Cpx0 as they represent the less re-equilibrated portion of the Cpx porphyroclasts.

Cpx0 is augite and shows the highest content in Fe. Cpx1 is Mg-rich augite to diopside, Cpx2 is diopside (Fig. 3.1.5.1).

Clinopyroxene trace element composition

In Fig. 3.1.5.2 and Fig. 3.1.5.3, the chondrite normalised REE pattern and the Spider diagram of Cpx0 are represented to better compare the composition of the most primitive pyroxenite Cpx with data of clinopyroxene not affected by subduction metamorphism. Cpx0 REE pattern shows LREE depletion relative to HREE, which are almost flat at about 100 times CI chondrite (Fig. 3.1.5.2). Eu shows a negative anomaly suggesting magmatic equilibrium crystallisation with plagioclase. The chondrite normalised incompatible trace element pattern reveal an Sr negative anomaly (see spider diagram in Fig. 3.1.5.3) consisting with Cpx cores crystallisation with plagioclase and a negative Ti anomaly, pointing to Ti-oxides exsolution. The REE pattern of Cpx0 fits almost perfectly the composition of

Sample	29		3		34	
Texture	Cpx0		Cpx1		Cpx1	
	min	max	min	max	min	max
Li7	0	0	11.31	36.88	12.39	15.16
Be9	3.85	3.85	5.17	14.42	19.14	19.14
B11	5.2	11.45	4.98	16.12	6.18	18.16
Sc45	126.27	129.41	15.37	83.47	1.77	9.35
Ti49	4232.36	4406.03	15.82	2885.39	37.46	1016.28
V51	393.39	398.65	1.98	315.53	2.19	156.3
Ni60	162.28	169.17	85.73	491.09	101.52	340.02
Sr88	12.59	13.74	5.42	14.7	5.79	20.54
Y89	118.46	126.32	3.51	17.36	0.703	15.26
Zr90	110.18	120.2	0.227	17.9	0.097	1.407
La139	3.4	3.63	0.409	1.243	0.254	2.259
Sm149	12.74	14.51	0.504	1.82	0.159	2.58
La/Sm	0.25	0.268	0.44	1.214	0.735	1.918
Eu151	3.61	3.94	0.287	0.735	0.046	0.924
Gd157	16.36	18.47	0.71	2.68	0.081	3.13
Tb159	3.48	3.72	0.1073	0.54	0.0261	0.642
Dy163	23.26	23.66	0.638	3.59	0.087	3.05
Ho165	4.66	5.15	0.165	0.755	0.0312	0.52
Er167	12.44	14.33	0.37	2.15	0.117	1.4
Tm169	1.607	1.916	0.0395	0.341	0.0034	0.224
Yb173	11.56	12.77	0.188	1.79	0.109	0.94
Lu175	1.666	1.76	0.017	0.217	0.0177	0.095
Hf177	4.39	4.98	0.312	0.782	0.042	0.079
Ta181	0.0183	0.0183	0.0111	0.0341	0.0101	0.0243
Pb208	0.091	0.091	0.062	0.169	0.106	0.354
Th232	0.0199	0.0397	0.0081	0.0284	0.0111	0.065
U238	0.0136	0.0186	0.0078	0.0194	0.0039	0.0045

Table 3.1.5.1 - Trace element content (ppm) in pyroxenite (Cpx0 sample 29, Cpx1 sample 3) and diopsidite (Cpx 1 sample 34)

clinopyroxene from the Fe-rich gabbros of the Ligurian ophiolites (Sample N1A, Tiepolo et al., 1997) and is very similar to the Cpx pattern from a gabbroic sequence from the Hess Deep of the East Pacific Rise (Coogan et al., 2002). All these features suggest that Cpx crystallised from an evolved gabbro melt intruding the peridotites.

In Fig. 3.1.5.4, the variation REE diagram of Cpx0, Cpx1 and Cpx2 is shown. Cpx1 is generally depleted in HREE than Cpx0 toward 10 times CI chondrite but slightly enriched in LREE. The Eu anomaly is preserved. Very few data of Cpx2 can be trusted despite metamorphism and their pattern is highly depleted to 1 to 10 times CI chondrite than Cpx0 especially for LREE and Eu negative anomaly is still perceptible beside a prominent Sm positive peak. Then, the chondrite normalized content of REE decrease as metamorphism proceeds and Cpx1 preserves a similar pattern while Cpx2 are almost totally re-equilibrated, whereas Cpx0 cores retain the most pristine primary composition.

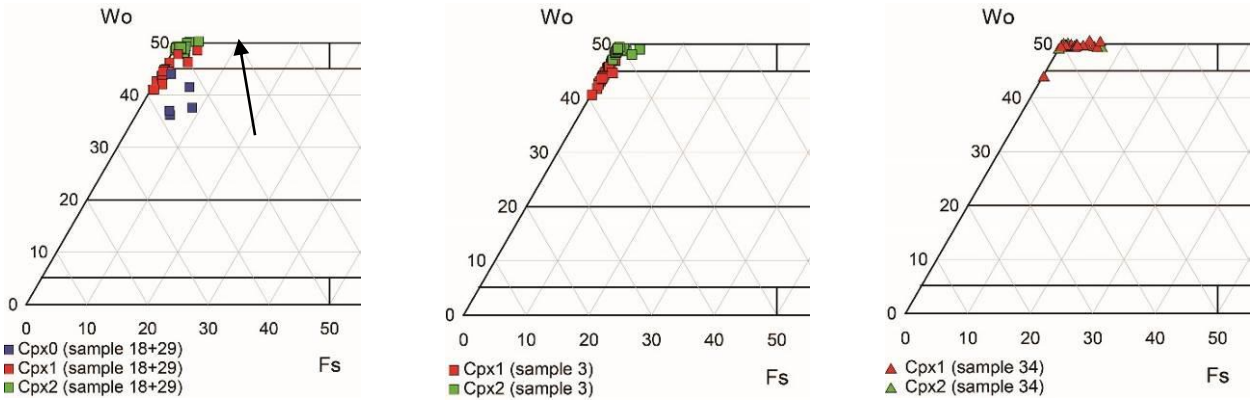

Fig. 3.1.5.1 - Cpx classification diagram. Samples 18, 29 and 3 = pyroxenites; sample 34 = diopsidite.

The high content of B (Fig 5.) in the Cpx0 cores indicate that Cpx was affected by fluid already during the magmatic crystallization. The fact that B contents are the same also for the metamorphic portion of the Cpx crystals could indicate that B remained stable during the whole Alpine metamorphic evolution.

Sample 3

Sample 3 is a pyroxenite from outcrop 1. In sample 3, Cpx1 constitutes deformed porphyroclasts with Fe-oxides and Ilm exsolutions, whereas Ti-humites + Mag + Ilm polygonal aggregates do not occur. Undeformed and exsolution-free Cpx2 new grains and rims occur. In difference from samples 18 and 29, in sample 3, no Cpx0 cores are preserved and Cpx1 varies from augite to diopside and Cpx2 is diopside in composition.

Clinopyroxene trace element composition

Cpx1 REE pattern is flatten around 10 times CI chondrite except for LREE that are more depleted than HREE (Fig. 3.1.5.2). The Eu and Ti negative anomaly in Fig. 3.1.5.3 spider diagram are very small. Cpx1 REE pattern is similar to those of Mg-gabbros Cpx from Ligurian ophiolites (sample CBC3, Tiepolo et al., 1997) and Mg-gabbros Cpx from Godzilla Megamullion of the EPR (Sanfilippo et al., 2016) and fits very well also with Ol-gabbro Cpx in the Mid Atlantic Ridge (MAR; Drouin et al., 2009). Thus, the magmatic REE pattern is quite preserved despite the Alpine metamorphic evolution. REE as Zr, Yb, and Sc are lower than those in Cpx0 from sample 29 (Fig. 3.1.5.5 and Table 3.1.5.1) and the wider variation of LREE with respect to those of Tiepolo et al. (1997) and Sanfilippo et al.

(2016), beside the slightly higher La-Sm ratio (Fig. 3.1.5.5), is typical of rock/fluid interaction during subduction metamorphism. In the spider diagram (Fig. 3.1.5.3), the smaller Eu anomaly with respect to Cpx0 from sample 29 suggests that sample 3 pyroxenite crystallised from a less evolved gabbro melt than sample 18 and 29 pyroxenite.

With respect to Cpx in Mg-gabbros of Ligurian ophiolite (Tiepolo et al., 1997), Cpx1 Cr content is higher, as Créton pyroxenites most likely intruded mantle peridotites as thin dikelets with more chances of chemical interaction with host rocks than the km-sized gabbro bodies of Ligurian ophiolites (Hoogerduijn Strating and Van Wamel, 1989). At the same time Ti, V, Sr, and Y are comparable between sample 3 Cpx1 and sample 29 Cpx0 (Fig. 3.1.5.5), therefore these elements in Sample 3 Cpx1 may represent a more pristine primary concentration with respect to other elements. High B in sample 3 Cpx1 values testifies the contact with fluids during the magmatic crystallization or metamorphism (Fig. 3.1.5.5 and Table 3.1.5.1).

In Fig. 3.1.5.5, the Zr-Yb diagram shows the evolution trend between pyroxenites from sample 18 and 29, and pyroxenites from sample 3 from low Zr and Yb content (Mg-gabbro and sample 3 Cpx1) to high Zr and Yb (Fe-gabbro and sample 29 Cpx0). The comparison with gabbroic post-cumulus Cpx from Tribuzio et al., 2000) excludes a cumulitic crystallization for all the pyroxenite samples as they contain high Zr-low Yb values and they don't fall along the trend described among sample 3 Cpx1, Ligurian Mg-gabbro Cpx, Ligurian Mg-gabbro Cpx (Tiepolo et al., 1997) and sample 29 Cpx0.

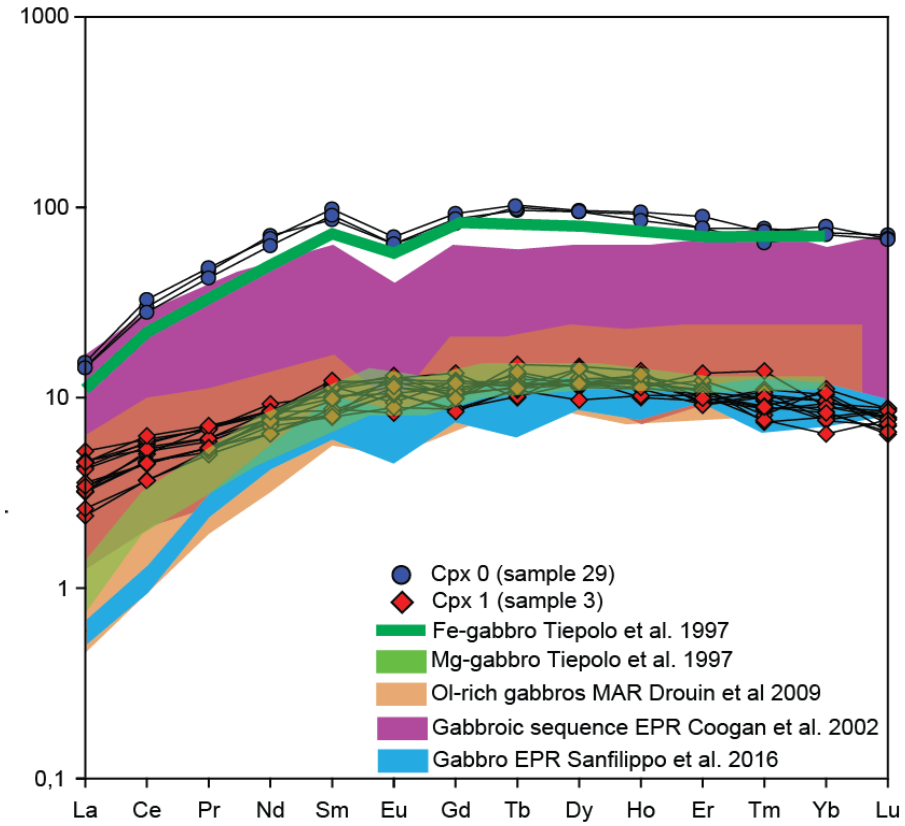

Fig. 3.1.5.2 - REE pattern of pyroxenites Cpx: Cpx0 from sample 29 and Cpx1 sample 3 only are reported as they represent the composition of the most relic textures in pyroxenite of the respective samples and to better compare their pattern to not metamorphosed Cpx composition from Ligurian ophiolites (Tiepolo et al., 1997) and present-day oceanic gabbros (Coogan et al., 2002, Drouin et al., 2009 and Sanfilippo et al., 2016)

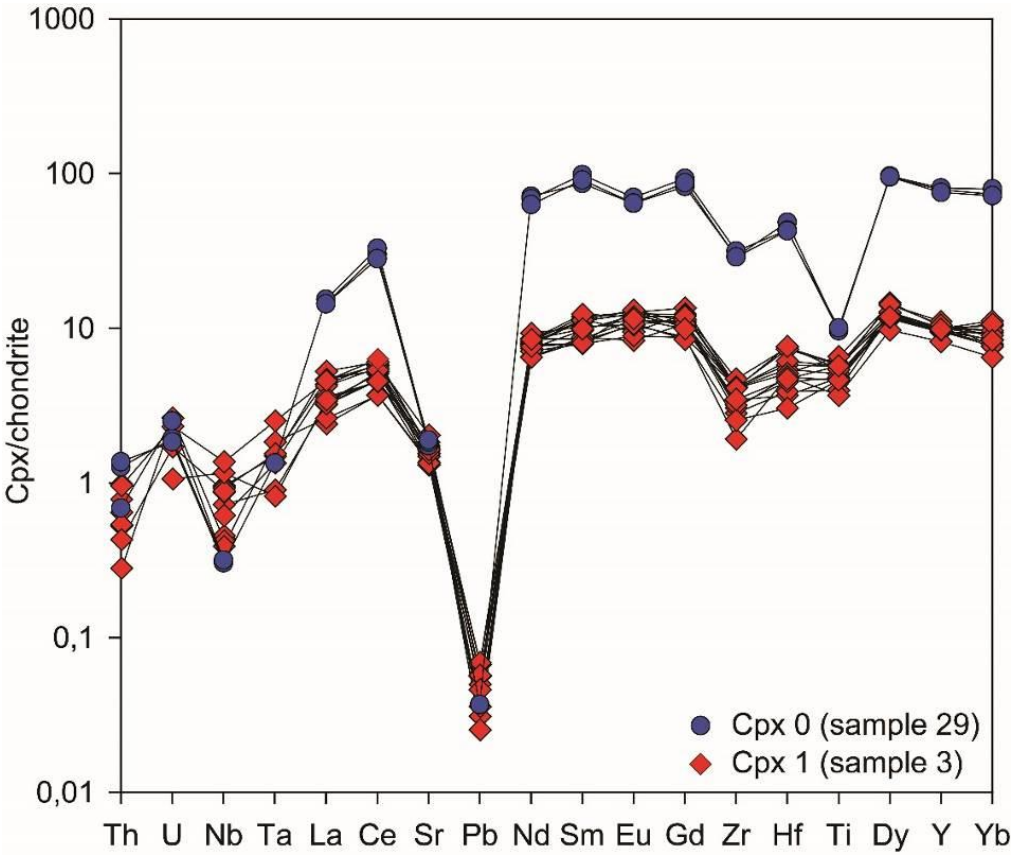

Fig. 3.1.5.3 - Spider diagram of pyroxenite Cpx (Cpx0 sample 29 and Cpx1 sample 3)

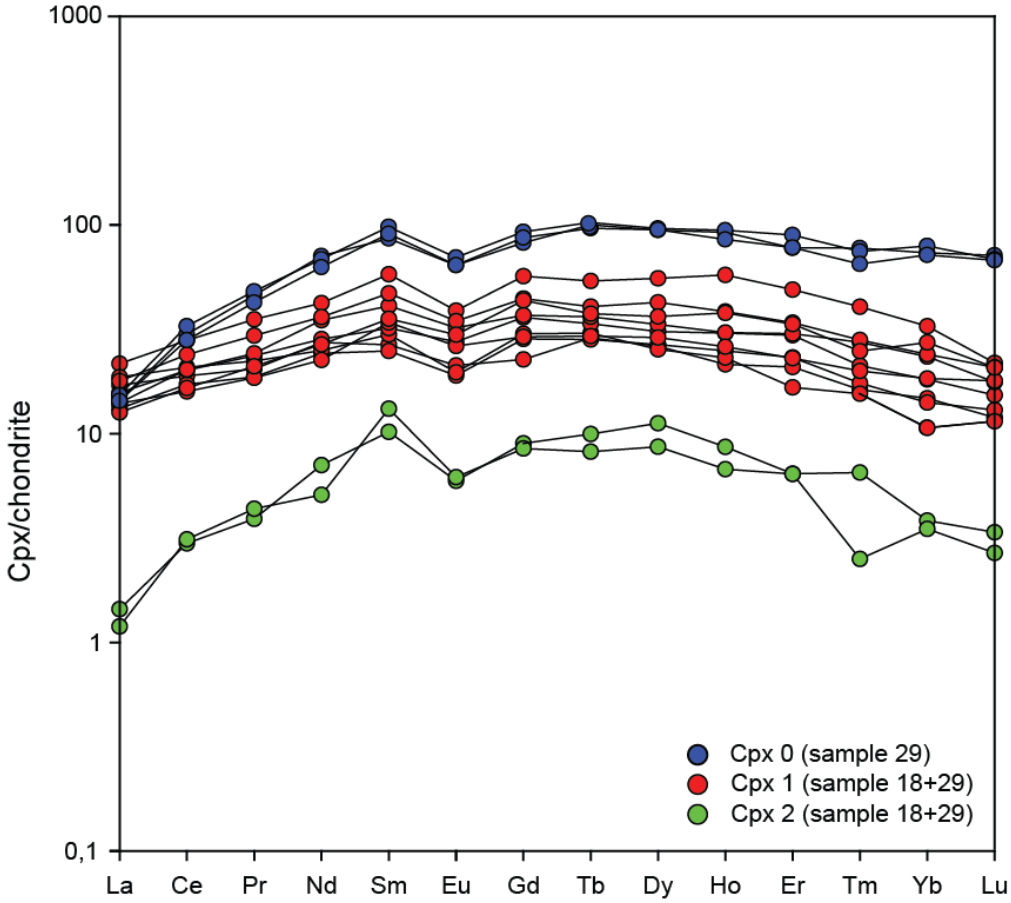

Fig. 3.1.5.4 - REE pattern of Cpx0, Cpx1 and Cpx2 from pyroxenite (sample 18 and 29) are reported together to show the depletion of REE with the progress of metamorphism.

3.1.5.2 Diopsidite

Sample 34

In sample 34, locally the core of Cpx1 porphyroclasts encloses Ti-Grt (Melanite) and Mag. Cpx1 porphyroclasts are rimmed by Cpx2 and often wrapped by Cpx2 crystals bearing S2 foliation.
Both Cpx1 and Cpx2 are Ca-rich diopside in composition (Fig. 3.1.5.1).

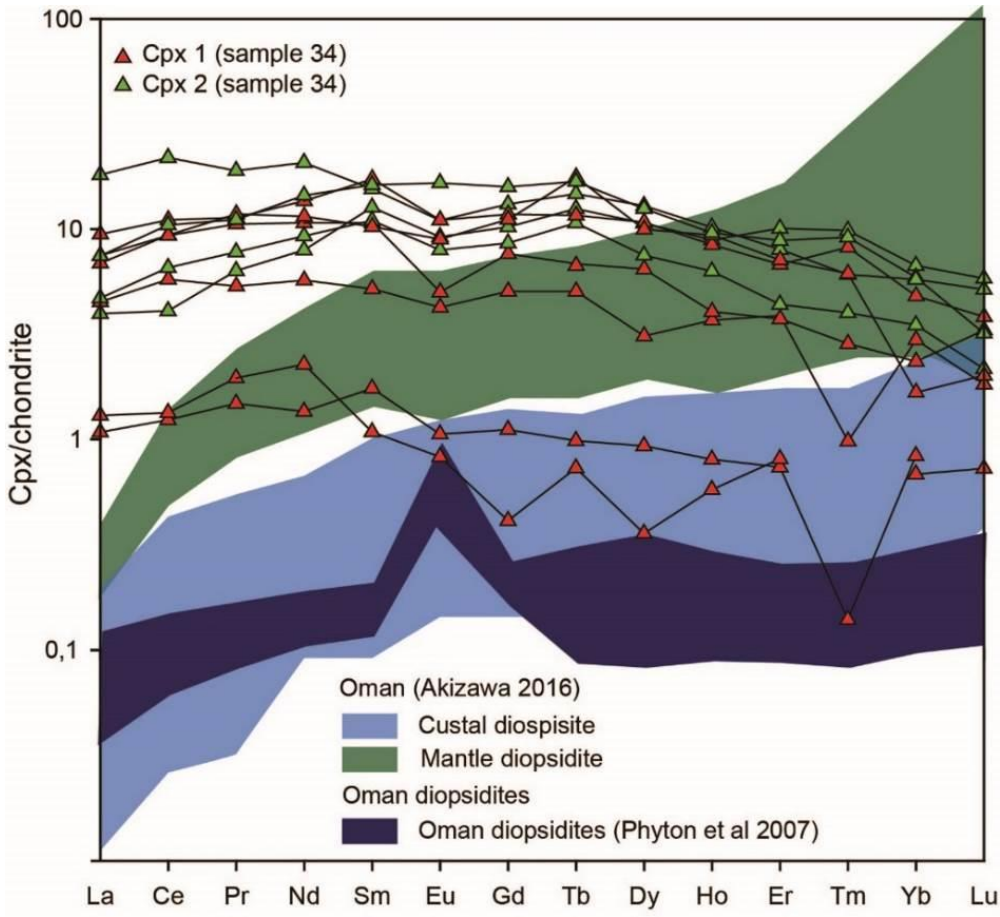

Fig. 3.1.5.6 - REE pattern of diopsidite Cpx (Sample 34, Cpx1 and Cpx 2).

Clinopyroxene trace element composition

The CI normalised REE pattern of clinopyroxene in diopsidites (Fig. 3.1.5.6) is almost flat around 10 times chondrite, except for 2 analyses that are around 1-time chondrite. Cpx1 and Cpx2 REE pattern overlap each other, reflecting a chemical homogeneity seen also for major elements (Fig. 3.1.5.1). The chondrite normalised incompatible trace element pattern shows very low Sc, high Ba, and heterogeneous Sr values that confirm this rock experimented a very strong metamorphic re-equilibration. B in Cpx diopsidite is less concentrated than B in Cpx pyroxenite (Fig. 3.1.5.5). Since B typically derives from sea water, B in Cpx pyroxenite may had been incorporated during magmatic crystallisation or subsequent solid state metasomatism, whereas in diopsidite Cpx B should derive from oceanic metasomatism, as diopsidite are considered metasomatic products pristine ophiolite section such as the Oman ophiolite (Python et al., 2007).

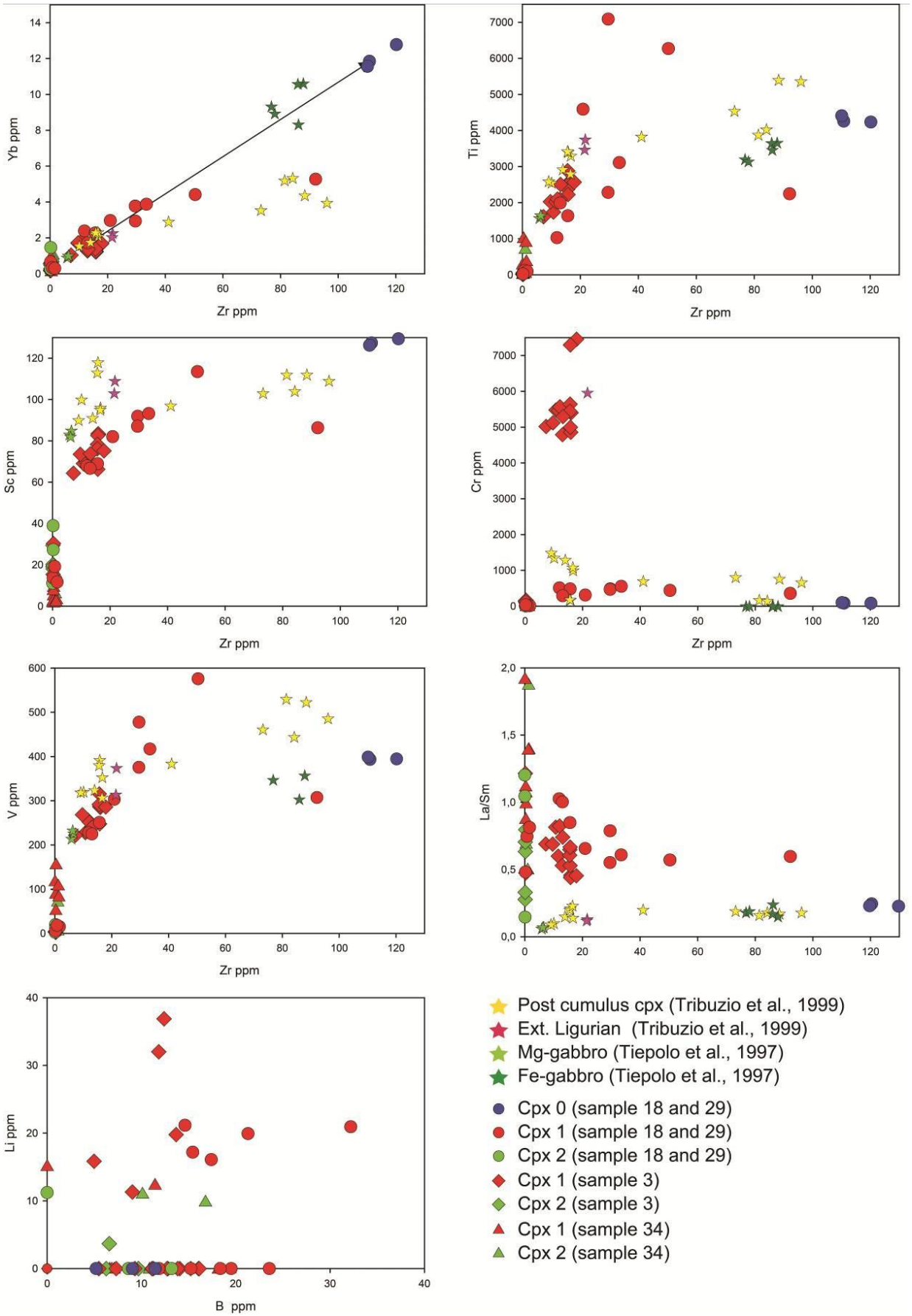

Fig. 3.1.5.5 - Trace elements diagrams. Samples 18, 29 (circles) and 3 = pyroxenites (diamonds); sample 34 = diopsidite (triangles).

The different concentration in Cpx diopsidite than in Cpx pyroxenite is consistent with lower amount of B incorporated during metasomatism in Cpx diopsidite than in Cpx pyroxenite or with a higher release of B from Cpx diopsidite than Cpx pyroxenite during the Alpine cycle.
Although major element composition is comparable with that of clinopyroxene in oceanic diopsidites from Oman described by Python et al., 2007), the REE composition is not comparable in terms of pattern and concentrations with that of the Oman diopsidites (Python et al., 2007; Akizawa et al., 2016).

3.1.5.4 Olivine rich layer

Sample 11

With respect to olivine-rich layers from other outcrops, sample 11 is from a lenticular olivine-rich layer of outcrop 2 that preserve the S1 foliation and is no affected by S2. Furthermore, this lens preserves a porphyroclastic texture (Luoni et al., 2019; Mercier and Nicolas, 1975) that may well predate the Alpine subduction. Ol occurs in different sizes: Ol0 constitutes almost centimetre-sized relic porphyroclasts, in a millimetre polygonal Ol1 + srp1 matrix. Also an interstitial sub-mm Ol2 occurs.
Ol0, Ol1, and Ol2 from sample 11 show homogenous Fe and Mg content (Fig. 3.1.5.7) with X_{Mg} mostly comprised between 0.91 and 0.92. The composition of olivine in olivine veins from Créton (Luoni et al., 2019) shows higher Mg and lower Fe content with X_{Mg} up to 0,96. Since in the general the composition of high pressure metamorphic phases is richer in Mg than the same phase in protoliths, it is possible arguing that olivine from the veins is more re-equilibrated during the syn-convergence metamorphism with respect to the olivine from the sample 11 layer.

Olivine trace element composition

In Fig. 3.1.5.8 Mn, Ni, and Cr content from Ol0 are plotted vs X_{Mg} together with olivine compositions of troctolites, harzburgites and dunites, from the Southern Lanzo massif (Sanfilippo et al., 2014) and olivine of MORB, OIB, komatites and picrites from a number of localities all over the world- 229 samples of tholeiitic to transitional compositions covering MORBs (40 samples) from Mid-Atlantic Ridge, East Pacific Rise, South-East Indian Ridge, and Knipovich Ridge; OIBs (138 samples) from Hawaiian Islands and Emperor Seamounts, Canary Islands, Reunion, Azores, and Iceland; LIPs (36 samples) from Ontong Java Plateau, Siberia, Emeishan, Karoo, Afar, and North Atlantic Province; komatiites and associated picrites (15 samples) from the Archean Abitibi greenstone belt in Canada and the Belingwe belt in Zimbabwe and South Africa; Proterozoic komatiitic basalts from Gilmour Island, Canada; and komatiites and picrites from Gorgona Island, Colombia (Sobolev et al., 2007).
Only Mn in Ol0 shows comparable content with Mn content of olivine from Sanfilippo et al. (2014) and Sobolev et al. (2007) while Ni and Cr are lower than any value reported in the literature for olivine in peridotite. Moreover, also the trends of trace element are not comparable with any of the magmatic trend reported in the diagrams (Fig. 3.1.5.8).

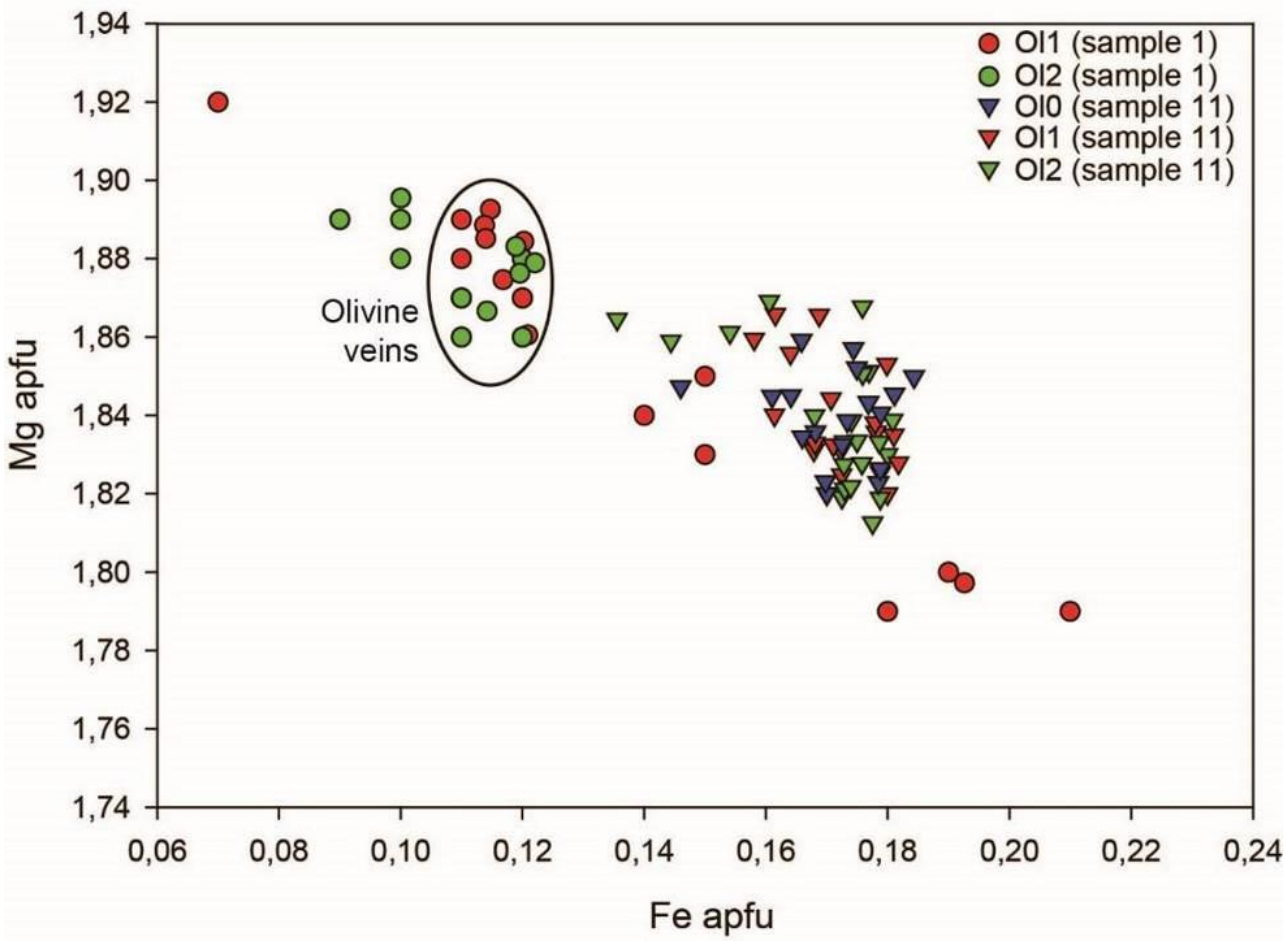

Fig. 3.1.5.7 - Fe vs. Mg diagram (Ol0, Ol1, Ol2 Sample 11 and Ol1, Ol2 sample 1)

Sample	11	
Texture	Ol0	
	Min	Max
Li7	0.72	1.17
Ca44	166.53	381.16
Cr53	3.41	20.77
Mn55	884.33	1136.94
Ni60	749.05	846.19

Table 3.1.5.2 - Trace element content (ppm) in Ol0 from olivine-rich layer (sample 11).

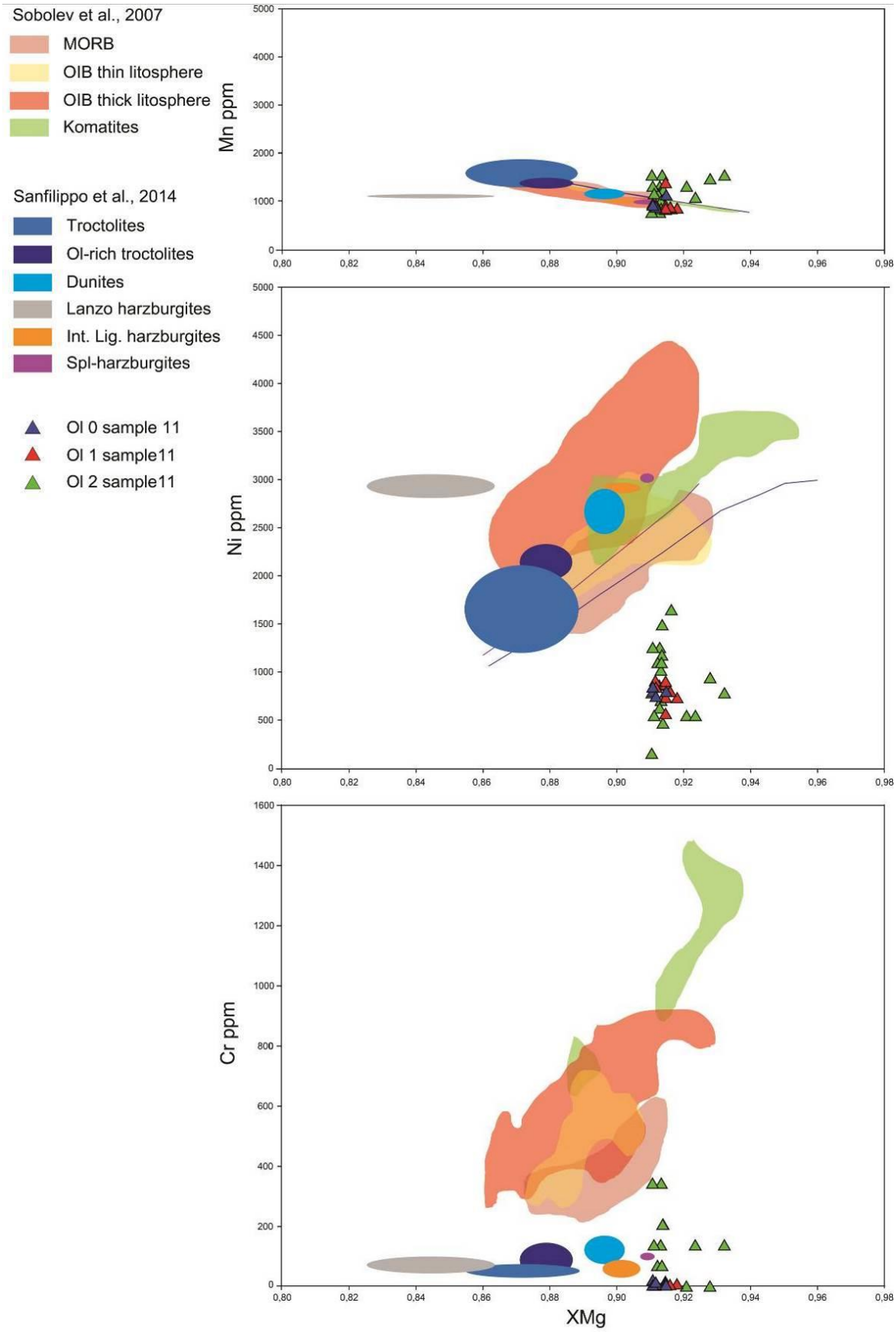

Fig. 3.1.5.8 - Trace elements diagrams: Ol0, Ol1, Ol2 from sample 11 olivine-rich layer. Compositional fields from Sobolev et al. (2007) and Sanfilippo et al. (2014).

3.1.5.4 Discussion and Conclusions

In conclusion, the trace element analysis, and the comparison with Cpx from not-metamorphosed gabbro from Ligurian ophiolites, MAR, and EPR, allow interpreting Créton pyroxenite layers as the relics of gabbroic melts percolated into the peridotite body of the Tethyan oceanic lithosphere. Furthermore, the geochemical investigation allows distinguishing two different protolith for Créton pyroxenites: Cpx0 in pyroxenite of samples 18 and 29 preserves the composition of an evolved melt from which crystallised a lithology comparable to an oceanic Fe-gabbro (Tiepolo et al., 1997; Coogan et al., 2002). Cpx in pyroxenite of sample 3 shows the composition of a less differentiated melt that crystallised as Mg-gabbro or Ol-rich gabbro (Tiepolo et al., 1997; Drouin et al., 2009; Sanfilippo et al., 2016). Therefore, pyroxenite layers embedded in the serpentinite (Luoni et al., 2019) are the remnants of gabbro dikelets that intruded the host rock during the oceanic evolution. The metric distance between the different pyroxenite dykes lead to suppose a common source and the LREE enrichment of sample 3 Cpx1 with respect to sample 29 Cpx0 could be due to metamorphism by subduction-related fluids.

Diopsidites are too chemically re-worked for deciphering their protolith and trace elements do not help to go back to a clear metasomatic origin.

Although sample 11 preserves the most relic texture with respect to the other sampled olivine rich layers, which could represent a relic oceanic texture as discussed in Luoni et al. (2019), compositions seem to be strongly affected by metamorphism and no magmatic chemical feature is preserved.

3.1.6 Diopsidite associated with the Zermatt-Saas serpentinite of Créton, Valtournenche

3.1.6.1 Introduction

The Zermatt-Saas serpentinite derives from a mantle that was variously affected by hydrothermal metasomatism and magmatic episodes testified by rodingite dykes and gabbroic bodies of different sizes (Bearth, 1967; Li et al., 2004; Zanoni et al., 2012; Zanoni et al., 2016) and successively was strongly reworked during Alpine subduction. In the frame of the structural and metamorphic exploration of Créton outcrops, diopsidite layers and boudins have been recognised within serpentinite. Within the Zermatt-Saas Zone, diopsidite has not been described yet, thus this contribution will attempt to depict the evolution of these peculiar rocks, found in oceanic assemblages. Within the quite small amount of papers focused on diopsidite genesis, the debate is still very open especially for what concerns the temperature under which metasomatism develops. In Oman ophiolite sequences, diopsidite has been described as a diagnostic lithotype for very high temperature hydrothermal circulation in mantle peridotite below oceanic spreading centres by Python et al. (2007). On the other hand, the model of Bach and Klein (2009), developed for the evolution of present day oceanic rock assemblages, predicted that diopsidite can be produced from gabbroic and clinopyroxenite precursor rocks up to 400 °C, thus suggesting that high temperatures on the order of 800 °C are not required in the formation of diopsidite veins,

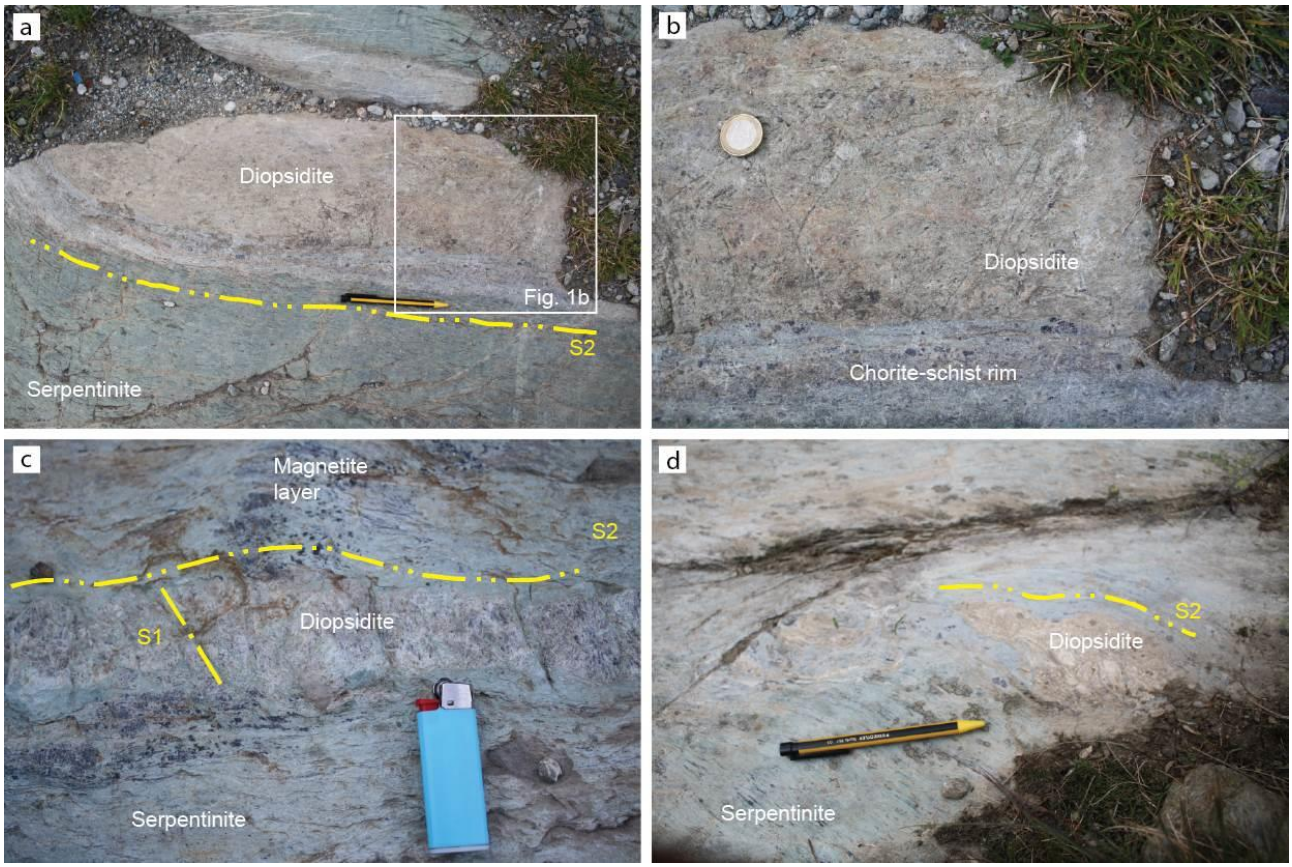

Fig. 3.1.6.1 - a, b) Yellowish diopsidite layers in Créton outcrop 1, rimmed by a Chl-schist rim, and parallel to S2 foliation; c) grey diopsidite layer parallel to S2 in serpentinite and crosscutting a magnetite layer (Créton, outcrop 6a); d) lens of whitish diopsidite wrapped by S2 (Créton, outcrop 6b).

3.1.6.2 Field relations

As analysed in detail in Luoni et al. (2019) (see the map in the thesis attachment), layers and boudins of diopsidites are embedded in Créton serpentinites and are wrapped by the S2 regional foliation of serpentinite. Diopsidite occurs in outcrops 1, 6a, and 6b of the outcrop map in Luoni et al. (2019) (see attachment 1). Here, three types of diopsidite have been distinguished. In outcrop 1 a layer of *yellowish diopsidite* is 5-m-long and 20-cm-thick (Fig. 3.1.6.1a-b), and it is rimmed on both sides by 5-cm-thick layers of chlorite schist. In outcrop 6a and 6b, *grey diopsidite* constitutes a 1-metre-long layer and a 20-cm-long lens parallel to the S2 foliation and with a thickness of 10 cm (Fig. 3.1.6.1c). In the western part of outcrop 6b, lenses of *whitish diopsidite* are 20-cm-long and 10-cm-thick (Fig. 3.1.6.1d).

3.1.6.3 Whole-rock composition

Whole rock analyses (Table 3.1.6.1) of yellowish and grey diopsidite were performed at Mineral Veritas Bureau (Krakow) by ICP-MS. *Yellowish diopsidite* is constituted mostly of SiO_2 (52.67 wt%), MgO (16.27 wt%) and CaO (22.17 wt%). Fe_2O_3 and TiO_2 are 5.12 and 1.01 wt% respectively; Al_2O_3, Na_2O, and MnO are < 1%. Cr_2O_3 and K_2O are negligible. *Grey diopsidite* is constituted mostly by Si (52.57 wt%), MgO (19.98 wt%) and Ca (19.89 wt%). Fe_2O_3 and Al_2O_3 are 2.88 and 1.13 wt% respectively; TiO_2, Na_2O, and MnO are < 1%. Cr_2O_3 and K_2O are negligible. Hence, yellowish diopsidite is richer in TiO_2, Fe_2O_3 and CaO but poorer in MgO than grey diopsidite. In Fig. 3.1.6.2a-d

Oman diopsidite compositions (Python et al., 2007) and data of rodingites from Zermatt-Saas Zone, Scandinavian Caledonides and Betic Cordillera (Puga et al., 1999; Li et al., 2004; Austrheim and Prestvik, 2008) are shown for comparison. Diopsidite compositions of Créton are very close to Oman diopsidite compositions (Fig. 3.1.6.2a and 2b), and different from rodingite compositions that are poorer in SiO_2 and higher in Al_2O_3 (Fig. 3.1.6.2a and 2b). CaO and TiO_2 show similar concentration Fig. 3.1.6.2b and 2c) to those diopsidite from Oman (Python et al., 2007). MORB normalised values (Fig. 3.1.6.2e) are flat around 1 time MORB values. Rb and U are significantly high. Sr, Zr, Nb negative anomalies are well pronounced and no Eu anomaly occurs.

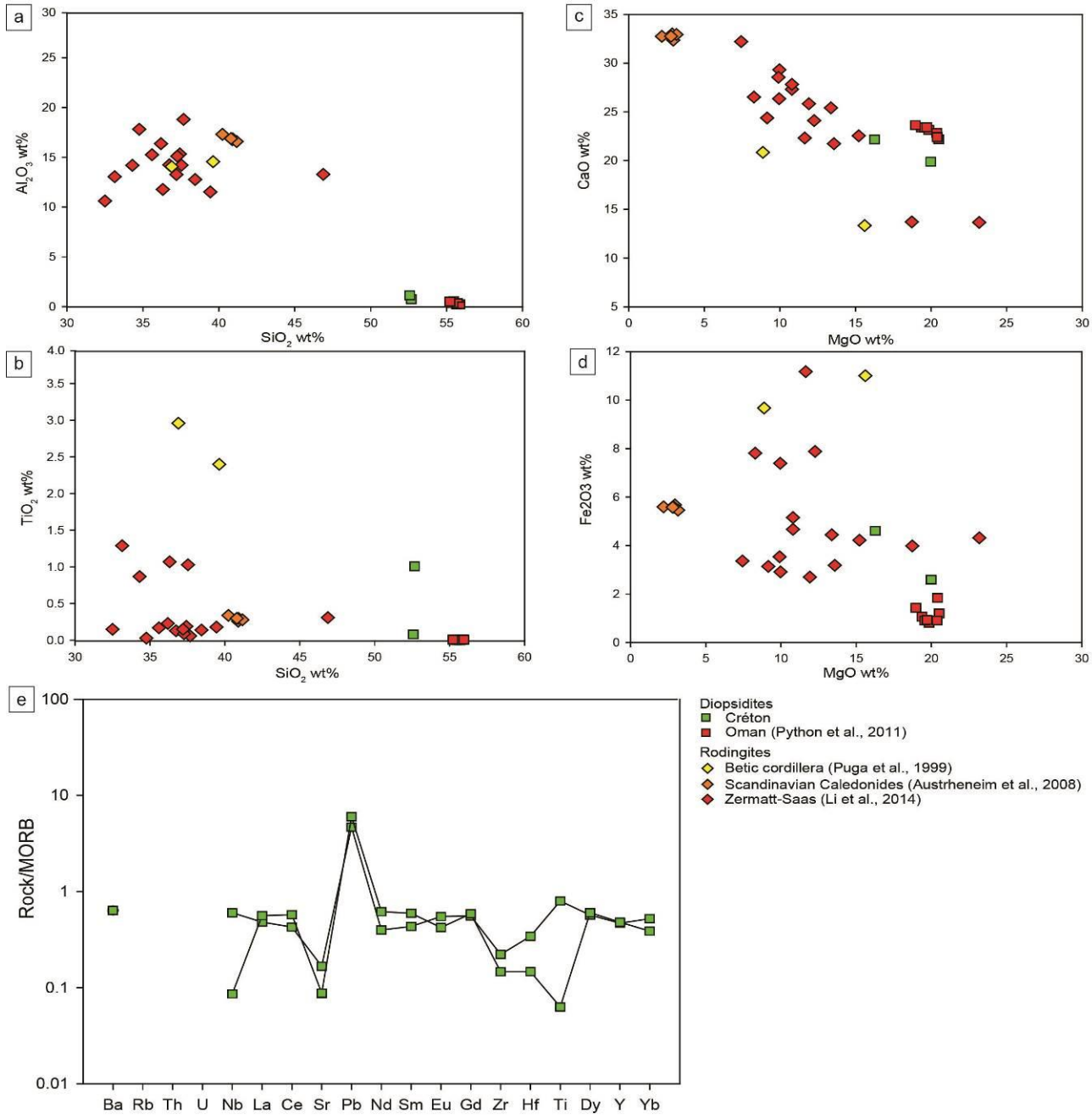

Fig. 3.1.6.2 - Whole rock composition diagrams. a-d) Major elements of bulk rock composition in comparison with Oman diopsidite bulk compositions (Python et al., 2007) and bulk composition of rodingites from Zermatt-Saas Zone, Scandinavian Caledonides, and Betic Cordillera (Puga et al., 1999; Li et al., 2004; Austrheim and Prestvik, 2008); e) MgO

vs. TiO_2 (wt.%) and f) Ti vs. V (ppm) with fields from Dilek and Furnes (2011); g) NORB normalised spider diagram (normalisation values from Eggins et al., 1998).

Diopsidite	Analyte	Wgt	SiO2	Al2O3	Fe2O3	MgO	CaO	Na2O	K2O	TiO2	P2O5	MnO	Cr2O3	Ba	Ni
	Unit	KG	%	%	%	%	%	%	%	%	%	%	%	PPM	PPM
	MDL	0.01	0.01	0.01	0.04	0.01	0.01	0.01	0.01	0.01	0.01	0.01	0.002	1	20
yellowish	Rock	0.05	52.67	0.74	5.12	16.27	22.17	0.37	0	1.01	0.02	0.24	0.018	4	270
grey	Rock	0.02	52.57	1.13	2.88	19.98	19.89	0.04	0	0.08	<0.01	0.08	0.061	<1	374

Diopsidite	Sc	LOI	Sum	Be	Co	Cs	Ga	Hf	Nb	Rb	Sn	Ta	Th	U
	PPM	%	%	PPM	PPM	PPM	PPM	PPM	PPM	PPM	PPM	PPM	PPM	PPM
	1	-5.1	0.01	1	0.2	0.1	0.5	0.1	0.1	0.1	1	0.1	0.2	0.1
yellowish	48	1	99.7	<1	41.9	<0.1	<0.5	0.7	1.4	<0.1	<1	<0.1	<0.2	<0.1
grey	7	2.9	99.65	<1	34.4	<0.1	<0.5	0.3	0.2	<0.1	<1	<0.1	<0.2	<0.1

Diopsidite	V	W	Zr	Y	La	Ce	Pr	Nd	Sm	Eu	Gd	Tb	Dy	Ho	Er
	PPM	PPM	PPM	PPM	PPM	PPM	PPM	PPM	PPM	PPM	PPM	PPM	PPM	PPM	PPM
	8	0.5	0.1	0.1	0.1	0.1	0.02	0.3	0.05	0.02	0.05	0.01	0.05	0.02	0.03
yellowish	103	<0.5	16.4	13.1	1.2	3.2	0.52	2.9	1.14	0.56	2.05	0.39	2.59	0.58	1.68
grey	63	3.9	10.8	13.4	1.4	4.3	0.79	4.5	1.56	0.43	2.16	0.41	2.74	0.57	1.52

Diopsidite	Tm	Yb	Lu	TOT/C	TOT/S	Mo	Cu	Pb	Zn	Ni	As	Cd	Sb	Bi	Ag
	PPM	PPM	PPM	%	%	PPM	PPM	PPM	PPM	PPM	PPM	PPM	PPM	PPM	PPM
	0.01	0.05	0.01	0.02	0.02	0.1	0.1	0.1	1	0.1	0.5	0.1	0.1	0.1	0.1
yellowish	0.23	1.59	0.28	0.16	<0.02	<0.1	7.2	1.4	39	165.8	1.5	0.1	<0.1	<0.1	<0.1
grey	0.18	1.18	0.16	0.15	<0.02	<0.1	11.4	1.8	53	252	0.6	<0.1	<0.1	<0.1	0.1

Diopsidite	Au	Hg	Tl	Se
	PPB	PPM	PPM	PPM
	0.5	0.01	0.1	0.5
yellowish	<0.5	<0.01	<0.1	<0.5
grey	<0.5	<0.01	<0.1	<0.5

Table 3.1.6.1 - Bulk rock analyses of major, minor and trace elements of yellowish and grey diopsidite.

3.1.6.4 Microstructures

Microstructures and mineral chemistry of three samples have been analysed by optical microscope and EMPA. Sample 4 is from outcrop 1 yellowish diopsidite, sample 34 is from outcrop 6a grey diopsidite layer, and sample 39 is from a whitish diopsidite lens of outcrop 6b. These three diopsidite types differ in mineralogy and texture.

Yellowish diopsidite (sample 4) composition is the richest in mineral phases: it is mostly composed by clinopyroxene with minor chlorite, amphibole, calcite, antigorite, ilmenite, titanite, apatite, and rare garnet. Pre-D2 subhedral clinopyroxene porphyroclasts are parallel to S2 and often rimmed by a corona of polygonal clinopyroxene 2 aggregate typical of core-mantle textures (Fig. 3.1.6.3a and 3b). Pre-D2 clinopyroxene is up to 8-9 mm; it displays undulose extinction, micro-fractures filled by clinopyroxene 2 and chlorite, and includes single grains of magnetite and chlorite. Rare micron-sized pre-D2 garnet inclusions have been detected using EMPA in clinopyroxene porphyroclasts

Whitish diopsidite (sample 39) is made of clinopyroxene with minor chlorite and antigorite, and rare Ti-rich garnet. Pre-D2 clinopyroxene forms as up to centimetre-sized porphyroclasts with undulose extinction, inclusions of Ti-rich garnet, chlorite, antigorite, and fractures locally filled by clinopyroxene2. The matrix is very fine-grained and is made of clinopyroxene2, antigorite2, and chlorite2. Clinopyroxene2 occurs in polygonal submillimetre granular aggregates that locally displays an acicular shape. Clinopyroxene2, antigorite2, and chlorite2 flakes SPO marks S2. Pre-D2 chlorite also constitutes kinked millimetre-sized porphyroclasts with undulose extinction (Fig. 3.1.6.3g).

Chlorite schist (Fig. 3.1.6.3h and 3i) is constituted by chlorite with minor clinopyroxene, ilmenite, magnetite, and amphibole. The dominant fabric is the mylonitic S2 foliation. Pre-D2 chlorite flakes with undulose extinction are wrapped by S2. Locally their SPO is parallel to S2 whereas LPO is mostly at high angle with respect to S2. Anhedral and up to 5 mm pre-D2 clinopyroxene porphyroclasts show undulose extinction, chlorite and magnetite exsolutions, and clinopyroxene2 rims. Pre-D2 clinopyroxene fractures are filled by clinopyroxene2. Continuous, mylonitic S2 foliation is marked by SPO of chlorite2 and clinopyroxene2. Also pre-D2 ilmenite porphyroclasts are wrapped by S2. Very rare Ti-clinohumite porphyroclasts are wrapped by S2 a rimmed by aggregate of Atg + Ilm + Mag. Chlorite3 rims pre-D2 Chlorite and Chlorite2, and amphibole3 locally overgrew S2 as euhedral crystals crosscutting chlorite2 flakes.

In table 3.1.6.2 mineral assemblages marking successive fabrics for each diopsidite type are synthesized.

3.1.6.5 Mineral chemistry

Mineral compositions from all the diopsidite types (one sample from yellowish diopsidite, one sample from grey diopsidite, one sample from whitish diopsidite) have been acquired using an electron microprobe (JEOL 8200 Super Probe) operating at the “A. Desio” Earth Science Department of Milan University. A 15 keV accelerating voltage and a beam current of 15nA were used. Natural silicates were used as standards and matrix corrections were calculated using the ZAF procedure. Mineral formulae were recalculated on the basis of the following number of oxygen atoms: 4 for olivine, 6 for clinopyroxene, 116 for serpentine, 28 for chlorite, 4 for magnetite (Ferracutti et al., 2015), 3 for ilmenite, 23 for amphibole (Locock, 2014), and 12 for garnet (Locock, 2008). Ti-clinohumite formula

was recalculated on the basis of 13 cations. Ilmenite Fe^{3+} was recalculated according to Droop and Road (1982). Representative mineral compositions are reported in table 3.1.6.3.

In all the *diopsidites* clinopyroxene is always diopside (Fig. 3.1.6.4a). Ti, Cr, Ni, and Na are below detection limits or occur in very small concentrations. Clinopyroxene from yellowish diopsidite has the widest variation in Ca and Mg content (0.88-0.98 apfu and 0.93-1.00 apfu, respectively) with no differences between pre-D2 clinopyroxene and clinopyroxene2. In the grey diopsidite, preD1 clinopyroxene has lower Mg content (0.88-0.98) than clinopyroxene1 (0.96-0.98 apfu) but homogeneous Ca content (0.97-0.99 apfu). Ca and Mg concentrations in whitish diopsidite are very similar (0.99-1.00 and 0.96-0.98 apfu, respectively). In Fig. 3.1.6.4b X_{Mg} vs TiO_2, Al_2O_3, and Cr_2O_3 are shown in comparison with clinopyroxene from Oman metasomatic diopsidites (Python et al., 2007) whose compositions are represented by the green fields. The great majority of Créton clinopyroxene compositions fall in the Oman clinopyroxene fields. Cr_2O_3 in Créton clinopyroxene fall in the same value range of Cr_2O_3 concentrations in clinopyroxene diopsidite from Oman.

In *Chl-schists* few preD2 clinopyroxene samples have small augitic component whereas clinopyroxene2 is pure diopside (Fig. 3.1.6.4a). In pre-D2 clinopyroxene, Ca and Mg (> 0.87 apfu and 0.92 apfu respectively) are generally lower than in clinopyroxene2 (0.97-1.00 apfu and mostly higher than 0.95 apfu, respectively). Again Ti, Cr, Ni, and Na are absent or occur in very small concentrations.

Garnet has been found in all diopsidite types and consists of Ti-rich andradite called melanite to Ti-rich grossular with minor morimotoite (Fig. 3.1.6.4c). Garnet from the whitish diopsidite is the richest in andradite (> 86%) with respect to the other analysed samples, with up to 20% morimotoite, whereas Garnet from the yellowish diopsidite is a Ti-rich grossular with the lowest content of morimotoite (< 5%). Garnet in grey diopsidite has 45 to 70% of andradite and the highest content of morimotoite (30%). Ti is lower than 0.1 apfu in the garnet from yellowish diopsidite and similar (0.14-0.51 apfu) in the other lithotypes (Fig. 3.1.6.4d). Ca varies between 2.89 and 3.05 apfu. In Fig. 3.1.6.4d a comparison with Ti-rich garnet from other localities is shown. Generally, garnet in Créton diopsidite has higher Ti/Si ratio than the garnet compositions of magmatic and hydrothermal origin (Russell et al., 1999). Ti is also higher than Ti- garnet in rodingites (Schmitt et al., 2019).

In diopsidite, chlorite is mostly penninite, except for preD2 chlorite in whitish diopsidite that is clinochlore and chlorite2 in yellowish diopsidite that is talc-chlorite. In chlorite schist, chlorite is penninite and chlorite2 is slightly richer in Fe than pre-D2 chlorite (Fig. 3.1.6.4d). In antigorite, X_{Mg} varies between 0.94 and 0.95 (Fe = 0.12-0.18 apfu) and Al content between 0.00 and 0.15 apfu, except for antigorite2 in yellowish diopsidite (X_{Mg} = 0.84-0.85 with Fe = 0.43-0.46 apfu) that shows also the highest Al content (0.17-0.20 apfu). Amphibole occurs only in the yellowish diopsidite, as tremolite and actinolite, and in the chlorite schist rim as tremolite. Ilmenite shows Ti content between 0.96 and 1.02 apfu. Mg is up to 0.23 apfu and Mn is up to 0.34 apfu. Fe^{2+} varies between 0.64 and 0.84 apfu while $Fe^{3+}$is up to 0.08 apfu.

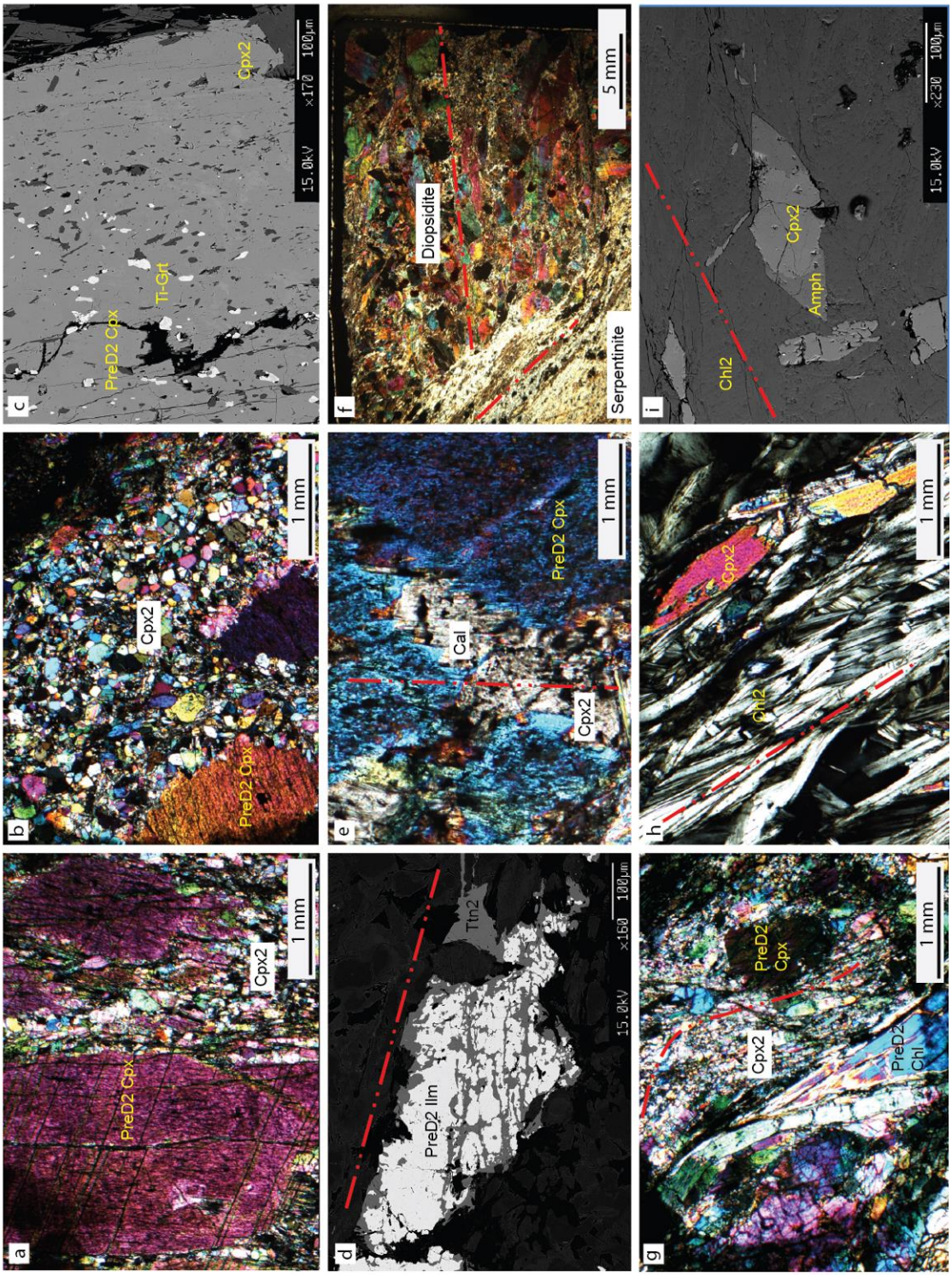

Fig. 3.1.6.3 - a, b) Pre-D2 clinopyroxene porphyroclasts with micro-cracks filled by polygonal clinopyroxene2 aggregates in yellowish diopsidite (crossed polars); c) inclusions of Ti-rich garnet (light grey) in a pre-D2 clinopyroxene, rimmed by clinopyroxene2 (yellowish diopsidite; BSE image); d) boundary between grey diopsidite and serpentinite (no chlorite schist rim occurs between the two) (crossed polars): S2 in serpentinite crosscut S1 in diopsidite forming a high angle; e) Pre-D2 chlorite and clinopyroxene porphyroclasts wrapped by S2 in whitish diopsidite (crossed polars); f) Pre-D2 ilmenite porphyroclasts rimmed by titanite2 films (yellowish diopsidite; BSE image); g) pre-D2 clinopyroxene with interstitial calcite2 (yellowish diopsidite; crossed polars); h) chlorite2 and clinopyroxene2 SPO marking S2 in Chlorite-schist rims (yellowish diopsidite; crossed polars); i) amphibole3 overgrowing clinopyroxene2 in chlorite-schist rims of yellowish diopsidite (BSE image) amphibole3

Diopsidite	preD2	D2	D3
	D1		
yellowish	Cpx+Ilm+Grt+Ap	Cpx+Chl+Atg+Cal+Ttn	Act+Tr
grey	Cpx+Atg+Mag+Chl+Grt	Cpx+Chl+Atg	
whitish	Cpx+Chl+Atg+Grt	Cpx+Chl+Atg	

Chl-schist rim	preD2	D2	D3
yellowish	Cpx+Chl+Ilm	Cpx+Chl	Tr
whitish	Cpx+Mag+Chl+Ti-Chu+Ilm	Cpx+Chl+Atg	

Table 3.1.6.2 - Synthesis of assemblages marking superposed textures in diopsidite layers and Chl-schist rim.

3.1.6.6 Discussion

Diopsidite occurs as layers and boudins wrapped by and parallelised into HP S2 foliation in Créton serpentinite and the boundary with serpentinite is often rimmed by chlorite schist. On the basis of composition, *yellowish diopsidite* differs from the others because it is the richest in Ti-bearing phases and carbonates. As pointed out by Luoni et al. (2019), diopsidite crosscuts magnetite layers and hence, it is successive to the layering of peridotite. Diopsidite locally preserves an S1 foliation (*grey diopsidite*) but its meso- and microstructural features are mostly affected by D2, as S2 occurs in *yellowish diopsidite* and in *whitish diopsidite* and they are wrapped by and parallelised into S2. These features are the key witness that diopsidite was affected by syn-D2 HP conditions during Alpine subduction.

A first attempt of PT modelling has been led but model predictions doesn't fit with observed assemblages. HP assemblages are Cpx + Chl + Atg + Ttn+ Cal in yellowish diopsidite, and Cpx + Chl + Atg in yellowish and grey diopsidite.

Despite Alpine subduction reworking, Créton diopsidites preserve characters similar to Oman diopsidite (Python et al., 2007) such as lithostratigraphic assemblage and whole rock, and clinopyroxene compositions. In ophiolitic sequences in Oman, diopsidite forms layers in peridotite very close to gabbroic percolation (Python et al., 2007). As shown in whole rock diagrams, Créton diopsidite composition is very close to that of Oman diopsidite with respect to rodingite composition. Similarly to Oman diopsidite, clinopyroxene is pure diopside with very low contents of TiO_2, Al_2O_3, and Cr_2O_3. In contrast, Créton diopsidite do not have olivine and plagioclase. Furthermore, whole rock spider diagram is not diagnostic for the reconstruction of the origin or the evolution of Créton diopsidite and as well as the absence of olivine and plagioclase that is probably due to the Alpine metamorphism that reached the climax under UHP conditions (see Luoni et al., 2018). Ti-rich garnet occurs as inclusion in preD2 clinopyroxene core. It is a diagnostic phase of silica undersaturated alkalic plutonic and volcanic rocks but also occurs in skarn and hydrothermal alteration assemblages (Russell et al., 1999) as recently pointed out by Schmitt et al. (2019) that described Ti-garnet in Nomo rodingite. Ti-rich garnet and pre-D2 clinopyroxene core can represent the relic of ocean floor metasomatism that produced diopsidite from serpentinite or gabbroic dykes (Bach and Klein, 2009; Python et al., 2007). Indeed as pointed out by Bach and Klein (2009), the occurrence of garnet and clinopyroxene, and clinopyroxene composition, are consistent with formation temperatures of 300-440 °C, and not with the high temperatures (800 °C) proposed by Python et al. (2007). In both cases, diopsidite represent a product of metasomatism and is a new costituent of the pattern of Zermatt –Saas Zone serpentinite. If diopsidite originated as proposed by Python et al. (2007), it could imply that the

lithostratigraphic assemblage of Créton may derive from an oceanic spreading centre that subsequently was subducted during Alpine orogeneis.

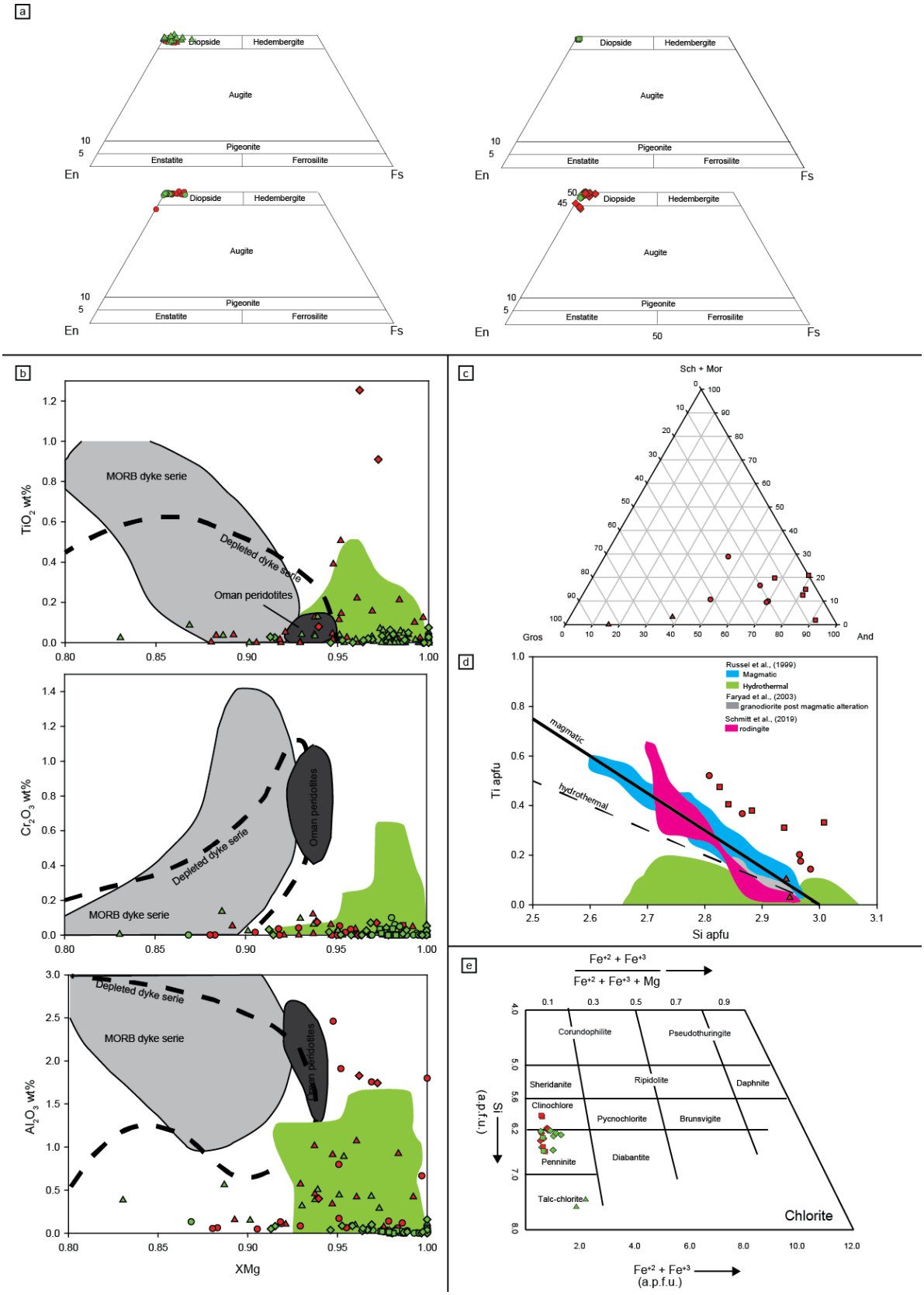

Fig. 3.1.6.4 - Mineral chemistry diagrams. a-b) clinopyroxene composition; c-d) garnet composition; e) chlorite composition. Wo-En-Fs and Chl diagrams are from Zussman et al. (1992). Symbols: triangles = diopsidite; diamonds: Chl-

schist; red: pre-D2 minerals; green synD2 minerals. In b) fields are from Python et al. (2007): green fields = Oman diopsidite Cpx composition; grey fields = Cpx compositions from MORB dyke series, black fields = Cpx compositions from Oman peridotites. In d) fields are from Faryad and Dianis (2003), Russell et al. (1999), and Schmitt et al. (2019).

	Diopsidites			Chlorite schist		
	preD2	D2	D3	preD2	D2	D3
Clinopyroxene						
Fe2	0.00-0.12	0.00-0.16	-	0.00-0.09	0.00-0.09	-
Fe3	0.00-0.15	0.00-0.16	-	0.00-0.13	0.00-0.08	-
Mg	0.82-1.04	0.76-1.02	-	0.90-1.05	0.94-1.01	-
Ca	0.88-1.00	0.89-1.00	-	0.87-1.01	0.96-1.01	-
Na	0.00-0.1	-	-	0.00-0.03	-	-
Ti	-	-	-	0.00-0.04	-	-
Magnetite						
Fe2				0.95-0.96	-	-
Fe3				1.96-1.98	-	-
Cr				-	-	-
Chlorite						
Fe tot	0.60-0.75	0.65-2.22	-	0.57-0.85	0.58-0.82	-
Mg	9.11-10.05	8.12-9.89	-	8.98-9.89	8.93-9.96	-
Al	2.86-4.28	1.19-3.41	-	3.02-3.86	2.98-3.61	-
Ilmenite						
Fe2	0.74	-	-	0.64-0.84	-	-
Fe3	0.01	-	-	0.00-0.08	-	-
Ti	0.99	-	-	0.96-1.01	-	-
Garnet						
Fe2	0.02-0.23	-	-	-	-	-
Fe3	0.60-1.30	-	-	-	-	-
Ti	0.10-0.52	-	-	-	-	-
Ca	2.95-3.03	-	-	-	-	-
Amphibole						
Si	-	-	7.89-8	8	-	-
Mg	-	-	4.33-4.61	4.64	-	-
Ca	-	-	1.86-1.99	1.93	-	-

Table 3.1.6.3 - Representative mineral analyses.

3.1.6.7 Conclusions

In Créton serpentinite, the performed multiscale structural analysis revealed the occurrence of diopsidite layers detected for the first time in the serpentinite of the Zermatt-Saas Zone. Compositional features allow to compare them to diopsidite described in Oman peridotite (Python et al., 2007). Despite the Alpine reworking, their oceanic evolution is testified by Ti-rich garnet (melanite) in preD2 clinopyroxene cores. Although diopsidite origin is still debated, the finding of diopsidite is a further proof of the oceanic-related metasomatism that affected serpentinite of the Zermatt-Saas Zone before entering the Alpine subduction zone, coherently with observations of Zanoni et al. (2016) on rodingites in nearby outcrops. Finally, as diopsidite layers are parallelised to S2 and they recorded D2, diopsidite was with that the surrounding serpentinite before syn-D2 HP re-equilibration. According to the occurrence of diopsidite itself and their geochemical characters, the rock assemblage of Créton may be a small remnant (2000 m^2 in surface) of the ocean ridge of the Alpine Tethys mechanically and thermally reworked during the Alpine subduction up to UHP conditions under a depressed thermal state.

3.2 Serpentinites of Gias Vej and related rocks: oceanic remnants at the contact between the Piemonte Zone and Sesia Lanzo Zone, upper Valle del Tesso

3.2.1 Introduction

The Piemonte Zone is widely known as an ophiolitic domain affected by the Alpine subduction. Despite this, the Piemonte Zone (PZ) is far from being completely explored. The upper Tesso Valley is located on a *triple point* among three main domains of the Western Alps, namely the Piemonte Zone, the Sesia-Lanzo Zone (SLZ), and the Lanzo Massif (LM). In particular, in the Lago Monastero-Punta Gias Vej area, the boundary between PZ and SLZ outcrops as a dense interdigitation of ophiolitic and continental material that resulted from a polyphase Alpine structural evolution (Spalla et al., 1983). Serpentinite is rarely studied as it often records complex superposition of syn-tectonic structures combined with little mineral changes in response to PT variations over large PT intervals. Nonetheless, serpentinites can contain traces of their oceanic and syn-orogenic evolution, as shown in the Zermatt-Saas Zone (Rebay et al., 2012; Luoni et al., 2018; Luoni et al., 2019). The aim of this study is to investigate the PTdt of the serpentinite of Punta Gias Vej located at the southern boundary of SLZ and PZ.

3.2.2 Geological Framework

At the southern border between SLZ and PZ (Fig. 3.2.1a, b), Punta Gias Vej (Fig. 3.2.1c) is located north of Chiaves (Monastero di Lanzo, Piemonte), in the territory of Tesso and Tessuolo valleys, not far from the triple junction of these two domains and the Lanzo Ultramafic Massif. Here, previous petro-structural analyses (Spalla et al., 1983) distinguished three different domains: an *ophiolitic domain* comprises serpentinites, metabasites (Fig. 3.2.2a), and abundant metasediments such as calcschist (Fig. 3.2.2a, b) and quartzite (Fig. 3.2.2c), a *continental affine zone* with metagranitoids, paragneisses, and continental metagabbros (Rebay and Spalla, 2001; Rebay and Messiga, 2007), and a portion characterized by the subtle alternation of ophiolitic and continental rocks of detrital or tectonic origin.

Spalla et al. (1983) recognised four groups of deformative ductile structures (F1-F4): F1 consists of rootless isoclinal folds associated with pervasive S1 foliation; F2 comprises tight to isoclinal folds with a very pervasive S2 foliation. F3 structures are the best preserved but have different style according to the rheology of the lithotype (Fig. 3.2.2a): this fact is responsible for a crenulation cleavage in calcschists and open folds in quartzites, with no axial plane foliation development. F4 structures are represented by a gentle folding with subvertical axial plane (Fig. 3.2.1c, Fig. 3.2.2b).

Only rare textural and mineral relics, such as gabbroic textures in the oceanic metabasites (Fig. 3.2.2d), and magmatic amphibole, pyroxene, and feldspar in the continental rocks, survived the subduction evolution. According to the assemblages, F1 structures developed under eclogite facies and F3 developed under greenschist facies conditions. Blueschist facies is suggested to be recorded during F2 but the relationships between deformation and mineral growth are not totally understood yet (Spalla et al., 1983).

3.2.3 Petrography and microstructures

On the ridge from Punta Gias Vej (cross-section in Fig. 3.2.1c) to the south, serpentinites and minor rodingites, calcschists with lawsonite relics, chloritoid + garnet-bearing quartzites, and eclogitic

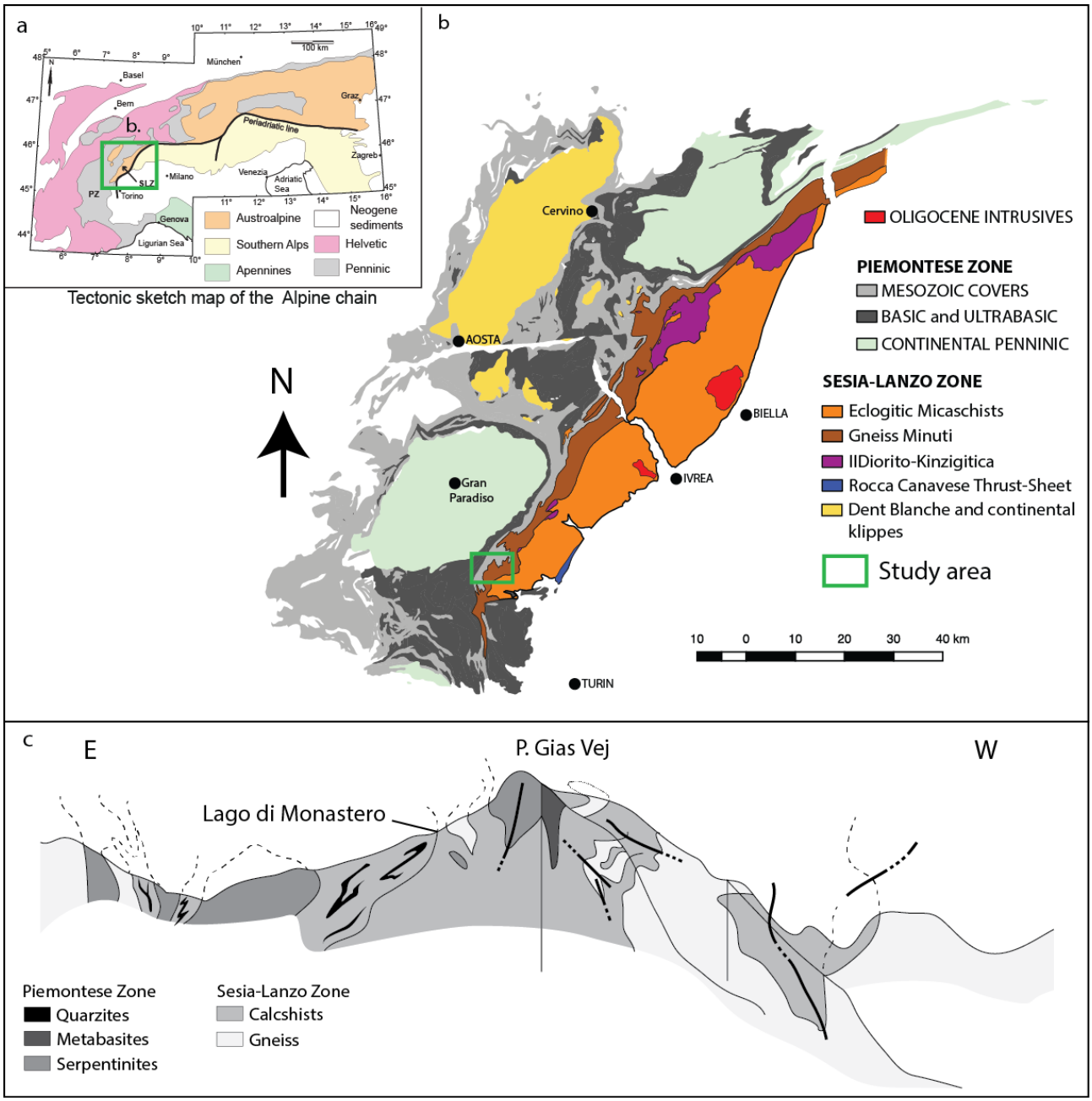

Fig. 3.2.1 - a) Simplified tectonic scheme of the Alps: SLZ = Sesia Lanzo Zone; PZ = Piemonte Zone; the green square localizes fig. 3.2.b; b) simplified tectonic scheme of the Western Alps; The studied area is in the green square; c) simplified cross-section of Gias Vej-Lago di Monastero area (after Spalla et al., 1983) showing the main lithologies and structural features.

metabasites and metagabbros are exposed (Fig. 3.2.2c, d). The dominant fabric is the S2 foliation. The studied serpentinite outcrops are in the northern slope of Punta Gias Vej (Fig. 3.2.3a). The dominant lithotype is *mylonitic serpentinite*. Four different types of layers have been distinguished within the serpentinite, according to their textural and compositional features: *Ol- Ti-Chu- Cpx- layers* (Fig. 3.2.3b, c) are ten-centimetres thick layers; their rims are crenulated by D2 but S2 is not recorded within them. *Foliated Ol-bearing layer* is green to yellow 20 cm-thick layer, strongly affected by S2 foliation (Fig. 3.2.3d). *Massive Ol-bearing layers* (Fig. 3.2.3e) are generally preserved as yellowish coarse-grained boudinaged layers wrapped by S2. *Cpx-bearing layers* constitute millimetre to few

centimetres thick whitish domains generally wrapped by and transposed into S2 foliation (Fig. 3.2.3f). In table 3.2.1, names of the analysed samples and the mineral assemblages are synthesised.

Mylonitic serpentinite is a very fine grained rock made of antigorite and minor magnetite and chlorite. It is strongly foliated by mylonitic S2 foliation. Antigorite occurs in submillimetre fibres marking the dominant foliation with their SPO. Magnetite constitutes rows of porphyroblasts aligned along the S2 foliation (Fig. 3.2.4a). Locally, S2 wraps small lenses of mylonitic serpentinite whose internal foliation S1 is at high angle with respect to S2. Millimetre aggregates of magnetite and Mg-chlorite, with rims of Fe-chlorite, are wrapped by S2 foliation and locally preserve an internal foliation S1 that is at low angle to S2 foliation. Small oval domains of antigorite and magnetite are wrapped by S2: magnetite forms globular grains, antigorite constitutes radial fibres that are rimmed by tangential antigorite fibres (Fig. 3.2.4b). S2 is often crenulated and is both parallel and at high angle with the layers described below.

Ol- Ti-Chu- Cpx- layers

The rock is not foliated and the grainsize is bimodal: antigorite, magnetite, and ilmenite form a micron- to millimetre-grained matrix, in which olivine, clinopyroxene, and Ti-clinohumite constitute up to centimetre-sized crystals. Olivine crystals are subhedral to anhedral and rounded, with undulose extinction and often rimmed by radial Atg fibres. Olivine encloses antigorite, magnetite, and Ti-clinohumite (Fig. 3.2.4c). Cracks are filled by Atg + Mag and Atg + Mag + Cal. Clinopyroxene occurs as mostly elongated anhedral crystals. It is often rimmed by radial antigorite and is locally almost completely overgrown by amphibole and calcite (Fig. 3.2.4d). Cracks are filled with calcite.

Clinopyroxene is also found as inclusions in olivine. Ti-Clinohumite crystals are up to centimetre-sized, locally with tapering lamellae. They are fractured, with Atg + Cal + Mag + Ilm fillings (Fig. 3.2.4e). Often Ti-clinohumite is rimmed by a fine matrix of Atg Mag. Locally, olivine, clinopyroxene, and Ti-clinohumite display sharp edges and they constitute polygonal aggregates partially serpentinised (Fig. 3.2.4f). BSE imaging shows that both olivine and Ti-clinohumite have discontinuous Fe-rich rims with antigorite and magnetite inclusions (Fig. 3.2.4g). Interlocking and mesh textures define the pseudomorphosed olivine and clinopyroxene shapes.

Clinopyroxene and the rock matrix are crosscut by veins filled by antigorite in the matrix, Atg + Mag ± Cal ± Ilm in olivine and Ti-clinohumite. Antigorite fibres are parallel and perpendicular to the vein in the core and rim, respectively. Calcite mostly occurs in the core of the veins, with antigorite at the rims, suggesting it has developed after antigorite. In the veins, rare fibres of talc occur and ilmenite rims magnetite.

Ol-bearing layers

The fabric of this rock is isotropic and the grainsize is fine to coarse. Centimetre- to millimetre-sized olivine crystals are aligned in ribbons wrapped by the S2 of the mylonitic serpentinite in which layers are embedded. Olivine has undulose extinction and is partially to totally overgrown by antigorite in mesh textures. Locally, around antigorite and magnetite inclusions in olivine, rims of Fe-rich olivine occur. Ti-clinohumite occurs as inclusions in olivine and locally rims olivine crystals (Fig. 3.2.4h). Anhedral Ti-clinohumite crystals also occur in the isotropic antigorite matrix. The boundary between Ol-bearing layers and the mylonitic serpentinite are evidenced by alignments of submillimetre magnetite grains and aggregates of polygonal Ti-Chu2 + Ol2 (Fig. 3.2.4i).

Foliated Ol-bearing layer

Foliated Ol-bearing layers are strongly foliated by S2 and with a submillimetre to millimetre grainsize. S2 is marked by the SPO of antigorite and olivine, alignments of magnetite grains with minor chlorite,

the elongation of oval antigorite aggregates, and by aggregates of carbonates. Antigorite aggregates are wrapped by S2; they are constituted by antigorite in mesh textures with minor magnetite. Locally the aggregates are externally rimmed by alignments of Mag ± Chl. Olivine constitutes ribbons parallel to the foliation (Fig. 3.2.5a). Larger olivine crystals have undulose extinction and fractures filled with antigorite. Towards the inclusions there are rim Fe-rich olivine rims, as it can be seen from BSE images (Fig. 3.2.4g). Smaller olivine crystals, with light or no undulose extinction, form polygonal aggregates. Mag + Chl constitute elonged aggregates. Locally S2 is marked by the SPO of submillimetre grains of olivine and antigorite, with sharp edges. Aggregates of magnesite with minor antigorite, magnetite, calcite, and dolomite are found in lenses parallel to S2. Magnesite constitutes a polygonal aggregate with interstitial Cal + Dol veinlets arranged into a regular net. Elongated magnesite grains are oriented along the S2 foliation

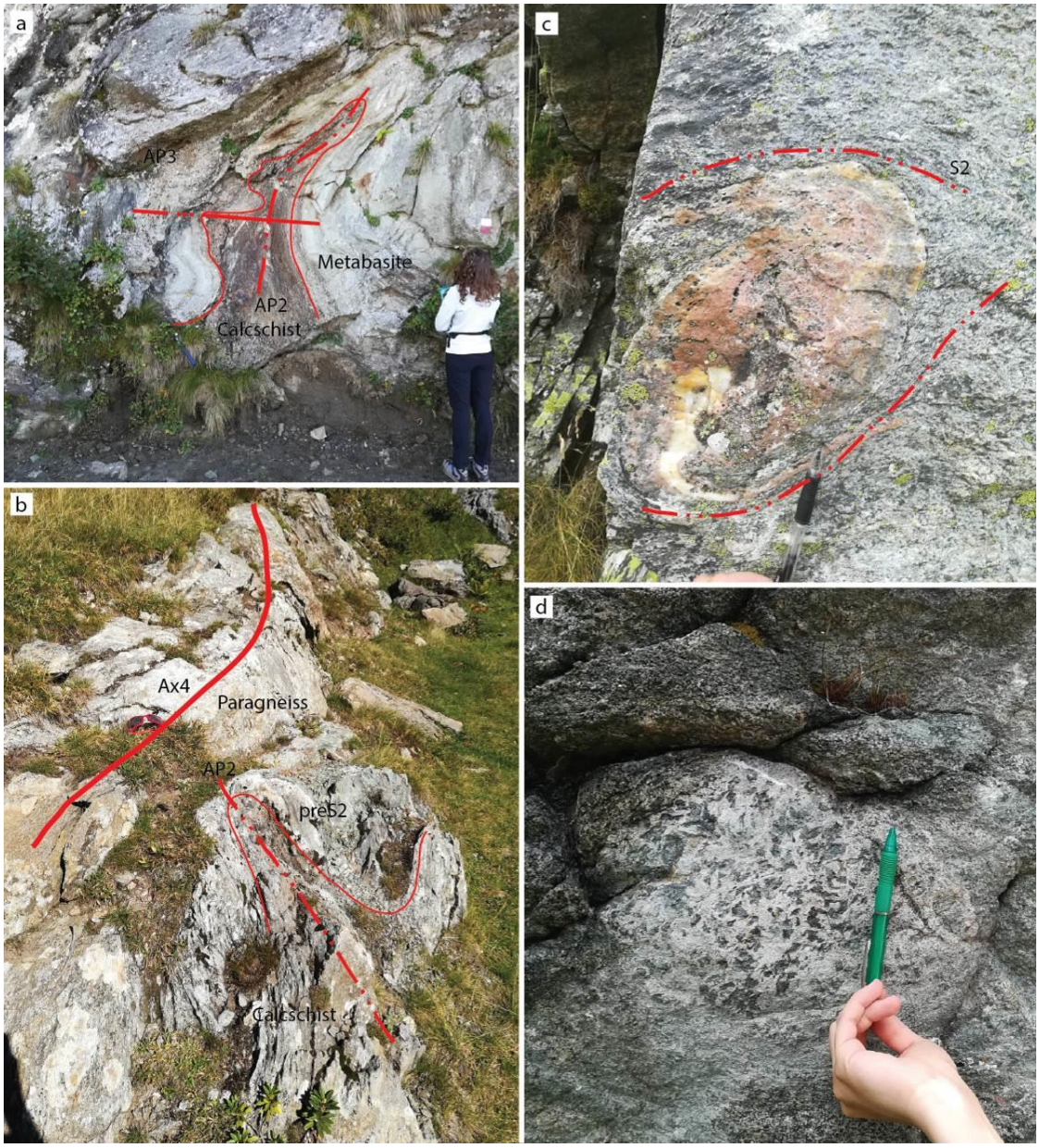

Fig. 3.2.2 - examples of structures of Gias Vej-Lago di Monastero area: a) metabasite and calcschists alternation folded by isoclinal D2 folds and D3 open folds (AP2 and AP3 respectively); b) alternation of paragneiss and calcschists, with the trace of pre-S2 foliation (thin red line) folded by D2 and D4, materialized by the traces of D2 axial plane (AP2) and D4

fold axes (Ax4); c) Grt + Qz lens wrapped by S2 foliation in quartzite; the sigmoidal pressure shadows indicate a clockwise sense of rotation d) gabbroic texture preserved in metabasite. Hammer: 70 cm; coin: 2.5 cm.

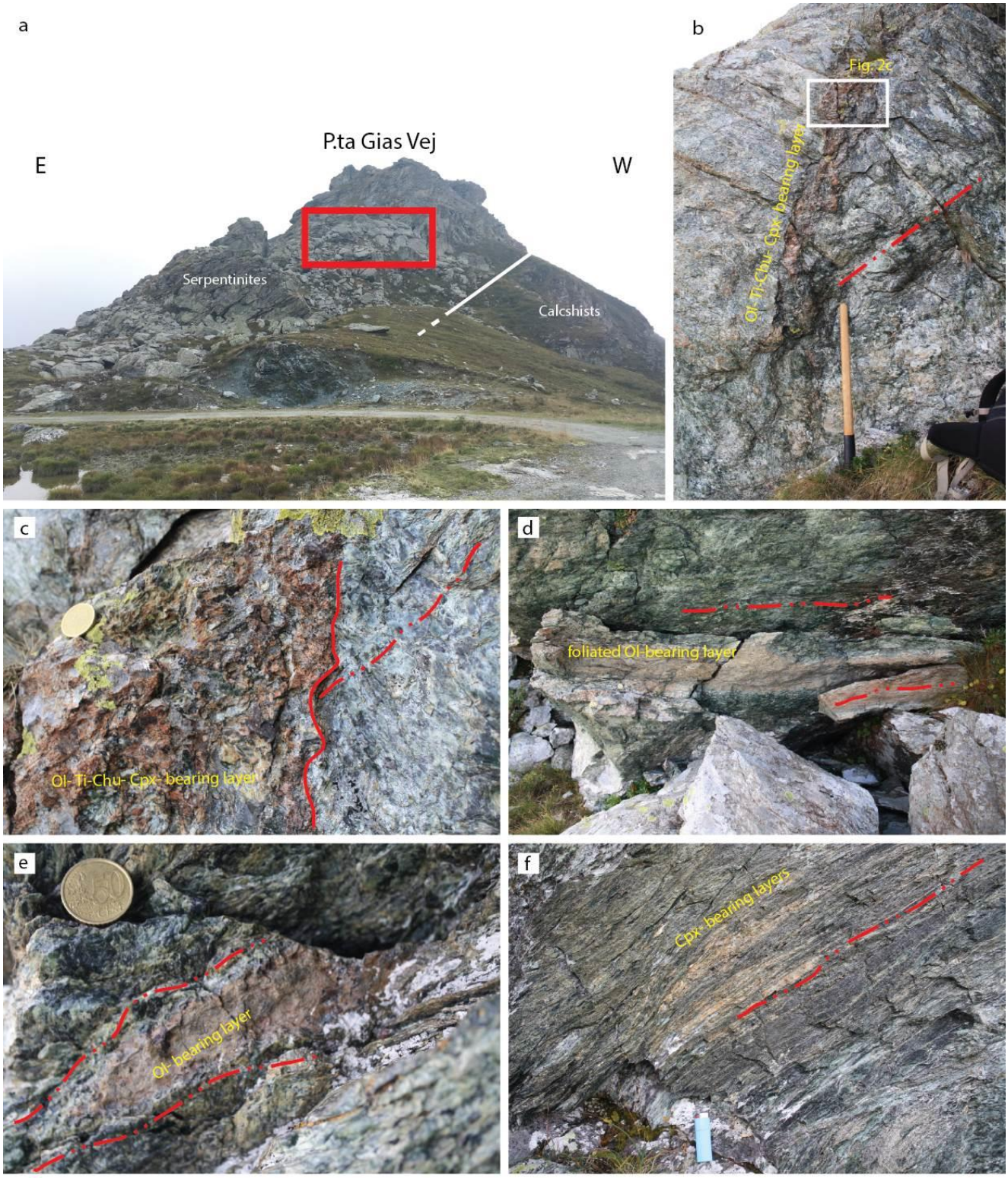

Fig. 3.2.3 - a) panoramic view of the north slope of Punta Gias Vej. Red square is the location of studied samples; b-c) Ol-Cpx- Ti-Chu layer crenulated by D2 and S2 foliation in mylonitic serpentinite; d) foliated Ol-bearing layer parallel to S2 foliation; e) Ol-bearing layer wrapped by S2 foliation; f) whitish Cpx-bearing layers folded by D2 and partially parallelised into S2 foliation.

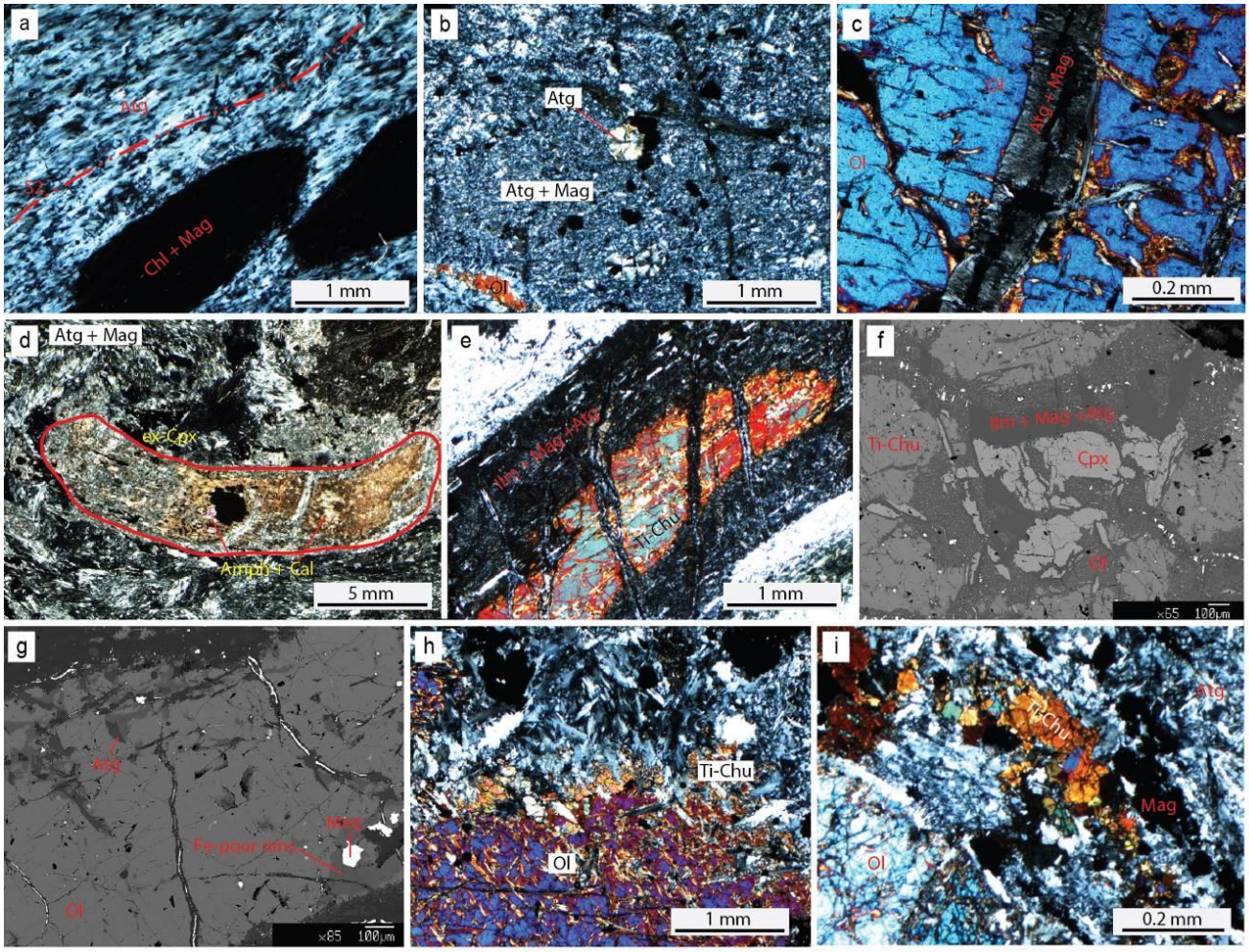

Fig. 3.2.4 - a) S2 in mylonitic serpentinite marked by Atg SPO, wrapping Chl + Mag aggregates (crossed polars); b) Non foliated matrix made of Atg + Mag in Ol- Cpx- Ti-Chu bearing layer, with radial Atg fibres (crossed polars); c) Ol with fractures filled by Atg and Mag (from an Ol- Cpx- Ti-Chu bearing layer; crossed polars); d) Cpx pseudomorphosed by Amph + Cal (Ol- Cpx- Ti-Chu bearing layer; crossed polars); e) Ti-Chu rimmed by Atg + Mag + Ilm aggregate (Ol- Cpx- Ti-Chu-bearing layer; crossed polars); f) relic polygonal texture of Ti-Chu, Ol, and Cpx. Ti-Chu is rimmed by Atg + Mag + Ilm (Ol- Cpx- Ti-Chu bearing layer; BSE image); g) Ol with dark, Fe-poor "rims" around Mag and Atg inclusions (Ol-bearing layer; BSE image); h) Ti-Chu rims of Ol crystal (Ol-bearing layer; BSE image); i) polygonal Ti-Chu aggregate between mylonitic serpentinite and an Ol-bearing layer (crossed polars).

Rock	Samples	preD1	D1 to D2		post-D2	
Mylonitic serpentinite	1		D1 Atg + Chl + Mag	D2 Atg + Mag + Chl		
Ol + Ti-Chu + Cpx layer	8; 16; 1	Ol + Ti-Chu + Cpx + Spl	Atg + Mag + Chl + Ilm + Ti-Chu + Ol		Amph	Cal
Ol layer	GV 5.8	Atg + Ol + Ti-Chu + Mag		Ol + Atg + Mag +Ti-Chu		
Foliated Ol layer	GV 3.4		D1 Ol + Atg + Chl + Cr-Mag	D2 (S2) Ol + Atg + Chl + Mag Mgs Cal	Dol	
Cpx layer	GV 2.2	Cpx	D1 (S1) Chl + Cpx + Atg + Mag		Cal + Amph	
Chl-schist	2527		Cpx + Chl	S2 Cpx + Chl + Rt	D3 Amph + Ttn	Amph

Table 3.2.1 - Synthesis of the mineral assemblages in the analysed samples.

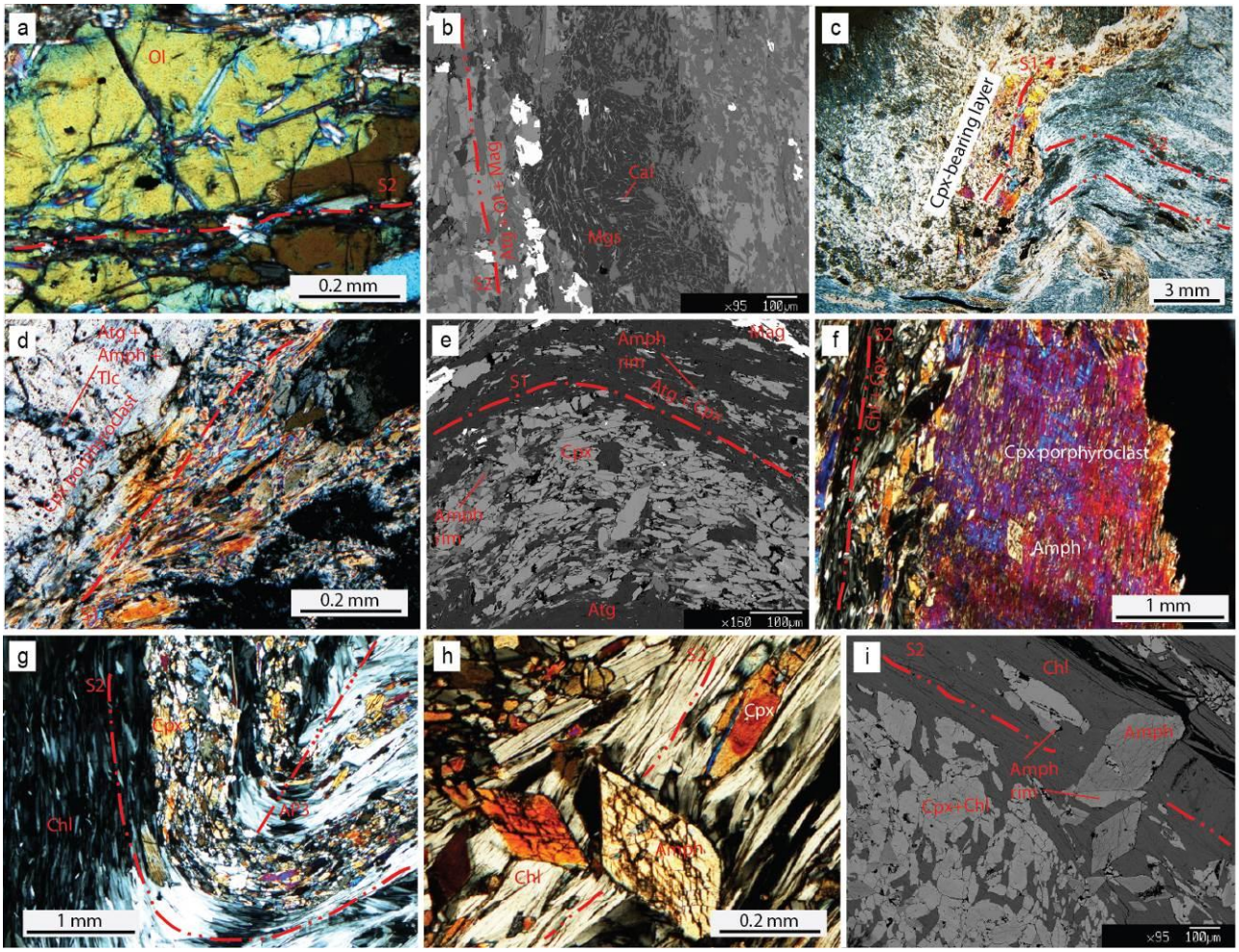

Fig. 3.2.5 - a) Ol crystal from a ribbon in foliated Ol-bearing layers (crossed polars); b) Mgs aggregate wrapped by Atg + Ol + Mag bearing S2 foliation (foliated Ol-bearing layer; crossed polars); c) S1 foliation in Cpx-bearing layer; S2 is at high angle respect to S1 foliation (crossed polars; d) Cpx porphyroclast, with micro-fractures filled by Amph + Atg + Tlc, and wrapped by S1 foliation (Cpx-bearing layer, crossed polars); e) S1 foliation in Cpx-bearing layer marked by Atg + Cpx SPO (BSE image); f) Cpx porphyroclast including euhedral Amph and wrapped by S2 (Chl + Cpx) (Chl-schist; crossed polars); g) S2 foliation underlined by Chl and Cpx SPO (in Chl-rich layers and Cpx-rich layers) folded by D3 (crossed polars); h) euhedral Amph crosscutting S2 foliation in Chl-schist (crossed polars); i) Amph rims overgrowing S2 Cpx and euhedral Amph (BSE).

defined by Ol + Atg, that wraps the aggregate. Dolomite mostly rims calcite. In these magnesite-bearing aggregates antigorite and calcite SPO is parallel to S2 (Fig. 3.2.5b).

Cpx-bearing layers

Cpx-bearing layers are millimetre- to centimetre-thick and are embedded in the mylonitic serpentinite. They are made of clinopyroxene, antigorite, chlorite, amphibole, and minor oxides. Layers are folded by D2 and are both parallel and at high angle with respect to S2 in the embedding serpentinite. They preserve a different generation of structures predating D2 but they do not record S2 (Fig. 3.2.5c). Cpx-bearing layers preserve an S1 foliation, mostly marked by fine grained clinopyroxene, chlorite, and magnetite, that wraps rare millimetre-sized pre-D1 clinopyroxene porphyroclasts elongated parallel to S1 (Fig. 3.2.5d). They are strongly deformed, as it can be seen by the kinking of cleavages and undulose extinction. Syn-D1 fractures are filled by amphibole, talc, and antigorite fibres perpendicular to the fractures' rim. Clinopyroxene1 grains are submillimetre, with no inclusions and undulose extinction, and they are often rimmed by Amph. SPO of submillimetre antigorite1 fibres marks S1

foliation. Contacts between clinopyroxene1 and antigorite1 are either sharp or wriggly. Magnetite1 grains are parallel to S1 foliation (Fig. 3.2.5e). Locally layers are not foliated and are made by a very fine isotropic matrix of antigorite, magnetite, and ilmenite. Rare post-D1- pre-D2 rootless microfolds are preserved.

Chlorite schist

Chlorite schist is a mylonitic fine grained rock and S2 foliation is the dominant fabric. S2 is marked by the alternation of Cpx-rich and minor Chl-rich layers, and by the SPO of clinopyroxene, chlorite and amphibole. Millimetre-sized clinopyroxene porphyroclasts are wrapped by S2. They are anhedral and elongated parallel to S2, strongly deformed, with undulose extinction and fractures. Chlorite overgrows clinopyroxene along its cleavages. Along major fractures and rims, new clinopyroxene2 grains occur (Fig. 3.2.5f), in the form of 10 to 100 µm sized grains with no inclusions and undulose extinction. Clinopyroxene2 grains rim clinopyroxene porphyroclasts, locally filling fractures, and are oriented parallel to S2, with sharp boundaries with the chlorite marking S2. Chlorite forms elongated flakes that constitute layers together with various amounts of clinopyroxene (Fig. 3.2.5f). Post-D2 Amphibole occurs in three main microstructural domains: i) as skeletal inclusions in clinopyroxene porphyroclasts, where clinopyroxene cleavages are crosscut by amphibole crystals and clinopyroxene is preserved in amphibole core; ii) as crystals sharply crosscutting S2 in both Cpx-rich and Chl-rich layers. In this last instance, its elongation is generally perpendicular to S2. Furthermore, clinopyroxene relic inclusions are often found in the cores of these amphibole (ii). Finally, Amph (iii) forms rims of clinopyroxene marking S2 and rims of euhedral amphibole (Fig. 3.2.5i). Rare anhedral and submillimetre grains of rutile underline S2 foliation and are rimmed by titanite.

3.2.4 Mineral Chemistry

WDS mineral analyses were acquired from different microstructural sites by using an electron microprobe (JEOL 8200 Super Probe) operating at the "A. Desio" Earth Science Department of Milan University. A 15 keV accelerating voltage and a beam current of 15nA were used. Natural silicates were used as standards and matrix corrections were calculated using the ZAF procedure. Mineral formulae were recalculated on the basis of the following number of oxygen atoms: 4 for olivine, 6 for clinopyroxene, 116 for serpentine, 28 for chlorite, 4 for spinels (Ferracutti et al., 2015), 3 for ilmenite, and 24 for amphibole (Locock, 2014). Ti-clinohumite was recalculated on the basis 13 cations. Ilmenite Fe^{3+} was recalculated according to Droop (1987). Representative analyses of minerals are in table 3.2.2.

Two compositional clusters in the Fe vs. Mg diagram (Fig. 3.2.6a) indicate that *antigorite* compositional variations are linked to some specific micro-domains rather than to the lithologies: Fe-rich antigorite is found mostly at the cores of veins and aggregates overgrowing Ti-clinohumite, clinopyroxene, and olivine (Fig. 3.2.6b). Fe-poor antigorite, which is the first constituent of serpentinite matrix, is usually richer in Si and shows the widest variation of Al (up to 0.14 apfu) with average Al contents higher (0.06-0.14 apfu) than those of Fe-rich Atg.

Olivine composition (Fig. 3.2.6c) is extremely fosteritic (up to 99% Fo). The Fe-Mg diagram highlight the compositional differences corresponding to different microstructural site: generally, X_{Mg} varies between 0.90 and 0.92 but Fe-poor rims show $X_{Mg} > 0.96$. These variations are consistent in all the lithotypes. Mn content is lower in foliated Ol-bearing layers (up to 0.5 wt% MnO) than in all other lithologies.

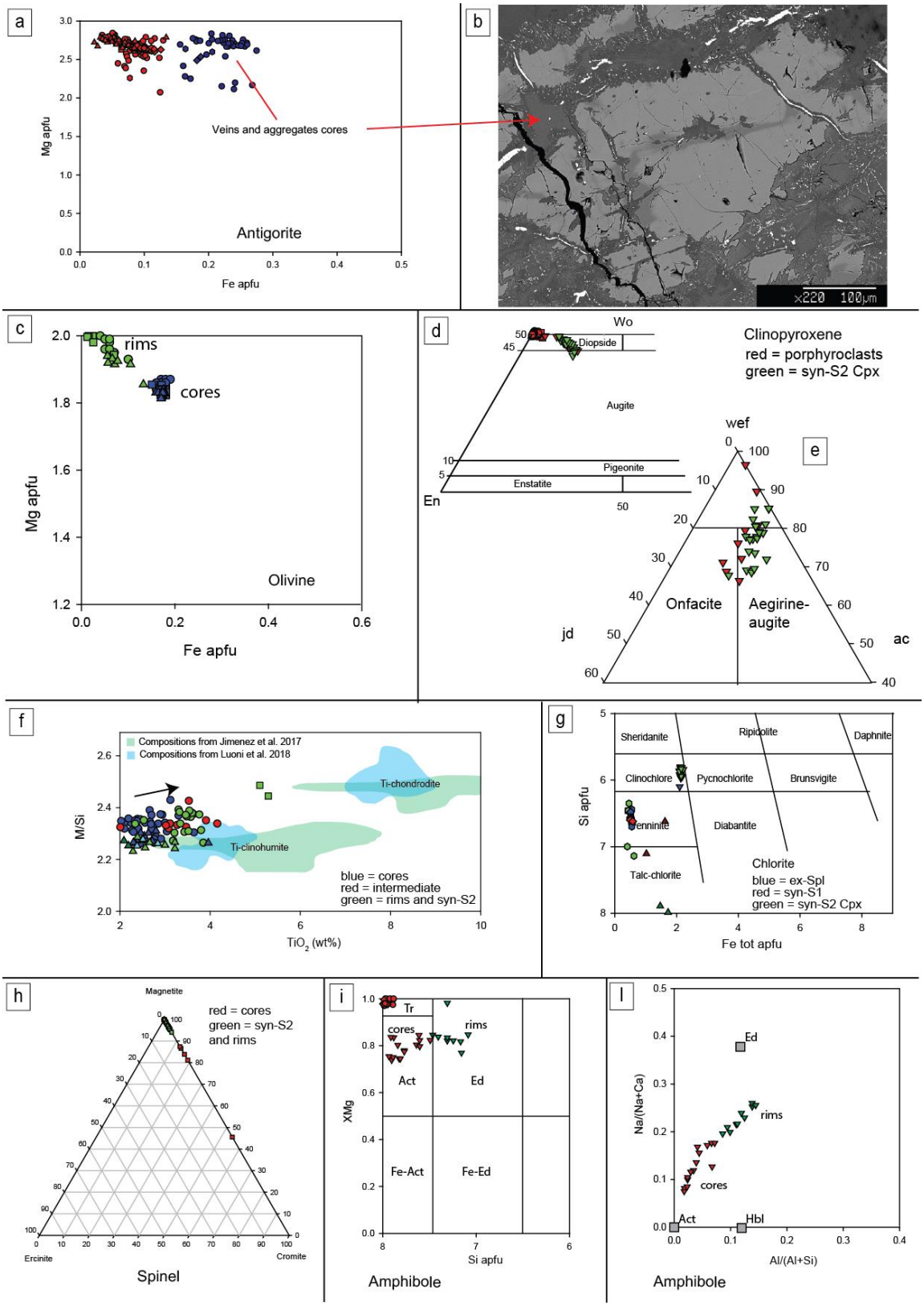

Fig. 3.2.6 - Mineral chemistry diagrams. Legend: hexagons = mylonitic serpentinite; circle = Ol- Cpx- Ti-Chu bearing serpentinite; square = foliated Ol-bearing layers; triangle up = Ol-bearing layers; diamond = Cpx-bearing layer; triangle down = Chl-schist. a) Mg vs. Fe in antigorite; b) Fe-rich antigorite in antigorite veins (BSE image); c) Mg vs. Fe in olivine; d-e) clinopyroxene classification with fields from (Zussman et al., 1992); f) TiO_2 vs. M/Si in Ti-clinohumite; g) chlorite classification (Fe tot. vs. Si) with fields from (Zussman et al., 1992); h) spinel classification (Zussman et al., 1992); i-l) Si vs. X_{Mg} and Al/(Al+Si) vs. Na/(Na+Ca) in amphibole (Zussman et al., 1992).

Table 3.2.2 - Representative mineral analyses.

	Amphibole				
Rock	Mylonitic serpentinite		Chl-schist		Cpx-beraing
Texture	ex cpx	ex cpx	matrix	rim	rim
SiO_2	50.82	54.06	54.22	56.60	58.90
TiO_2	0.05	0.02	0.06	0.00	0.00
Al_2O_3	6.15	3.25	3.31	1.13	0.01
Cr_2O_3	0.39	0.10	0.11	0.25	0.01
FeO	10.12	8.32	7.76	6.99	0.97
MnO	0.05	0.07	0.07	0.13	0.04
MgO	16.36	18.34	18.72	19.62	23.91
CaO	12.23	12.43	12.89	12.86	14.23
Na_2O	2.01	1.47	1.03	0.66	0.02
K_2O	0.11	0.05	0.07	0.04	0.03
NiO	0.03	0.07	0.06	0.03	0.03
Sum	97.84	98.19	98.31	98.31	98.15
FeO	0.95	8.00	7.48	6.98	0.97
Fe_2O_3	0.00	0.35	0.31	0.02	0.00
New Sum	100.05	100.34	100.47	100.45	100.35
T (ideally 8 apfu)					
Si	8.00	7.61	7.60	7.88	7.99
Al	0.00	0.39	0.40	0.12	0.00
Ti	0.00	0.00	0.00	0.00	0.00
Fe^{3+}	0.00	0.00	0.00	0.00	0.00
T subtotal	8.00	8.00	8.00	8.00	7.99
C (ideally 5 apfu)					
Ti	0.00	0.00	0.01	0.00	0.00
Al	0.01	0.15	0.15	0.07	0.00
Cr	0.00	0.01	0.01	0.03	0.00
Fe^{3+}	0.00	0.04	0.03	0.00	0.00
Ni	0.01	0.01	0.01	0.00	0.00
Mn^{+3}	0.00	0.00	0.00	0.02	0.00
Fe^{2+}	0.09	0.94	0.88	0.81	0.11
Mg	4.89	3.85	3.91	4.07	4.83
XMg	0.98	0.80	0.82	0.83	0.98
C subtotal	5.00	5.00	5.00	5.00	4.95
B (ideally 2 apfu)					
Mn^{2+}	0.02	0.01	0.01	0.00	0.00
Fe^{2+}	0.01	0.00	0.00	0.00	0.00
Mg	0.00	0.00	0.00	0.00	0.00
Ca	1.95	1.88	1.94	1.92	2.00
Na	0.02	0.11	0.05	0.08	0.00
B subtotal	2.00	2.00	2.00	2.00	2.00
A (from 0 to 1 apfu)					
Ca	0.00	0.00	0.00	0.00	0.07
Na	0.00	0.29	0.23	0.10	0.00
K	0.00	0.01	0.01	0.01	0.01
A subtotal	0.00	0.30	0.24	0.10	0.08
O (non-W)	22.00	22.00	22.00	22.00	22.00
W (ideally 2 apfu)					
OH	2.00	2.00	2.00	2.00	2.00
W subtotal	2.00	2.00	2.00	2.00	2.00
Sum T,C,B,A	15.00	15.00	15.30	15.24	15.02

	Antigorite					
Rock	Mylonitic serpentinite	Ti-Chu- Ol- Cpx bearing		Foliated Ol- bearing		Ol-bearing
Texture	S2	Matrix	Matrix	S2	ex Ol	Matrix
SiO_2	41.14	40.84	45.31	41.27	43.56	42.11
TiO_2	0.02	0.08	0.00	0.00	0.02	0.00
Al_2O_3	1.48	1.65	0.08	2.48	0.98	1.89
Cr_2O_3	0.05	0.09	0.03	1.28	0.11	0.40
FeO	4.16	5.22	1.74	2.86	1.95	1.96
MnO	0.07	0.09	0.09	0.01	0.06	0.08
MgO	37.53	36.99	39.42	38.27	39.56	39.18
CaO	0.03	0.03	0.02	0.01	0.01	0.00
Na_2O	0.00	0.04	0.00	0.03	0.00	0.00
K_2O	0.01	0.02	0.01	0.00	0.00	0.01
NiO	0.20	0.32	0.21	0.13	0.30	0.12
Sum	84.69	85.37	86.91	86.33	86.55	85.74
116 ox.						
Si	1.94	1.93	2.04	1.90	1.98	1.94
Al	0.08	0.09	0.00	0.13	0.05	0.10
Ti	0.00	0.00	0.00	0.00	0.00	0.00
Cr	0.00	0.00	0.00	0.00	0.00	0.01
Fe^{2+}	0.16	0.21	0.07	0.11	0.07	0.08
Mn	0.00	0.00	0.00	0.00	0.00	0.00
Mg	2.64	2.60	2.65	2.63	2.68	2.69
Ca	0.00	0.00	0.00	0.00	0.00	0.00
Na	0.00	0.00	0.00	0.00	0.00	0.00
K	0.00	0.00	0.00	0.00	0.00	0.00
Ni	0.01	0.01	0.01	0.00	0.01	0.00

	Carbonates			
Rock	Ti-Chu- Ol- Cpx- bearing		Foliated Ol- bearing	
Mineral	Cal	Mgs	Cal	Dol
Texture	ex cpx	aggregate	aggregate	aggregate
SiO_2	0.06	0.00	0.04	0.06
TiO_2	0.10	0.01	0.04	0.03
Al_2O_3	0.02	0.03	0.01	0.00
Cr_2O_3	0.02	0.00	0.00	0.03
FeO	0.59	0.24	0.02	0.04
MnO	0.51	0.38	0.00	0.00
MgO	1.38	47.89	0.05	18.57
CaO	57.28	0.61	65.19	45.08
Na_2O	0.02	0.00	0.00	0.06
K_2O	0.00	0.01	0.01	0.00
NiO	0.04	0.02	0.00	0.01
Sum	60.02	49.18	65.37	63.87

	Talc	
Rock	Ti-Chu- Ol- Cpx- bearing	Cpx- bearing
Texture	Vein	Vein
SiO_2	51.07	62.60
TiO_2	0.04	0.00
Al_2O_3	0.00	0.38
Cr_2O_3	0.06	0.00
FeO	2.41	1.00
MnO	0.07	0.01
MgO	35.98	30.34
CaO	0.04	0.02
Na_2O	0.00	0.02
K_2O	0.02	0.14
NiO	0.26	0.00
Sum	89.95	94.52

	Titanite and Rutile		
Rock	Chl-schist		
Mineral	Rt	Ttn	
Texture	S2	Rim	
SiO_2	0.00	30.80	
TiO_2	98.57	38.79	
Al_2O_3	0.00	0.62	
Cr_2O_3	0.51	0.16	
FeO	0.31	0.31	
MnO	0.00	0.00	
MgO	0.00	0.00	
CaO	0.17	29.79	
Na_2O	0.03	0.01	
K_2O	0.01	0.00	
NiO	0.00	0.00	
Sum	99.59	100.49	

	Ti-clinohumite				
Rock	Ti-Chu- Ol- Cpx- bearing		Foliated Ol- bear	Ol-bearing	
Texture	Core	Rim	S2	Core	Rim
SiO_2	37.10	36.70	34.54	36.90	37.31
TiO_2	3.64	2.53	5.10	2.54	2.66
Al_2O_3	0.00	0.00	0.00	0.00	0.01
Cr_2O_3	0.09	0.02	0.06	0.00	0.00
FeO	7.90	8.57	2.82	7.79	5.35
MnO	0.52	0.56	0.67	0.46	0.61
MgO	50.60	51.27	52.94	50.66	51.88
CaO	0.01	0.02	0.02	0.01	0.02
Na_2O	0.01	0.00	0.00	0.00	0.00
K_2O	0.00	0.00	0.01	0.00	0.00
NiO	0.19	0.32	0.13	0.23	0.20
Sum	100.06	100.01	96.29	98.58	98.04
13 cat.					
Si	3.93	3.88	3.73	3.95	3.98
Ti	0.29	0.20	0.41	0.20	0.21
Al	0.00	0.00	0.00	0.00	0.00
Cr	0.01	0.00	0.00	0.00	0.00
Fe^{2+}	0.70	0.76	0.25	0.70	0.48
Mn	0.05	0.05	0.06	0.04	0.06
Mg	8.00	8.08	8.52	8.09	8.25
Ca	0.00	0.00	0.00	0.00	0.00
Na	0.00	0.00	0.00	0.00	0.00
K	0.00	0.00	0.00	0.00	0.00
Ni	0.02	0.03	0.01	0.02	0.02
Sum	13.00	13.00	13.00	13.00	13.00

Table 3.2.2 - Representative mineral analyses.

Chlorite

Rock	Mylonitic serpentinite	Foliated Ol- bearing	Chl-schist	Cpx- bearing	
Texture	Ex spl	S2	S2	S1	S1
SiO_2	34.33	37.47	29.49	34.24	34.66
TiO_2	0.00	0.10	0.07	0.00	0.02
Al_2O_3	12.02	5.58	18.16	12.11	12.23
Cr_2O_3	1.11	0.50	1.29	1.07	1.16
FeO	3.29	3.90	12.89	3.17	3.11
MnO	0.02	0.00	0.03	0.02	0.07
MgO	35.44	38.92	25.35	34.71	34.76
CaO	0.01	0.00	0.03	0.02	0.00
Na_2O	0.00	0.01	0.01	0.00	0.00
K_2O	0.01	0.01	0.02	0.02	0.02
NiO	0.10	0.05	0.24	0.05	0.13
Sum	86.33	86.54	87.59	85.41	86.17
28 ox.					
Si	6.54	7.14	5.83	6.58	6.60
Ti	0.00	0.01	0.01	0.00	0.00
Al	2.70	1.25	4.23	2.74	2.75
Cr	0.17	0.08	0.20	0.16	0.17
Fe^{+r}	0.52	0.62	2.13	0.51	0.50
Mn	0.00	0.00	0.01	0.00	0.01
Mg	10.07	11.06	7.48	9.95	9.87
Ca	0.00	0.00	0.01	0.00	0.00
Na	0.00	0.00	0.00	0.00	0.00
K	0.00	0.00	0.01	0.00	0.00
Ni	0.02	0.01	0.04	0.01	0.02
Sum	20.03	20.18	19.94	19.97	19.93

Spinel

Rock	Mylonitic serpentinite	Ti-Chu- Ol- Cpx- bearing	Foliated Ol- bearing		Cpx- bearing	
Mineral	Mag	Mag	Cr-mag	Mag	Mag	Mag
Texture	S2	Matrix	Core	Rim	Matrix	Matrix
SiO_2	0.00	0.07	0.02	0.05	0.06	0.06
TiO_2	0.00	0.00	0.10	0.00	0.04	0.12
Al_2O_3	0.02	0.00	0.03	0.02	0.00	0.00
Cr_2O_3	0.36	0.03	8.92	2.24	1.35	0.03
FeO	93.28	94.46	75.32	83.18	92.42	90.86
MnO	0.26	0.15	1.70	0.85	0.10	0.69
MgO	0.24	0.23	8.54	6.81	0.08	3.10
CaO	0.00	0.01	0.00	0.06	0.03	0.00
Na_2O	0.03	0.00	0.00	0.00	0.08	0.00
K_2O	0.00	0.00	0.00	0.00	0.00	0.00
NiO	1.00	1.74	0.54	0.75	0.47	0.73
Sum	95.19	96.69	95.17	93.97	94.63	95.58
Fe_2O_3	70.33	71.51	65.43	70.97	68.73	72.17
FeO	30.00	30.11	16.44	19.32	30.58	25.92
Cations						
Si	0.00	0.00	0.00	0.00	0.00	0.00
Ti	0.00	0.00	0.00	0.00	0.00	0.00
Al	0.00	0.00	0.00	0.00	0.00	0.00
Cr	0.01	0.00	0.25	0.06	0.04	0.00
$Fe3^{+}$	1.99	1.99	1.74	1.93	1.96	1.99
Fe^{+r}	0.94	0.93	0.49	0.58	0.97	0.79
Mn	0.01	0.01	0.05	0.03	0.00	0.02
Mg	0.01	0.01	0.45	0.37	0.01	0.17
Ca	0.00	0.00	0.00	0.00	0.00	0.00
Na	0.00	0.00	0.00	0.00	0.01	0.00
K	0.00	0.00	0.00	0.00	0.00	0.00
Ni	0.03	0.05	0.02	0.02	0.01	0.02
Sum	3.00	3.00	3.00	3.00	3.00	3.00

Clinopyroxene

Rock	Ti-Chu- Ol- Cpx- bearing	Chl-schist		Cpx- bearing	
Texture	Core	porphyroclast	S2	S1	
SiO_2	54.73	55.26	53.70	55.03	
TiO_2	0.00	0.02	0.00	0.02	
Al_2O_3	0.02	2.18	0.86	0.00	
Cr_2O_3	0.11	0.21	0.16	0.00	
FeO	0.73	6.59	6.78	1.17	
MnO	0.04	0.00	0.12	0.14	
MgO	18.18	13.05	13.65	17.67	
CaO	26.04	20.73	22.64	26.86	
Na_2O	0.06	2.92	2.04	0.02	
K_2O	0.02	0.01	0.00	0.00	
NiO	0.07	0.07	0.05	0.06	
Sum	100.00	101.05	100.00	100.97	
4 cat. 6 ox.					
Si	1.98	1.99	1.97	1.98	
Ti	0.00	0.00	0.00	0.00	
ALIV	0.00	0.01	0.03	0.00	
ALVI	0.00	0.09	0.00	0.00	
Cr	0.00	0.01	0.00	0.00	
$Fe3^{+}$	0.02	0.12	0.17	0.04	
Fe^{+r}	0.00	0.08	0.04	0.00	
Mn	0.00	0.00	0.00	0.95	
Mg	0.98	0.70	0.75	0.95	
Ca	1.01	0.80	0.89	1.03	
Na	0.00	0.20	0.14	0.00	
K	0.00	0.20	0.14	0.00	
Ni	0.00	0.00	0.00	0.00	
Sum	4.00	4.00	4.00	4.00	
FeO	0.00	2.64	1.26	0.00	
Fe_2O_3	0.82	4.39	6.14	1.30	
New sum	100.08	101.49	100.62	101.10	

Olivine

Rock	Ti-Chu- Ol- Cpx- bearing		Foliated Ol- bearing		Ol-bearing	
Texture	Core	Rim	Core	S2	Core	Rim
SiO_2	40.98	41.28	40.81	41.92	41.04	40.65
TiO_2	0.07	0.02	0.03	0.00	0.00	0.00
Al_2O_3	0.01	0.00	0.01	0.02	0.01	0.01
Cr_2O_3	0.05	0.05	0.00	0.05	0.00	0.02
FeO	8.12	3.44	7.42	1.23	7.85	5.21
MnO	0.47	0.53	0.38	0.31	0.40	0.53
MgO	51.39	54.85	51.27	57.17	50.58	53.30
CaO	0.02	0.00	0.02	0.00	0.04	0.01
Na_2O	0.00	0.01	0.00	0.00	0.00	0.02
K_2O	0.00	0.01	0.00	0.00	0.02	0.00
NiO	0.22	0.18	0.21	0.07	0.39	0.41
Sum	101.33	100.37	100.16	100.76	100.32	100.15
4 ox.						
Si	0.99	0.98	0.99	0.98	1.00	0.98
Ti	0.00	0.00	0.00	0.00	0.00	0.00
Al	0.00	0.00	0.00	0.00	0.00	0.00
Cr	0.00	0.00	0.00	0.00	0.00	0.00
Fe^{+r}	0.16	0.07	0.15	0.02	0.16	0.11
Mn	0.01	0.01	0.01	0.01	0.01	0.01
Mg	1.84	1.95	1.85	2.00	1.83	1.92
Ca	0.00	0.00	0.00	0.00	0.00	0.00
Na	0.00	0.00	0.00	0.00	0.00	0.00
K	0.00	0.00	0.00	0.00	0.00	0.00
Ni	0.00	0.00	0.00	0.00	0.01	0.01
Sum	3.01	3.02	3.01	3.02	3.00	3.02

Ilmenite

Rock	Ti-Chu- Ol- Cpx- bearing	Cpx- bearing
texture	Matrix	Matrix
SiO_2	2.42	0.06
TiO_2	48.58	51.85
Al_2O_3	0.02	0.00
Cr_2O_3	0.04	0.02
FeO	27.61	32.85
MnO	17.37	13.54
MgO	2.67	0.40
CaO	0.02	0.01
Na_2O	0.02	0.01
K_2O	0.00	0.00
NiO	0.03	0.03
Sum	98.78	98.77
FeO	24.78	32.85
Fe2O3	3.14	0.00
3 ox		
Si	0.06	0.00
Ti	0.91	0.99
Al	0.00	0.00
Cr	0.00	0.00
Fe^{+r}	0.58	0.70
Mn	0.37	0.29
Mg	0.10	0.02
Ca	0.00	0.00
Na	0.00	0.00
K	0.00	0.00
Ni	0.00	0.00
Sum	2.02	2.00

Clinopyroxene in Cpx-bearing layers and in Ol- Ti-Chu- Cpx-bearing layers clinopyroxene is diopside (Fig. 3.2.6d), extremely rich in Ca (0.99-1.04) and Mg (0.93-1.00 apfu); Ti is low (0-0.8 wt% TiO_2). In Chlorite-schist, clinopyroxene porphyroclasts compositions partially fall in the Omphacite field while S2 Cpx shows diopsidic to Aegirine-Augitic compositions (Fig. 3.2.6e). Ti is always very low (<0.8 wt% TiO_2).

Ti-clinohumite cores are richer in Fe (0.7-0.8 apfu) and poorer in Ti and Mg than rims. Rims around inclusions are poorer in Fe (0.15-0.5 apfu) and with higher content of Mg and Ti than Ti- clinohumite cores. Ti-clinohumite from foliated Ol-bearing layers has M/Si ratio similar to Ti-chondrodite M/Si from González-Jiménez et al. (2017) and Luoni et al. (2018) (Fig. 3.2.6f), whereas TiO_2 content is typical of Ti-Clinohumite. Ti-clinohumite is always F-free.

Chlorite is penninite in all the lithotypes except for Chl-schist where it is clinochlore (Fig. 3.2.6g). In this latter case, Fe and Mg contents are constant in chlorite occupying different micro-domains as clinopyroxene porphyroclasts inclusions and in S2 foliation, whereas Si is usually lower (< 6 apfu) in chlorite marking S2 foliation.

Pure magnetite is the dominant *spinel* (Fig. 3.2.6h) in Ol- Ti-Chu- Cpx-bearing layers and Ol-bearing layers. In foliated Ol-bearing layers spinels have Cr-rich cores and syn-S2 magnetite rims.

Amphibole is tremolite in Cpx-bearing layers and in Ol-, Cpx- and Ti-Chu-bearing layers (Fig. 3.2.6i). In Chl-Schist, all the euhedral amphibole crystals consist of actinolite and the amphibole rims are edenite (Fig. 3.2.6i and 6l).

3.2.5 Metamorphic Evolution

The combination of microstructural and compositional analyses allowed defining successive mineral assemblages indicating changing of physical conditions of metamorphism. In fig. 3.2.7, experimental stability fields for peridotites (Poli and Schmidt, 2002), stability curves for Ti-clinohumite (Fig. 3.2.7a and 7b; López Sánchez-Vizcaíno et al., 2009; Nishio et al., 2019) and curves from pseudosections in fig. 3.2.7c (see Fig. 3.1.4.7) are superposed to define qualitatively the PT conditions registered by Gias Vej serpentinites, by comparing similar assemblages and lithologies. Black curves are from the schematic petrogenetic grid of Poli and Schmidt (2002) for a lherzolite composition at H_2O saturated conditions. Antigorite occurs at low T up to 3.5 GPa and at T < 680 °C. Olivine is always stable. At high T, clinopyroxene is stable above 2.3 GPa, while at lower T is stable up to very high P. At T > 680 °C, amphibole is stable up to 2.3 GPa and talc up to 1.5 GPa at T < 670 °C. Ortopyroxene occurs at T > 680 °C and P > 2.3 GPa. Blue curves are from the pseudosection calculated for Crèton Cpx-rich serpentinite (see Fig. 3.1.4.7) using the composition SiO_2 = 42.56, Al_2O_3 = 184, CaO = 1.84, MgO = 35.10, FeO = 4.63 in the CFMASH system. In this pseudosection the horizontal divariant field with Di - Atg - Chl - Mag, separates two trivariant fields: at lower temperatures (<650°C), a field where actinolite is stable at P < 1.6 GPa, and a field where T is stable with Di + Atg + Chl (and Mag) for P > 1.7 GPa. Green curves represent Ti-clinohumite stability field in ultramafic rocks from López Sánchez-Vizcaíno et al. (2009). Red curves from Nishio et al. (2019) represent Ti-Chu destabilisation in Ti-Chu + Ol + Ilm and Ol + Ilm + H_2O at decreasing P and T.

In the *Ol- Ti-Chu- Cpx-bearing layers* the preD2 Ol + Ti-Chu + Cpx + Spl assemblage is followed by the pre to syn-D2 Atg + Mag + Chl + Ilm + Ti-Chu + Ol with the pseudomorphosis of Ti-clinohumite by Ilm + Atg aggregates, and then, by the tremolite occurrence at the expenses of clinopyroxene. As shown in fig. 3.2.7a, this succession can correspond to a decompression from the

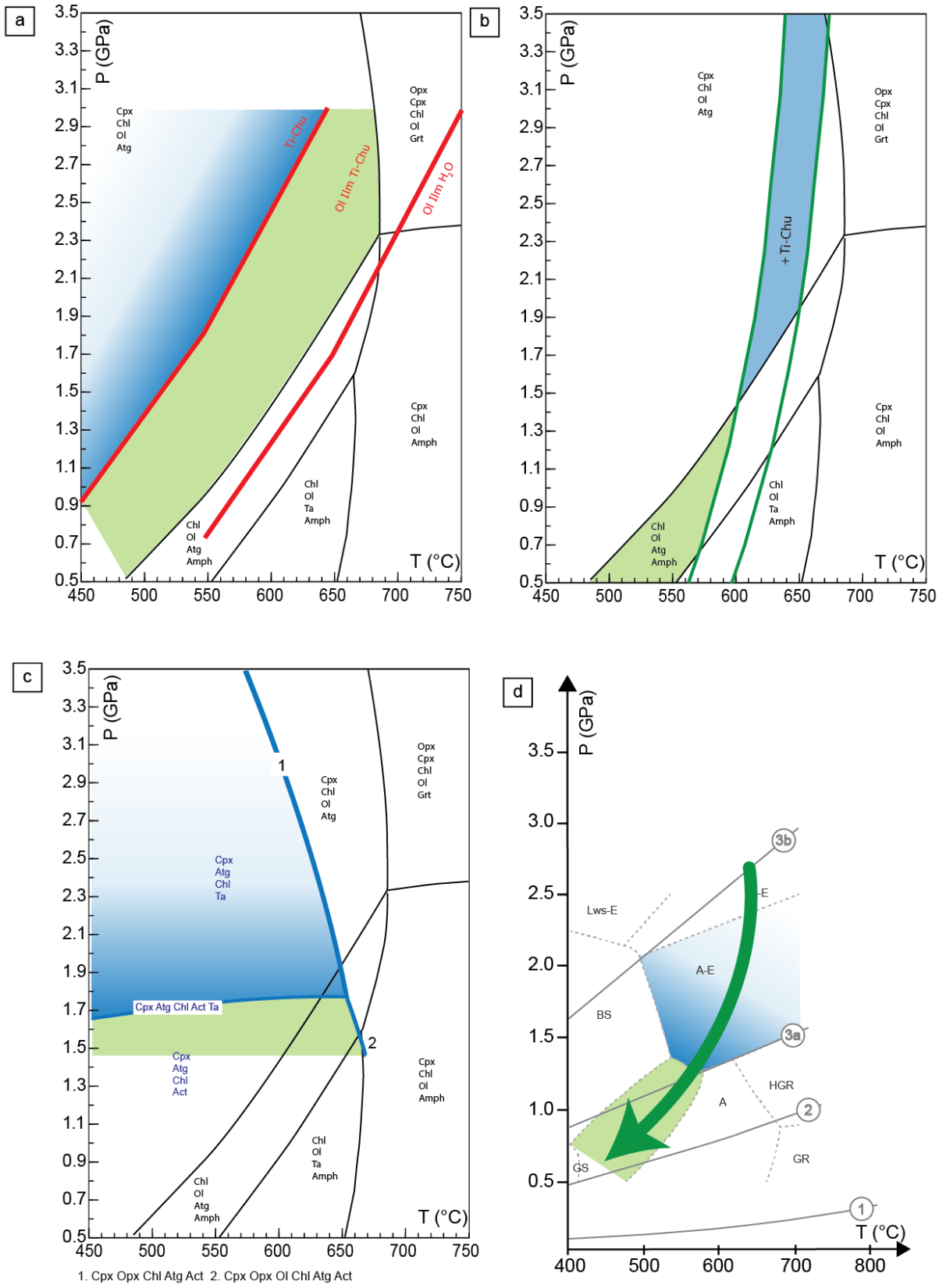

Fig. 3.2.7 - Metamorphic evolution of Gias Vej serpentinite: black curves are from petrogenetic grid for lherzolite composition from Poli and Schmidt (2002). Red curves are drawn after Nishio et al. (2019). Green curves constrains Ti-clinohumite stability field from López Sánchez-Vizcaíno et al. (2009) Blue curves (with blue labels) are from Fig. 3.1.4.7 pseudosection. Blue fields indicate PT stability conditions for D1 to D2 assemblages; green fields represent stability conditions for post-D2 assemblages. Grey geotherms in fig. 3.2.7d are after Cloos (1993): (1) near spreading ridge or volcanic arc; (2) normal gradient of old plate interior; (3a) cold subduction zones; (3b) warm subduction zones.

Cpx + Ol + Atg (+ Ti-Chu) to the Act bearing field passing through the Ti-Chu → Ol + Ilm + Ti-Chu curve. Furthermore, the superposition of the petrogenetic grid Poli and Schmidt (2002) with Ti-clinohumite stability field of López Sánchez-Vizcaíno et al. (2009), constrain a field between 610 and 670 °C down to 1.4 GPa for the coexistence of Atg + Cpx + Ol + Ol and Ti-clinohumite (Fig. 3.2.7b). Then in Cpx-rich layers, S1 is marked by Chl + Cpx + Atg + Mag, where Cpx is rimmed by Tr during post-D1: S1 can be stable at higher P than 1.7 GPa, as suggested by blue curves in Fig. 3.2.7c, while the occurrence of Tr can be due to the partial re-equilibration of this rock at lower P where Tr (Act) is stable.
The proposed metamorphic evolution results in a retrograde path. From this initial petrological analyses Gias Vej serpentinite experimented P_{min} > 1.4-1-7 GPa and T_{max} < 680 during the development of D1 to D2 assemblages, to P_{max} < 1.7 GPa during post-D2 stage.

3.2.6 Discussion

The Gias Vej serpentinite is part of an ophiolitic complex of the Piemonte Zone and it preserves the remnants of a lithostratigraphy affected by a multistage structural evolution, as testified by at least two different superposed foliations. Layers characterized by different compositions and fabrics have been recognized and analysed at the meso- and at the microscale. At Gias Vej the oceanic metamorphic evolution can only be inferred by the high degree of serpentinisation whereas the occurrence of Cpx-bearing layers may be the extreme result of the syn-subduction transposition of clinopyroxene-rich lithologies (such as gabbros) that percolated the ocean floor peridotite, as observed in ZSZ, where only clinopyroxene porphyroclasts survived the Alpine evolution as demonstrated in this thesis. However, this statement is rather speculative as geochemical data would be necessary and no pristine primitive fabric is preserved in gabbroic rocks.
The dominant lithotype is the *mylonitic serpentinite* that, even though it is affected by a pervasive mylonitic S2 foliation, preserves the remnants of S1 foliation in rare lithons and in Chl + Mag aggregates, which are interpreted as products of the destabilisation of spinel during serpentinisation (Carbonin et al., 2015). *Ol- Ti-Chu- Cpx-bearing layers* and *Ol-bearing layers* are locally deformed by D2 that caused the *boudinage* and the crenulation of their rims. *Foliated Ol-bearing layers* are parallelised into S2 and foliated by mylonitic S2 foliation; D1 minerals occur as porphyroclasts and mineral aggregates wrapped by S2. Despite *Cpx-bearing layers* being strongly transposed to very thin layers, they preserve an S1 foliation. In *chlorite schist* only Cpx porphyroclasts are preserved as relics in the S2 foliation. D3 has been recognized in Cpx-bearing layers and chlorite schist, in the form of a crenulation with no foliation development. D1 and D2 are therefore syn-metamorphic deformation stages that occurred in a ductile regime.
The determination of successive mineral assemblages allowed deciphering qualitatively the Alpine syn-subduction peak and exhumation PT condition of Gias Vej serpentinite. Curves that constrain mineral stability fields have been superposed. The obtained evolution (Fig. 3.2.7d) shows a retrograde path from Eclogite facies conditions P_{min} > 1.4-1-7 GPa and T_{max} < 680 °C during D1 to D2 stages to Epidote-Amphibole facies conditions at lower pressure during D3, where actinolite and tremolite are stable. HP conditions are attained during D1 to D2 stages as it is strongly suggested by Ol + Cpx + Ti-Chu + Atg bearing assemblage occurrence that has been described as HP paragenesis in Valtournanche serpentinite (Rebay et al., 2012). These estimates are very preliminary results and a first approximation of the metamorphic evolution of these serpentinites.

3.2.7 Conclusion

In conclusion, this study constitutes a preliminary result in approaching the metamorphic evolution of Gias Vej serpentinite. The multiscale structural analysis allowed to correlate the structural evolution of these rocks with the structural evolution proposed by Spalla et al. (1983), detailing the mineral assemblage variations during the different deformation stages registered over a long deformation history. Recognised mineral assemblages in serpentinite, as Ti-clinohumite bearing assemblages, allowed to infer that Gias Vej serpentinite reached eclogitic peak condition during Alpine subduction depressed thermal regime and were successively exhumed to Epidote-Amphibole facies conditions in a still depressed thermal state that predates the Alpine collision. These preliminary results are coherent and possibly coeval with those determined in the adjacent lithotypes. Finally, the lithostratigraphy and the HP metamorphic evolution suggest that Gias Vej serpentinite is part of a *Zermatt-Saas type ophiolite* that was tectonically mixed up with continental material during Alpine subduction and exhumed at the PZ-SLZ southern border.

Chapter 4
Variscan diopsidites associated with serpentinized lherzolite and migmatites of the Argentera Massif

4.1 Introduction

The Variscan belt of Europe is the result of the convergence between Laurasia and Gondwana that produced several suture zones known as Rheno-Hercynian, Saxo-thuringian, and Eo-Variscan (Arthaud and Matte, 1977; Franke, 1989; ; Matte, 2001; Faure et al., 2005; Guillot et al., 2009). These three suture zones are described from the Iberian Massif to the Bohemian Massif and are constituted by mafic and ultramafic rocks interpreted as ophiolites (Arenas and Sánchez-Martínez, 2015). Furthermore, ultramafic rocks in the pre-Alpine basement of the Central and Eastern Alps are often associated with metagabbros and metabasalts and interpreted as suboceanic mantle slices (e.g. Melcher et al., 2002).

In the External Crystalline Massif of the Alps, Rheic suture zones are not so well constrained in terms of lithostratigraphy, and their position has been interpreted thanks to a correlation among the major tectonic structures, lithostratigraphy and metamorphism (e.g. Guillot et al., 2009). The only Palaeozoic ophiolitic unit in the ECM is the well preserved and overturned Chamrousse Ophiolite, in the Belledonne-Grand Rousse Massif (von Raumer et al., 1999). The Chamrousse complex is composed of an obducted slab of back-arc layered sequence of ultramafic and mafic cumulates, layered metagabbros cut by metadoleritic dykes, metabasalts, and minor metasediments (Bodinier et al., 1982) and overlies a leptyno-amphibolitic complex that is considered the volcanic - volcaniclastic member of the Chamrousse back-arc.

The Argentera Massif is mainly composed of migmatitic paragneiss, orthogneiss, and amphibolite intruded by Late Carboniferous to Permian granites. These rocks experienced a polyphasic deformation history and registered a HT Variscan metamorphism, similarly to other Variscan Crystalline Massifs, locally preserving relicts of HP metamorphism (Ferrando et al., 2008). Its present-day structure is the result of the superposition of Variscan and Alpine tectonic histories (Corsini et al., 2004 and refs therein). Petro-structural fieldwork and mapping undertaken during this PhD project in the upper Valle Gesso (Italian part of Argentera Massif) revealed mafic and ultramafic rocks, associated with rare marbles, in layers and boudins wrapped by the regional migmatitic foliation. Ultramafic rocks are represented by variably serpentinised rocks, amphibolite and diopsidite. This rock assemblage could represent the remnants of the Palaeozoic ocean, sutured during the Variscan collision, and transposed in the embedding migmatitic foliation. In this study, the structural and metamorphic evolution of serpentinite and diopsidite boudins is explored to unravel their Variscan evolution.

4.2 Geological setting

The Argentera-Mercantour External Crystalline Massif (Fig. 4.1a and 1b) is the southernmost one of the External Crystalline Massifs (Bigi et al., 1990) of the Alps. It consists of migmatized paragneisses, amphibolites, and granitoids that registered Variscan early eclogitic and granulite metamorphisms followed by a syn-migmatitic event, late tilting of the nappes stack and horizontal shearing (Latouche and Bogdanoff, 1987). These rocks are successively intruded by the post-metamorphic Argentera Massif granite (Latouche and Bogdanoff, 1987; Dal Piaz, 1993; Corsini et al., 2004).

The Argentera Massif is divided into two complexes (Faure-Muret, 1955) by the NW-SE Valletta Shear Zone (Carosi et al., 2016; Simonetti et al., 2018). The Tineé Complex, in the SW sector, is constituted by gneisses interlayered with amphibolites, marbles, quartzites, horizons of graphite schist and a metadiorite, whereas the Malinvern-Argentera Complex, to the NE, also known as Gesso-Stura-Vésubie Terrain (GSV - Compagnoni et al., 2010), is made up of migmatitic gneisses, which are intruded by the late calc-alkaline Argentera granite.

The Tineé Complex has been subdivided into three series (Faure-Muret, 1955): the Varélios-Fougieret metasediments, the Anelle-Valabres-Iglière Formation, comprising mafic granulites, coronitic gabbros and marbles, and the gneissic Rabouns series. Granitoids are represented by the Igliére metagranodiorites intruded in the Anelle-Valabres-Iglière Formation and by small dykes in the Rabouns Series (Bogdanoff and Ploquin, 1980; Latouche and Bogdanoff, 1987; Malaroda, 1999).

The GSV Complex is constituted by migmatitic Ordovician granitoids banded by paragneisses with boudins of mafic, ultramafic, and carbonate rocks (i.e. amphibolites, eclogites, granulites, peridotites and serpentinites, diopsidites and marbles; Compagnoni et al., 2010 and references therein). The migmatitic leucosome contains amphibolite facies mineral assemblages formed at 650-700°C and 0.4-0.6 GPa (Compagnoni et al., 1974); anatexites can contain sillimanite and cordierite. The best preserved mafic bodies occur in the localities of Laghi del Frisson, Valle della Meris, and Lago di Nasta.

Concerning the interpretation of the timing of metamorphism in these rocks, Paquette et al. (1989) proposed two eclogitic metamorphic events at 424 Ma and 351 Ma, whereas Rubatto et al. (2001) suggested two different possibilities: a single HP-HT metamorphic event (443-332 Ma) or two eclogitic Ordovician and Devonian HT-HP events, followed by Variscan amphibolite facies metamorphism (323 ± 12 Ma), culminated in a diffused anatectic event. The granulitic metamorphism at Laghi del Frisson and Valle della Meris is estimated at 750-720 °C and 1.5-1.4 GPa (Ferrando et al., 2008; Compagnoni et al., 2010; Rubatto et al., 2010) followed by decompression at 710 °C and 1.10 GPa and mylonitic deformation in amphibolite facies conditions at 665 ±15 °C and 0.85 GPa (Ferrando et al., 2008). The GSV is intruded by Carboniferous-Permian granitoids, such as the "Granito Centrale dell'Argentera" and other intrusive bodies of Visean and Stephanian ages. Corsini et al. (2004) dated the Granito Centrale and the end of the HT metamorphism at 296-299 Ma. Remnants of Carboniferous covers, which consist of Stephanian black shales and sandstones, are preserved within narrow fault zones cutting through the crystalline basement. Permian-Triassic sedimentary successions unconformably cover the crystalline basement and consist of quartzites, conglomerates, sandstones, and siltstones. The Jurassic sediments comprise dolomites and limestones (Malaroda and Carraro, 1970).

The structural setting of the Argentera massif (Fig. 4.1b) is the result of the superposed Variscan and Alpine convergences. The regional migmatitic foliation developed during the high grade Variscan

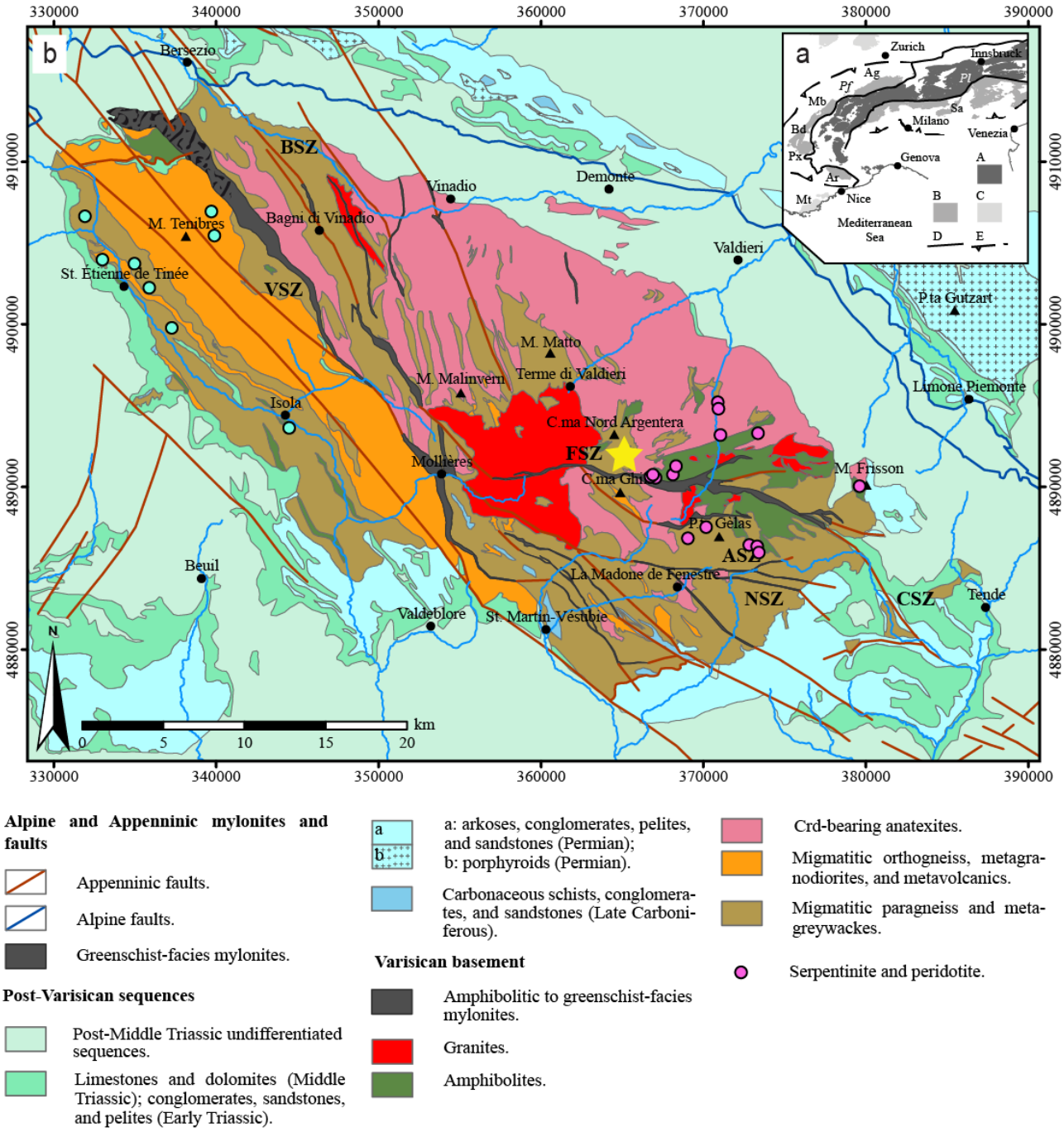

Alpine and Appenninic mylonites and faults

- Appenninic faults.
- Alpine faults.
- Greenschist-facies mylonites.

Post-Varisican sequences

- Post-Middle Triassic undifferentiated sequences.
- Limestones and dolomites (Middle Triassic); conglomerates, sandstones, and pelites (Early Triassic).
- a: arkoses, conglomerates, pelites, and sandstones (Permian); b: porphyroids (Permian).
- Carbonaceous schists, conglomerates, and sandstones (Late Carboniferous).

Varisican basement

- Amphibolitic to greenschist-facies mylonites.
- Granites.
- Amphibolites.
- Crd-bearing anatexites.
- Migmatitic orthogneiss, metagranodiorites, and metavolcanics.
- Migmatitic paragneiss and metagreywackes.
- Serpentinite and peridotite.

Fig. 4.1 - a) Simplified tectonic sketch of the Alps; abbreviations: A - Variscan basement rocks into the axial zone of the Alps; B - Variscan basement rocks preserved at the external margins of the Alps (Ag: Aar-Gothard Massifs, Ar: Argentera-Mercantour Massif, Bd: Belledonne Massif, Mb: Mont Blanc Massif, Px: Pelvoux Massif, Sa: Southern Alps); C - Variscan basement rocks external to the Alpine fronts (Mt: Maures-Tanneron Massif, Vs: Vosges); D - lithospheric structures delimiting the axial zone of the Alps (Pf: Penninic Front, Pl: Periadriatic Lineament); E - Alpine fronts; b) Argentera-Mercantour Massif with legend: ASZ - Autier Shear Zone; BSZ - Bersezio Shear Zone; CSZ - Casterino Shear Zone; FSZ - Fremamorta Shear Zone; NSZ - Neiglier Shear Zone; VSZ - Valletta Shear Zone (also known as Ferriere-Mollières Shear Zone). Projected coordinate system: WGS 84- UTM zone 32N; pink dots localize the variously serpentinised peridotite boudins; yellow star indicates the study area. Modified after Gosso et al. (2019).

metamorphism trends NW-SE with dip direction and NE to SW with medium to high angle. The massif is crosscut by various Variscan and Alpine shear zones. In the central part of the massif, the

Valletta and the Bersezio Shear Zones trend both N150-N160 and display a vertical pervasive foliation and a dextral strike-slip kinematic (Corsini et al., 2004). The Fremamorta Shear Zone crosscuts the entire eastern part of the Argentera massif, affecting the Granito Centrale. The Ferriere-Mollières Shear Zone, dated at 327 ± 3 Ma (Musumeci and Colombo, 2002), displays dextral strike-slip kinematic. The Alpine deformation caused the reactivation of NW-SE trending shear zones, such as the Ferriere-Mollières Shear Zone, while the WNW-ESE lineaments are reactivated as thrusts (Guillot et al., 2009). Alpine exhumation is dated between 22 and 8 Ma (Corsini et al., 2004; Sanchez et al., 2011 and references therein) and caused the tectonic reactivation and new faulting through strike-slip dextral faults and thrusting. To the southwest of Entracque (Fig. 4.1b), the SW trending Rovina Valley ends up at the Lago Brocan (2000 m) aphiteatre, beneath the mountain sides of Cima Sud Argentera, Cima di Nasta, Cima Ghilié, and Punta Gelas. On the eastern side of Lago Brocan, amphibole agmatite is the dominant lithotype. In the south, amphibole agmatite is juxtaposed to a kilometre W-E mylonitic band and in the southeast it is intruded by aplitic granite dykes. Malaroda and Carraro (1970) reported here the occurrence of serpentinite, amphibolite, and marble boudins.

4.3 Lithostratigraphy

In order to describe, the occurrence of diopsidite and serpentinite boudins and lenses in the migmatitic basement of the Argentera Massif, a 1:500 scale structural map has been performed. The surveyed area stands on the eastern slope of Lago Brocan, Upper Valle Gesso, next to Rifugio Genova-Figari. The outcrop map is reported in Fig. 4.2. The surveyed area extends from 2000 to 2260 m and comprises very steep and indented slopes with narrow gullies and ridges in the south and eastern portions of the map, turning to whaleback surfaces in the northern and western parts (nearby the Lake Brocan). In the central part of the map, detritus from the gullies feeds a wide debris accumulation fan. In the western part, a rocky ledge is on the verge of Lago Brocan and is separated from the rest of the outcrops by the accumulation debris channel and by a narrow notch on the eastern side.

Here, different migmatitic rock types embed boudin of ultramafic, mafic, and carbonatic rocks. Diatexites and anatexites are dominant in the northern part of the map and constitute the whaleback rocks near Rifugio Genova-Figari. Agmatites with mafic, ultramafic, and carbonatic boudins occur in the southern and eastern part of the map.

Paragneiss Diatexite (Fig. 4.3a) is a millimetre-grained rock and it is mostly foliated with the alternance of millimetre Bt-bearing layers and up to centimetre Qz + Plg + Kfs layers. This compositional alternance marks the dominant tectonitic foliation (S1). Locally, centimetre-sized lenses and veins of anatectic granite, mostly composed by of quartz and plagioclase with rare cordierite, crosscut the foliation with sharp edges.

Paragneiss diatexite is often intruded by decimetre- to metre-thick dykes of quartz and aplitic granite, and locally encloses boudins of biotitite, calc-silicate rock, amphibolite, and eclogite.

Anatexite (Fig. 4.3b) is mostly composed by leucosome of millimetre-sized crystals of quartz, K-feldspar, and plagioclase with minor biotite and has granoblastic texture. Locally, biotite flakes are aligned in rows marking a discontinuous strand-like foliation. Cordierite and white mica occur in lenses and veins in a nebulitic texture. Lens of micro-granite and pegmatite show fuzzy and smooth contacts. Centimetre to metre-sized boudins of amphibolite, biotitite, and diatexite have been found, such as, for example, the 5 metre-long biotitite boudin at the bottom of the wall in the northern part of the map, or the diatexite boudins at the top of the whaleback rocks in northern part of the map.

Anatexite is also intruded by decimetre-thick dykes of aplitic granite with sharp edges. The contact between diatexite and anatexite is sharp to fuzzy and gradual, as the leucosome volume increases and biotite-rich layers occurrence decreases.

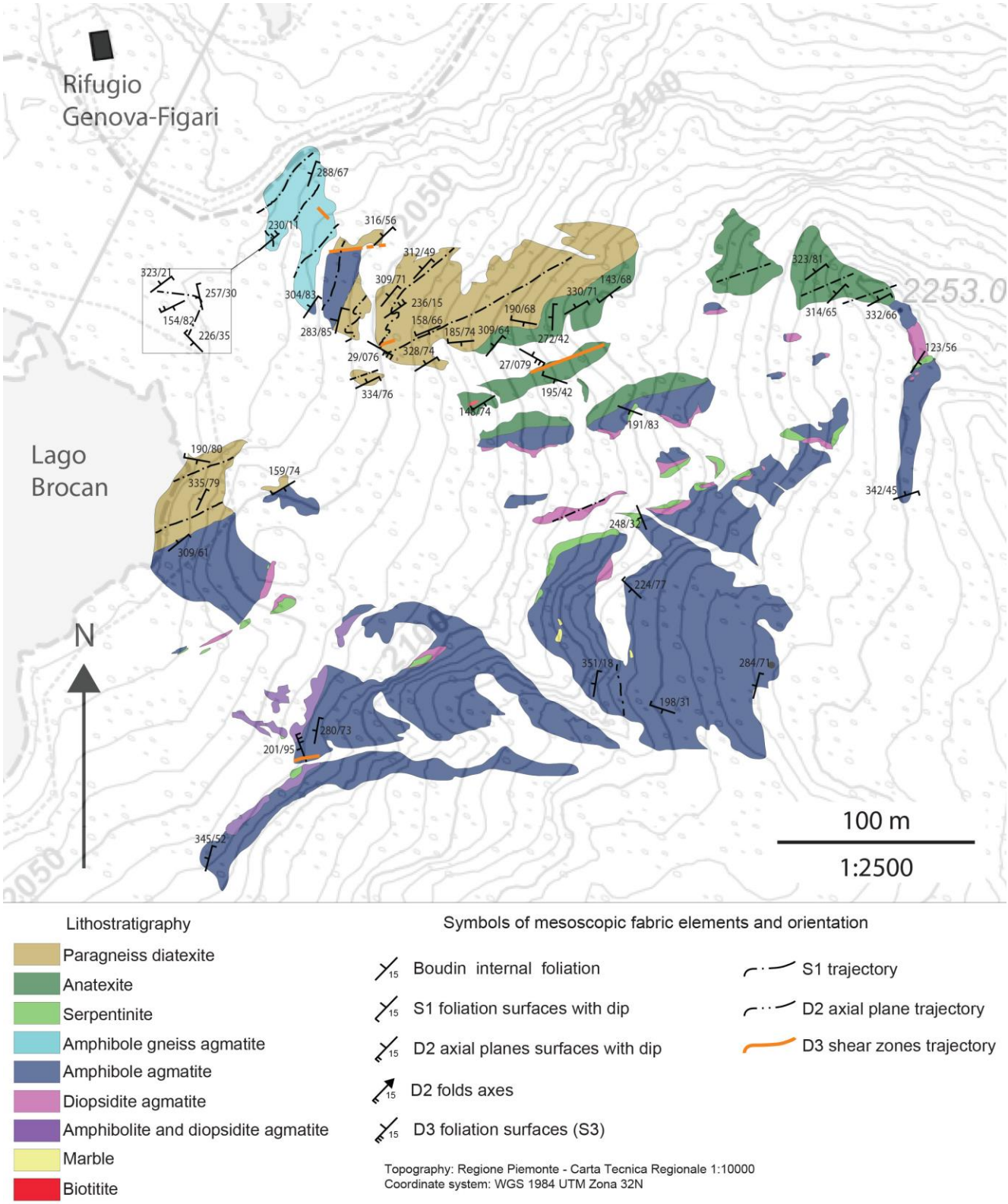

Fig. 4.2 - form surface map, with lithostratigraphy and superposed structures, of the mafic and ultramafic boudins embedded in migmatites of the eastern slope of Lago Brocan, upper Valle Gesso. Topography: Regione Piemonte - Carta Tecnica Regionale 1:10000. Coordinate system: WGS 1984 UTM Zona 32N.

Serpentinite (Fig. 4.3e-f) constitutes mostly rounded-shaped boudins of centimetre to decametre size (Fig. 4.3c). The rock is foliated and composed by serpentine + spinel with minor amphibole, chlorite, and rare clinopyroxene. Grainsize varies from submillimetre for serpentine and spinel to millimetre for amphibole crystals. Textures span from mesh textures to foliated fabric (Fig. 4.3d). Up to 5 cm thick layers rich in amphibole (amphibole-rich layers) (Fig. 4.3e) and millimetre-thick serpentine veins occur (Fig. 4.3f), and often crosscut the serpentinite main foliation. Locally, a centimetre-thick rim of radial amphibole (+biotite) developed between serpentinite boudin and the embedding anatexite.

Agmatite is a rock composed by a leucosome that wraps centimetre- to metre-sized boudins of different rocks. The leucosome is fine to coarse-grained and mostly composed by quartz, feldspar, and minor amphibole and mica. Different types of agmatite are distinguished according to the enclosed boudins.

Amphibole gneiss agmatite (Fig. 4.3g) outcrops near Rifugio Genova-Figari. This rock is composed by quartz-feldspar leucosome surrounding amphibole gneiss boudins with rounded to angular shape. The leucosome is composed by quartz + plagioclase with minor amphibole, and its grainsize is mostly centimetre-sized up to 2-3 cm, with minor portions with millimetre-sized crystals. It constitutes layers of centimetre to decimetre thickness. Foliated amphibole gneiss occurs as up to metre, rounded to angular shaped boudins, wrapped and boudinaged by the leucosome. Gneiss grainsize is from submillimetre to millimetre, and the foliation is marked by layers of euhedral amphibole with rare biotite and quartz + plagioclase layers. In the leucosome, the shape orientation and the foliation orientation of the gneiss boudins is mostly chaotic. An incipient foliation, marked by amphibole alignments in the leucosome, mostly wraps boudins but, rarely, the elongation of the boudins and their foliation is parallel to leucosome foliation.

Amphibole agmatite (Fig. 4.4a) is the dominant lithotype in the surveyed area and outcrops in the south-eastern part of the map. The quartz-feldspar leucosome wraps and fills boudin necks in the amphibolite blocks. Leucosome is made up of millimetre to centimetre quartz + plagioclase occurring in granoblastic aggregates. Rarely, an incipient foliation is marked by the amphibole alignments, and wraps the amphibolite boudins. Amphibolite is a fine grained rock and occurs as centimetre to metre boudins and blocks. It is mostly foliated by continuous millimetre layers of euhedral amphibole in polygonal aggregates with minor plagioclase. There is no clear relationship between the internal foliation and the rare foliation of the leucosome, as the amphibolite boudins and their internal foliation are often kinked and the orientation of their shape and internal foliation varies in each boudin. Rarely the elongation of the boudins and/or their internal foliation is parallel to the foliation of the leucosome.

Diopsidite agmatite occurs as a discontinuous layer of metric thickness and 70°N trending, embedded in the amphibole agmatite (Fig. 4.2). Contacts between amphibole agmatite and diopsidite agmatite are often gradual and transitional. The leucosome is mostly up to centimetre-grained with minor millimetre-sized portions, and constitutes a net of centimetre to decimetre layers of granoblastic quartz + plagioclase aggregate, with minor micas and epidote. Diopsidite boudins are centimetre to metre sized and round-shaped (Fig. 4.4b), sometimes elongated. The rock is composed by clinopyroxene with minor amphibole, and spinel. The grainsize varies from millimetre to submillimetre. The fabric is mostly coronitic and polygonal and no foliation occurs. Boudins are often rimmed by millimetre thick polygonal aggregates of dark green amphibole (Fig. 4.4b) or by a centimetre radial aggregate of amphibole fibres (Fig. 4.4c).

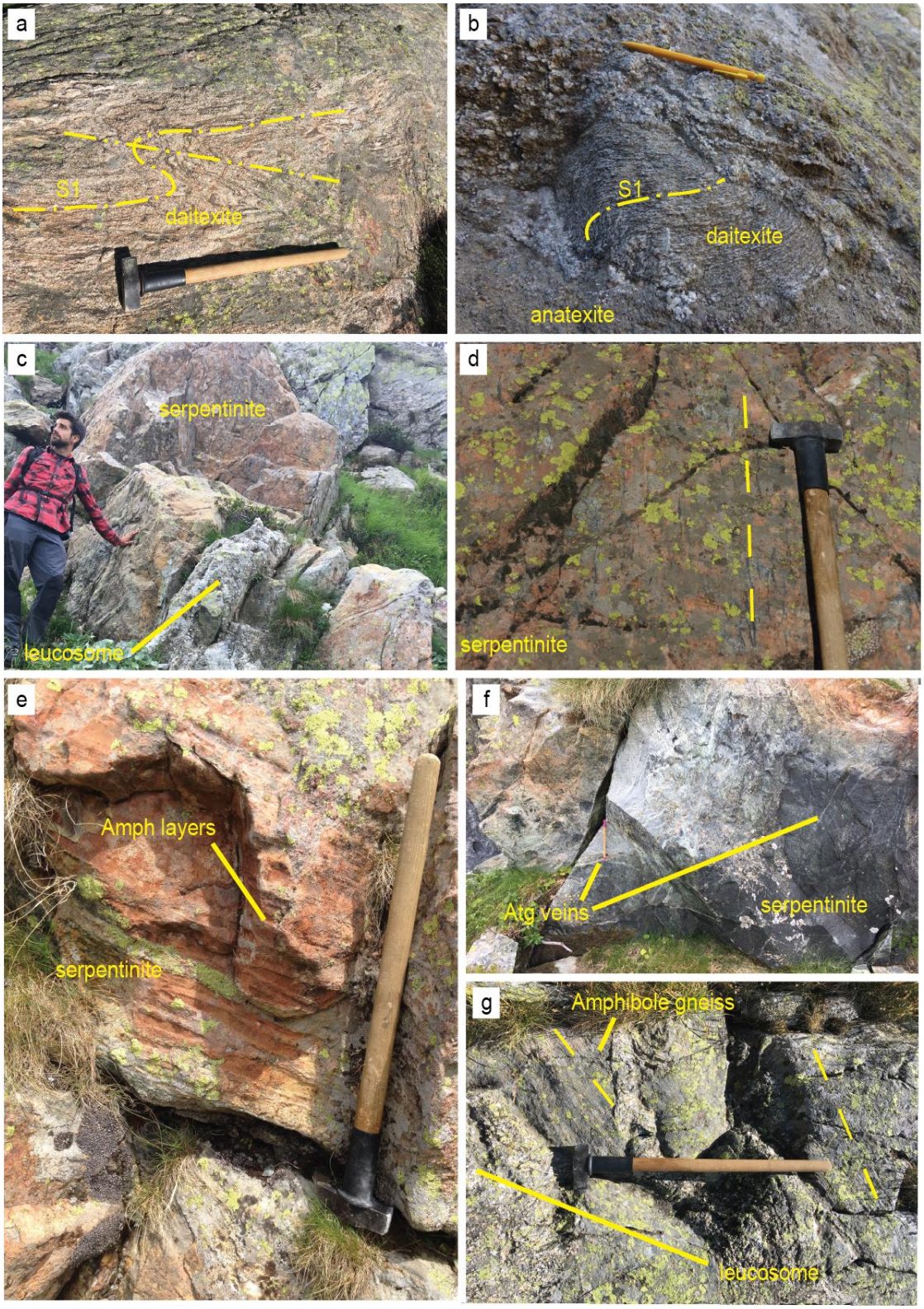

Fig. 4.3 - lithostratigraphy and mesostructures: single dotted line = S1 foliation trace; double dotted line = D2 axial plane surface trace; dashed line: trace of boudin internal foliation. a) S1 foliated paragneiss diatexite with S1 folded by D2. S1 is marked by mafic films and quartz feldspar lithons; b) diatexite boudin in anatexite leucosome; c) meter-sized serpentinite boudin wrapped by leucosome; d) internal foliation in serpentinite boudins marked by the alignment of Spl layers; e) amphibole rich layers in serpentinite; f) serpentine veins in a serpentinite boudin; g) amphibole gneiss agmatite.

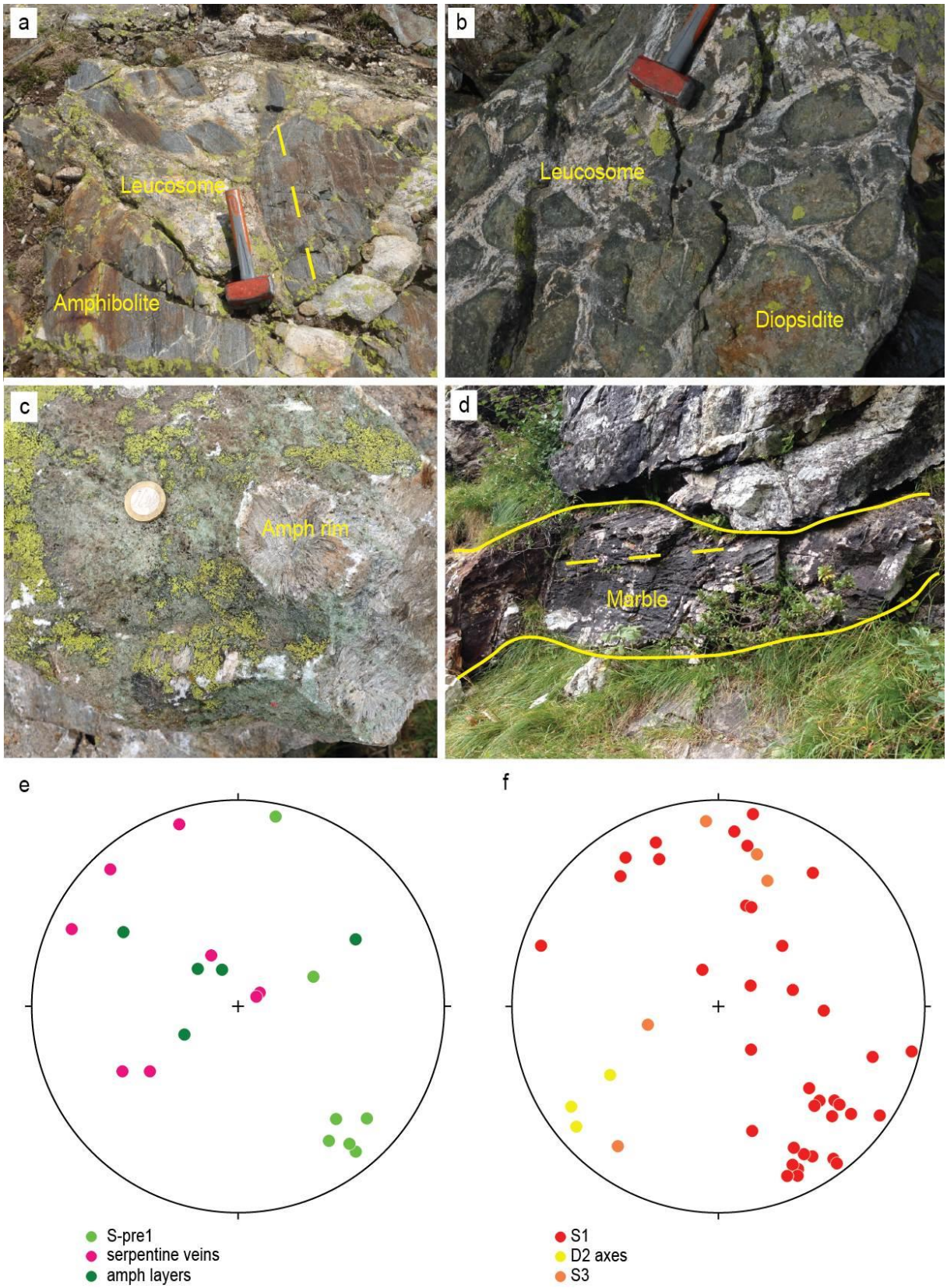

Fig. 4.4 - lithostratigraphy and mesostructures: dashed line = trace of boudin internal foliation; continuous line = lithological surface. a) angular amphibolite boudins of various sizes, wrapped by leucosome, in amphibole agmatite; b) angular to rounded boudins of diopsidite in diopsidite agmatite; locally a dark green rim of amphibole occurs between leucosome and diopsidite; c) radial amphibole fibres rimming diopsidite boudin; d) marble boudin enclosed in leucosome; e-f) orientation data of serpentinite (e) and diatexite (f) plotted in Schmidt projection (lower hemisphere).

Diopsidite and Amphibole agmatite occur at the contact between amphibole agmatite and diopsidite agmatite, with a metre-sized thickness. Leucosome is the same of the amphibole agmatite, finer than the diopsidite agmatite leucosome. Both diopsidite and amphibolite boudins occur.
Biotitite is a very fine-grained rock composed by biotite with minor quartz, forming up to 5 metre long boudins. The internal foliation is marked by the SPO of biotite and is discordant with respect to the diatexite external foliation. Locally biotite boudins are crosscut by fractures filled by leucocratic melt.
Meta-carbonate occurs in the form of few lenses of marble in the amphibole agmatite (Fig. 4.4d). Boudins are 1.5 to 5-metre-long. The rock is millimetre-grained and is mostly constituted by carbonates with saccaroid texture. Locally serpentinised sites of former olivine crystals occur. Chlorite, phlogopite, oxides, and Ti-Clinohumite have been recognized.

4.4 Mesostructures

Relationships among lithotypes are very complex mostly due to the heterogeneous volume of leucosome occurring in the different lithotypes and because of the Variscan and Alpine deformative evolutions. Generally, the majority of lithological surfaces are parallel to S1, as can be seen from the contact between paragneiss diatexite, anatexite, and amphibole agmatite that are all about 70° N trending (Fig. 4.2). Moreover, also diopsidite agmatite occurs as elonged lenses mostly parallel to S1 (Fig. 4.2). Anatexite outcrops only in the northern part of the map as a lenticular body trending parallel to S1.
Pre-D1 structures comprise the internal foliation of amphibolite (Fig. 4.3g), amphibole gneiss (Fig. 4.4a), and serpentinite (Fig. 4.3d and 4e) boudins that occur in the agmatite rocks, as these lithotypes registered minor migmatisation. The shape orientation of boudins is random. Pre-D1 foliation in different boudins is mostly found in a random order. Rarely, the boudins elongation and pre-D1 foliation in boudins are parallel to S1 foliation. As shown in Fig. 4.4e stereogram, serpentinite veins and amphibole-rich layers are not preferentially oriented, whereas the internal foliation of serpentinite is sub-parallel to S1 in diatexite (Fig. 4.4f)
D1 stage produced the regional HT foliation called S1 that affects pervasively the paragneiss diatexite (Fig. 4.3a) and locally the rocks with higher volume of leucosome as anatexites. In the surveyed area, S1 trace trends mostly 70°N to 40°N in the most northern outcrops (Fig. 4.2). S1 dips NW/ 6°-85°; locally S1 dips to the SE because of D2 folds (Fig. 4.4f), as suggested by the bimodal to girdle distribution in the stereogram in Fig. 4.4e. In the paragneiss diatexite, S1 is marked by biotite SPO and locally by sillimanite and garnet, and wraps lenses and anastomosed lithons of Qz + Plg + Kfs granoblastic leucosome. Biotite is locally overgrown by white mica and chlorite. Because of the high volume of granoblastic leucosome in agmatite rocks, it is difficult to relate the boudinage of mafic, ultramafic, and carbonatic rocks with the S1 development, as boudins could have formed before S1 and successively have been re-oriented, as, locally, the incipient Amphibole-bearing foliation in leucosome wraps the boudins.
D2 stage developed metre to centimetre-scale folds of the S1 foliation with no axial plane foliation development; these folds have been observed only into paragneiss diatexite (Fig. 4.3d). D2 folds axes are 11° to 37° SW dipping and axial planes dip at high angle towards the SE (Fig. 4.4f). D2 folds are very tight and asymmetrical.
D3 shear zones crosscut S1 foliation and are fine grained mylonitic bands. In paragneiss diatexites and anatexite, mylonitic S3 foliation is marked by Wm + Chl films wrapping Qz + Plg + Kfs lithons. D3 shear zones mostly dip 50°-70° with a dominant NW-SE trend (Fig. 4.4f).

4.5 Whole-rock composition

Whole rock analyses (Table 4.1) from two samples of diopsidite have been acquired at Mineral Veritas Bureau (Krakow) by ICP-MS. SiO_2 (54.22-54.66 wt%), MgO (17.44-18.18 wt%) and CaO (16.12-19.52 wt%) are the most abundant components. Fe_2O_3 and Al_2O_3 have relatively low

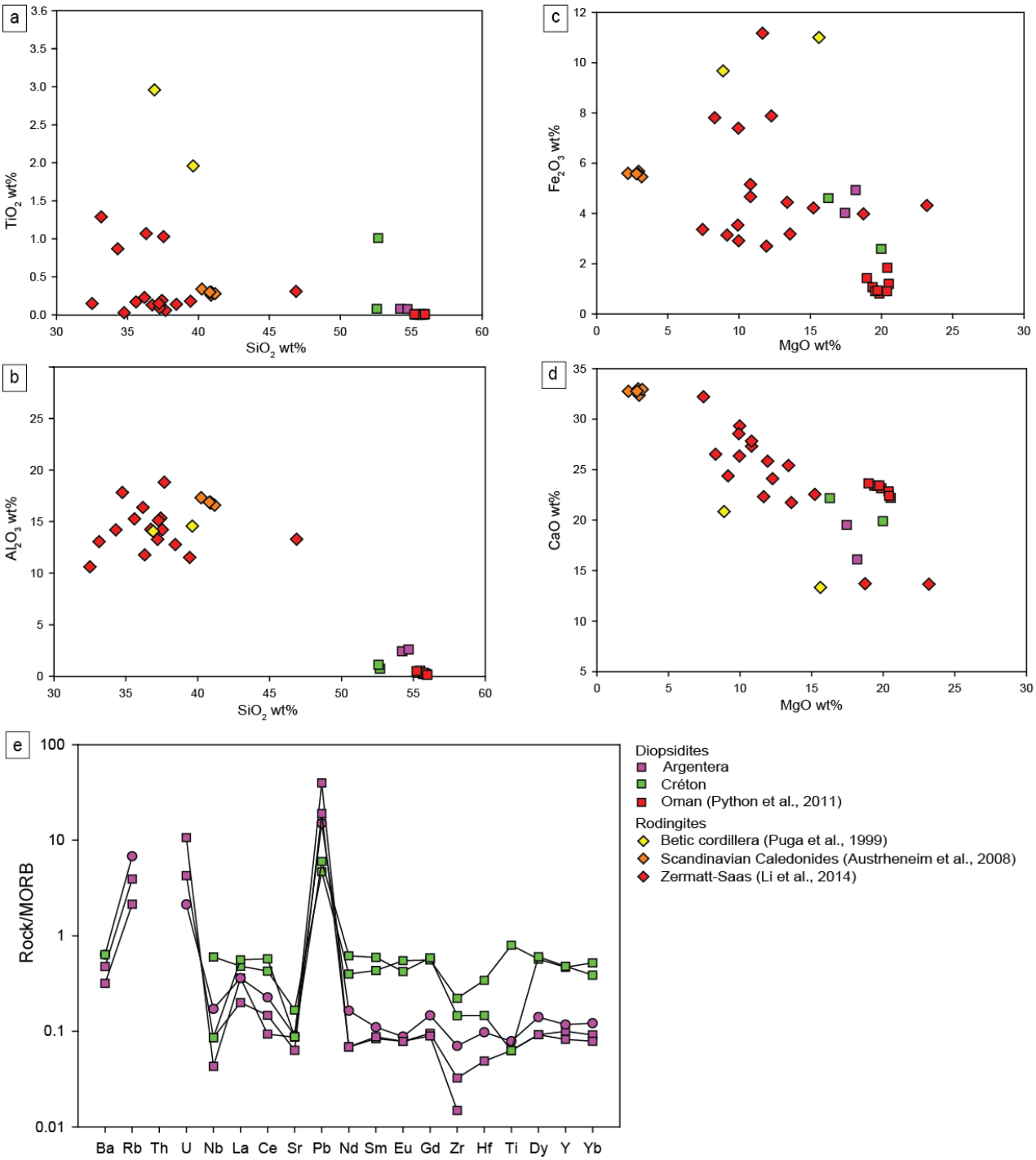

Fig. 4.5 - Whole rock composition diagrams. a-d) Major elements composition in comparison with Créton and Oman diopsidite compositions (Python et al., 2007) and data of rodingites from Zermatt-Saas Zone, Scandinavian Caledonides, and Betic Cordillera (Puga et al., 1999; Li et al., 2004; Austrheim and Prestvik, 2008); e) MORB normalised spider diagram. Values from Eggins (1998).

concentrations (4.47-5.48 and 2.43-3.42 wt% respectively). Cr_2O_3, Na_2O, and MnO are < 1%, and TiO_2 and K_2O are negligible. Diopsidite compositions are shown in diagrams in Fig. 4.5a-d and are compared with data from Oman diopsidite (Python et al., 2007) and data of rodingites from Zermatt-Saas Zone, Scandinavian Caledonides, and Betic Cordillera

Sample	Method	WGHT	LF200	LF200	LF200	LF200	LF200	LF200	LF200	LF200	LF200	LF200	LF200	LF200	LF200	LF200	LF200	LF200
	Analyte	Wgt	SiO2	Al2O3	Fe2O3	MgO	CaO	Na2O	K2O	TiO2	P2O5	MnO	Cr2O3	Ba	Ni	Sc	LOI	Sum
	Unit	KG	%	%	%	%	%	%	%	%	%	%	%	PPM	PPM	PPM	%	%
	MDL	0.01	0.01	0.01	0.04	0.01	0.01	0.01	0.01	0.01	0.01	0.01	0.002	1	20	1	-5.1	0.01
G 33	Rock	0.11	54.22	2.43	4.47	17.44	19.52	0.36	0.09	0.08	<0.01	0.12	0.289	3	239	68	0.6	99.67
G 26	Rock	0.03	54.66	2.63	5.48	18.18	16.12	0.32	0.08	0.08	<0.01	0.15	0.309	2	178	65	1.6	99.66
G 5	Rock	0.02	49.59	3.42	7.04	24.63	7.44	0.29	0.14	0.1	<0.01	0.18	0.32	4	711	27	6.3	99.56

Sample	LF200	LF200	LF200	LF200	LF200	LF200	LF200	LF200	LF200	LF200	LF200	LF200	LF200	LF200	LF200	LF200	LF200	LF200
	Be	Co	Cs	Ga	Hf	Nb	Rb	Sn	Sr	Ta	Th	U	V	W	Zr	Y	La	Ce
	PPM	PPM	PPM	PPM	PPM	PPM	PPM	PPM	PPM	PPM	PPM	PPM	PPM	PPM	PPM	PPM	PPM	PPM
	1	0.2	0.1	0.5	0.1	0.1	0.1	1	0.5	0.1	0.2	0.1	8	0.5	0.1	0.1	0.1	0.1
G 33	3	51	<0.1	1.8	0.1	0.1	2.2	<1	7.8	<0.1	<0.2	0.5	192	<0.5	2.4	2.8	0.9	0.7
G 26	1	32.9	<0.1	2.4	<0.1	0.2	1.2	2	5.7	<0.1	<0.2	0.2	188	<0.5	1.1	2.3	0.5	1.1
G 5	2	64.7	1	2.2	0.2	0.4	3.8	3	8.1	<0.1	<0.2	0.1	82	1.1	5.2	3.3	0.9	1.7

Sample	LF200	LF200	LF200	LF200	LF200	LF200	LF200	LF200	LF200	LF200	LF200	LF200	LF200	LF200	LF200	LF200	LF200	LF200
	Pr	Nd	Sm	Eu	Gd	Tb	Dy	Ho	Er	Tm	Yb	Lu	W	Hg	Tl	Se	Au	
	PPM	PPM	PPM	PPM	PPM	PPM	PPM	PPM	PPM	PPM	PPM	PPM	PPB	PPB	PPB	PPB	PPB	
	0.02	0.3	0.05	0.02	0.05	0.01	0.05	0.02	0.03	0.01	0.05	0.01	0.5	0.01	0.1	0.5	0.5	
G 33	0.06	0.5	0.22	0.08	0.35	0.06	0.42	0.1	0.28	0.03	0.28	0.04	<0.5	<0.01	<0.1	<0.5	<0.5	
G 26	0.11	0.5	0.23	0.08	0.33	0.06	0.42	0.09	0.32	0.04	0.24	0.03	<0.5	<0.01	<0.1	<0.5	<0.5	
G 5	0.2	1.2	0.29	0.09	0.54	0.09	0.64	0.15	0.44	0.05	0.37	0.05	<0.5	<0.01	<0.1	<0.5	0.7	

Table 4.2 – Whole rock analyses.

(Puga et al., 1999; Li et al., 2004; Austrheim and Prestvik, 2008). Argentera diopsidite composition is very close to Oman diopsidite compositions in terms of TiO_2 and SiO_2. TiO_2 in Argentera diopsidite is also similar to rodingites and SiO_2 is higher in diopsidite respect to rodingite. Al_2O_3 is slightly higher and MgO is slightly lower in Argentera diopsidite than in Oman diopsidite (Fig. 4.5a and 5b). Fe_2O_3 and MgO contents are similar with respect to rodingites of Zermatt Saas Zone; CaO is generally lower than Oman diopsidite and Zermatt-Saas rodingite (Fig. 4.5c e 5d). In the MORB normalised diagram in Fig. 4.5g, diopsidite is flat around 0.1 times MORB. Rb and U are up to 10 times MORB. Eu anomaly is just hinted while great negative anomalies occur for Nb, Sr, and Zr.

4.6 Microstructural analysis

The microstructural analysis allows distinguishing three (M1-M3) and four (M1-M4) metamorphic assemblages in serpentinite and diopsidite boudins, respectively. A synthesis of the recognised mineral assemblages is reported in table 4.2.

Rock	Analysed samples	Composition	Mineral Assemblages				
			M1	M2	M3		
Serpentinite	G5 AR1A G34	Atg Amph Spl Chl Cpx Phl Atg Amph Chl Spl Phl Atg Amph Spl Cpx Chl	Amph1 + Spl + Phl	Amph2 + Atg + Mag + Chl	Tr + Atg + Chl + Cpx		
Amph-layers	G5	Amph Atg Chl Cpx			Tr + Atg + Chl + Cpx		
			M1	M2	M3	M4	M5
Diopsidite	G26 G33 RG1211A RG1210A	Cpx Amph Spl Chl Cpx Amph Spl Chl Ph Cpx Amph Spl Chl Cpx Amph Spl Chl Ep	Cpx1+Spl1	Cpx2+Amph1 (rims, veins, polygonal)+Spl2+Ep	Amph2 (rims)	Amph3 (veins and aggregates)+Chl+Ph	Amph4 (aggregate)
Leucosome	RG1210A	Qz Ab Kfs Ph Ep		Pl+Kfs+Qz			

Table 4.2 – Mineral assemblages in diopsidite and serpentinite.

Serpentinite is made by serpentine with minor amphibole and spinel (Fig. 4.6a-i). Phlogopite and calcite are also found. Serpentine forms a submillimetre matrix (Fig. 4.6b) that contains up to centimetre-sized amphibole and spinel crystals aggregates (Fig. 4.6c, 6d, and 6e). The shape preferred orientation of amphibole aggregates marks the foliation of the serpentinite (Fig. 4.6a). This internal foliation (pre-D1) is crosscut by amphibole layers, amphibole-bearing veins, and serpentine-bearing veins. Serpentine occurs as submillimetre fibres in aggregate characterized by mesh and interlocking texture (Wicks and Whittaker, 1977) with no preferred orientation (Fig. 4.6b). These aggregates are underlined by elonged aggregates of spinel. In aggregate, spinel1 preserves an euhedral to rounded habit with up to 60-70 µm grainsize (Fig. 4.6e). As it can be seen by BSE image, spinel is zoned (Spinel1 to 2) and often the most external portion is a skeletal rim of magnetite (Spinel2). In the core of spinel aggregate, phlogopite flakes have been detected (Fig. 4.6e). Similar zoning has been observed in spinel inclusion in amphibole crystals, where the habit of the spinel is less preserved than spinel habit in the matrix and locally has a skeletal habit (Fig. 4.6f). In the matrix, amphibole1 occurs as up to 8 millimetres long subhedral crystals, with undulose extinction and magnetite and serpentine exsolution along cleavages. The amphibole1 has fractures perpendicular to the pre-D1 foliation, filled by serpentine. Edges of the crystals are indented with matrix serpentine fibres. Amphibole encloses clinopyroxene1 relic crystals (up to 10 µm) (Fig. 4.6g): they are mostly iso-oriented by at different

angles with respect to amphibole cleavages. Amphibole2 constitutes polygonal aggregates of submillimetre grains that partially rim amphibole1 (Fig. 4.6d). Amphibole2 is exsolution-free but its edges are indented with serpentine fibres too. Phlogopite flakes locally occur in amphibole1 aggregate, where and they are rimmed by films of chlorite (Fig. 4.6h). Chlorite also occurs in the serpentine matrix, close to spinel. Calcite has been detected in globular aggregate of serpentine and skeletal magnetite.

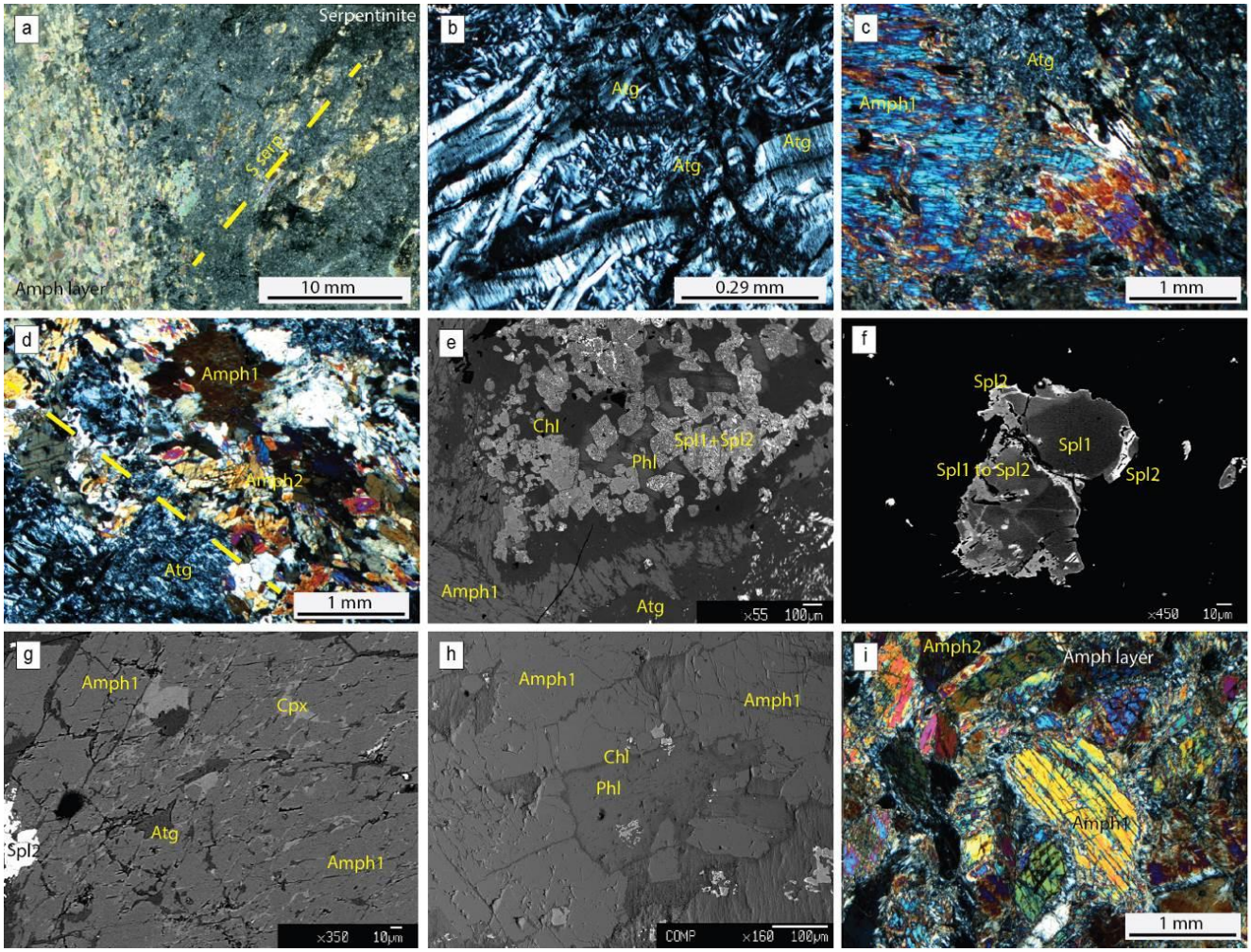

Fig. 4.6 - serpentinite microstructures. a) Crossed polar view of a serpentinite thin section. The foliation is marked by the elongation of amphibole aggregates and is crosscut by the amphibole layer; b) mesh and interlocking textures of the serpentine in the same rock (crossed polars); c) amphibole1 crystal with serpentine-filled fractures (crossed polars); d) amphibole1 surrounded by amphibole2 in polygonal aggregate (crossed polars); e) spinel aggregate with chlorite and phlogopite in the core of the aggregate; spinel crystals are rimmed by magnetite (white) (BSE image); f) zoned spinel enclosed in amphibole1. Spinel1 is the darker core; spinel1 to 2 includes the different grey zonings; spinel2 is magnetite at the rim of the spinel grain; g) clinopyroxene relics in amphibole1 (BSE image; h) phlogopite flake in sharp contact with amphibole1, rimmed by chlorite (BSE image; i) amphibole layer matrix (crossed polars).

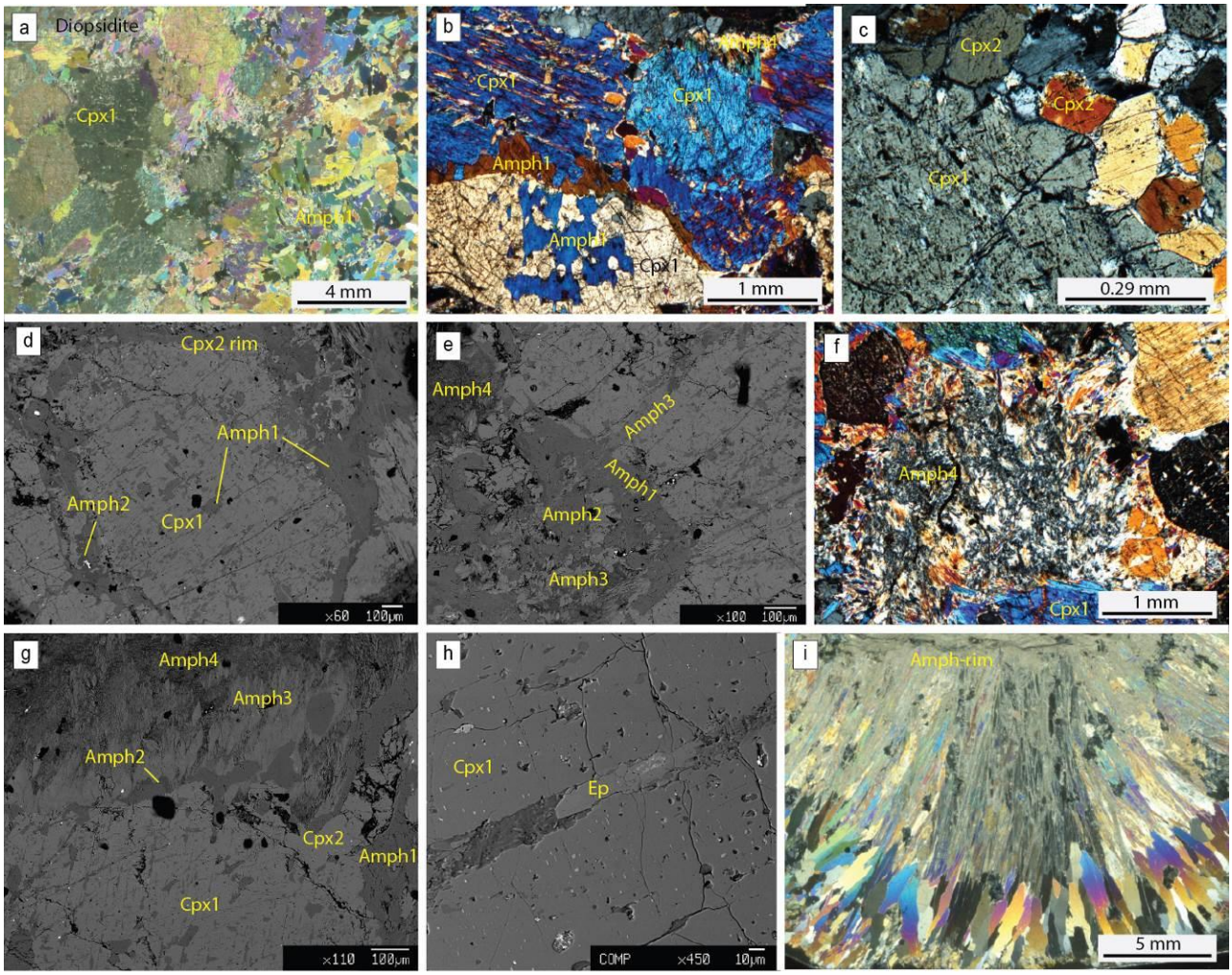

Fig. 4.7 - diopsidite microstructures. a) diopsidite polygonal texture (crossed polars); b) clinopyroxene1 crystals with amphibole1 rims (crossed polars); c) clinopyroxene2 new grains around clinopyroxene1 (crossed polars); d) clinopyroxene1 with amphibole1 rims and inclusions and amphibole2 rims (BSE image); e) amphibole3 vein crosscutting clinopyroxene1 and amphibole1 rim (BSE image); f) amphibole4 aggregate (crossed polars); g) clinopyroxene1 is rimmed by amphibole1 and thin amphibole2; amphibole3 overgrew amphibole1 and amphibole2 rims (BSE image); h) epidote in clinopyroxene1 cleavage (BSE image); i) radial fibres of amphibole rimming diopsidite boudin (crossed polars).

The preD1 foliation in serpentinite is crosscut by *amphibole rich layers* (Fig. 4.3a) where aggregates of decussate Amph3 occur together with Srp, Chl, and Mag. Amphibole3 forms up to 2-3 mm-sized subhedral crystals. Srp rims Amph3 crystals (Fig. 4.3i). Mag occurs as very fine grains in the matrix with chlorite and serpentine. Moreover, clinopyroxene1 relics were found in Amph3 from amphibole rich layers. Locally the contact between serpentinite and amphibole layers are gradual and Amph3 constitutes veins that are transverse to the serpentinite foliation. Locally, preD1 foliation in serpentinite is crosscut by a net of veins filled by serpentine fibres that are perpendicular to the veins.
Diopsidite is constituted mostly by clinopyroxene, minor amphibole, spinel, chlorite, and rare phengite and epidote. (Fig. 4.7a). Clinopyroxene1 shows granoblastic texture and clinopyroxene2 forms polygonal aggregates and rims of clinopyroxene1. Clinopyroxene1 forms up to 7 mm-sized crystals with slight undulose extinction, irregular edges and amphibole and magnetite exsolutions. Exsolution-free clinopyroxene2 forms micron-sized rims of clinopyroxene1 or up to mm-sized new subhedral grains (Fig. 4.7c, 7d). Amphibole1 constitutes discontinuous rims around clinopyroxene1, inclusions

in clinopyroxene1 and veins crosscutting clinopyroxene1 crystals (Fig. 4.7d). As it can be seen at the mesoscale in Fig. 4.4b, in the external part of diopsidite boudin, millimetre-sized amphibole1 are found in polygonal aggregates. Amphibole1 euhedral grains usually show sharp grain boundaries with clinopyroxene2 new grains. Amphibole2 constitutes the external rims around amphibole1 rims or rims clinopyroxene1 (Fig 6c). Locally, between amphibole1 and amphibole2 rims, a very thin rim of amphibole3 occurs (usually darker than amphibole1 and amphibole2 in BSE images as in Fig. 4.7d). Amphibole3 also occurs as submillimetre spikes, usually in radial aggregates around clinopyroxene1 and amphibole1 and amphibole2 rims, and in veins crosscutting clinopyroxene1 and clinopyroxene2 rims and rims of amphibole1 and amphibole2 (Fig. 4.7e). Finally, amphibole4 fibres are the finest-grained minerals in the rock matrix and in interstitial aggregates with respect to clinopyroxene1 crystals and amphibole rims (Fig. 4.7f and 7g). Euhedral to rounded spinel is found at the rims of clinopyroxene1, in amphibole1 rims and in polygonal aggregates. Chlorite occurs as flakes in amphibole3 veins and aggregates. Very rare phengite flakes occur in amphibole3 veins. Epidote is rarely found in clinopyroxene1 cleavages (Fig. 4.7h) and in polygonal amphibole1 aggregate.

Leucosome of diopsidite agmatite is constituted by quartz, plagioclase, and K-feldspar with minor amphibole, phengite, and epidote. Plagioclase and K-feldspar constitute up to centimetre-sized euhedral crystals in granoblastic texture with interstitial quartz that shows undulose extinction. Plagioclase is both albitic and anorthitic, with epidote exsolution. K-feldspar has white mica fine exsolution. Euhedral amphibole occurs in millimetre-sized grains often concentrated toward the diopsidite rims against the leucosome of the agmatite.

Both serpentinite and diopsidite boudin rims towards leucosome have up to 1 cm long amphibole radial fibres (Fig. 4.7i) that could represent the reaction rim with the melt.

4.7 Mineral chemistry

Clinopyroxene is diopside in serpentinite and in diopsidite (Fig. 4.8a and 8b). In serpentinite and amphibole-rich layer, clinopyroxene1, has Ca between 0.88 and 1.00 apfu and Mg between 0.79 and 0.95 apfu (Fig. 4.8c). Fe^{2+} is up to 0.14 apfu while Fe^{3+} is < 0.08 apfu. As shown in Fig. 4.4c, in diopsidite, clinopyroxene2 X_{Mg} is higher than in clinopyroxene1: Fe^{2+} in clinopyroxene2 varies between 0.06 and 0.18 apfu while it is up to 0.23 apfu in clinopyroxene1. Ca content is rather similar in both clinopyroxene1 and 2, and comprised between 0.89 and 1 apfu. Ti and Al are absent. Clinopyroxene compositions from Oman diopsidite (Python et al., 2007) are plotted in Fig. 4.8d-f for comparison. Clinopyroxene from the present study has lower X_{Mg} than Oman Clinopyroxene. Besides, Al_2O_3, Cr_2O_3, and TiO_2 (wt%) contents are comparable. Presuming the Argentera diopsidite has the same origin of Oman diopsidite, differences in Mg and Fe content can be due to the HT evolution. EMPA representative analyses are reported in table 4.3.

Amphibole composition is represented in Fig. 4.9a-d. In diopsidite amphibole1 is Mg-Hornblende (Fig. 4.4b) and amphibole2 is Tremolite. Amphibole3 and amphibole4 are actinolite, but amphibole3 has higher Al/(Al+Na) than amphibole4. In serpentinite, amphibole1 and amphibole2 are Mg-Hornblende (Fig. 4.4c), and amphibole2 Al/(Al+Na) is higher than in amphibole1. X_{Mg} is > 0.85 in amphibole1 and amphibole2. In amphibole-rich layers, amphibole1 is Mg-Hornblende while amphibole2 is Tremolite.

Spinel composition is shown in Fig. 4.9e. In serpentinite, spinel1 is Chromite (Cr and Fe up to 1.34 and 0.85 apfu respectively). Al is up to 1.25 apfu. In spinel1 to 2, Al varies between 1.68 and 1.89 apfu and Mg between 0.37 and 0.67 apfu; Fe^{2+} is up to 0.59 apfu and Cr is up to 0.32 apfu.

Spinel2 varies from Cr-Mag to Mag (Cr up to 0.35 apfu). In diopsidite, spinel1 preserves the highest Al and Mg contents (up to 1.67 and 52 apfu, respectively) with high Cr content (up to 1.06 apfu); spinel2 is Cr-Hercynite with slightly lower Mg (up to 0.5 apfu) than spinel1.

As shown in Fig. 4.9f, in serpentinite, X_{Mg} of serpentine varies between 0.90 and 0.95 with Fe = 0.14-0.27 apfu and Al up to 0.43 apfu. The Mg-richest Srp (X_{Mg}>0.93) occurs close to spinel aggregates. In amphibole-rich layer, compositions are similar to serpentinite: X_{Mg} varies between 0.89 and 0.93, and Fe ranges between 0.18 and 0.31 apfu; Al is comprised between 0.05 and 0.16 apfu. *Chlorite* composition is represented in Fig. 4.9g. In serpentinite, the Si poorest chlorite (Si<5.61 apfu sheridanite) occurs in spinel aggregates; in the rock matrix chlorite is mostly pennine. Clinochlore (Si>6.2 apfu) occurs in amphibole exsolution and at the rims of phlogopite. In diopsidite, Chl composition falls in penninite, clinochlore, and ripidolite fields. In diopsidite, *Epidote* Fe^{3+} is comprised between 0.25 and 0.26 apfu and Al between 2.54 and 2.63 apfu. In the diopsidite agmatite leucosome, *feldspar* is both albitic and anorthitic plagioclase.

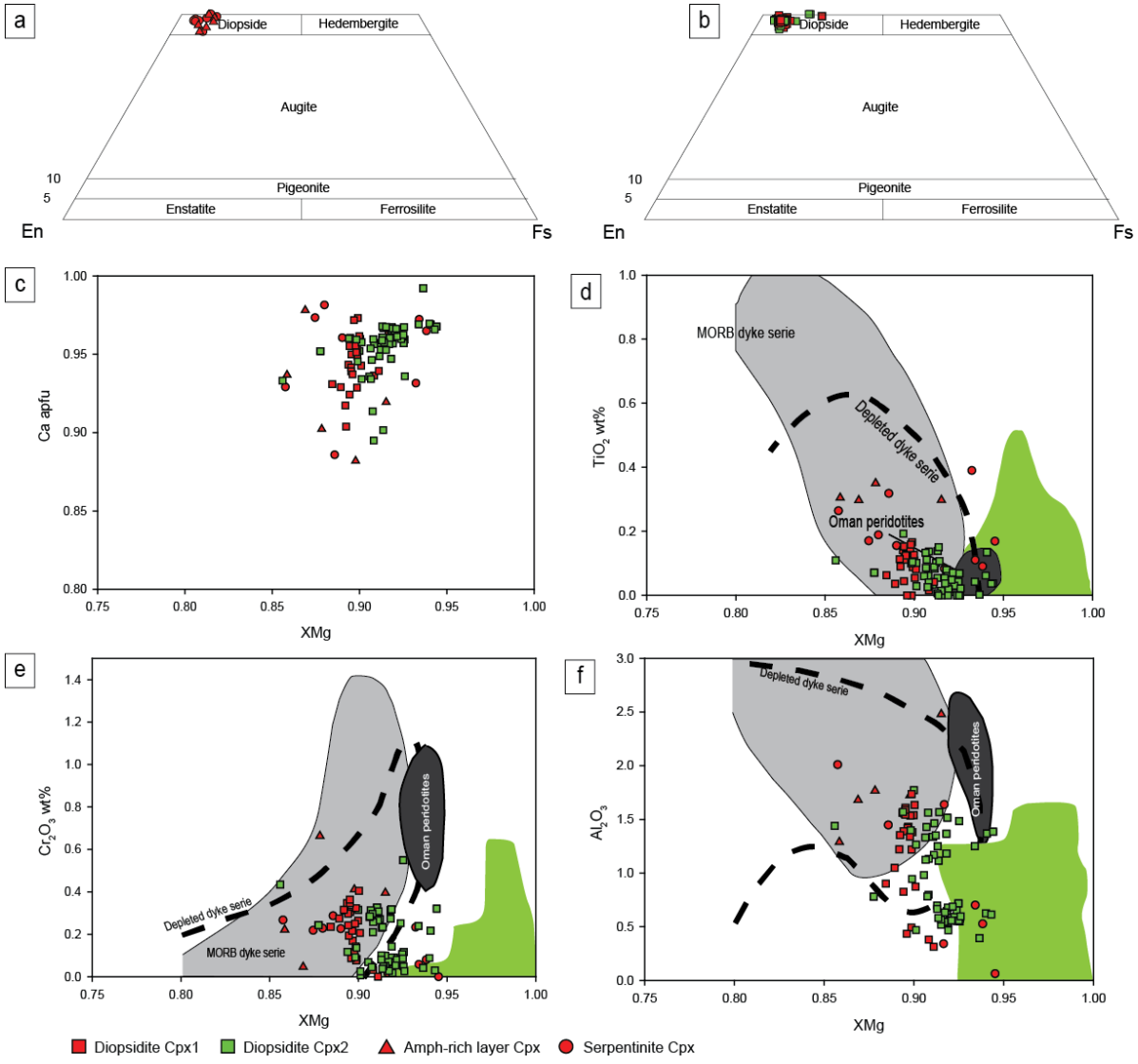

Fig. 4.8 - Clinopyroxene composition. Symbols: circle = serpentinite; triangle = amphibole layer; square = diopsidite; red = clinopyroxene1; green = clinopyroxene2. a) and b) classification diagrams are from Deer et al. (1992). In d, e, f, fields are from Python et al. (2007): green fields = Oman diopsidite clinopyroxene composition; grey fields = clinopyroxene compositions from MORB dyke series, black fields = clinopyroxene compositions from Oman peridotites.

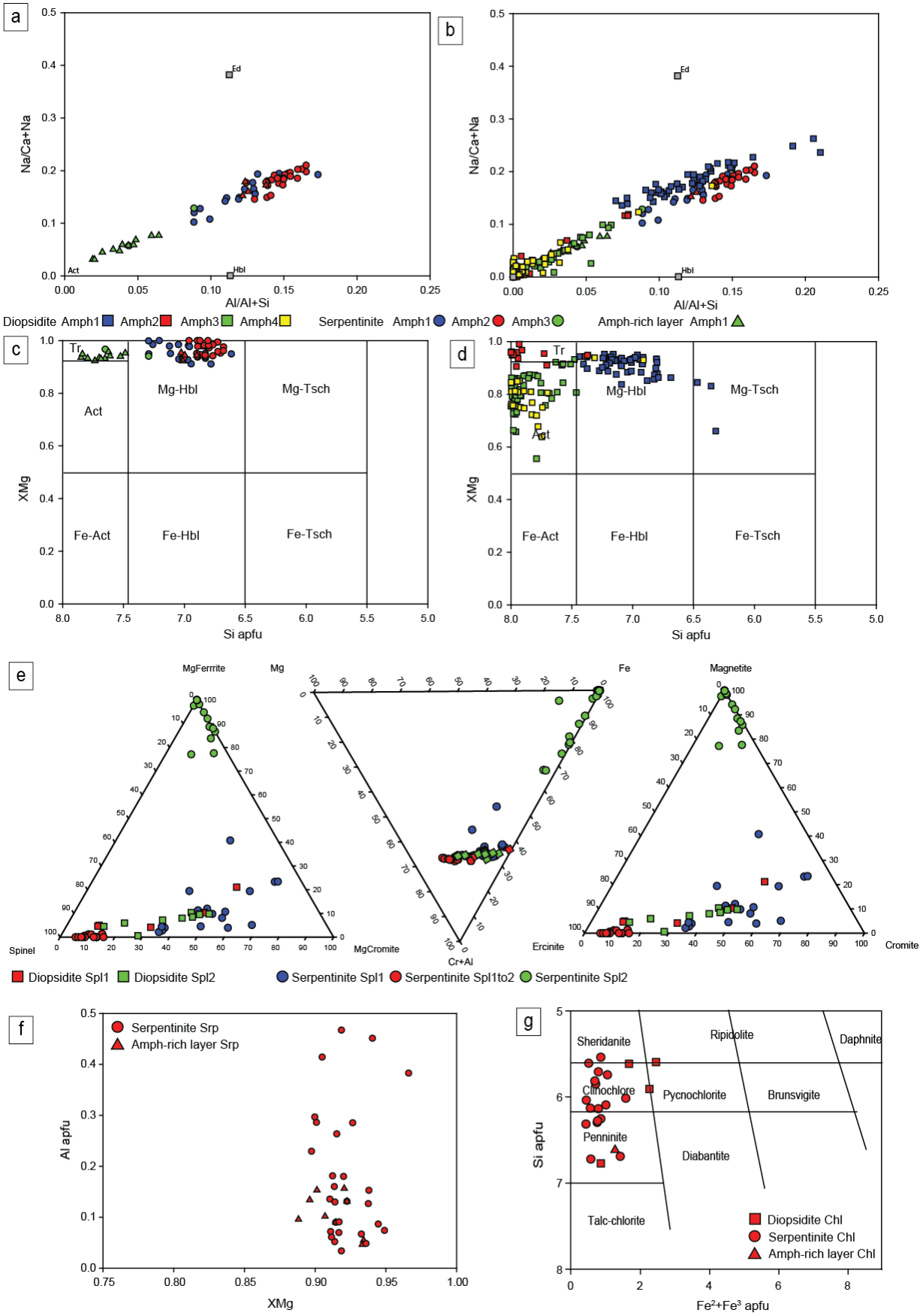

Fig. 4.9 - Mineral compositions. Symbols: circle = serpentinite; triangle = amphibole layer; square = diopsidite; a-d) amphibole composition; e) Spinel; f) serpentine; g) chlorite. Amphibole fields are from Deer et al. (1992); chlorite fields are from Python et al. (2007).

Table 4.3 – Representative EMPA analyses.

	Amphibole							
Roccia	Diopsidite				Serpentinite			
Texture	Amph1	Amph2	Amph3	Amph4	Amph1	Amph2	Amph3	Amph3
Species	Mg-Hbl	Tr	Act	Act	Mg-Hbl	Mg-Hbl	Mg-Hbl	Tr
SiO_2	51.32	58.08	55.30	56.33	52.19	48.40	49.10	55.90
TiO_2	0.11	0.03	0.00	0.00	0.25	0.29	0.29	0.06
Al_2O_3	6.91	0.03	0.40	0.38	6.12	9.28	9.27	2.14
Cr_2O_3	0.41	0.09	0.04	0.06	0.27	0.52	0.29	0.13
FeO	4.26	2.44	9.97	9.80	3.44	4.09	4.48	3.87
MnO	0.08	0.08	0.15	0.18	0.08	0.08	0.08	0.08
MgO	19.88	23.07	17.16	17.75	20.45	19.09	19.17	21.39
CaO	12.55	13.34	12.58	12.77	12.76	12.49	12.58	12.46
Na_2O	1.34	0.00	0.08	0.09	0.96	1.54	1.45	0.33
K_2O	0.06	0.02	0.05	0.04	0.11	0.31	0.24	0.06
NiO	0.03	0.00	0.02	0.00	0.12	0.04	0.02	0.00
Sum	96.94	97.18	95.74	97.39	96.76	96.14	96.97	96.41
Final wt% values								
MnO	0.08	0.08	0.15	0.18	0.08	0.08	0.08	0.08
Mn_2O_3	0.00	0.00	0.00	0.00	0.00	0.00	0.00	0.00
FeO	2.78	2.44	9.97	9.80	2.21	2.24	2.34	3.29
Fe_2O_3	1.64	0.00	0.00	0.00	1.37	2.06	2.38	0.65
H_2O+	2.16	2.19	2.12	2.12	2.17	2.15	2.15	2.18
Sum	99.26	99.37	97.86	99.51	99.06	98.50	99.36	98.65
Formula Assignments								
T (ideally 8 apfu)								
Si	7.19	7.99	8.00	8.00	7.29	6.87	6.90	7.79
Al	0.81	0.01	0.00	0.00	0.71	1.13	1.10	0.21
Ti	0.00	0.00	0.00	0.00	0.00	0.00	0.00	0.00
Fe^{3+}								
T subtotal	8.00	8.00	8.00	8.00	8.00	8.00	8.00	8.00
C (ideally 5 apfu)								
Ti	0.01	0.00	0.00	0.00	0.03	0.03	0.03	0.01
Zr		0.00	0.00	0.00	0.00	0.00	0.00	0.00
Al	0.33	0.00	0.07	0.06	0.30	0.42	0.43	0.15
Cr	0.05	0.01	0.01	0.01	0.03	0.06	0.03	0.01
Fe^{3+}	0.17	0.00	0.00	0.00	0.14	0.22	0.25	0.07
Ni	0.00	0.00	0.00	0.00	0.01	0.01	0.00	0.00
Mn^{2+}	0.00	0.00	0.02	0.01	0.00	0.00	0.00	0.00
Fe^{2+}	0.29	0.26	1.21	1.16	0.23	0.23	0.24	0.32
Mg	4.15	4.73	3.70	3.76	4.26	4.04	4.02	4.45
C subtotal	5.00	5.00	5.00	5.00	5.00	5.00	5.00	5.00
B (ideally 2 apfu)								
Mn^{2+}	0.01	0.01	0.00	0.01	0.01	0.01	0.01	0.01
Fe^{2+}	0.04	0.02	0.00	0.00	0.03	0.04	0.04	0.06
Ca	1.88	1.97	1.95	1.94	1.91	1.90	1.89	1.86
Na	0.07	0.00	0.02	0.02	0.05	0.05	0.06	0.07
B subtotal	2.00	2.00	1.97	1.98	2.00	2.00	2.00	2.00
A (from 0 to 1 apfu)								
Na	0.30	0.00	0.00	0.00	0.21	0.37	0.34	0.02
K	0.01	0.00	0.01	0.01	0.02	0.06	0.04	0.01
A subtotal	0.31	0.00	0.01	0.01	0.23	0.43	0.38	0.03
O (non-W)	22.00	22.00	22.00	22.00	22.00	22.00	22.00	22.00
W (ideally 2 apfu)								
OH	2.00	2.00	2.00	2.00	2.00	2.00	2.00	2.00
W subtotal	2.00	2.00	2.00	2.00	2.00	2.00	2.00	2.00
Sum T,C,B,A	15.31	15.00	14.98	14.99	15.23	15.43	15.38	15.03

	Antigorite	
Rock	Serpentinite	Amph layer
Texture	Atg2	Atg3
SiO_2	42.52	42.22
TiO_2	0.04	0.03
Al_2O_3	2.84	1.75
Cr_2O_3	0.00	0.00
FeO	0.15	7.84
MnO	4.38	0.32
MgO	37.20	34.96
CaO	0.20	0.05
Na_2O	0.00	0.00
K_2O	0.01	0.00
NiO	0.03	0.03
Sum	87.37	87.19
116 ox.		
Si	1.94	1.97
Al	0.15	0.10
Ti	0.00	0.00
Cr	0.00	0.00
Fe^{2+}	0.17	0.31
Mn	0.01	0.01
Mg	2.53	2.43
Ca	0.00	0.00
Na	0.01	0.00
K	0.00	0.00
Ni	0.00	0.00

	Phengite
Rock	Diopsidite
texture	Ph1
SiO_2	48.69
TiO_2	0.05
Al_2O_3	26.92
Cr_2O_3	0.69
FeO	2.27
MnO	0.09
MgO	5.55
CaO	0.37
Na_2O	0.05
K_2O	11.06
NiO	0.11
Sum	95.85

	Chlorite		
Roccia	Serpentinite	Amph layer	Diopsidite
Texture	Chl2	matrix	Chl
SiO_2	32.90	33.65	35.28
TiO_2	0.07	0.04	0.00
Al_2O_3	15.50	12.32	14.28
Cr_2O_3	0.38	0.18	0.80
FeO	4.70	7.72	5.36
MnO	0.05	0.12	0.05
MgO	32.53	30.90	29.60
CaO	0.03	0.07	0.34
Na_2O	0.00	0.11	0.01
K_2O	0.00	0.31	0.00
NiO	0.03	0.09	0.15
Sum	86.19	85.51	85.86
28 ox.			
Si	6.30	6.62	6.77
Ti	0.01	0.01	0.00
Al	3.50	2.85	3.23
Cr	0.06	0.03	0.12
Fe^{2+}	0.75	1.27	0.86
Mn	0.01	0.02	0.01
Mg	9.28	9.06	8.47
Ca	0.01	0.01	0.07
Na	0.00	0.04	0.00
K	0.00	0.08	0.00
Ni	0.00	0.01	0.02
Sum	19.92	20.00	19.56

	Clinopyroxene					Epidote		Phlogopite		Spinel			
Rock	Serpentinite	Amph- layer	Diopsidite			Rock	Diopsidite	Rock	Serpentinite	Rock	Serpentinite		Diopsidite	
Texture	Cpx1	Cpx1	Cpx1	Cpx2		Texture	Ep1	texture	Phl1	Mineral	Cr-Mg erc 1 to 2	Mag	Al-Crm1	Cr-Erc2
SiO_2	51.86	52.83	54.04	54.01		SiO_2	37.79	SiO_2	38.62	Texture	1 to 2	2	1	2
TiO_2	0.39	0.35	0.06	0.11		TiO_2	0.08	TiO_2	0.21	SiO_2	0.01	1.54	0.04	0.07
Al_2O_3	3.28	1.77	1.18	1.44		Al_2O_3	27.17	Al_2O_3	17.39	TiO_2	0.00	0.09	0.45	0.02
Cr_2O_3	0.23	0.66	0.27	0.43		Cr_2O_3	1.86	Cr_2O_3	0.60	Al_2O_3	50.43	1.02	11.50	49.75
FeO	4.06	4.95	2.91	4.52		FeO	3.95	FeO	5.18	Cr_2O_3	13.20	0.04	36.80	12.48
MnO	0.17	0.20	0.11	0.21		MnO	0.29	MnO	0.10	FeO	25.98	90.64	42.47	24.62
MgO	15.45	15.44	17.04	15.07		MgO	0.03	MgO	23.73	MnO	1.56	0.00	2.97	0.28
CaO	23.72	22.87	24.26	23.63		CaO	21.02	CaO	0.17	MgO	8.27	2.57	0.37	12.15
Na_2O	0.43	0.54	0.09	0.02		Na_2O	0.01	Na_2O	0.11	CaO	0.50	0.01	0.23	0.18
K_2O	0.10	0.05	0.00	0.31		K_2O	0.01	K_2O	8.12	Na_2O	0.12	0.15	0.09	0.22
NiO	0.00	0.00	0.00	0.03		NiO	0.06	NiO	0.09	K_2O	0.06	0.00	0.08	0.00
Sum	99.68	99.66	99.96	99.79		Sum	92.27	Sum	94.33	NiO	0.02	0.00	0.00	0.00
4 cat. 6 ox.						8 cat., 15 ox.		22 ox.	22.00	Sum	100.15	96.07	95.01	99.77
Si	1.90	1.95	1.97	1.99		Si	3.10	Si	5.50	Fe_2O_3	1.25	67.27	15.25	4.33
Ti	0.10	0.05	0.03	0.01		Al.IV	0.00	Ti	0.02	FeO	24.86	30.11	28.75	20.72
Al.IV	0.04	0.02	0.02	0.05		Al.VI	2.63	Al	2.92	Cation				
Al.VI	0.01	0.01	0.00	0.00		Ti	0.00	Cr	0.07	Si	0.00	0.06	0.00	0.00
Cr	0.01	0.02	0.01	0.01		Cr	0.12	Fe^{2+}	0.62	Ti	0.01	0.00	0.01	0.00
$Fe3^+$	0.06	0.04	0.01	0.00		Fe3+	0.25	Mn	0.01	Al	1.18	0.04	0.50	1.63
Fe^{2+}	0.06	0.12	0.08	0.14		Fe2+	0.02	Mg	5.04	Cr	0.72	0.00	1.06	0.27
Mn	0.00	0.00	0.00	0.00		Mg	0.00	Ca	0.03	Fe3+	0.08	1.84	0.42	0.09
Mg	0.84	0.85	0.93	0.83		Ni	0.00	Na	0.03	Fe2+	0.53	0.91	0.88	0.48
Ca	0.93	0.90	0.95	0.93		Mn	0.02	K	1.48	Mn	0.01	0.00	0.09	0.01
Na	0.01	0.01	0.00	0.01		Ca	1.85	Ni	0.01	Mg	0.47	0.14	0.02	0.50
K	0.03	0.04	0.01	0.02		Na	0.00	Sum	15.73	Ca	0.00	0.00	0.01	0.01
Ni	0.00	0.00	0.00	0.00		K	0.00			Na	0.00	0.00	0.01	0.00
Sum	4	4	4	4						K	0.00	0.00	0.00	0.00
FeO	2.00	3.81	2.71	4.52		FeO	0.33			Ni	0.00	0.00	0.00	0.01
Fe_2O_3	2.29	1.27	0.22	0.00		Fe_2O_3	4.02			Sum	3.00	3.00	3.00	3.00
New sum	99.91	99.79	99.99	99.79		New sum	92.68							

Table 4.3 – Representative EMPA analyses.

4.8 Metamorphic evolution

The metamorphic evolution of diopsidite boudins has been modelled using Theriak-Domino software (de Capitani and Brown, 1987) in the CFMASH system with H_2O in excess and the database tcds62c. The composition has been obtained from whole rock analysis (sample G33; table 4.1). All Fe has been considered as FeO, and Fe_2O_3 and TiO_2 were neglected. The resulting composition in moles is SiO_2 50.8, Al_2O_3 2.68, FeO 3.15, MgO 24.36, CaO 19.59. Minerals activity models are from Green 2016) for clinopyroxene and amphibole, White et al. (2014) for chlorite, garnet, and ortopyroxene. Endmember clinozoisite was used. This attempt of modelling is a preliminary result that will be useful to furtherly constrain diopsidite metamorphic evolution. In the obtained pseudosection (Fig. 4.10), clinopyroxene is always stable; garnet occurs at HT-HP conditions while epidote is stable up to P < 1.4 GPa and T < 700 °C. Plg occurs at HT-LP conditions; amphibole is stable at high P and disappears at HT-LP conditions. Quartz occurs at T > 620 °C. The field Cpx + Amph + Ep is the most representative of the Cpx2 + Amph1 + Spl2 + Ep assemblage (M2 stage; table 4.2) observed in diopsidite. Spinel is not predicted as Fe_2O_3 was neglected. The field extends, with a temperature intervals of 50 °C, between 590 and 690 °C, and up to 1.8 GPa. In this field, the relative modal amount of minerals is close to that observed in the rocks. Further development of the modelling will aim at refining the chosen composition by estimating the FeO-Fe_2O_3 ratio according to oxides occurrence, and the H_2O content by T-X and P-X calculations.

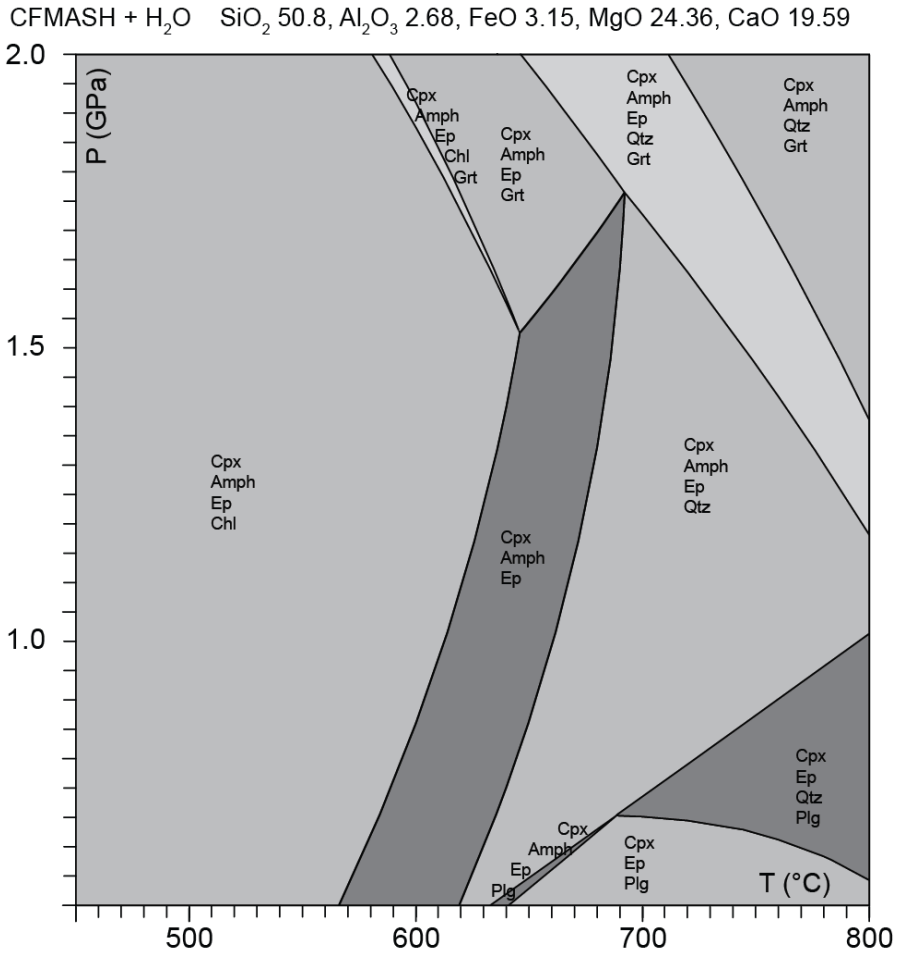

Fig. 4.10 - CFMASH pseudosection with H_2O in excess for the composition SiO_2 50.8, Al_2O_3 2.68, FeO 3.15, MgO 24.36, CaO 19.59 (mol%), corresponding to diopsidite boudins.

4.9 Discussions

On the eastern slope of Lago Brocan, paragneiss diatexite and anatexite are juxtaposed to different types of agmatite rocks. In agmatite, boudins of amphibolite, amphibole gneiss, marble, serpentinite, and diopsidite occur. In diatexite, the dominant fabric is the S1 foliation that is locally folded by D2. Although S1 is not recorded in anatexite and in the different types of agmatite, the majority of the lithostratigraphic contacts are parallelised into S1 as can be seen in Fig. 4.2. In paragneiss diatexite, D2 asymmetrical tight folds locally affect S1. As leucosome in diatexite is parallel to S1, S1 foliation is contemporaneous to the migmatisation. Despite this, the occurrence of gradual and fuzzy contacts between diatexite and anatexite, and the occurrence of diatexite boudins in anatexite, indicate that migmatisation continued after the complete development of S1.

Agmatite boundaries and, in particular, diopsidite agmatite lenses, occur mostly parallelised to S1, as can be seen in Fig. 4.2, suggesting that the juxtaposition of diatexite, anatexite, diopsidite and amphibole agmatites is controlled by the development of S1 and contemporaneous to D1. In agmatites, the leucosome volume is up to 30%. As observed at the microscale by Rosenberg and Handy (2005), little percentages (< 10%) of melt cause a dramatic drop of the strength of the partially molten rock. Despite this, agmatites are only locally mixed up. This suggests that the rheology of different agmatites was different and that their juxtaposition can have been non-contemporaneous to S1 development. However, the preserved compositional differences among agmatites, allows the present-day lithostratigraphy to be interpreted as the vestiges of a migmatized and deformed "original" lithostratigraphy that included the protoliths of paragneisses, amphibolites, and amphibole gneisses, carbonate-rich rocks, diopsidites, and serpentinites.

Centimetre- to metre-sized diopsidite boudins preserve a polygonal texture of clinopyroxene aggregates, overprinted by polyphase coronitic fabric of four different stages of amphibole growth. The comparison of whole rock composition with those of Oman diopsidite (Python et al., 2007) shows that WR major elements of Argentera diopsidite are very close to Oman and Créton diopsidites (Fig. 4.5) despite olivine and plagioclase occurring in Oman diopsidite and not in Argentera diopsidite. Similarly to Oman diopsidite, clinopyroxene composition of the studied diopsidite has very low contents in Al_2O_3, Cr_2O_3, and TiO_2, but X_{Mg} is lower than X_{Mg} in Oman diopside. The relative depletion of Mg in clinopyroxene can be due to the HT metamorphism with the growth of coronitic hornblende.

Locally, serpentinite boudins are associated with diopsidite agmatite. Serpentinite preserves rare clinopyroxene relics in metamorphic hornblende. Furthermore, spinel locally preserve compositions that are comparable to spinel composition of oceanic origin (see for comparison spinels from MAR in Picazo et al., 2016). Hence, serpentinite could represent the relic of a spinel lherzolite. Diopsidite is a peculiar lithotype and, even though the temperature of its formation is still debated, the association of diopsidite and serpentinite is recognised as product of ocean-floor metasomatism (Python et al., 2007; Bach and Klein, 2009; Python et al., 2011).

The consequence of an oceanic origin of diopsidite is that serpentinite and diopsidite of Lago Brocan is that the remnants of the oceanic lithosphere entrapped in the Variscan belt and would represent remnants of lithosphere of Rheic ocean. This confirms the importance of ultramafic rocks in localising the suture zone of the Variscan belt, as already observed in other Variscan complexes (Guillot and Ménot, 2009; Arenas and Sanchez, 2015). The occurrence of phlogopite in hornblende-bearing

assemblage in serpentinite can be due to the interaction of serpentinite with K-rich fluids that could be related to the melting of continental affinity material during the migmatisation. PT conditions for Cpx2 + Amph1 + Spl2 + Ep bearing assemblage (M2 metamorphic stage) in diopsidite have been obtained by the construction of a pseudosection and they represent a preliminary result. The assemblage is stable at temperatures comprised between 590 and 690 °C, and at pressures up to 1.8 GPa. Although temperatures are well constrained, pressure variation is very wide, from eclogite to amphibolite facies conditions (Fig. 4.11), and a further modelling refinement is necessary to detail diopsidite evolution.

4.10 Conclusion

The petro-structural study of the migmatized rocks at Lago Brocan, part of the Argentera ECM, allowed identifying relics of a migmatized lithostratigraphy that was made of metasediments, mafic and ultramafic rocks. The structural analysis clearly suggests that these rocks were juxtaposed thanks to the high percentage of melt that percolated the lithostratigraphy during the development of S1 foliation. In particular, microstructural and minero-chemical analyses, indicate that diopsidite and spinel lherzolite boudins acted as refractory lithotypes, preserving textural and compositional relics that predate S1. The preliminary petrological modelling indicates that during M2 metamorphic stage, diopsidite registered metamorphic condition compatible with a geothermal gradient typical of a warm subduction zone then evolving to a higher temperature gradient, compatible with continental collision (Fig. 4.11).

Finally, serpentinite and diopsidite boudins represent very likely the vestiges of an oceanic lithosphere, that underwent the entire Variscan metamorphic evolution, and a fragment of the suture of the Variscan orogenic belt, transposed at the orogen-scale by the syn-collisional migmatisation of the Argentera Massif.

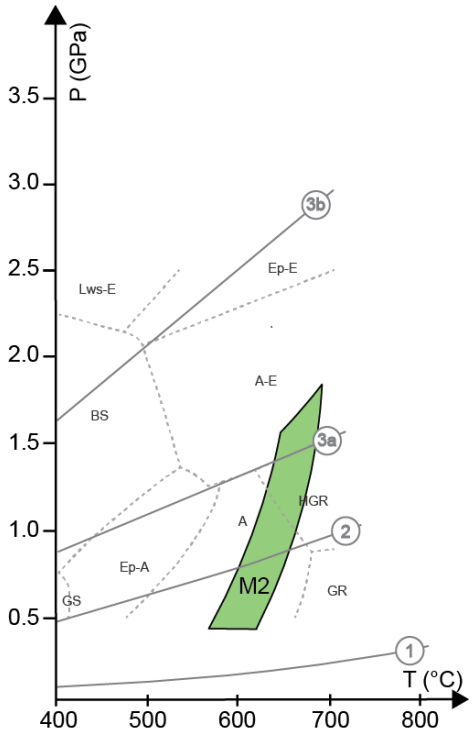

Fig. 4.11 - metamorphic conditions of M2 assemblage in diopsidite boudins. Geotherms are after Cloos (1993): (1) near spreading ridge or volcanic arc; (2) normal gradient of old plate interior; (3a) cold subduction zones; (3b) warm subduction zones.

Chapter 5
Discussions and Conclusions

5.1 Comparison of tectono-metamorphic record in ultramafics from Penninic and Helvetic domains: insights into the geodynamic evolution of Piemonte Zone and Argentera Massif

The tectono-metamorphic evolution of serpentinites and associated rocks has been investigated in the Alpine ophiolitic Piemontese Zone (PZ) – in the Zermatt-Saas Zone (ZSZ) and near the Sesia-Lanzo Zone (SLZ) rim – and in the Variscan migmatites of the Argentera External Crystalline Massif (ECM). In the Zermatt-Saas Zone serpentinite of Valtournanche, meso- and microstructural analyses have been coupled with petrological investigation, geochemistry, and radiometric dating: results indicate that serpentinite has been affected by Jurassic percolation (Rebay et al., 2018) of Fe- and Mg- gabbros; this is suggested by pyroxenite trace elements analysis and zircon dating, and ocean-floor to syn-subduction metasomatism, testified by rodingite and diopsidite, in agreement with Zanoni et al. (2012, 2016). Fold systems and related grain-scale foliation history reveals four deformation phases (D1 to D4). The metamorphic peak was reached under UHP conditions (P = 2.8–3.3 GPa, T = 600–630 °C), manifested by Ti-chondrodite and Ti-chondrodite + Ti-clinohumite bearing assemblages, predating the regionally dominant S2 foliation (2.2–2.8 GPa and 580–660 °C) dated at 60-70 Ma (Luoni et al., 2018; Luoni et al., 2019; Rebay et al., 2012, 2018), and the exhumation under Epidote-Amphibolite facies condition (550 ± 50 °C and 1 ± 0.4 GPa). The comparison of PT conditions estimated for the subsequent stages with geotherms extracted from a numerical modelling of Alpine (e.g. Regorda et al., 2017) admits a "vertical paleogeography" for Valtournanche serpentinite evolution, indicating that serpentinite was at 100 - 145 km from the trench, at a depth of 80-110 km between 80 and 72 Ma (pre-D2), and at a distance from the trench variable from 125 km at 70 Ma to 155 km, for a depth ranges between 85 and 55 km (D2) at 60 Ma. The new UHP peak conditions in Créton serpentinite allow to individuate a new UHP unit in the Piemonte Zone of the Western Alps, besides the Cignana Lake Unit (Reinecke, 1991; Frezzotti et al., 2011). The comparison of the obtained evolution for Valtournanche serpentinite with PT conditions and ages for Zermatt-Saas P-peaks (see Rebay et al., 2018) goes along with the idea that Zermatt-Saas Zone is composed of slices of oceanic lithosphere that registered heterogeneous and diachronic metamorphic peaks (Luoni et al., 2018; Luoni et al., 2019). Furthermore, the geochemistry of pyroxenites and the serpentinite-diopsidite association indicate that Créton rocks may well represent the relic of an oceanic lithosphere affected by mid-ocean ridge HT hydrothermal metasomatism. According to the Wilson cycle, this would be a proof that Zermatt-Saas Zone lithosphere reached the oceanic-stage maturity. These localised traces of ocean-floor HT evolution suggest that the Zermatt-Saas Zone is a puzzle of different portions of oceanic lithosphere - as already suggested by Rebay et al. (2018) and Gilio et al. (2019) - that were heterogeneously coupled and decoupled in the mantle wedge during the subduction-collision process, registering different PTdt

paths, and amalgamated most probably according to their rheology and became conspicuous part of the Alpine subduction complex.

The petro-structural study of Gias Vej serpentinite (SLZ rim) add a new mosaic-tile to the tectono-metamorphic evolution of the polydeformed and polymetamorphosed rocks at the PZ-SLZ boundary. During the Alpine convergence, serpentinite reached eclogite-facies conditions (Pmin > 1.4-1-7 GPa and T_{max} < 680°C) under a depressed thermal state, testified by Ti-clinohumite-bearing assemblages predating S2 foliation development, and was successively exhumed under epidote-amphibolite facies conditions materialised in coronitic fabrics. HP conditions are compatible with a cold subduction zone geotherm, whereas exhumation conditions could be contemporaneous to Alpine collisional stages. Such an evolution is similar to that proposed for ZSZ serpentinite, and includes the Gias Vej serpentinite to a Zermatt-Saas type ophiolite. On the other hand, Gias Vej serpentinite belongs to a mixture of up-to-kilometre continental and oceanic slices of subduction-related material that reached lower P-peak conditions with respect to ZSZ serpentinite; furthermore, its structural and metamorphic evolution is coherent with that of the adjacent rocks (Spalla et al., 1983) indicating that continental and oceanic crustal slices of this portion of the Alpine subduction complex were coupled before they reach climax conditions. The less dense continental material probably acted as a "float" for the denser oceanic lithosphere material (such as serpentinite and gabbros), not allowing the attainment of higher P conditions that are documented in mostly oceanic domains as ZSZ.

At Lago Brocan, in the Argentera External Crystalline Massif, the syn-collisional Variscan migmatisation did not disrupt the pre-migmatitic lithostratigraphic sequence consisting of metasediments, amphibolites, serpentinites, and diopsidites; presently these rocks constitute a sequence preserving its compositional uniqueness. Syn-migmatitic deformation parallelised lithological boundaries and the S1 foliation. Integration of microstructural and minero-chemical analysis of selected microsites underlined pre-S1 mineralogical and textural relics ; (i) diopsidite preserves a granoblastic fabric overgrown by coronitic amphibole, that might well represent the original fabric of the rock; (ii) diopsidite mineral assemblages indicate a pervasive re-equilibration of these rocks under HT-LP conditions; (ii) in serpentinite, pre-S1 foliation, mantle-like spinel composition and diopside relics suggest that serpentinite protolith might well be a spinel lherzolite; (iii) the association of diopsidite, serpentinite, and rare marbles, may attest an oceanic provenance for these lithotypes, also on the basis of geochemical data, as more robustly proposed for the Créton serpentinite.

The Argentera Massif, as the other EMCs, is a portion of the Variscan belt that was fragmented and re-equilibrated during Alpine collisional tectonics. In contrast to the Alpine belt, where ophiolitic units mark the Alpine suture zone in well-defined structural and lithostratigraphic domains (e.g. Piemontese Zone), in EMCs continental and oceanic domains are strongly re-elaborated by the late orogenic collapse of the Variscan chain (e.g. von Raumer and Stampfli, 2008 and refs. therein). Therefore, rocks of oceanic lithosphere affinity could represent the rare fragments of the ophiolitic units that marked the Variscan suture and were successively transposed by the (syn-S1) migmatisation, as recently suggested by eclogitic relics in Argentera magmatic gneiss (Jouffray et al., 2019).

5.2 Resolution of analytical methods

Complexities of finite strain fields of poly-orogenic zones, are to be solved to reconstruct earlier rock sequences that may indicate original environments, and to delimit rock associations that underwent the same tectonic trajectory as coherent tectonometamorphic units during orogeny. Materials selected for laboratory work contain sequences of meso- and microstructural imprints containing parts of the tectonic evolution of both mono- and poly-orogenic environments (in our case the Piemontese Zone in the Penninic of the Western Alps and the Argentera EMC – Provençal domain of the Alpine collisional front at the Alpine belt termination within the Western Mediterranean).
Single minerals and equilibrium assemblages, within planar fabrics and separated according to temporal sequences, constitute the base of thermobarometric estimates and/or petrological modelling. Similarly, the timing constrains leads to dating of selected microstructural sites and to the geochemical investigation of the most preserved pristine mineral compositions. The physical model tests the compatibility of the data set.
In Créton, for example, 1:20 structural mapping led (i) to outline the pre-Alpine structural evolution of the lithostratigraphy; (ii) to correlate pre-D2 structures and fabrics with the S2 regional foliation; (iii) to constrain the radiometric data on Alpine metamorphic minerals in a well-established fabric chronology at the regional scale (D2 structures are dated at 65 ± 5 Ma); (iv) to select pre-D2 mineral aggregates, allowing to infer UHP peak conditions, thanks to Ti-chondrodite and Ti-clinohumite occurrence, and to detail the oceanic evolution, through the trace element analyses of pyroxene cores in pyroxenite and the occurrence of hydrothermal garnet micro-inclusions in diopsidite. In Gias Vej serpentinite, the multiscale structural analysis correlates the serpentinite structural evolution with the regional structural setting and determined the sampling (as in the case of Ti-Chu Cpx- Ol- bearing layers) where eclogite-facies mineral assemblages survived the development of subsequent fabrics. In the Argentera Massif, the mesostructural analysis at the Lago Brocan revealed the relationships between S1 foliation and the pre-Variscan lithostratigraphy, the juxtaposition of the different types of migmatites, the relative chronology between the main fabrics and the superposed metamorphic assemblages supporting fabric succession. Furthermore, the coupling of microstructural and minero-chemical analyses of selected sites indicated the relic textures and mineral compositions that predate the migmatisation and transposition of a lithostratigraphic association from a Variscan suture zone.

5.3 Conclusive remarks

In conclusion, the investigation of ultramafic rocks by a structure-driven multidisciplinary approach, can unravel the most complete memory of the divergent and convergent tectonic evolution of old oceans. In Valtournanche, Créton serpentinite has been interpreted as a slice of mid-ocean ridge lithosphere, affected by gabbroic percolation and hydrothermalism, deeply involved in the Alpine subduction complex, reaching UHP conditions prior to be exhumed at HP conditions 60-70 Ma and incorporated in a mix of slices of oceanic material of heterogeneous origin and metamorphic evolution. Gias Vej serpentinite registered Eclogite facies conditions and was coupled with slices of continental material at the southern border of the Sesia Lanzo Zone before the record of Pmax conditions. At Lake Brocan in Valle Gesso, remnants of serpentinised spinel lherzolite and diopsidite are suggested to

represent a most probable vestigial suture zone of the Rheic Ocean in the External Crystalline Massif of Argentera; this relict survived repeated transpositions and dismembering during migmatisation of the deep Variscan crust related to Variscan continental collision. More generally, similar investigation strategies of laboratory procedures, based on solid structural fieldwork, may more diffusely support circumscription of tectonic units in ocean-derived sequences and contribute to redefine their translational tectonic trajectories during mountain-building processes.

Chapter 6
References

Afonso, J. C., and Ranalli, G. (2004). Crustal and mantle strengths in continental lithosphere: is the jelly sandwich model obsolete? Tectonophysics, 394, 221–232. https://doi.org/10.1016/j.tecto.2004.08.006

Alvarez, W. (1976). A former continuation of the Alps. Geological Society of America Bulletin, (60609), 891–896.

Amato, J. M., Johnson, C. M., Baumgartner, L. P., and Beard, B. L. (1999). Rapid exhumation of the Zermatt-Saas ophiolite deduced from high precision Sm-Nd and Rb-Sr geochronology. Earth and Planetary Science Letters 171, 425–438.

Angiboust, S., and Agard, P. (2010). Initial water budget: The key to detaching large volumes of eclogitized oceanic crust along the subduction channel? Lithos, 120(3–4), 453–474. https://doi.org/10.1016/j.lithos.2010.09.007

Angiboust, S., Agard, P., Jolivet, L., and Beyssac, O. (2009). The Zermatt-Saas ophiolite: The largest (60-km wide) and deepest (c. 70-80km) continuous slice of oceanic lithosphere detached from a subduction zone? Terra Nova, 21(2008), 171–180. https://doi.org/10.1111/j.1365-3121.2009.00870.x

Angiboust, S., Langdon, R., Agard, P., Waters, D. and Chopin, C. (2012). Eclogitization of the Monviso ophiolite (W. Alps) and implications on subduction dynamics. Journal of Metamorphic Geology 30, 37–61.

Aoki, K. I., Fujino, K., and Akaogi, M. (1976) Titanochondrodite and titanoclinohumite derived from the upper mantle in the Buell Park kimberlite, Arizona, USA. Contributions to Mineralogy and Petrology, 56(3), 243-253.

Arenas, R. and Sánchez-Martínez, S. (2015). Variscan ophiolites in NW Iberia: Tracking Lost Palaeozoic Oceans and the Assembly of Pangea. Episodes, 38(4), 315–330. https://doi.org/10.18814/epiiugs/2015/v38i4/82427

Argand, E. (1916). Sur l'arc des Alpes occidentales. Eclogae Geologicae Helvetiae, 14, 149–204.

Argand, E., Blösch, E., and Heim, A. (1911). Les nappes de recouvrement des Alpes pennines et leurs prolongements structuraux. In Kommission Bei A. Francke (Vorm. Schmid and Francke), 31–33, 31.

Arthaud, F., and Matte, P. (1977). Late Palaeozoic strike-slip faulting in southern Europe and northern Africa: Result of a right-lateral shear zone between the Appalachians and the Urals. Bulletin of the Geological Society of America, 88(9), 1305–1320. https://doi.org/10.1130/0016-7606(1977)88<1305:LPSFIS>2.0.CO;2

Austrheim, H., and Prestvik, T. (2008). Rodingitization and hydration of the oceanic lithosphere as developed in the Leka ophiolite, north-central Norway. Lithos, 104(1–4), 177–198. https://doi.org/10.1016/j.lithos.2007.12.006

Bach, W., and Klein, F. (2009). The petrology of sea floor rodingites: Insights from geochemical reaction path modelling. Lithos, 112(1–2), 103–117. https://doi.org/10.1016/j.lithos.2008.10.022

Balestro, G., Festa, A., and Dilek, Y. (2019). Structural architecture of the Western Alpine Ophiolites, and the Jurassic seafloor spreading tectonics of the Alpine Tethys. Journal of the Geological Society, jgs2018-099.

Baletti, L., Zanoni, D., Spalla, M. I., and Gosso, G. (2012). Structural and petrographic map of the Sassa gabbro complex (Dent Blanche nappe, Austroalpine tectonic system, Western Alps, Italy). Journal of Maps, 8(4), 413–430. https://doi.org/10.1080/17445647.2012.745678

Ballèvre, M., and Merle, O. (1993). The Combin Fault: compressional reactivation of a Late Cretaceous-Early Tertiary detachment fault in the Western Alps. Schweizerische Mineralogische Und Petrographische Mitteilungen, 73(2), 205–227.

Barnicoat, A. C., and Fry, N. (1986). High-pressure metamorphism of the Zermatt-Saas ophiolite zone, Switzerland. Journal of the Geological Society, 143(4), 607–618. https://doi.org/10.1144/gsjgs.143.4.0607

Barnicoat, A. C. (1988). Zoned high-pressure assemblages in pillow lavas of the Zermatt-Saas ophiolite zone, Switzerland. Lithos, 21, 227–36.

Baumann, C., Gerya, T. V. and Connolly, J. A. D. (2010). Numerical modelling of spontaneous slab-breakoff dynamics during continental collision. Geological Society, London, Special Publications, 332, 99–114.

Bearth, P. (1956). Geologische Beobachtungen im grenzgebiet der lepontischen und Penninischen Alpen. Eclogae Geologicae Helvetiae, 49, 279–290.

Bearth, P. (1967). Die ophiolite der Zone von Zermatt-Sass Fee. Beitrag Geologische Karte Schweitz, 132, 1–130.

Bearth, P., and Schwandler, H. (1981). The post-Triassic sediments of the ophiolite zone Zermatt-Saas Fee and the associated manganese mineralizations. Eclogae Geologicae Helvetiae, 74(1), 189–205.

Beltrando, M., Rubatto, D., and Manatschal, G. (2010). From passive margins to orogens: The link between ocean-continent transition zones and (ultra)high-pressure metamorphism. Geology, 38(6), 559–562. https://doi.org/10.1130/G30768.1

Bigi, G., Cosentino, D., Parotto, M., Sartori, R., and Sandone, P. (1990). Structural Model of Italy and gravity map. Scale 1: 500.000, Sheets 1-9 C.N.R., Progetto finalizzato Geodinamica. Quaderni de «La Ricerca Scientifica», 114(3).

Bodinier, J. L., Dupuy, C., Dostal, J., and Carme, F. (1982). Geochemistry of ophiolites from the Chamrousse complex (Belledonne Massif, Alps). Contributions to Mineralogy and Petrology, 78(4), 379–388. https://doi.org/10.1007/BF00375200

Bogdanoff, S., and Plauen, A. (1980). Les gneiss et migmatites du massif de l'Argentera (Alpes maritimes); apport de deux coupes geochimiques. Bulletin de La Societe Geologique de France, 7(3), 353–358.

Bousquet, R., Engi, M., Gosso, G., Oberhänsli, R., Berger, A., Spalla, M. I., and Goffè, B. (2004). Explanatory notes to the map: Metamorphic structure of the Alps Transition from the Western to the Central Alps. Mitteilungen Der Österreichischen Mineralogischen Gesellschaft, 149, 145–156.

Bowtell, S. A., Cliff, R. A., and Barnicoat, A. C. (1994). Sm-Nd isotopic evidence on the age of eclogitization in the Zermatt-Saas ophiolite. Journal of Metamorphic Geology, 12(2), 187–196. https://doi.org/10.1111/j.1525-1314.1994.tb00013.x

Brongniart, A. (1813). Essai d'une classification minéralogique des roches mélangéese. Journal Des Mines, 34, 190–199.

Bucher, K., Fazis, Y., de Capitani, C., and Grapes, R. (2005). Blueschists, eclogites, and decompression assemblages of the Zermatt-Saas ophiolite: High-pressure metamorphism of subducted Tethys lithosphere. American Mineralogist, 90(5–6), 821–835. https://doi.org/10.2138/am.2005.1718

Bucher, K., and Grapes, R. (2009). The eclogite-facies Allalin gabbro of the Zermatt-Saas ophiolite, Western alps: A record of subduction zone hydration. Journal of Petrology, 50(8), 1405–1442. https://doi.org/10.1093/petrology/egp035

Canales, J. P., Detrick, R. S., Lin, J., Collins, J. A., and Toomey, D. R. (2000). Crustal and upper mantle seismic structure beneath the rift mountains and across a non-transform offset at the Mid-Atlantic Ridge (35°N). Journal of Geophysical Research: Solid Earth, 105(B2), 2699–2719. https://doi.org/10.1029/1999JB900379

Cannat, M., Fontaine, F., and Escartín, J. (2013). Serpentinization and Associated Hydrogen and Methane Fluxes at Slow Spreading Ridges. In Diversity Of Hydrothermal Systems On Slow Spreading Ocean Ridges (pp. 241–264). American Geophysical Union (AGU). https://doi.org/10.1029/2008GM000760

Carbonin, S., Martin, S., Tumiati, S., and Rossetti, P. (2015). Magnetite from the Cogne serpentinites (Piemonte ophiolite nappe, Italy). Insights into seafloor fluid–rock interaction. European Journal of Mineralogy, 27(1), 31–50. https://doi.org/10.1127/ejm/2014/0026-2410

Carlson, R. L., and Miller, D. J. (1997). A new assessment of the abundance of serpentinite in the oceanic crust. Geophysical Research Letters, 24(4), 457–460. https://doi.org/10.1029/97GL00144

Caron, J. M., Polino, R., Pognante, U., Lombardo, B., Lardeaux, J. M., Lagabrielle, Y., Gosso, G. and Allenbach, B. (1984). Ou sont les sutures majeures dans les Alpes internes? (transversale Briançon-Torino). Memorie della Società Geologica Italiana 29, 71–78.

Carosi, R., D'Addario, E., Mammoliti, E., Montomoli, C., and Simonetti, M. (2016). Geology of the northwestern portion of the Ferriere-Mollieres Shear Zone, Argentera Massif, Italy. Journal of Maps, 12, 466–475. https://doi.org/10.1080/17445647.2016.1243491

Cartwright, I., and Barnicoat, A. C. (2002). Petrology, geochronology, and tectonics of shear zones in the Zermatt-Saas and Combin Zones of the Western Alps. Journal of Metamorphic Geology, 20(2), 263–281. https://doi.org/10.1046/j.0263-4929.2001.00366.x

Cenki-Tok, B., Oliot, E., Rubatto, D., Berger, A., Engi, M., Janots, E., Thomsen, T. B., Manzotti, P., Regis, D., Spandler, C., Robyr, M. and Goncalves, P. (2011). Preservation of Permian allanite within an Alpine eclogite facies shear zone at Mt Mucrone, Italy: Mechanical and chemical behaviour of allanite during mylonitization. Lithos 125, 40–50.

Chemenda, A. I., Mattauer, M., Malavieille, J. and Bokun, A. N. (1995). A mechanism for syn-collisional rock exhumation and associated normal faulting: Results from physical modelling. Earth and Planetary Science Letters 132, 225–232.

Chinner, G. A. and Dixon, J. E. (1973). Some high pressure parageneses of the Allalin gabbro, Valis, Switzerland. Journal of Petrology 14, 185–202.

Chopin, C. (1984). Coesite and pure pyrope in high-grade blueschists of the Western Alps: a first record and some consequences. Contributions to Mineralogy and Petrology, 86(2), 107–118.

Chopin C., Klaska R., Medenbaeh 0. and Dron D. (1986) Ellenbergerite, a new high-pressure Mg-AI-(Ti,Zr)-silicate with a novel structure based on face-sharing octahedra. Contrib. Mineral. Petrol., 92, 316-321.

Chopra, P. N., and Paterson, M. S. (1981). The experimental deformation of dunite. Tectonophysics, 78(1–4), 453–473. https://doi.org/10.1016/0040-1951(81)90024-X

Christensen, N. I. (2004). Serpentinites, Peridotites, and Seismology. International Geology Review, 46(9), 795–816. https://doi.org/10.2747/0020-6814.46.9.795

Cimmino, F., Messiga, B., Piccardo, G. B., and Zeda, O. (1979). Titanian clinohumite-bearing assemblages within antigorite serpentinites of the Gruppo di Voltri (Western Liguria): inferences on the geodynamic evolution on the Piemontese ultramafic section. Ofioliti, 4(2), 97–120.

Cliff, R. A., Barnicoat, A. C. and Inger, S. (1998). Early Tertiary eclogite facies metamorphism in the Monviso ophiolite. Journal of Metamorphic Geology 16, 447-455.

Cloos, M. (1982). Flow melanges: numerical modelling and geological constraints on their origin in the Franciscan subduction complex. Geological Society of America Bulletin 93, 330–345.

Cloos, M. (1993). Lithospheric buoyancy and collisional orogenesis: Subduction of oceanic plateaus, continental margins, island arcs, spreading ridges, and seamounts. Geological Society of America Bulletin, 105(6), 715–737.

Compagnoni, R., Dal Piaz, G. V., Fiora, L., Gosso, G., Lombardo, B., Maffeo, B., and Williams, P. F. (1977). EXCURSION TO THE SESIA-LANZO ZONE. Rendiconto Della Società Geologica Italiana, 33(1), 473–491.

Compagnoni, R., Ferrando, S., Lombardo, B., Radulesco, N., and Rubatto, D. (2010). Paleo-European crust of the Italian Western alps: Geological history of the Argentera Massif and comparison with Mont Blanc-Aiguilles Rouges and Maures-Tanneron Massifs. Journal of the Virtual Explorer, 36. https://doi.org/10.3809/jvirtex.2009.00228

Compagnoni, R., Lombardo, B., and Prato, R. (1974). and alousite et sillimanite aux contacts du granite central de l'Argentera (Alpes Maritimes). Rendiconti Della Società Italiana Di Mineralogia e Petrologia, 30, 31–54.

Compston, W. (1999). Geological age by instrumental analysis: the 29th Hallimond Lecture. Mineralogical Magazine 63, 297-311.

Connors, K. A., and Lister, G. S. (1995). Polyphase deformation in the western Mount Isa Inlier, Australia: episodic or continuous deformation? Journal of Structural Geology, 17(3), 305–328. https://doi.org/10.1016/0191-8141(94)00057-7

Coogan, L. A., Gillis, K. M., MacLeod, C. J., Thompson, G. M., and Hékinian, R. (2002). Petrology and geochemistry of the lower ocean crust formed at the East Pacific Rise and exposed at Hess Deep: A synthesis and new results. Geochemistry, Geophysics, Geosystems, 3(11), 1–30. https://doi.org/10.1029/2001gc000230

Corsini, M., Ruffet, G., and Caby, R. (2004). Alpine and late-hercynian geochronological constraints in the Argentera Massif (Western Alps). Eclogae Geologicae Helvetiae, 97(1), 3–15. https://doi.org/10.1007/s00015-004-1107-8

Dale, C. W., Burton, K. W., Pearson, D. G., Gannoun, A., Alard, O., Argles, T. W. and Parkinson, I. J. (2009). Highly siderophile element behaviour accompanying subduction of oceanic crust: Whole rock and mineral-scale insights from a high-pressure terrain. Geochimica et Cosmochimica Acta 73, 1394–1416.

Dal Piaz, G. V. (1972). La Zona Sesia-Lanzo e l'evoluzione tettonico-metamorfica delle Alpi nordoccidentali interne. Memoirs of the Geological Society of Italy, 11, 433-460.

Dal Piaz, G. V. (1988). Revised setting of the Piedmont Zone in the northern Aosta Valley, Western Alps. Ofioliti, 13, 157–162.

Dal Piaz, G. V. (1974). Le métamorphisme de haute pression et basse température dans l'évolution structurale du bassin ophiolitique alpino-apenninique. Schweizerische Mineralogische Und Petrographische Mitteilungen, 54(2/3), 399–424.

Dal Piaz, G. (1992). Guida geologica. Vol. 3/1: Le Alpi dal Monte Bianco al lago Maggiore. (BeMa, Ed.) (Guide geol.).

Dal Piaz, G. V. (1993). Evolution of Austroalpine and Upper Penninic basement in the Northwestern Alps from Variscan convergence to post-Variscan extension. In J. F. von Raumer and F. Neubauer (Eds.), Pre-Mesozoic Geology in the Alps (pp. 325–342). Heidenberg: Springer Berlin Heidelberg.

Dal Piaz, G. V. (1999). The Austroalpine-Piedmont nappe stack and the puzzle of Alpine Tethys. In: 3rd Workshop on Alpine Geological Studies. Memorie Di Scienze Geologiche, 155–176.

Dal Piaz, G. V. (2001). History of tectonic interpretations of the Alps. Journal of Geodynamics, 32(1–2), 99–114. https://doi.org/10.1016/S0264-3707(01)00019-9

Dal Piaz, G. V. (2010). The Italian Alps: A journey across two centuries of Alpine geology. Journal of the Virtual Explorer, 36. https://doi.org/10.3809/jvirtex.2010.00234

Dal Piaz, G. V., Bistacchi, A., and Massironi, M. (2003). Geological outline of the Alps. Episodes, 26(3), 175–180. https://doi.org/10.18814/epiiugs/2003/v26i3/62456

Dal Piaz, G. V., Cortiana, G., Del Moro, A., Martin, S., Pennacchioni, G., and Tartarotti, P. (2001). Tertiary age and paleostructural inferences of the eclogitic imprint in the Austroalpine outliers and Zermatt-Saas ophiolite, Western Alps. International Journal of Earth Sciences, 90, 668–684. https://doi.org/10.1007/s005310000177

Dal Piaz, G. V., Di Battistini, G., Gosso, G., and Venturelli, G. (1979). Micascisti granatiferi a relitti di onfacite e quarziti a glaucofane e granato nell'unità di Zermatt-Saas della Falda Ofiolitica Piemontese tra St. Jacques ed il Breuil. Rendiconti Società Italiana Di Mineralogia e Petrologia, 35(2), 815–830.

Dal Piaz, G. V., Di Battistini, G., Kienast, J. R., and Venturelli, G. (1979). Manganiferous quartzitic schists of the Piemonte ophiolite nappe in the Valsesia-Valtournanche area (Italian Western Alps). Memorie Di Scienze Geologiche, 32, 24 pp.

Dal Piaz, G. V., and Ernst, W. G. (1978). Areal geology and petrology of eclogites and associated metabasites of the Piemonte ophiolite nappe, Breuil—St. Jacques area, Italian Western Alps. Tectonophysics, 51(1–2), 99–126.

Dal Piaz, G. V., Gosso, G., and Lombardo, B. (1983). Metamorphic evolution of the Mt. Emilius klippe, Dent Blanche nappe, western Alps. American Journal of Science, 283A, 438–458.

Dal Piaz, G. V., Venturelli, G., Spadea, P. and Di Battistini, G. (1981). Geochemical features of metabasalts and metagabbros from the Piemonte ophiolite nappe, Italian Western Alps. Neues Jahrbuch für Mineralogie - Abhandlungen 142, 248–269.

de Capitani, C., and Brown, T. H. (1987). The computation of chemical equilibrium in complex systems containing non-ideal solutions. Geochimica et Cosmochimica Acta, 51(10), 2639–2652.

De Giusti, F., Dal Piaz, G. V., Schiavo, A., Massironi, M., Monopoli, B., Bistacchi, A., and Schiavo, A. (2003). Carta geotettonica della Valle d'Aosta. Memorie Di Scienze Geologiche, 55, 129–149.

De Hoog, J. C. M., Gall, L., and Cornell, D. H. (2010). Trace-element geochemistry of mantle olivine and application to mantle petrogenesis and geothermobarometry. Chemical Geology, 270(1–4), 196–215. https://doi.org/10.1016/j.chemgeo.2009.11.017

de Meyer, C. M. C., Baumgartner, L. P., Beard, B. L., and Johnson, C. M. (2014). Rb–Sr ages from phengite inclusions in garnets from high pressure rocks of the Swiss Western Alps. Earth and Planetary Science Letters, 395, 205–216. https://doi.org/10.1016/j.epsl.2014.03.050

Deer, W. A., Howie, R. A., and Zussman, J. (1992). An introduction to rock-forming minerals. (Longman, Ed.) (Second).

Diener, J. F. A., Powell, R., White, R. W., and Holland, T. J. B. (2007). A new thermodynamic model for clino- and orthoamphiboles in the system Na_2O-CaO-FeO-MgO-Al_2O_3-SiO_2 -H_2O-O. Journal of Metamorphic Geology, 25(6), 631–656. https://doi.org/10.1111/j.1525-1314.2007.00720.x

Dilek, Y., and Furnes, H. (2011). Ophiolite genesis and global tectonics: Geochemical and tectonic fingerprinting of ancient oceanic lithosphere. Bulletin of the Geological Society of America, 123(3–4), 387–411. https://doi.org/10.1130/B30446.1

Dilek, Y., and Furnes, H. (2014). Ophiolites and their origins. Elements, 10(2), 93–100. https://doi.org/10.2113/gselements.10.2.93

Dobrzhinetskaya, L. F., Bozhilov, K. N., and Green, H. W. (2000). The solubility of TiO2 in olivine: Implications for the mantle wedge environment. Chemical Geology, 163(1–4), 325–338. https://doi.org/10.1016/S0009-2541(99)00181-3

Dobrzhinetskaya, L. F., Larsen, R. B., Sturt, B. A., Trønnes, R. G., Smith, D. C., Taylor, W. R., and Posukhova, T. V. (1995). Microdiamond in high-grade metamorphic rocks of the Western Gneiss region, Norway. Geology, 23(7), 597–600. https://doi.org/10.1130/0091-7613(1995)023<0597:MIHGMR>2.3.CO;2

Doglioni, C. (1987). Tectonics of the Dolomites (Southern Alps, northern Italy). Journal of Structural Geology. https://doi.org/10.1016/0191-8141(87)90024-1

Doglioni, C. (2007). Tectonics of the Dolomites. Bulletin Für Angewandte Geologie, 12(June), 11–15.

Droop, G. T. R. (1987). A general equation for estimating Fe3+ concentrations in ferromagnesian silicates and oxides from microprobe analyses, using stoichiometric criteria. Mineralogical Magazine, 51(361), 431–435. https://doi.org/10.1180/minmag.1987.051.361.10

Drouin, M., Godard, M., Ildefonse, B., Bruguier, O., and Garrido, C. J. (2009). Geochemical and petrographic evidence for magmatic impregnation in the oceanic lithosphere at Atlantis Massif, Mid-Atlantic Ridge (IODP Hole U1309D, 30°N). Chemical Geology, 264(1–4), 71–88. https://doi.org/10.1016/j.chemgeo.2009.02.013

Dubois, J., and Diament, M. (1997). Géophysique. Masson, Paris.

Duchêne, S., Blichert-Toft, J., Luais, B., Télouk, P., Lardeaux, J. M. and Albarède, F. 1997. The Lu-Hf dating of garnets and the ages of the Alpine high-pressure metamorphism. Nature 387, 586–589.

Eggins, S., Rudnick, R., and McDonough, W. (1998). The composition of peridotites and their minerals: a laser-ablation ICP–MS study. Earth and Planetary Science Letters, 154(February 1997), 53–71. https://doi.org/10.1016/S0012-821X(97)00195-7

Ernst, W. Gary, and Dal Piaz, G. V. (1978). Mineral parageneses of eclogitic rocks and related mafic schists of the Piemonte ophiolite nappe, Breuil-St. Jacque. American Mineralogist, 63(1827), 621–640.

Ernst, W. Gary, and Liou, J. G. (2008). High- and ultrahigh-pressure metamorphism: Past results and future prospects. American Mineralogist, 93(11–12), 1771–1786. https://doi.org/10.2138/am.2008.2940

Fassmer, K., Obermüller, G., Nagel, T. J., Kirst, F., Froitzheim, N., Sandmann, S., Miladinova, I., Fonseca, R. O. C. and Münker, C. (2016). High-pressure metamorphic age and significance of eclogite-facies continental fragments associated with oceanic lithosphere in the Western Alps (Etirol-Levaz Slice, Valtournenche, Italy). Lithos, 252–253, 145–159. https://doi.org/10.1016/j.lithos.2016.02.019

Faure-Muret, A. (1955). Etudes géologiques sur le massif de l'Argentera-Mercantour et ses enveloppes sédimentaires. Memoirs de la Carte Geologique François.

Faure, M., Mézème, E. B., Cocherie, A., Rossi, P., Chemenda, A., and Boutelier, D. (2005). Devonian geodynamic evolution the Variscan Belt, insights from the French Massif Central and Massif Armoricain. Tectonics, 27(2), 1–19. https://doi.org/10.1029/2007TC002115

Federico, L., Capponi, G., Crispini, L., Scambelluri, M. and Villa, I. M. 2005. 39Ar/40Ar dating of high-pressure rocks from the Ligurian Alps: Evidence for a continuous subduction–exhumation cycle. Earth and Planetary Science Letters 240(3), 668–680.

Ferracutti, G. R., Gargiulo, M. F., Ganuza, M. L., Bjerg, E. A., and Castro, S. M. (2015). Determination of the spinel group end-members based on electron microprobe analyses. Mineralogy and Petrology, 109(2), 153–160. https://doi.org/10.1007/s00710-014-0363-1

Ferrando, S., Frezzotti, M. L., Orione, P., Conte, R. C., and Compagnoni, R. (2010). Late-Alpine rodingitization in the Bellecombe meta-ophiolites (Aosta Valley, Italian Western Alps): evidence from mineral assemblages and serpentinization-derived H2-bearing brine. International Geology Review, 52(10–12), 1220–1243. https://doi.org/10.1080/00206810903557761

Ferrando, S., Lombardo, B., and Compagnoni, R. (2008). Metamorphic history of HP mafic granulites from the Gesso-Stura Terrain (Argentera Massif, Western Alps, Italy). European Journal of Mineralogy, 20(5), 777–790. https://doi.org/10.1127/0935-1221/2008/0020-1891

Ferraris G., Ivaldi G. and Chopin C. (1995) Mg-dumortierite, a new mineral from very-high-pressure rocks (Western Alps). Part I: Crystal structure. European Journal of Mineralogy, 7,167-174.

Filippi, M., Zanoni, D., Gosso, G., Lardeaux J.M., Verati, C. and Spalla, M.I. (2019). Structure of lamprophyres: a discriminant marker for Variscan and Alpine tectonics in the Argentera-Mercantour Massif, Maritime Alps. Earth Sciences Bulletin, 190(1).

Fontana, E., Panseri, M., and Tartarotti, P. (2008). Oceanic relict textures in the Mount Avic serpentinites, Western Alps. Ofioliti, 33(2), 105–118.

Fontana, E., Tartarotti, P., Panseri, M., and Buscemi, S. (2014). Geological map of the Mount Avic massif (Western Alps Ophiolites). Journal of Maps, 11(1), 126–135. https://doi.org/10.1080/17445647.2014.959567

Forster, M., Lister, G. S., Compagnoni, R., Giles, R., and Hills, D. (2004). Mapping of oceanic crust with “HP” to “UHP” metamorphism: The Lago di Cignana Unit, (Western Alps). In G. Pasquarè, G. Venturini, C. and Groppelli (Ed.), Mapping geology in Italy. (pp. 279–286). Firenze: APAT - Dip. Difesa del Suolo, Servizio Geologico d’Italia, Roma 2004 (2006), Map 33, printed by S.EL.CA. Firenze.

Franke, W. (1989). Tectonostratigraphic units in the Variscan belt of central Europe. Geological Society of America, Special Paper, 230, 67–90.

Frezzotti, M. L., Selverstone, J., Sharp, Z. D., and Compagnoni, R. (2011). Carbonate dissolution during subduction revealed by diamond-bearing rocks from the Alps. Nature Geoscience, 4(10), 703–706. https://doi.org/10.1038/ngeo1246

Furnes, H., De Wit, M., Staudigel, H., Rosing, M., and Muehlenbachs, K. (2007). A vestige of earth’s oldest ophiolite. Science, 315(5819), 1704–1707. https://doi.org/10.1126/science.1139170

Gerya, T. V. (2011). Future directions in subduction modeling, Journal of Geodynamics 52, 344–378.

Gerya, T. V., and Stöckhert, B. (2005). Two-dimensional numerical modeling of tectonic and metamorphic histories at active continental margins. International Journal of Earth Science (Geol. Rundsch.), 95(2), 250–274. https://doi.org/10.1007/s00531-005-0035-9

Gerya, T. V., and Yuen, D. A. (2003). Characteristics-based marker-in-cell method with conservative finite-differences schemes for modeling geological flows with strongly variable transport properties. Physics of the Earth and Planetary Interiors, 140, 293–318. https://doi.org/10.1016/j.pepi.2003.09.006

Gilio, M., Scambelluri, M., Agostini, S., Godard, M., Peters, D., and Pettke, T. (2019). Petrology and Geochemistry of Serpentinites Associated with the Ultra-High Pressure Lago di Cignana Unit (Italian Western Alps). Journal of Petrology, 60(6), 1229–1262. https://doi.org/10.1093/petrology/egz030

González-Jiménez, J. M., Plissart, G., Leonardo, N. G., Padrón-Navarta, J. A., Aiglsperger, T., Romero, R., Marchesi, C., Moreno-Abril, A. J., Reich, M. Barra, F. and Morata, D. (2017). Ti-clinohumite and Ti-chondrodite in antigorite serpentinites from Central Chile: evidence for deep and cold subduction. European Journal of Mineralogy, 29(6), 959–970. https://doi.org/10.1127/ejm/2017/0029-2668

Gosso, G., Brizio, D., Deregibus, C., Eusebio, A., Gallo, M., Rattalino, E., and Tosetto, S. (1983). Due cinematiche possibili per la coppia di falde Brianzonese ligure-Flysch ad Elmintoidi. Memorie Della Società Geologica Italiana, 26(2), 463–472.

Gosso, G., Lardeaux, J. M., Zanoni, D., Volante, S., Corsini, M., Bersezio, R., and Camera, L. (2019). Mapping the progressive geologic history at the junction of the Alpine mountain belt and the Western Mediterranean ocean. Ofioliti, 44(2), 97–110. https://doi.org/10.4454/ofioliti.v44i2.527

Gosso, G., Messiga, B., Rebay, G., and Spalla, M. I. (2010). Interplay between deformation and metamorphism during eclogitization of amphibolites in the Sesia–Lanzo Zone of the Western Alps. International Geology Review, 52(10-12), 1193-1219.

Gosso, G., Rebay, G., Roda, M., Spalla, M. I., Tarallo, M., Zanoni, D., and Zucali, M. (2015). Taking advantage of petrostructural heterogeneities in subduction- collisional orogens, and effect on the scale of analysis. Periodico Di Mineralogia, 84(3B), 779–825. https://doi.org/10.2451/2015PM0452

Gosso, G., and Spalla, M. I. (2009). Stratigraphy in the continental crust: lithologic and tectonic records. Bollettino della Societa Geologica Italiana, 128(2), 473-482.

Gouzu, C., Yagi, K., Thanh, N. X., Itaya, T., and Compagnoni, R. (2016). White mica K–Ar geochronology of HP–UHP units in the Lago di Cignana area, western Alps, Italy: tectonic implications for exhumation. Lithos, 248, 109-118.

Gouzu, C., Itaya, T., Hyodo, H. and Matsuda, T. (2006). Excess 40Ar-free phengite in ultrahigh-pressure metamorphic rocks from the Lago di Cignana area, Western Alps. Lithos 92(3-4), 418–430.

Green, E. C. R., White, R. W., Diener, J. F. A., Powell, R., Holland, T. J. B., and Palin, R. M. (2016). Activity–composition relations for the calculation of partial melting equilibria in metabasic rocks. Journal of Metamorphic Geology, 34(9), 845–869. https://doi.org/10.1111/jmg.12211

Grigull, S., Krohe, A., Moos, C., Wassmann, S., and Stöckhert, B. (2012). "Order from chaos": A field-based estimate on bulk rheology of tectonic melanges formed in subduction zones. Tectonophysics, 568–569, 86–101. https://doi.org/10.1016/j.tecto.2011.11.004

Groppo, C., Beltrando, M., and Compagnoni, R. (2009). The P-T path of the ultra-high pressure Lago Di Cignana and adjoining high-pressure meta-ophiolitic units: Insights into the evolution of the subducting Tethyan slab. Journal of Metamorphic Geology, 27(3), 207–231. https://doi.org/10.1111/j.1525-1314.2009.00814.x

Groppo, C., and Compagnoni, R. (2007). Metamorphic veins from the serpentinites of the Piemonte Zone, western Alps, Italy: A review. Periodico Di Mineralogia, 76(3), 127–153. https://doi.org/10.2451/2007PM0021

Guillot, S., Di Paola, S., Ménot, R. P., Ledru, P., Spalla, M. I., Gosso, G., and Schwartz, S. (2009). Suture zones and importance of strike-slip faulting for Variscan geodynamic reconstructions of the External Crystalline Massifs of the western Alps. Bulletin de La Societe Geologique de France, 180(6), 483–500. https://doi.org/10.2113/gssgfbull.180.6.483

Guillot, S., and Ménot, R. P. (2009). Paleozoic evolution of the External Crystalline Massifs of the Western Alps. Comptes Rendus - Geoscience, 341(2–3), 253–265. https://doi.org/10.1016/j.crte.2008.11.010

Guillot, S., Schwartz, S., Hattori, K., Auzende, A. L., and Lardeaux, J. M. (2004). The Monviso ophiolitic Massif (Western Alps), a section through a serpentinite subduction channel. Journal of the Virtual Explorer, 16(3), 1–17. https://doi.org/10.3809/jvirtex.2004.00099

Guillot, S., Schwartz, S., Reynard, B., Agard, P., and Prigent, C. (2015). Tectonic significance of serpentinites. Tectonophysics, 646, 1–19. https://doi.org/10.1016/j.tecto.2015.01.020

Guiraud, M., Powell, R., and Rebay, G. (2001). H2O in metamorphism and unexpected behaviour in the preservation of metamorphic mineral assemblages. Journal of Metamorphic Geology, 19(4), 445–454. https://doi.org/10.1046/j.0263-4929.2001.00320.x

Haenel, R., Rybach, L., and Stegena, L. (1988). Handbook of Terrestrial Heat-Flow Density Determination. Handbook of Terrestrial Heat-Flow Density Determination. Kluwer Academic Publishers. https://doi.org/10.1007/978-94-009-2847-3

Handy, M. R., and Oberhänsli, R. (2004). Explanatory notes to the map: Metamorphic structure of the Alps. Age map of the metamorphic structure of the Alps – Tectonic interpretation and outstanding problems. Mitteilungen Der Österreichischen Mineralogischen Gesellschaft, 149, 201–226.

Handy, M. R., Schmid, S. M., Bousquet, R., Kissling, E., and Bernoulli, D. (2010). Reconciling plate-tectonic reconstructions of Alpine Tethys with the geological--geophysical record of spreading and subduction in the Alps. Earth-Science Reviews, 102, 121–158. https://doi.org/10.1016/j.earscirev.2010.06.002

Herwartz, D., Münker, C., Scherer, E. E., Nagel, T. J., Pleuger, J. and Froitzheim, N. (2008). Lu-Hf garnet geochronology of eclogites from the Balma Unit (Pennine Alps): implications for Alpine paleotectonic reconstructions. Swiss Journal of Geosciences 101(S1), 173–189.

Hiess, J., Condon, D. J., Mclean, N. and Noble, S. R. (2012). 238U/235U systematics in terrestrial Uranium-bearing minerals. Geology 335, 1610–1614.

Holland, T. J. B., Baker, J., and Powell, R. (1998). Mixing properties and activity-composition relationships of chlorites in the system MgO-FeO-Al2O3-SiO2-H2O. European Journal of Mineralogy, 10, 395–406. https://doi.org/10.1127/ejm/10/3/0395

Holland, T. J. B., and Powell, R. (1998). An internally consistent thermodynamic data set for phases of petrological interest. Journal of Metamorphic Geology, 16(3), 309–343. https://doi.org/10.1111/j.1525-1314.1998.00140.x

Hoogerduijn Strating, E. H. (1991). The evolution of the Piemonte-Ligurian ocean: a structural study of ophiolite complexes in Liguria (NW Italy). Geologica Ultraiectina (Vol. 74).

Hoogerduijn Strating, E. H., and Van Wamel, W. A. (1989). The structure of the Bracco Ophiolite complex (Ligurian Apennines, Italy): a change from Alpine. Geological Society London, 146, 933–944.

Horstwood M. S. A., Foster G. L., Parrish R. R., Noble S. R. and Nowell G. M. (2003). Common-Pb corrected in situ U–Pb accessory mineral geochronology by LA –MC –ICP –MS. Journal of Analytical Atomic Spectrometry 18, 837-846.

Jackson, S. E., Pearson, N. J., Griffin W. L. and Belousova, E. (2004). The application of laser ablation inductively coupled plasma mass spectrometry to in situ U–Pb zircon geochronology. Chemical Geology 211, 47-69.

Johnson, S. E., and Duncan, A. C. (1992). Fault identification in complexly deformed schist terrains: examples from the USA and Australia. Tectonophysics, 216(3–4), 291–308. Retrieved from http://www.sciencedirect.com/science/article/pii/004019519290402R.

Jouffray, F., Spalla, M.I., Lardeaux, J.M., Filippi, M., Rebay, G., Corsini, M., Zanoni, D., Zucali, M. and Gosso, G. (2019). Variscan eclogites from the Argentera-Mercantour Massif (External Crystalline Massifs, SW Alps): a dismembered cryptic suture zone. International Journal of Earth Science, accepted.

Juteau, T., and Maury, R. (1999). The Oceanic Crust, From Accretion to Mantle Recycling, Springer-Verlag, New York, 1999. Praxis Springer.

Ketchum, J.W.F, Jackson, S.E., Culshaw, N.G. and Barr, S.M. (2001). Depositional and tectonic setting of the Paleoproterozoic Lower Aillik Group, Makkovik Province, Canada: evolution of a passive margin – foredeep sequence based on petrochemistry and U-Pb (TIMS and LAM-ICP-MS) geochronology. Precambrian Research 105, 331-356

Kienast, J. R. (1983). Le métamorphisme de haute pression et basse température (éclogites et schistes bleus): données nouvelles sur la pétrologie des roches de la croute océanique subductée et des sédiments associés VI. Université Pierre et Marie Curie.

Kirby, S. H. (1983). Rheology of the Lithosphere. Review of Geophysics, 21(6), 1459–1487. https://doi.org/10.1029/RG021i006p01458

Kirst, F., and Leiss, B. (2017). Kinematics of syn - and post - exhumational shear zones at Lago di Cignana (Western Alps, Italy): constraints on the exhumation of Zermatt – Saas (ultra) high - pressure rocks and deformation along the Combin Fault and Dent Blanche Basal Thrust. International Journal of Earth Sciences, 106(1), 215–236. https://doi.org/10.1007/s00531-016-1316-1

Lapen, T. J., Johnson, C. M., Baumgartner, L. P., Mahlen, N. J., Beard, B. L. and Amato, J. M. (2003). Burial rates during prograde metamorphism of ultrahigh-pressure terrane: an example from Lago di Cignana, Western Alps, Italy. Earth and Planetary Science Letters 215, 57–72.

Lardeaux, J. M., Ledru, P., Daniel, I., and Duchene, S. (2001). The Variscan French Massif Central - A new addition to the ultra-high pressure metamorphic "club": Exhumation processes and geodynamic consequences. Tectonophysics, 332(1–2), 143–167. https://doi.org/10.1016/S0040-1951(00)00253-5

Latouche, L., and Bogdanoff, S. (1987). Evolution précoce du massif de l'Argentera : apport des eclogites et des granulites. Géologie Alpine, 63, 151–164.

Li, X. P., Rahn, M., and Bucher, K. (2004a). Metamorphic Processes in Rodingites of the Zermatt-Saas Ophiolites. International Geology Review, 46(January), 28–51. https://doi.org/10.2747/0020-6814.46.1.28

Li, X. P., Rahn, M., and Bucher, K. (2004b). Serpentinites of the Zermatt-Saas ophiolite complex and their texture evolution. Journal of Metamorphic Geology, 22(3), 159–177. https://doi.org/10.1111/j.1525-1314.2004.00503.x

Liati, A., Froitzheim, N., and Fanning, M. (2005). Jurassic ophiolites within the Valais domain of the Western and Central Alps: Geochronological evidence for re-rifting of oceanic crust. Contributions to Mineralogy and Petrology, 149(4), 446–461. https://doi.org/10.1007/s00410-005-0658-7

Locock, A. J. (2008). An Excel spreadsheet to recast analyses of garnet into end-member components, and a synopsis of the crystal chemistry of natural silicate garnets. Computers and Geosciences, 34(12), 1769-1780.

Locock, A. J. (2014). An Excel spreadsheet to classify chemical analyses of amphiboles following the IMA 2012 recommendations. Computers and Geosciences, 62, 1–11. https://doi.org/10.1016/j.cageo.2013.09.011

Lombardo, B., Rubatto, D. and Castelli, D. (2002). Ion microprobe U-Pb dating of zircon from a Monviso metaplagiogranite: implications for the evolution of the Piedmont-Liguria Tethys in the Western Alps. Ofioliti 27(2), 109–117.

López Sánchez-Vizcaíno, V., Gómez-Pugnaire, M. T., Garrido, C. J., Padrón-Navarta, J. A., and Mellini, M. (2009). Breakdown mechanisms of titanclinohumite in antigorite serpentinite (Cerro del Almirez massif, S. Spain): A petrological and TEM study. Lithos, 107(3–4), 216–226. https://doi.org/10.1016/j.lithos.2008.10.008

Ludwig K. R. (2003). Isoplot/Ex version 3.0: a geochronological toolkit for Microsoft Excel. Berkeley Geochronology Center Special Publication 4. Berkeley, Berkeley Geochronology Center, 70 p.

Luoni, P., Rebay, G., Spalla, M. I., and Zanoni, D. (2018). UHP Ti-chondrodite in the Zermatt-Saas serpentinite: Constraints on a new tectonic scenario. American Mineralogist, 103, 1002–1005. http://doi.org/10.2138/am-2018-6460

Luoni, P., Zanoni, D., Rebay, G., and Spalla, M. I. (2019). Deformation history of ultra high-pressure ophiolitic serpentinites in the Zermatt-Saas zone, Créton, upper Valtournanche (Aosta valley, Western Alps). Ofioliti, 44(2), 111–123. https://doi.org/10.4454/ofioliti.v44i2.468

Mahlen, N. J., Johnson, C. M., Baumgartner, L. P., and Beard, B. L. (2005). Provenance of Jurassic Tethyan sediments in the HP/UHP Zermatt-Saas ophiolite, western Alps. Bulletin of the Geological Society of America, 117(3–4), 530–544. https://doi.org/10.1130/B25545.1

Mahlen, N. J., Johnson, C. M., Baumgartner, L. P., Lapen, T. J., Skora, S. and Beard, B. L. (2006). The protracted subduction history and HP/UHP metamorphism of the Zermatt–Saas ophiolite, western Alps, as constrained by Lu–Hf geochronology. In EOS Trans. AGU Fall Meeting, pp. V41E–05.

Malaroda, R. (1999). L'Argentera meridionale: memoria illustrativa della "Geological map of Southern Argentera Massif (Maritime Alps), 1: 25 000". Memorie Di Scienze Geologiche, 51(2), 241–331.

Malaroda, R., and Carraro, F. (1970). Carta Geologica del Massiccio dell'Argentera alla scala 1: 50.000. (P. Mariotti, Ed.).

Malatesta, C., Crispini, L., Federico, L., Capponi, G. and Scambelluri, M. (2012). The exhumation of high pressure ophiolites (Voltri Massif, Western Alps): insights from structural and petrologic data on metagabbro bodies. Tectonophysics 568-569, 102-123.

Malatesta C., Gerya T. V., Crispini L., Federico L. and Capponi G. (2016). Interplate deformation at early-stage oblique subduction: 3-D thermomechanical numerical modelling. Tectonics, 35(7), 1610-1625 doi: 10.1002/2016TC004139.

Manzotti, P., Ballèvre, M., Zucali, M., Robyr, M., and Engi, M. (2014). The tectonometamorphic evolution of the Sesia–Dent Blanche nappes (internal Western Alps): review and synthesis. Swiss Journal of Geosciences, 107(2–3), 309–336. https://doi.org/10.1007/s00015-014-0172-x

Marotta, A. M., Roda, M., Conte, K., and Spalla, M. I. (2016). Thermo-mechanical numerical model of the transition from continental rifting to oceanic spreading: the case study of the Alpine Tethys. Geological Magazine, 155(October), 1–30. https://doi.org/10.1017/S0016756816000856

Marotta, A. M., Spelta, E., and Rizzetto, C. (2006). Gravity signature of crustal subduction inferred from numerical modelling. International Journal of Geophysics, 166, 923–938. https://doi.org/10.1111/j.1365-246X.2006.03058.x

Martin, S., and Cortiana, G. (2001). Influence of the whole rock composition on the crystallization of sodic amphiboles (Piemonte Zone, Western Alps). Ofioliti, 26(2b).

Martin, S., Rebay, G., Kienast, J. R., and Mevel, C. (2008). An eclogitic oceanic palaeo-hydrothermal field from the St. Marcel Valley. Ofioliti, 31(1), 49–63.

Martin, S., Tartarotti, P., and Dal Piaz, G. V. (1994). Alpine ophiolites: a review. Bollettino Di Geofisica Teorica Ed Applicata, 36, 175–219.

Matte, P. (2001). The Variscan collage and orogeny (480-290 Ma) and the tectonic definition of the Armorica microplate: A review. Terra Nova, 13(2), 122–128. https://doi.org/10.1046/j.1365-3121.2001.00327.x

Meda, M., Marotta, A. M., and Spalla, M. I. (2010). The role of mantle hydration in continental crust recycling in the wedge region. Geological Society, London, Special Publications, 332, 149–172. https://doi.org/10.1144/SP332.10

Melcher, F., Meisel, T., Puhl, J., and Koller, F. (2002). Petrogenesis and geotectonic setting of ultramafic rocks in the Eastern Alps: Constraints from geochemistry. Lithos, 65(1–2), 69–112. https://doi.org/10.1016/S0024-4937(02)00161-5

Mercier, J. C., and Nicolas, A. (1975). Textures and fabrics of upper-mantle peridotites as illustrated by xenoliths from basalts. Journal of Petrology, 16(1), 454–487.

Meyer, J. (1983). Mineralogie und Petrologie des Allalingabbros. Universitat Basel.

Monié, P. and Philippot, P. 1989. Mise en évidence de l'âge éocène moyen du métamorphisme de haute-pression dans la nappe ophiolitique du Monviso (Alpes occidentales) par la méthode 39Ar-40Ar. Comptes rendus de l'Académie des sciences. Série 2, Mécanique, Physique, Chimie, Sciences de l'univers, Sciences de la Terre 309(2), 245–251.

Morimoto, N. (1988). Nomenclature of pyroxenes. Mineralogical Magazine, 52, 535–550.

Musumeci, G., and Colombo, F. (2002). Late Visean mylonitic granitoids in the Argentera Massif (western Alps, Italy): age and kinematic constraints on the Ferrière–Mollières shear zone. Comptes Rendus Geoscience, 334(3), 213–220. https://doi.org/10.1016/s1631-0713(02)01722-4

Nishio, I., Morishita, T., Szilas, K., Pearson, G., Tani, K., Tamura, A., … Guotana, J. M. (2019). Titanian Clinohumite-Bearing Peridotite from the Ulamertoq Ultramafic Body in the 3. 0 Ga Akia Terrane of Southern West Greenland. Geoscience, 9(4), 153. https://doi.org/10.3390/geosciences9040153

Paquette, J. L., Menot, R. P., and Peucat, J. J. (1989). REE, Sm/Nd and U/Pb zircon study of eclogites from the Alpine External Massifs (Western Alps): evidence for crustal contamination. Earth and Planetary Science Letters, 96(1–2), 181–198. https://doi.org/10.1016/0012-821X(89)90131-3

Padrón-Navarta, J.A., López Sánchez-Vizcaíno, V., Hermann, J., Connolly, J.A.D., Garrido, C.J., Gómez-Pugnaire, M.T. and Marchesi, C. (2013) Tschermak's substitution in antigorite and consequences for phase relations and water liberation in high-grade serpentinites. Lithos, 15, 186–196.

Passchier, C. W., Myers, J. S., and Kröner, A. (1990). Field Geology of High-Grade Gneiss Terrains (Springer V). Heidenberg. https://doi.org/10.1007/978-3-642-76013-6

Passeri, L., Ciarapica, G., and Dal Piaz, G. V. (2018). The problematic origin of the Pancherot-Cime Bianche-Bettaforca unit (PCB) in the Piemonte zone (Western Alps). Italian Journal of Geosciences, 137(3), 478–489. https://doi.org/10.3301/IJG.2018.21

Piccardo, G. B., Zanetti, A. and Müntener, O. (2007a). Melt/peridotite interaction in the Southern Lanzo peridotite: Field, textural and geochemical evidence. Lithos 94(1), 181–209.

Piccardo, G. B., Zanetti, A., Pruzzo, A. and Padovano, M. (2007b). The North Lanzo peridotite body (NW Italy): lithospheric mantle percolated by MORB and alkaline melts. Periodico di Mineralogia 76(2-3), 199–221.

Powell, R., Holland, T.J.B., and Worley, B. (1998) Calculating phase diagrams involving solid solutions via non-linear equations, with examples using THERMOCALC. Journal of Metamorphic Geology, 16, 577–588.

Pfeifer, H. R., Biino, G., Ménot, R. P., and Stille, P. (2011). Ultramafic Rocks in the Pre-Mesozoic Basement of the Central and External Western Alps. Pre-Mesozoic Geology in the Alps, 119–143. https://doi.org/10.1007/978-3-642-84640-3_8

Picazo, S., Müntener, O., Manatschal, G., Bauville, A., Karner, G., and Johnson, C. (2016). Mapping the nature of mantle domains in Western and Central Europe based on clinopyroxene and spinel chemistry: Evidence for mantle modification during an extensional cycle. Lithos, 266–267, 233–263. https://doi.org/10.1016/j.lithos.2016.08.029

Pleuger, J., Roller, S., Walter, J. M., Jansen, E., and Froitzheim, N. (2007). Structural evolution of the contact between two Penninic nappes (Zermatt-Saas zone and Combin zone, Western Alps) and implications for the exhumation mechanism and paleogeography. International Journal of Earth Sciences, 96(2), 229–252. https://doi.org/10.1007/s00531-006-0106-6

Poli, S., and Schmidt, M. W. (2002). Petrology of Subducted Slabs. Annual Review of Earth and Planetary Sciences, 30(1), 207–235. https://doi.org/10.1146/annurev.earth.30.091201.140550

Polino, R., Dal Piaz, G. V., and Gosso, G. (1990). Tectonic erosion at the Adria margin and accretionary processes for the Cretaceous orogeny of the Alps. Mémoires de La Société Géologique de France, 156(6), 345–367.

Powell, R., Holland, T. J. B., and Worley, B. (1998). Calculating phase diagrams involving solid solutions via non-linear equations, with examples using THERMOCALC. Journal of Metamorphic Geology, 16, 577–588.

Puga, E., Nieto, J. M., Díaz De Federico, A., Bodinier, J. L., and Morten, L. (1999). Petrology and metamorphic evolution of ultramafic rocks and dolerite dykes of the Betic Ophiolitic Association (Mulhacen Complex, SE Spain): Evidence of eo-Alpine subduction following an ocean-floor metasomatic process. Lithos, 49, 23–56. https://doi.org/10.1016/S0024-4937(99)00035-3

Python, M., Ceuleneer, G., Ishida, Y., Barrat, J., and Arai, S. (2007). Oman diopsidites: A new lithology diagnostic of very high temperature hydrothermal circulation in mantle peridotite below oceanic spreading centres. Earth and Planetary Science Letters, 255, 289–305. https://doi.org/10.1016/j.epsl.2006.12.030

Python, M., Ishida, Y., Ceuleneer, G., and Arai, S. (2007). Trace element heterogeneity in hydrothermal diopside: Evidence for Ti depletion and Sr-Eu-LREE enrichment during hydrothermal metamorphism of mantle harzburgite. Journal of Mineralogical and Petrological Sciences, 102(2), 143–149. https://doi.org/10.2465/jmps.060830

Python, M., Yoshikawa, M., Shibata, T., and Arai, S. (2011). Diopsidites and rodingites: Serpentinisation and Ca-Metasomatism in the Oman ophiolite mantle. In Dyke swarms: keys for geodynamic interpretation (pp. 401–435).

Rahn, M., and Bucher, K. (1998). Titanian clinohumite formation in the Zermatt-Saas ophiolites, Central Alps. Mineralogy and Petrology, 64(1–4), 1–13. https://doi.org/10.1007/BF01226561

Ranalli, G., and Murphy, D. C. (1987). Rheological stratification of the lithosphere. Tectonophysics, 132(4), 281–295. https://doi.org/10.1016/0040-1951(87)90348-9

Rebay, G., and Messiga, B. (2007). Prograde metamorphic evolution and development of chloritoid-bearing eclogitic assemblages in subcontinental metagabbro (Sesia-Lanzo zone, Italy). Lithos, 98(1–4), 275–291. https://doi.org/10.1016/j.lithos.2007.04.002

Rebay, G., Powell, R., and Diener, J. F. A. (2010). Calculated phase equilibria for a MORB composition in a P-T range, 450-650 °C and 18-28 kbar: the stability of eclogite. Journal of Metamorphic Geology, 28(6), 635–645. https://doi.org/10.1111/j.1525-1314.2010.00882.x

Rebay, G., and Spalla, M. I. (2001). Emplacement at granulite facies conditions of the Sesia-Lanzo metagabbros: An early record of Permian rifting? Lithos, 58(3–4), 85–104. https://doi.org/10.1016/S0024-4937(01)00046-9

Rebay, G., Spalla, M. I., and Zanoni, D. (2012). Interaction of deformation and metamorphism during subduction and exhumation of hydrated oceanic mantle: Insights from the Western Alps. Journal of Metamorphic Geology, 30(7), 687–702. https://doi.org/10.1111/j.1525-1314.2012.00990.x

Rebay, G., Spalla, M. I., and Zanoni, D. (2012b). Multi-scale structural analysis of the serpentinites of the upper Valtournanche. Rendiconto Online Della Società Geologica Italiana, 22, 197–200.

Rebay, G., Zanoni, D., Langone, A., Luoni, P., Tiepolo, M., and Spalla, M. I. (2018). Dating of ultramafic rocks from the Western Alps ophiolites discloses Late Cretaceous subduction ages in the Zermatt-Saas Zone. Geological Magazine, 155(2), 298–315. https://doi.org/10.1017/S0016756817000334

Reddy, S. M., Wheeler, J., and Cliff, R. A. (1999). The geometry and timing of orogenic extension: an example from the Western Italian Alps. Journal of Metamorphic Geology, 17, 573–589.

Regorda, A., Roda, M., Marotta, A. M., and Spalla, M. I. (2017). 2-D numerical study of hydrated wedge dynamics from subduction to post-collisional phases. Geophysical Journal International, 211(2), 974–1000. https://doi.org/10.1093/gji/ggx336

Reinecke, T. (1991). Very high pressure metamorphism and uplift of coesite-bearing metasediments from the Zermatt-Saas Zone, Western Alps. European Journal of Mineralogy, 3, 7–17.

Reinecke, T. (1995). Ultrahigh and high-pressure metamorphic rocks of the Zermatt-Saas zone, Western Alps-records of burial and exhumation paths. Bochumer Geologische und Geotechnische Arbeiten, 44, 152-157.

Reinecke, T. (1998). Prograde high- to ultrahigh-pressure metamorphism and exhumation of oceanic sediments at Lago di Cignana, Zermatt-Saas Zone, western Alps. Lithos, 42(3–4), 147–189. https://doi.org/10.1016/S0024-4937(97)00041-8

Reinecke, T., van der Klauw, S. N. G. C., and Stöckhert, B. (1994). UHP metamorphic oceanic crust of the Zermatt-Saas zone (Piemontese zone) at Lago di Cignana, Valtournanche, Italy. In Compagnoni, R., Messiga, B. (Eds.), High Pressure Metamorphism in the Western Alps. 16th IMA Meeting. Guide Book to Field Excursion B1. (pp. 117–126).

Ring, U. (1995). Horizontal contraction or horizontal extension? Heterogeneous Late Eocene and early Oligocene general shearing during blueschist and greenschist facies metamorphism at the Pennine-Austroalpine boundary zone in the Western Alps. Geologische Rundschau, 84(4), 843–859.

Roda, M., Marotta, A. M., and Spalla, M. I. (2010). Numerical simulations of an ocean-continent convergent system: influence of subduction geometry and mantle wedge hydration on crustal recycling. Geochemistry, Geophysics, Geosystems, 11, 1–21.

Roda, M., Marotta, A. M., and Spalla, M. I. (2011). The effects of the overriding plate thermal state on the slab dip in an ocean-continent subduction system. Comptes Rendus - Geoscience, 343(5), 323–330. https://doi.org/10.1016/j.crte.2011.01.005

Roda, M., Spalla, M. I., and Marotta, A. M. (2012). Integration of natural data within a numerical model of ablative subduction: a possible interpretation for the Alpine dynamics of the Austroalpine crust. Journal of Metamorphic Geology, 30, 973–996.

Roda, M. and Zanoni, D. (2016). Testing the thermal state of Biella pluton country rocks via numerical model of magma cooling. In GeoMod Conference.

Roda, M., Regorda, A., Spalla, M. I., and Marotta, A. M. (2019). What drives Alpine Tethys opening? Clues from the review of geological data and model predictions. Geological Journal, 54(4), 2646-2664.

Roda, M., Zucali, M., Regorda, A., and Iole Spalla, M. (2019). Formation and evolution of a subduction-related mélange: The example of the Rocca Canavese Thrust Sheets (Western Alps). Geological Society of America Bulletin.

Rosenberg, C. L., and Handy, M. R. (2005). Experimental deformation of partially melted granite revisited: Implications for the continental crust. Journal of Metamorphic Geology, 23(1), 19–28. https://doi.org/10.1111/j.1525-1314.2005.00555.x

Rubatto, D., Ferrando, S., Compagnoni, R., and Lombardo, B. (2010). Carboniferous high-pressure metamorphism of Ordovician protoliths in the Argentera Massif (Italy), Southern European Variscan belt. Lithos, 116(1–2), 65–76. https://doi.org/10.1016/j.lithos.2009.12.013

Rubatto, D., Gebauer, D., and Compagnoni, R. (1999). Dating of eclogite facies zircons: the age of Alpine metamorphism in the Sesia–Lanzo Zone (Western Alps). Earth and Planetary Science Letters, 167, 141–158.

Rubatto, D., Gebauer, D., and Fanning, M. (1998). Jurassic formation and Eocene subduction of the Zermatt-Saas-Fee ophiolites: implications for the geodynamic evolution of the Central and Western Alps. Contributions to Mineralogy and Petrology, 132, 269–287.

Rubatto, D., Schaltegger, U., and Lombardo, B. (2001). Complex Paleozoic magmatic and metamorphic evolution in the Argentera Massif (Western Alps) resolved with U-Pb dating Complex Paleozoic magmatic and metamorphic evolution in the. Schweizerische Mineralogische Und Petrographische Mitteilungen, 81, 213–228.

Rubatto, R. and Hermann, J. (2003). Zircon formation during fluid circulation in eclogites (Monviso, Western Alps): Implications for Zr and Hf budget in subduction zones. Geochimica et Cosmochimica Acta 67, 2173-2187.

Rubatto, D., Regis, D., Hermann, J., Boston, K., Engi, M., Beltrando, M. and Mcalpine, S. R. B. (2011). Yo-yo subduction recorded by accessory minerals in the Italian Western Alps. Nature Geoscience 4(5), 338–342.

Rüpke, L. H., and Hasenclever, J. (2017). Global rates of mantle serpentinization and H 2 production at oceanic transform faults in 3-D geodynamic models. Geophysical Research Letters, 44(13), 6726–6734. https://doi.org/10.1002/2017GL072893

Sanchez, G., Rolland, Y., Jolivet, M., Brichau, S., Corsini, M., and Carter, A. (2011). Exhumation controlled by transcurrent tectonics: The Argentera-Mercantour massif (SW Alps). Terra Nova, 23(2), 116–126. https://doi.org/10.1111/j.1365-3121.2011.00991.x

Sanfilippo, A., Dick, H. J. B., Ohara, Y., and Tiepolo, M. (2016). New insights on the origin of troctolites from the breakaway area of the Godzilla Megamullion (Parece Vela back-arc basin): The role of melt-mantle interaction on the composition of the lower crust. Island Arc, 25(3), 220–234. https://doi.org/10.1111/iar.12137

Sanfilippo, A., Tribuzio, R., and Tiepolo, M. (2014). Mantle-crust interactions in the oceanic lithosphere: Constraints from minor and trace elements in olivine. Geochimica et Cosmochimica Acta, 141, 423–439. https://doi.org/10.1016/j.gca.2014.06.012

Scambelluri, M., Müntener, O., Hermann, J., Piccardo, G. B., and Trommsdorff, V. (1995). Subduction of water into the mantle: History of an Alpine peridotite. Geology, 23(5), 459–462.

Scambelluri, M., Pettke, T., and Van Roermund, H. L. M. (2008). Majoritic garnets monitor deep subduction fluid flow and mantle dynamics. Geology, 36(1), 59–62. https://doi.org/10.1130/G24056A.1

Scambelluri, M., and Rampone, E. (1999). Mg-metasomatism of oceanic gabbros and its control on Ti-clinohumite formation during eclogitization. Contributions to Mineralogy and Petrology, 135(1), 1–17. https://doi.org/10.1007/s004100050494

Schettino, A., and Turco, E. (2011). Tectonic history of the western Tethys since the Late Triassic. Geological Society of America Bulletin, 123(1–2), 89–105. https://doi.org/10.1130/B30064.1

Schmid, S. M., Aebli, H. R., Heller, F., and Zingg, A. (1989). The role of the Periadriatic Line in the tectonic evolution of the Alps. Geological Society London, Special Publications, 45, 153–171. https://doi.org/10.1144/GSL.SP.1989.045.01.08

Schmid, S. M., Fügenschuh, B., Kissling, E., and Schuster, R. (2004). Tectonic map and overall architecture of the Alpine orogen. Eclogae Geologicae Helvetiae, 97(1), 93–117. https://doi.org/10.1007/s00015-004-1113-x

Schmid, S. M., Rück, P., and Schreurs, G. (1990). The significance of the Schams Nappes for the paleotectonic and orogenic evolution of the Penninic Zone along the NFP 20 East traverse (Grisons, Eastern Switzerland). Mémoires de La Société Géologique de France, 156, 263–287.

Schmidt, M. W., and Poli, S. (1998). Experimentally based water budgets for dehydrating slabs and consequences for arc magma generation. Earth and Planetary Science Letters, 163, 361–379. https://doi.org/10.1016/S0012-821X(98)00142-3

Schulz, B., and von Raumer, J. F. (2011). Discovery of Ordovician-Silurian metamorphic monazite in garnet metapelites of the Alpine External Aiguilles Rouges Massif. Swiss Journal of Geosciences, 104(1), 67–79. https://doi.org/10.1007/s00015-010-0048-7

Schwartz, S., Lardeaux, J. M., Guillot, S. and Tricart, P, (2000). Diversité du métamorphisme éclogitique dans le massif ophiolitique du Monviso (Alpes Occidentales, Italie). Geodinamica Acta 13, 169-188.

Shen, T., Hermann, J., Zhang, L., Lü, Z., Padrón-Navarta, J. A., Xia, B., and Bader, T. (2015). UHP Metamorphism Documented in Ti-chondrodite- and Ti-clinohumite-bearing Serpentinized Ultramafic Rocks from Chinese Southwestern Tianshan. Journal of Petrology, 56(7), 1425–1458. https://doi.org/10.1093/petrology/egv042

Shen, T., Zhang, L., Hermann, J., Chen, J., Xia, B., and Padrón-Navarta, J. A. (2014). Petrological study of Ti-chondrodite- and Ti-clinohumite-bearing serpentinites from Chinese southwestern Tianshan. In GSA Annual Meeting in Vancouver, British Columbia.

Simonetti, M., Carosi, R., Montomoli, C., Langone, A., D'Addario, E., and Mammoliti, E. (2018). Kinematic and geochronological constraints on shear deformation in the Ferriere-Mollières shear zone (Argentera-Mercantour Massif, Western Alps): implications for the evolution of the Southern European Variscan Belt. International Journal of Earth Sciences, 107(6), 2163–2189. https://doi.org/10.1007/s00531-018-1593-y

Skora, S., Lapen, T. J., Baumgartner, L. P., Johnson, C. M., Hellebrand, E., and Mahlen, N. J. (2009). The duration of prograde garnet crystallization in the UHP eclogites at Lago di Cignana, Italy. Earth and Planetary Science Letters, 287, 402–411.

Skora, S., Mahlen, N. J., Johnson, C. M., Baumgartner, L. P., Lapen, T. J., Beard, B. L., and Szilvagyi, E. T. (2015). Evidence for protracted prograde metamorphism followed by rapid exhumation of the Zermatt-Saas Fee ophiolite. Journal of Metamorphic Geology, 33(7), 711–734. https://doi.org/10.1111/jmg.12148

Smith, D. (1977) Titanochondrodite and titanoclinohumite derived from the upper mantle in the Buell Park kimberlite, Arizona, USA. A discussion. Contributions to Mineralogy and Petrology, 61, 213–215.

Smith, D. C. (1984). Coesite in clinopyroxene in the Caledonides and its implications for geodynamics. Nature, 310(5979), 641–644. https://doi.org/10.1038/310641a0

Sobolev, A. V., Hofmann, A. W., Kuzmin, D. V., Yaxley, G. M., Arndt, N. T., Chung, S., and Nikogosian, I. K. (2007). The Amount of Recycled Crust in Sources of Mantle-Derived Melts. Science, 316(2007), 412–418. https://doi.org/10.1126/science.

Sobolev, N. V., and Shatsky, V. S. (1990). Diamond inclusions in garnets from metamorphic rocks: a new environment for diamond formation. Nature, 343(6260), 742–746. https://doi.org/10.1038/343742a0

Spalla, M. I., De Maria, L., Gosso, G., Miletto, M., and Pognante, U. (1983). Deformazione e metamorfismo della Zona Sesia - Lanzo meridionale al contatto con la falda piemontese e con il massiccio di Lanzo, Alpi occidentali. Memorie Della Società Geologica Italiana, 26, 499–514.

Spalla, M. I., and Gosso, G. (1999). Pre-Alpine tectono-metamorphic units in the central Southern Alps: structural and metamorphic memory. In Workshop on Alpine geological studies (Vol. 51, No. 1, pp. 221-229). Società cooperativa tipografica.

Spalla, M. I., Gosso, G., Marotta, A. M., Zucali, M., and Salvi, F. (2010). Analysis of natural tectonic systems coupled with numerical modelling of the polycyclic continental lithosphere of the Alps. International Geology Review, 52(10–12), 1268–1302. https://doi.org/10.1080/00206814.2010.482737

Spalla, M. I., Lardeaux, J. M., Dal Piaz, G. V., and Gosso, G. (1991). Métamorphisme et tectonique a la marge externe de la zone Sesia-Lanzo (Alpes occidentales). Memorie Di Scienze Geologiche, 43, 361–369.

Spalla, M. I., Lardeaux, J. M., Dal Piaz, G. V., Gosso, G., and Messiga, B. (1996). Tectonic significance of alpine eclogites. Geodynamics, 21(3), 257–285.

Spalla, M. I., Zanoni, D., Marotta, A. M., Rebay, G., Roda, M., Zucali, M., and Gosso, G. (2014). The transition from Variscan collision to continental break-up in the Alps: insights from the comparison between natural data and numerical model predictions. Geological Society, London, Special Publications, 405(1), 363–400. https://doi.org/10.1144/SP405.11

Spalla, M. I., and Zucali, M. (2004). Deformation vs. metamorphic re-equilibration heterogeneities in polymetamorphic rocks: a key to infer quality PTdt path. Rivista Italiana di Mineralogia e Petrologia, 73, 249.

Spalla, M. I., Zucali, M., Di Paola, S., and Gosso, G. (2005). A critical assessment of the tectono-thermal memory of rocks and definition of tectono-metamorphic units: evidence from fabric and degree of metamorphic transformations. Geological Society London, Special Publications, 243(1), 227–247.

Spear, F. S. (1993). Metamorphic phase equilibria and pressure-temperature-time paths. Mineralogical Society of America, Chelsea, Michigan: BookCrafters, Inc., 799p.

Springer, K., Lapen, T. J., Baumgartner, L. P., Johnson, C. M., and Beard, B. L. (2009). Sm-Nd geochronology of the Zermatt- Saas ophiolite, northern Italy. Geochimica et Cosmochimica Acta Supplement, 73, A1258.

Steinmann, G. (1927). Die ophiolitshen zonen in den mediterranen Kettengebirgen, translated and reprinted by Bernoulli and Friedman, In Ophiolite Concept and the Evolution of Geologic thought (eds. Y. Dilek and S. Newcomb), pp. 77-91. Geological Society of America, Special Publication, 373.

Stoeckhert, B. and Gerya, T. (2005). Pre-collisional high pressure metamorphism and nappe tectonics at active continental margins: a numerical simulation. Terra Nova 17, 102–110.

Tartarotti, P., Festa, A., Benciolini, L., and Balestro, G. (2017). Record of Jurassic mass transport processes through the orogenic cycle: Understanding chaotic rock units in the high-pressure Zermatt-Saas ophiolite (Western Alps). Lithosphere, 9(3), 399–407. https://doi.org/10.1130/L605.1

Tartarotti, P., Zucali, M., Panseri, M., Lissandrelli, S., Capelli, S., and Ouladdiaf, B. (2011). Mantle origin of the Antrona serpentinites (Antrona ophiolite, Pennine Alps) as inferred from microstructural, microchemical, and neutron diffraction quantitative texture analysis. Ofioliti, 36(2), 167–189.

Tiepolo, M., Bottazzi, P., Palenzona, M., and Vannucci, R. (2003). A laser probe coupled with ICP-double-focusing sector-field mass spectrometer for in situ analysis of geological samples and U-Pb dating of zircon. The Canadian Mineralogist, 41, 259–272. https://doi.org/DOI 10.2113/gscanmin.41.2.259

Tiepolo, M., Tribuzio, R., and Vannucci, R. (1997). Mg-and Fe-gabbroids from Northern Apennine ophiolites: parental liquids and igneous differentiation processes. Ofioliti, 22(1), 57–69.

Tribuzio, R., Garzetti, F., Corfu, F. Tiepolo, M. and Renna, M. R. (2016). U–Pb zircon geochronology of the Ligurian ophiolites (Northern Apennine, Italy): Implications for continental breakup to slow seafloor spreading. Tectonophysics 666, 220-243.

Tribuzio, R., Tiepolo, M., and Vannucci, R. (2000). Evolution of gabbroic rocks of the Northern Apennine ophiolites (Italy): comparison with the lower oceanic crust from modern slow-spreading ridges. Special Papers-Geological Society of America, 129-138.

Turco, F., and Tartarotti, P. (2006). The Antrona nappe: Lithostratigraphy and metamorphic evolution of ophiolites in the Antrona Valley (Pennine Alps). Ofioliti, 31(2), 207–221.

Turcotte, D. L., and Schubert, G. (2002). Geodynamics (2nd ed.). Cambridge University Press, New York.

Van Achterbergh E., Ryan C. G., Jackson S. E. and Griffin W. (2001). Data reduction software for LAICPMS. In Laser ablation ICPMS in the earth sciences: principles and applications. (ed P. Sylvester), pp. 239-243. Mineralogical Association of Canada Short Course Ser. 29.

van der Klauw, S. N. G. C., Reinecke, T., and Stöckhert, B. (1997). Exhumation of ultrahigh-pressure metamorphic oceanic crust from Lago di Cignana, Piemontese zone, Western Alps: the structural record in metabasites. Lithos, 41(1–3), 79–102. https://doi.org/10.1016/S0024-4937(97)82006-3

Van Roermund, H. L. M., Drury, M. R., Barnhoorn, A., and De Ronde, A. A. (2000). Super-silicic garnet microstructures from an orogenic garnet peridotite, evidence for an ultra-deep (>6 GPa) origin. Journal of Metamorphic Geology, 18(2), 135–147. https://doi.org/10.1046/j.1525-1314.2000.00251.x

Vannay, J. C., and Alleman, R. (1990). La Zone Piémontaise dans le Haute Valtournenche. Eclogae Geologicae Helvetiae, 83, 21–39.

von Raumer, J. F., Abrecht, J., Bussy, F., Lombardo, B., Ménot, R. P., and Schaltegger, U. (1999). The Paleozoic metamorphic evolution of the Alpine External Massifs. Schweizersche Mineralogische Und Petrographische Mitteilungen, 79, 5–22.

von Raumer, J. F., Bussy, F., and Stampfli, G. M. (2009). The Variscan evolution in the External massifs of the Alps and place in their Variscan framework. Comptes Rendus Geoscience, 341, 239–252. https://doi.org/10.1016/j.crte.2008.11.007

von Raumer, J. F., Finger, F., Veselá, P., and Stampfli, G. M. (2014). Durbachites-Vaugnerites - a geodynamic marker in the central European Variscan orogen. Terra Nova, 26(2), 85–95. https://doi.org/10.1111/ter.12071

von Raumer, J. F., and Stampfli, G. M. (2008). The birth of the Rheic Ocean - Early Palaeozoic subsidence patterns and subsequent tectonic plate scenarios. Tectonophysics, 461(1–4), 9–20. https://doi.org/10.1016/j.tecto.2008.04.012

Wang, X., Liou, J. G., and Mao, H. K. (1989). Coesite-bearing eclogite from the Dabie Mountains in central China. Geology, 17(12), 1085. https://doi.org/10.1130/0091-7613(1989)017<1085:CBEFTD>2.3.CO;2

Weber, S., and Bucher, K. (2015). An eclogite-bearing continental tectonic slice in the Zermatt–Saas high-pressure ophiolites at Trockener Steg (Zermatt, Swiss Western Alps). Lithos, 232(November), 336–359. https://doi.org/10.1016/j.lithos.2015.07.010

Weber, S., Sandmann, S., Miladinova, I., Fonseca, R. O. C., Froitzheim, N., Münker, C., and Bucher, K. (2015). Dating the initiation of Piemonte-Liguria Ocean subduction: Lu–Hf garnet chronometry of eclogites from the Theodul Glacier Unit (Zermatt-Saas zone, Switzerland). Swiss Journal of Geosciences, 108(2), 183–199. https://doi.org/10.1007/s00015-015-0180-5

White, R. W., Powell, R., and Holland, T. J. B. (2007). Progress relating to calculation of partial melting equilibria for metapelites. Journal of Metamorphic Geology, 25(5), 511–527. https://doi.org/10.1111/j.1525-1314.2007.00711.x

White, R. W., Powell, R., and Johnson, T. E. (2014). The effect of Mn on mineral stability in metapelites revisited: New a-x relations for manganese-bearing minerals. Journal of Metamorphic Geology, 32(8), 809–828. https://doi.org/10.1111/jmg.12095

Whitney, D. L., and Evans, B. W. (2010). Abbreviations for names of rock-forming minerals. American Mineralogist, 95(1), 185–187. https://doi.org/10.2138/am.2010.3371

Wiedenbeck M., Allé P., Corfu F., Griffin W. L., Meier M., Oberlin F., Von Quadt A., Roddick J. C. and Spiegel W. 1995. Three natural zircon standards for U–Th–Pb, Lu–Hf, trace elements and REE analyses. Geostandards Newsletter 19, 1-23.

Wicks, F. J., and Whittaker, E. J. W. (1977). Serpentinite Textures and Serpentinization. Canadian Mineralogist, 459–488.

Winter, J. (2007). Igneous Petrology: Metamorphism. Blackwell Sci., London.

Yang, J. J. (2003). Titanian clinohumite - garnet - pyroxene rock from the Su-Lu UHP metamorphic terrane, China: Chemical evolution and tectonic implications. Lithos, 70(3–4), 359–379. https://doi.org/10.1016/S0024-4937(03)00106-3

Zanoni, D., Rebay, G., Bernardoni, J., and Spalla, M. I. (2012). Using multiscale structural analysis to infer high-/ultrahigh-pressure assemblages in subducted rodingites of the Zermatt-Saas Zone at Valtournanche, Italy. Journal of the Virtual Explorer, 41, 2-30. https://doi.org/10.3809/jvirtex.2011.00290

Zanoni, D., Rebay, G., and Spalla, M. I. (2016). Ocean floor and subduction record in the Zermatt-Saas rodingites, Valtournanche, Western Alps. Journal of Metamorphic Geology, 34, 941–961. https://doi.org/10.1111/jmg.12215

Zanoni, D., Spalla, M. I. and Gosso, G. (2010). Structure and PT estimates across late-collisional plutons: constraints on the exhumation of western Alpine continental HP units. International Geology Review 52(10-12), 1244–1267.

Zanoni, D., Spalla, M. I., and Gosso, G. (2010). Vestiges of lost tectonic units in conglomerate pebbles? A test in Permian sequences of the Southalpine Orobic Alps. Geological Magazine, 147(01), 98. https://doi.org/10.1017/S0016756809990252

Zeh, A., Holland, T. J. B., and Klemd, R. (2005). Phase relationships in grunerite-garnet-bearing amphibolites in the system CFMASH, with applications to metamorphic rocks from the Central Zone of the Limpopo Belt, South Africa. Journal of Metamorphic Geology, 23(1), 1–16. https://doi.org/10.1111/j.1525-1314.2005.00554.x

Zhang, R. Y., Liou, J. G., and Cong, B. L. (1995). Talc-, Magnesite- and Ti-Clinohumite-Bearing Ultrahigh-Pressure Meta-Mafic and Ultramafic Complex in the Dabie Mountains, China. Journal of Petrology, 36(4), 1011–1037. https://doi.org/10.1093/petrology/36.4.1011

Zhang, R. Y., Shu, J. F., Mao, H. K., and Liou, J. G. (1999). Magnetite lamellae in olivine and clinohumite from Dabie UHP ultramafic rocks, central China. American Mineralogist, 84(4), 564–569.

Zingg, A., Handy, M. R., Hunziker, J. C., and Schmid, S. M. (1990). Tectonometamorphic history of the Ivrea Zone and its relationship to thee crustal evolution of the Southern Alps. Tectonophysics, 182(139), 169–192.

Zucali, M., Spalla, M. I., and Gosso, G. (2002). Strain partitioning and fabric evolution as a correlation tool: the example of the Eclogitic Micaschists Complex in the Sesia-Lanzo Zone (Monte Mucrone-Monte Mars, Western Alps, Italy). Schweizerische Mineralogische Und Petrographische Mitteilungen, 82(3), 429–454.

Zussman, J., Deer, W. A., and Howie, R. A. (1992). An Introduction to the Rock Forming Minerals. (Zanichelli, Ed.).

Appendix

Form surface maps of Ultra High Pressure serpentinites outcrops in the Zermatt-Saas Zone, Créton, upper Valtournanche (Aosta Valley, Western Alps)

Pietro Luoni[1], Davide Zanoni[1], Gisella Rebay[2], Maria Iole Spalla[1]

[1] Università degli Studi di Milano, Dipartimento di Scienze della Terra "A. Desio", Via Mangiagalli 34 - 20133 Milano, Italy; [2] Università degli Studi di Pavia, Dipartimento di Scienze della Terra e dell'Ambiente, Via Ferrata 1 - 27100 Pavia, Italy

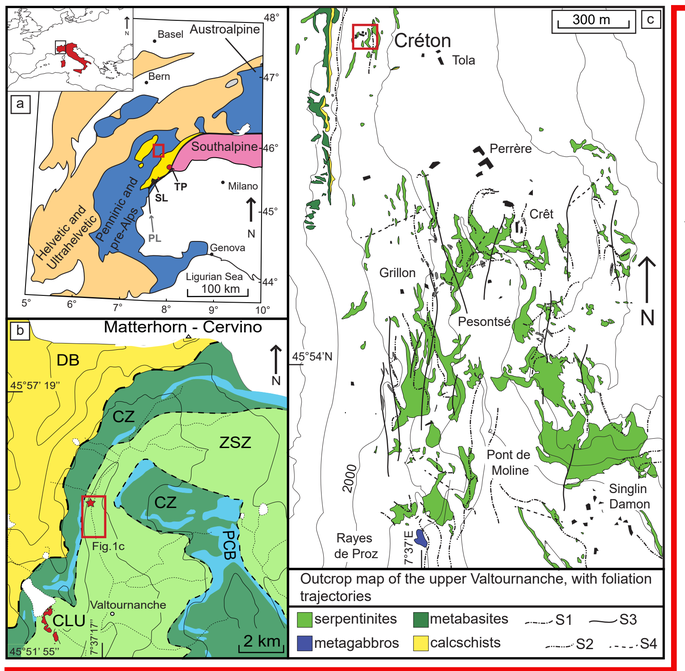

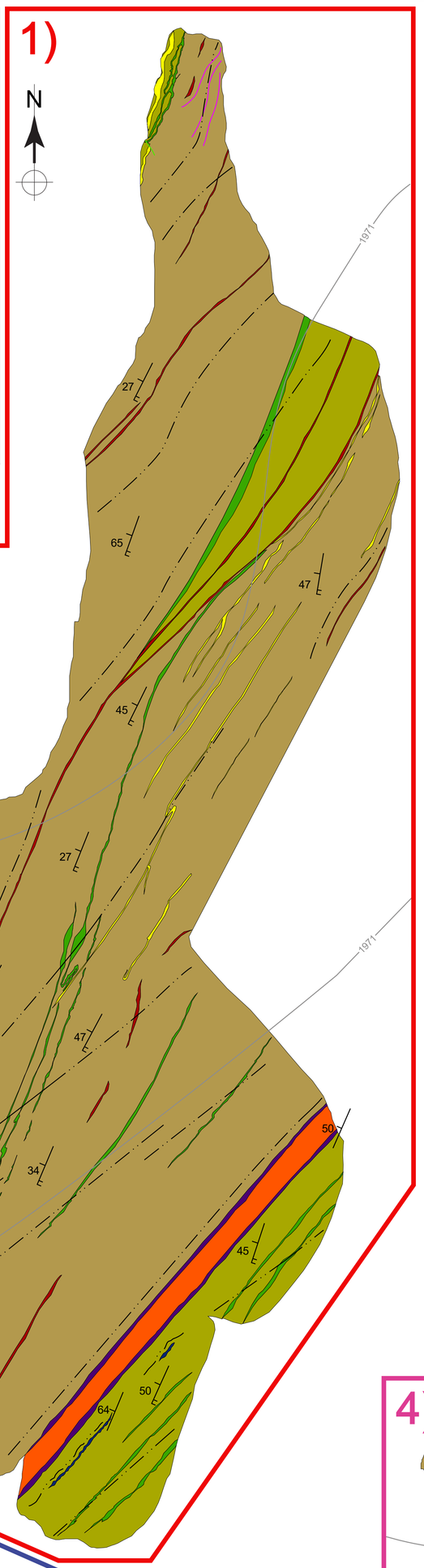

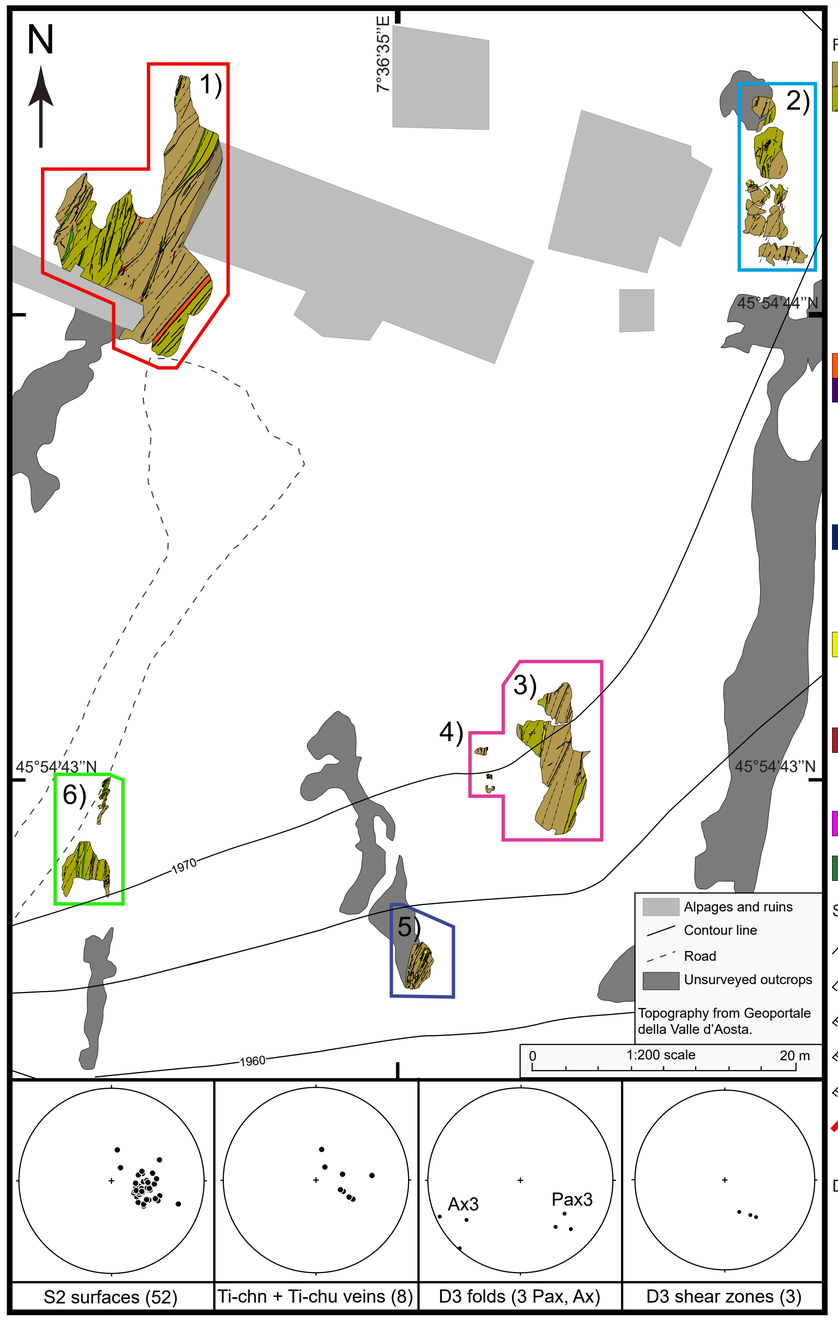

LEGEND

Rock types

White porphyroclasts serpentinite (a)
Mylonitic serpentinite. Antigorite (60-90%), magnetite (5-15%), olivine/clinopyroxene (5-10%), calcite + dolomite (<5%), and locally Ti-clinohumite, chlorite and apatite. Outcrop altered surface are rich in white and pale grey of centimetre-sized oval domains in an aqua-green matrix.
Assemblages
Pre-D2: Atg + Mag + Ti-Chu + Dol + Ap + Dol. Syn-D2: Atg + Mag + Di/Ol + Ti-Chu + Chl + Cal + Dol. Post-D2: Atg + Mag + Chl.

Olivine-rich serpentinite (b)
Mylonitic serpentinite. Antigorite (50-80%), olivine (20-30%), magnetite (5-15%), chlorite (<5%).
Rich in millimetre- to submillimetre-thick olivine veins, the rock and the olivine veins are affected by mylonitic S2 foliation. Outcrop altered surface is from ocher, yellow to brownish.
Assemblages
Pre-D2: Atg + Mag + Ol + Ti-Chu. Syn-D2: Atg + Mag + Ol + Ti-Chu. Post-D2: Atg + Mag + Chl.

Magnetite layers (c)
Both serpentinite types are rich in layers constituted by magnetite (50-90%), antigorite (10-30%), and locally olivine (10-20%). The texture of magnetite layers is strongly affected by S2. Magnetite grains are concentrated in thin films parallelised into the S2 foliation.

Diopsidite
Pyroxenite. Diopside (70-80%), antigorite ± chlorite (10-20%), tremolite + actinolite (5-20%), and ilmenite ± titanite (5%). Locally, magnetite, calcite, and apatite (<5%).
Assemblages
Pre-D2: Di + Ap + Ilm + Atg + Chl ± Mag. Syn-D2: Di + Atg + Ttn + Chl + Cal ± Ilm. Post-D2: Amp

Chlorite schist (b)
5 to 10 cm thick rim of mylonitic chlorite schist. Chlorite (60%), clinopyroxene (augite + diopside) (20%), antigorite (10-15%), ilmenite (10%), tremolite and magnetite (2-3%), and Ti-clinohumite.
Assemblages:
Pre-D2: Cpx + Chl + Ilm + Atg + Mag + Ti-Chu. Syn-D2: Chl + Di + Atg + Ilm Post-D2: Chl, Tr, Act.

Pyroxenite
Layers and lenses wrapped and boudined into S2 foliation. Clinopyroxene (augite + diopside) (70-80%), antigorite ± chlorite (10-20%), ilmenite ± magnetite (5%), Ti-chondrodite + Ti-clinohumite (5%), and tremolite (<2%).
Assemblages
Pre-D2: Cpx (augitic core) + Spl + Atg (+ Ti-Chn). Pre-D2 to early D2: Cpx + Srp + Chl + Ti-Chn + Ti-Chu + Ilm + Mag. Syn-D2: Cpx + Atg + Chl + Ti-Chu + Mag. Post-D2: Atg + Chl + Mag + Tr.

Olivine-rich layers
Layers and lenses wrapped by and boudined into S2 foliation. Olivine (60-90%), antigorite (10-20%), magnetite ± Cr-magnetite (10%), chlorite (<5%), Ti-chondrodite + Ti-clinohumite (<5%), dolomite (<2%), and diopside (<1%).
Assemblages
Pre-D2: Ol + Atg + Cr-Mag + Mag + Di ± Ti-Chn + Chl. Pre-D2 to early D2: Ol + Atg + Mag + Ti-Chu + Dol + Di. Syn-D2: Ol + Atg + Mag + Ti-Chu. Post-D2: Atg + Cal.

Ti-chondrodite + Ti-clinohumite veins
Ti-chondrodite + Ti-clinohumite (70-80%), olivine (10-20%), antigorite (5-10%), magnetite ± ilmenite (5-10%), chlorite (<5%).
Assemblages
Pre-D2: Ti-Chn + ex-Spl + Ol + Atg ± Chl. Pre-D2 to early D2: Ti-Chn + Ti-Chu + Ol + Ilm + Mag + Chl + Atg. Syn-D2: Ti-Chu + Ol + Atg + Chl + Mag.

Olivine veinlets
Ocher-yellow veinlets of few milimeters thickness. They are composed by olivine (90-95%), antigorite (10-15%), magnetite (5%). Veins are transposed by S2 foliation.

Calcite veins
Post-D2 calcite.

Symbols of mesoscopic fabric elements and orientation

- Litological surfaces with dip
- S1 foliation surfaces with dip
- D2 axial planes (AP2) and S2 foliation surfaces with dip
- D3 axial planes (AP3) with dip
- D3 folds axes
- Faults trajectory
- D1 axial plane trajectory
- S2 trajectory
- D3 axial plane trajectory
- D3 shear zones
- Approximate topography contours

Datum: WGS84

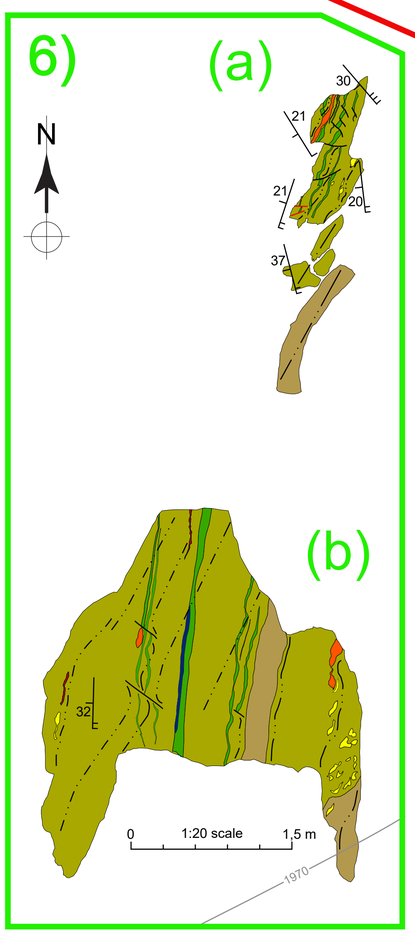

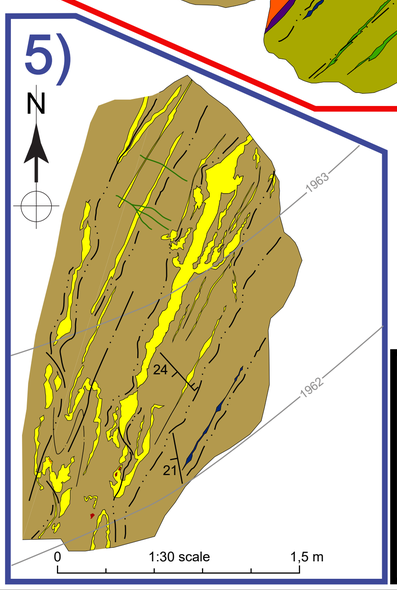

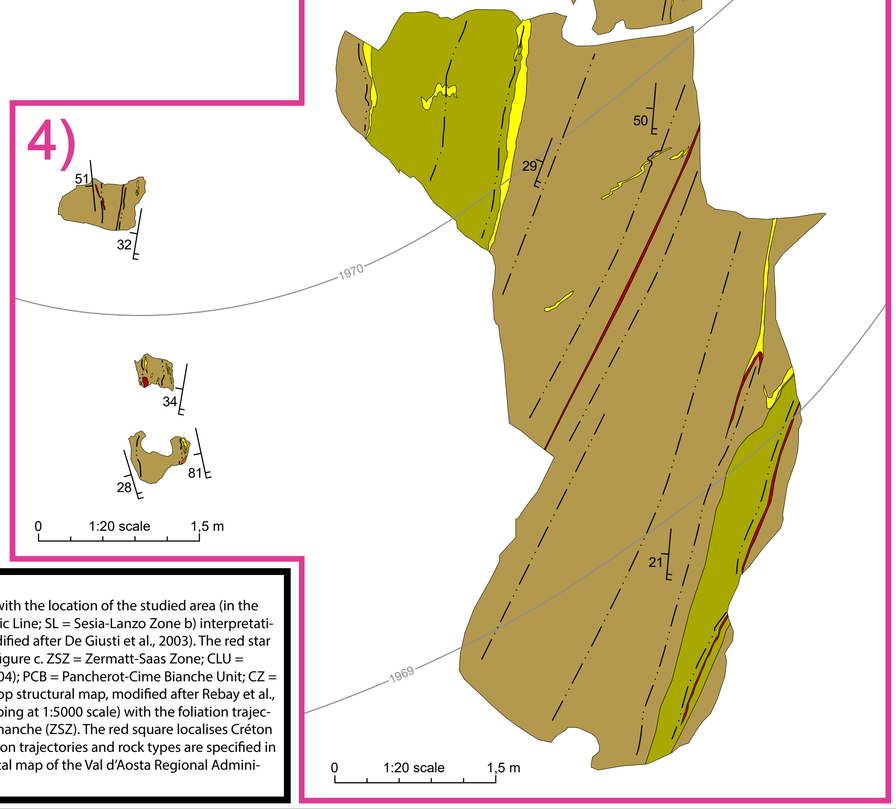

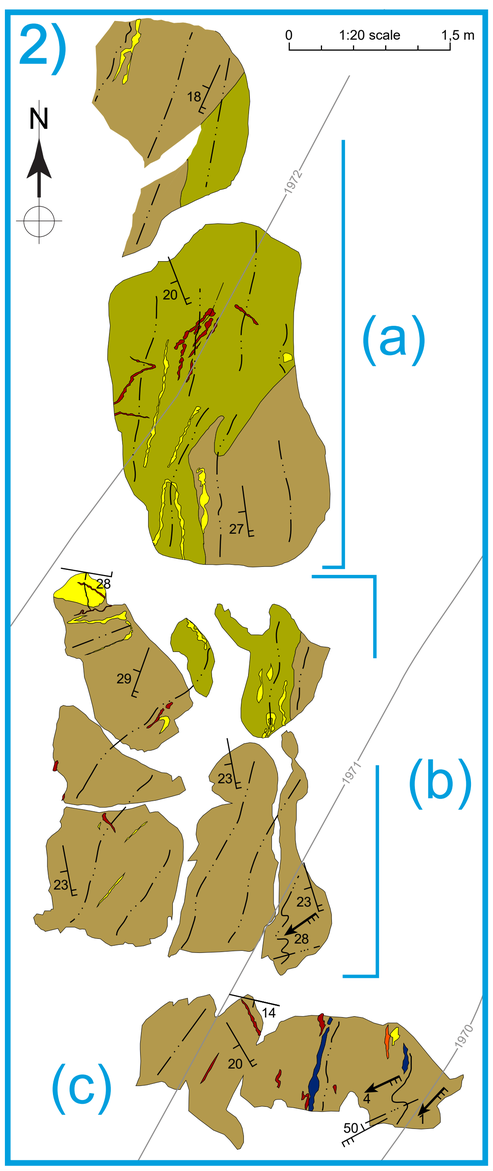

GEOLOGICAL FRAMEWORK
a) Simplified tectonic sketch of the Western Alps with the location of the studied area (in the blue square). TP = Tertiary plutons; PL = Periadriatic Line; SL = Sesia-Lanzo Zone b) interpretative tectonic map of the upper Valtournanche (modified after De Giusti et al., 2003). The red star localises Créton, the red rectangle circumscribes figure c. ZSZ = Zermatt-Saas Zone; CLU = Cignana Lake Unit (redrawn after Forster et al., 2004); PCB = Pancherot-Cime Bianche Unit; CZ = Combin Zone; DB = Dent Blanche nappe; c) outcrop structural map, modified after Rebay et al., (2018) and by Zanoni (unpublished: original mapping at 1:5000 scale) with the foliation trajectories in the meta-ophiolites of the upper Valtournanche (ZSZ). The red square localises Créton outcrops. Relative chronology of successive foliation trajectories and rock types are specified in the legend. Topography redrawn from the technical map of the Val d'Aosta Regional Administration, without hydrography.

Submitted to: The First ASRO Geological Congress – [ASRO – GC 2017] (El Jadida, Morocco - March 15-17, 2017)

U-Pb dating assisted by multiscalar structural analysis of HP/UHP serpentinites in Italian Western Alps (Zermatt-Saas Zone)

Rebay, G.[1], Luoni, P. [2], Tiepolo, M.[2], Zanoni, D.[2], Langone, A.[3] and Spalla, M.I.[2]

[1]Università degli Studi di Pavia, Dipartimento di Scienze della Terra e dell'Ambiente, Italy
[2]Università degli Studi di Milano, Dipartimento di Scienze della Terra "A. Desio", Italy
[3]IGG-CNR U.O.S. of Pavia, Italy

Regional- to micro-scale structural analysis has been applied to Zermatt-Saas Zone (ZSZ) serpentinites to explore their tectonic history by means of PTDt path reconstruction. ZSZ is a slice of oceanic lithosphere tectonically sampled from the Tethyan realm. ZSZ is heterogeneously affected by oceanic metamorphism predating subduction-related structural and metamorphic evolution. At present the ZSZ is located in the axial belt and represents part of the oceanic suture developed in the European Alps during the Alpine subduction and collision. The Zermatt-Saas rocks are characterized by a dominant HP to UHP metamorphic imprint, which is only locally overprinted by greenschist facies metamorphism. Ages of oceanic protolith vary between 164 and 153 Ma, whereas the Alpine metamorphic peak recorded during subduction is constrained between 50 and 39.

Metaophiolites in the upper Valtournanche are dominated by a regional S2 foliation mapped with spatial continuity in serpentinite, metarodingite and eclogite. HP mineral assemblages underline S2 and indicate that physical conditions of metamorphism reached 2.5 ± 0.3GPa and 600 ± 20°C during the Alpine subduction. Serpentinites occur in two types, eclogitised serpentinite and Ti-clinohumite-bearing serpentinite.

Locally, in serpentinites clinopyroxeneI and zirconI porphyroclasts are wrapped by S2 foliation and fringes and/or new grains of clinopyroxeneII and zirconII define S2. New clinopyroxeneII fringes have compositions similar to those of new clinopyroxene grains marking S2. Trace element composition of clinopyroxene crystals is consistent with a crystallisation from a melt in equilibrium with plagioclase as it occurs in gabbroic percolation of oceanic. Microstructures similar to those observed in the clinopyroxenes characterise zircons. Under cathodoluminescence, zircon cores show sector zonings, which are typical of magmatic growth. U-Pb dates suggest that zircon cores crystallised during Middle Jurassic. The thin fringes overgrowing magmatic cores are parallel to the S2 foliation and U-Pb concordant analyses on these domains reveal an Upper Cretaceous blastesis age. Due to deformation-metamorphism relationships these dates are interpreted as the ages of HP to UHP Alpine re-equilibration. These results allow widening the time span under which rocks of ZSZ recorded P-peak conditions and suggest that different portions of this Zone reached the deepest part of the subduction system diachronically. Therefore, some sections of the ZSZ have likely experienced HP to UHP metamorphism earlier than previously thought. The obtained ages are comparable to those already described for the HP re-equilibration in the subducted continental crust of the Sesia-Lanzo Zone, which records the oldest subduction ages in all the tectonic units of the Western Alps. This finding goes along with the cold thermal regime under which the Sesia-Lanzo Zone was exhumed, which is compatible with on-going oceanic subduction.

HP-UHP serpentinites from Zermatt-Saas Zone: new insights on UHP metamorphism of ultramafic rocks

[1]Luoni, P., [2]Rebay, G., [1]Zanoni, D., [1]Spalla, M.I.

[1] Department of Earth Sciences, Università degli Studi di Milano, Via Mangiagalli 34, 20133 Milano, Italy
[2] Department of Earth and Environmental Sciences, Università di Pavia, Via Ferrata, 1, 27100 Pavia, Italy

The Zermatt-Saas Zone, part of the Middle and Late Jurassic Tethyan lithosphere, underwent oceanic metamorphism during Mesozoic and subduction during Upper Cretaceous to Eocene (HP to UHP metamorphism). In upper Valtournanche, serpentinite, metarodingite, and eclogite record a dominant S2 foliation that developed under 2.5 ± 0.3 GPa and 600 ± 20 °C, during Alpine subduction (Rebay et al., 2012; Zanoni et al., 2016). U-Pb zircon dating (Rebay et al., 2017) shows crystallisation at 166 ± 4 Ma for the cores, in agreement with the known ages for the oceanic accretion of the Tethyan lithosphere, and Upper Cretaceous – Pleocene ages for the metamorphic syn-D2 rims, showing that Zermatt-Saas Zone experienced HP to UHP metamorphism about 16 Ma earlier than previously reported.

A detailed structural study of serpentinites preserving relic fabrics within the dominant HP/UHP S2 pervasive foliation, allowed to reconstruct a detailed tectono-metamorphic evolution for such rocks, that preserve records of prograde and peak conditions of re-equilibration during Alpine subduction. Relics of structures and parageneses associated to early oceanic metamorphism prior to subduction are recognized. Serpentinite in less deformed domains preserve clinopyroxene mantled by S2 foliation, layers and lenses of pyroxenite and dunite and magnetite bands. Several fluid circulation episodes taking place during prograde evolution are evidenced by olivine, olivine-Ti-clinohumite and magnetite bearing veins predating and deformed by S2, and the mineral associations in such domains and their evolution at P-peak conditions allow to reconstruct a complex and composite P-T-d-t path.

Results, compared with the metamorphic evolutions described in adjacent portions of Zermatt-Saas Zone support the evidence that it is not a coherent tectonic unit, but is composed of slices, that have experienced different P-T-t paths during the subduction-collision-exhumation cycle involving the Piedmont oceanic lithosphere over a period of at least 30 Ma.

Rebay, G., Spalla, M. I., Zanoni, D. (2012) Interaction of deformation and metamorphism during subduction and exhumation of hydrated oceanic mantle: insights from the Western Alps. Journal of Metamorphic Geology 30, 687–702.

Zanoni, D., Rebay, G., Spalla, M. I. (2016) Ocean floor and subduction record in the Zermatt-Saas rodingites, Valtournanche, Western Alps. Journal of Metamorphic Geology 34:941–961.

Rebay, G., Zanoni, D., Langone, A., Luoni, P., Tiepolo, M., Spalla, M. I., (2017) Dating of ultramafic rocks from the Western Alps ophiolites discloses Late Cretaceous subduction ages in the Zermatt-Saas Zone. Geological Magazine, in press, doi:10.1017/S0016756817000334.

New constraints for the tectono-metamorphic evolution of Zermatt-Saas Zone, Western Alps

Pietro Luoni[1], Gisella Rebay[2], Davide Zanoni[1], Maria Iole Spalla[1]
[1] – Department of Earth Sciences, University of Milano, Italy; [2] - Department of Earth Sciences, University of Pavia, Italy;
[*] pietro.luoni@unimi.it

Multiscale structural analysis and detailed mapping (1:20 scale) integrated with petrological investigation was applied to Zermatt-Saas serpentinites outcropping in upper Valtournenche, Zermatt-Saas Zone (Italy). The analysis resulted into a map with foliation trajectories that allowed recognizing the transposed original litostratigraphy of serpentinites comprising magnetite layers and rare, decimeter-thick, pyroxenite layers. Locally veins of Ti-clinohumite, layers and lenses of dunites, veins of olivine, and layers of dark clinopyroxenes are embedded in serpentinites. Serpentinites record three stages of ductile deformation: D1 consists of rare folds and S1 foliation; D2 produced isoclinal folds and a very pervasive foliation (S2) that is the dominant structure; D3 includes crenulation and shear zones affecting S2. The meso- and micro-structural observations revealed that the structural evolution is equivalent to that proposed by Rebay et al. (2012) with the addition of pre-D2 paragenesis. Dark clinopyroxene layers are interpreted as evolved melt percolations in oceanic lithosphere such as gabbro veins (Rebay et al., 2017) as also suggested by the augitic core. The oceanic/metasomatic evolution of the serpentinites is also suggested by the proximity of gabbro bodies and rodingite dykes (Zanoni et al., 2016 and refs. therein). The microstructural analysis supported by extreme detailed structural survey allowed to clearly define pre-D2 mineralogical and textural relicts that are preserved regardless the pervasive S2 HP-UHP foliation. Pre-D2 parageneses, in serpentinites, dunites and clinopyroxene layers, allow to better constrain metamorphic conditions predating D2 for Valtournenche serpentinites. Furthermore the P-T conditions for D2 are similar to those of the surrounding serpentinites (Rebay et al., 2012) that were dated at 65 ± 5.6 Ma (Rebay et al., 2017). These results, coupled with P-T peak condition proposed in this work, lead to consider that the ZSZ was already buried at depth before 70 Ma and dramatically widen the time span under which ZSZ recorded P-T peak conditions. Such observations support the idea that ZSZ is a mosaic of ophiolitic tectono-metamorphic units, recording P-peak conditions in different times (Mahlen et al., 2006; Skora et al., 2015; Rubatto et al., 1998, and references therein), and that were coupled during Alpine exhumation.

References:

Skora, S., Baumgartner, L. P., Mahlen, N. J., Johnson, C. M., Pilet, S., Hellebrand, E., 2006. Diffusion-limited REE uptake by eclogite garnets and its consequences for Lu–Hf and Sm–Nd geochronology. Contributions to Mineralogy and Petrology, 152, 703-720.

Skora, S., Mahlen, N. J., Johnson, C. M., Baumgartner, L. P., Lapen, T. J., Beard, B. L., Szilvagyi, E. T., 2015. Evidence for protracted prograde metamorphism followed by rapid exhumation of the Zermatt-Saas Fee ophiolite. Journal of Metamorphic Geology, 33, 711-734.

Rebay, G., Spalla, M. I., Zanoni, D., 2012. Interaction of deformation and metamorphism during subduction and exhumation of hydrated oceanic mantle: insights from the Western Alps. Journal of Metamorphic Geology, 30, 687-702.

Rebay, G., Zanoni, D., Langone, A., Luoni, P., Tiepolo, M., Spalla, M. I., 2017. Dating of ultramafic rocks from the western alps ophiolites discloses late cretaceous subduction ages in the Zermatt-Saas Zone. Geological Magazine, 1-18.

Rubatto, D., Gebauer, D., Fanning, M., 1998. Jurassic formation and Eocene subduction of the Zermatt–Saas-Fee ophiolites: implications for the geodynamic evolution of the Central and Western Alps. Contributions to Mineralogy and Petrology, 132, 269-287.

Zanoni, D., Rebay G., Spalla, M. I., 2016. Ocean floor and subduction record in the Zermatt-Saas rodingites, Valtournanche, Western Alps. Journal of Metamorphic Geology, 34, 941-961.

Dating of ultramafic rocks from the western Alps ophiolites discloses Late Cretaceous subduction ages in the Zermatt-Saas Zone

Rebay G.[1], Zanoni D.[2], Langone A.[3], Luoni P.*[2], Tiepolo M.[2] & Spalla M.I.[2]

[1] Dipartimento di Scienze della Terra e dell'Ambiente, Università di Pavia
[2] Dipartimento di Scienze della Terra "A. Desio", Università di Milano
[3] Istituto di Geoscienze e Georisorse, Consiglio Nazionale delle Ricerche, Pavia

* *Corresponding email*: pietro.luoni@unimi.it

Keywords: serpentinites, subduction metamorphism, microstructural analysis, U-Pb dating, Tethys opening.

Regional- to micro-scale structural analysis has been applied to Zermatt-Saas Zone (ZSZ) serpentinites to explore their tectonic history by means of *PT*Dt path reconstruction. ZSZ is a slice of oceanic lithosphere tectonically sampled from the Tethyan realm, characterized by a dominant *HP*-*UHP* metamorphic imprint, locally overprinted by greenschist facies metamorphism. Ages of oceanic protolith vary between 164 and 153 Ma. The Alpine metamorphic peak recorded during subduction is constrained between 50 and 39 Ma. Serpentinites and rodingites in the upper Valtournanche are dominated by a regional S2 foliation mapped with spatial continuity (Rebay et al., 2012; Zanoni et al., 2016). *HP* mineral assemblages underlining S2 indicate that physical conditions of Alpine metamorphism reached 2.5 ± 0.3 GPa and 600 ± 20°C (Rebay et al., 2012). Locally, in serpentinites clinopyroxene-I and zircon-I porphyroclasts are wrapped by S2 foliation and fringes and/or new grains of clinopyroxene-II and zircon-II define S2. New clinopyroxene-II fringes have compositions similar to those of new clinopyroxene grains marking S2. Trace element composition of clinopyroxene crystals is consistent with a crystallisation from a melt in equilibrium with plagioclase as it occurs in gabbroic percolation of oceanic mantle. Microstructures similar to those observed in clinopyroxenes characterise zircons. Under cathodoluminescence, zircon cores show sector zonings typical of magmatic growth. U-Pb data suggest that zircon cores crystallised during Middle Jurassic. The thin fringes overgrowing magmatic cores are parallel to the S2 foliation and U-Pb concordant analyses on these domains reveal an Upper Cretaceous blastesis age. These dates are interpreted as the ages of *HP* to *UHP* Alpine re-equilibration. These results allow widening the time span under which rocks of ZSZ recorded *P*-peak, and suggest that different portions of ZSZ reached the deepest part of the subduction system diachronically. Therefore, some sections of the ZSZ have likely experienced *HP* to *UHP* metamorphism earlier than previously thought. The obtained ages are comparable to those already described for the *HP* re-equilibration in the subducted continental crust of the Sesia-Lanzo Zone (SLZ) and this finding goes along with the cold thermal regime under which the SLZ was exhumed, which is compatible with on-going oceanic subduction.

Rebay, G., Spalla, M.I., Zanoni, D. (2012): Interaction of deformation and metamorphism during subduction and exhumation of hydrated oceanic mantle: insights from the Western Alps. J. Metamorph. Geol., 30, 687-702.

Zanoni, D., Rebay, G., Spalla, M.I. (2016): Ocean floor and subduction record in the Zermatt-Saas rodingites, Valtournanche, Western Alps. J. Metamorph. Geol., 34, 941-961.

3rd EMAW PAVIA 2018
3rd EUROPEAN MANTLE WORKSHOP
Pavia, 26-28th June

UHP TI-CHONDRODITE IN THE ZERMATT-SAAS SERPENTINITE: CONSTRAINTS ON A NEW TECTONIC SCENARIO

PIETRO LUONI
Università degli Studi di Milano, Dipartimento di Scienze della Terra 'A. Desio', Via Mangiagalli, 34-20133 Milano, Italy
GISELLA REBAY
Università degli Studi di Pavia, Dipartimento di Scienze della Terra e dell'Ambiente, Via Ferrata, 1-27100 Pavia, Italy
MARIA IOLE SPALLA
Università degli Studi di Milano, Dipartimento di Scienze della Terra 'A. Desio', Via Mangiagalli, 34-20133 Milano, Italy
DAVIDE ZANONI
Università degli Studi di Milano, Dipartimento di Scienze della Terra 'A. Desio', Via Mangiagalli, 34-20133 Milano, Italy

Zermatt-Saas serpentinites in Valtournanche are characterized by a dominant S2 HP-UHP foliation, defined by Ol+Cpx+Ti-Chu+Chl+Atg+Mag (Rebay *et al*., 2012 and 2018). A detailed structural survey (1:20 scale) of selected outcrops preserving this syn-D2 paragenesis, together with microstructural analyses, has allowed to recognize relationships between D2 and pre D2 mineral and structural relics, preserved in centimetre- to metre-sized domains wrapped by S2. Pre-D2 mineral assemblages consist of Cpx or Ol + Ti-Chn + Spl porphyroclasts + Atg ± Chl. Ti-Chn + Ti-Chu polygonal aggregates (with minor Chl + Ilm + Mag + Atg + Cpx or Ol) can be interpreted as either predating S2 or being synkinematic with the early stages of S2 development (pre-D2 to early D2). The occurrence of Ti-chondrodite and/or Ti-clinohumite indicates that these rocks re-equilibrated at UHP conditions (P = 2.8–3.5 GPa, T = 600–670 °C) and syn-D2 assemblages indicate P-T conditions in agreement with those already determined in the surrounding serpentinitites and rodingites (P<2.8, T = 580 - 620°C; Zanoni *et al.*, 2016 and refs. therein), dated at 65 ± 5.6 Ma (Rebay *et al*., 2018). The finding of UHP peak conditions similar to the 44-40 Ma old UHP (Rubatto *et al*., 1998) in the near Cignana Unit, where coesite in garnet (Reinecke, 1991) and microdiamonds (Frezzotti *et al*., 2011) have been found, dramatically widen to at least 60 Ma the time interval under which ZSZ has been involved in the Alpine subduction. In addition, these results support the idea that ZSZ represents a mosaic of ophiolitic tectono-metamorphic units, which recorded different and diachronic P-T-d-t paths and that coupled together during Alpine exhumation.

REFERENCES

Frezzotti, M. L., Selverstone, J., Sharp, Z. D., Compagnoni, R. (2011): Carbonate dissolution during subduction revealed by diamond-bearing rocks from the Alps. *Nat. Geosci.*, **4(10)**, 703-706.

Rebay, G., Spalla, M. I., Zanoni, D. (2012): Interaction of deformation and metamorphism during subduction and exhumation of hydrated oceanic mantle: insights from the Western Alps. *J. Metamorp. Geol.*, **30(7)**, 687-702.rere

Rebay, G., Zanoni, D., Langone, A., Luoni, P., Tiepolo, M., Spalla, M. I. (2018). Dating of ultramafic rocks from the western alps ophiolites discloses late cretaceous subduction ages in the Zermatt-Saas Zone. *Geol. Mag.*, **155(2)**, 298-315.

Reinecke, T. (1991): Very-high-pressure metamorphism and uplift of coesite-bearing metasediments from the Zermatt-Saas zone, Western Alps. *Eur. J. of Miner.*, **3**, 7-18.

Rubatto, D., Gebauer, D., Fanning, M. (1998): Jurassic formation and Eocene subduction of the Zermatt–Saas-Fee ophiolites: implications for the geodynamic evolution of the Central and Western Alps. *Contrib. Mineral. Petr.*, **132(3)**, 269-287.

Zanoni, D., Rebay G., Spalla, M. I. (2016). Ocean floor and subduction record in the Zermatt-Saas rodingites, Valtournanche, Western Alps. *J. Metamorp. Geol.*, **34**, 941-961.

New finding of UHP relics in the Zermatt-Saas Zone (Italian Western Alps): insights into a new geodynamic scenario

Luoni, Pietro [1] - *Rebay, Gisella* [2] - *Roda, Manuel* [1] - *Spalla, Maria Iole* [1] - *Zanoni, Davide* [1]

1) Dipartimento di Scienze della Terra "A. Desio", Università degli Studi di Milano, Italy
2) Dipartimento di Scienze della Terra e dell'Ambiente, Università degli Studi di Pavia, Italy

The finding of Ti-chondrodite (Ti-Chn) and Ti-clinohumite (Ti-Chu) assemblages in the eclogitized serpentinites of the Zermatt-Saas Zone (ZSZ) indicates that UHP conditions are attained outside of Cignana Unit, changing the tectonic scenario of the northern portion of the Western Alps. This recognition has been possible by the use of multiscale structural analysis and detailed mapping (1:20 scale) integrated with petrological investigation, applied to serpentinites of upper Valtournanche (Italy). Polyphasic deformation transposed original litostratigraphy of serpentinites comprising magnetite-rich layers, rare veins of Ti-chondrodite + Ti-clinohumite, layers and lenses of dunites, veins of olivine, and layers of pyroxenites. Serpentinites record polyphase ductile deformation and S_2 is the dominant fabric at the regional scale, preserving relics of earlier foliation or isoclinal rootless folds (pre-D_2). S_2 is crenulated and intersected by shear zones. The microstructural analysis allowed to clearly define pre-D_2 mineralogical and textural relicts that are preserved regardless the pervasive S_2 HP-UHP foliation in serpentinites. Pre-D_2 mineral assemblages consist of Cpx or Ol + Ti-Chn + Spl porphyroclasts + Atg ± Chl. Ti-Chn + Ti-Chu polygonal aggregates (with minor Chl + Ilm + Mag + Atg + Cpx or Ol) can be interpreted as either predating S_2 or being synkinematic with the early stages of S_2 development (pre-D_2 to early D_2). The occurrence of Ti-Chn implies recrystallization at UHP conditions (P = 2.8–3.5 GPa, T = 600–670 °C). Such conditions are similar to those registered by the nearby Cignana unit, where coesite and microdiamond have been found. Furthermore, the P–T conditions for D_2 are similar to those of the surrounding serpentinites that were dated at 65 ± 5.6 Ma. These results, coupled with P–T peak condition proposed in this work, lead to consider that the ZSZ was already buried at depth before 70 Ma and dramatically widen the time span under which ZSZ recorded P–T peak conditions. Such observations support the idea that ZSZ is a mosaic of ophiolitic tectono-metamorphic units, recording P-peak conditions in different times, and that were coupled during Alpine exhumation, as suggested by quantitative geodynamic modelling.

Structural mapping of UHP serpentinites at Créton, upper Valtournenche valley, Zermatt-Saas Zone

Luoni P.*[1], Zanoni D.[1], Rebay G.[2] & Spalla M.I.[1]

[1] Università degli Studi di Milano, Dipartimento di Scienze della Terra 'A. Desio'
[2] Università degli Studi di Pavia, Dipartimento di Scienze della Terra e dell'Ambiente

* *Corresponding email:* pietro.luoni@unimi.it

Keywords: form surface map, petro-structural analysis, Alpine subduction.

Detailed field mapping (1:20 scale) and multiscale petro-structural analysis were applied to a portion of the Zermatt-Saas Zone in upper Valtournanche (Western Italian Alps). The analysis is focused to infer, by the superposed fabrics and structures and the associated mineral assemblages, the relative chronology of successive tectonic stages in polydeformed serpentinites involved in a subduction system. The results are synthesised into a map with foliation trajectories, transposed lithostratigraphy and syn-kinematic mineral assemblages of key-outcrops at Créton barns. Serpentinites comprise magnetite layers and rare, dm-thick, diopsidite layers and lenses. Moreover, veins and aggregates of Ti-chondrodite and Ti-clinohumite, layers and lenses of dunites, veinlets of olivine, and layers of dark pyroxenite are embedded in serpentinites. All these rocks record three groups of syn-metamorphic ductile structures: D1 consists of rare fold hinges and a relic S1 foliation, preserved in S2 lithons; D2 comprises isoclinal folds and a very pervasive foliation (S2), which is the dominant fabric at the regional scale (Zanoni et al., 2012; 2016); D3 includes a crenulation, shear zones and open folds. The detailed structural fieldwork, supported by microstructural analysis, allowed to correlate these outcrops with the regional setting described in previous works (Rebay et al., 2012; Zanoni et al., 2012) and to identify pre-D2 structural, mineralogical, and textural relicts that are preserved regardless the strong transposition produced during the development of S2 HP-UHP foliation (Zanoni et al., 2016 and refs therein) which was recently dated at ˜65 Ma (Rebay et al., 2018). The occurrence of Ti-chondrodite in pre-D2 Alpine assemblages suggests that suck rocks re-equilibrated at UHP conditions (P= 2.8-3.5 GPa, T= 600-670 °C; Luoni et al., 2018), similar to those of the adjacent Cignana Unit, suggesting a new Alpine tectonic setting for the ZSZ.

Luoni, P., Rebay, G., Spalla, M. I. & Zanoni, D. (2018): UHP Ti-chondrodite in the Zermatt-Saas serpentinite: constraints on a new tectonic scenario. Letters of Am. Mineral. DOI: 10.2138/am-2018-6460.

Rebay, G., Spalla, M.I. & Zanoni, D. (2012): Interaction of deformation and metamorphism during subduction and exhumation of hydrated oceanic mantle: Insights from the Western Alps. J. Metam. Geol., 30, 687-702.

Rebay, G., Zanoni, D., Langone, A., Luoni, P., Tiepolo, M. & Spalla, M.I. (2018): Dating of ultramafic rocks from the Western Alps ophiolites discloses Late Cretaceous subduction ages in the Zermatt-Saas Zone. Geol. Mag., 155, 298-315.

Zanoni, D., Rebay, G., Bernardoni, J. & Spalla, M.I. (2012): Using multiscale structural analysis to infer high-/ultrahigh-pressure assemblages in subducted rodingites of the Zermatt-Saas Zone at Valtournanche, Italy. J. Virtual Expl., 41, 1-30.

Zanoni, D., Rebay, G. & Spalla, M.I. (2016): Ocean floor and subduction record in the Zermatt-Saas rodingites, Valtournanche, Western Alps. J. Metam. Geol., 34, 941-961.

Deformation history of Ultra High Pressure ophiolitic serpentinites in the Zermatt-Saas Zone, Créton, upper Valtournanche, Western Alps

Pietro Luoni[1], Davide Zanoni[1], Gisella Rebay[2], M. Iole Spalla[1]

[1]Università degli Studi di Milano, Dipartimento di Scienze della Terra "A. Desio", Via Mangiagalli 34, 20133 Milano (Italy)
[2]Università degli Studi di Pavia, Dipartimento di Scienze della Terra e dell'Ambiente, Via Ferrata 1, 27100 Pavia (Italy)

Detailed multiscale structural analysis and mapping (1:20 scale) integrated with petrological investigations were used to study a portion of the Zermatt-Saas serpentinites that outcrop in upper Valtournanche (north-western Italy). Results are shown in a foliation trajectory map that displays the transposed original lithostratigraphy of a serpentinite body exposed at Créton. The serpentinite body comprises magnetite-rich and rare centimetre- to decimetre-thick pyroxenite layers and lenses. Moreover, veins and aggregates of Ti-chondrodite and Ti-clinohumite, olivine-rich layers, lenses and veinlets. Serpentinites and associated rocks record three superposed groups of ductile structures: D1 consists of rare isoclinal and rootless folds, associated with S1 foliation; D2 consists of tight to isoclinal folds and a pervasive foliation (S2), which is the dominant fabric at the regional scale; D3 includes a crenulation and shear zones overprinting S2. The microstructural analysis suggests the metamorphic conditions of successive deformation stages (Luoni et al., 2018). The resulting tectono-metamorphic evolution is correlated with those already inferred in surrounding areas (Rebay et al., 2012; Zanoni et al., 2012; Zanoni et al., 2016; Rebay et al., 2018). In addition, metre- to submillimetre-sized pre-D2 structural, mineralogical, and textural relics have been clearly identified in spite of the strong HP-UHP D2 transposition: these relict fabrics are marked by either UHP or hydrothermal oceanic mineral assemblages.

References

Luoni P., Rebay G., Spalla M.I. &Zanoni D. (2018). UHP Ti-chondrodite in the Zermatt-Saas serpentinite: Constraints on a new tectonic scenario. Amer. Miner., 103, 1002–1005.

Rebay G., Spalla M.I., Zanoni D. (2012). Interaction of deformation and metamorphism during subduction and exhumation of hydrated oceanic mantle: Insights from the Western Alps. J. metam. Geol., 30, 687-702.

Rebay G., Zanoni D., Langone A., Luoni P., Tiepolo M., &Spalla M.I. (2018). Dating of ultramafic rocks from the Western Alps ophiolites discloses Late Cretaceous subduction ages in the Zermatt-Saas Zone. Geol. Mag., 155(2), 298-315.

Zanoni D., Rebay G., Spalla M.I., Bernardoni J. (2012). Using multiscale structural analysis to infer high-/ultrahigh-pressure assemblages in subducted rodingites of the Zermatt-Saas Zone at Valtournanche, Italy. J. Virt. Expl., 41., 2-30.

Zanoni D., Rebay G., Spalla M.I. (2016). Ocean floor and subduction record in the Zermatt-Saas rodingites, Valtournanche, Western Alps. J. metam. Geol., 34, 941-961.

UHP relics in the Zermatt-Saas Zone serpentinites: insights into a new geodynamic scenario

Pietro Luoni[1], Gisella Rebay[2], Manuel Roda[1], Iole Spalla[1], Davide Zanoni[1]

[1]Università degli Studi di Milano, Dipartimento di Scienze della Terra "A. Desio", Via Mangiagalli 34, 20133 Milano (Italy)
[2]Università degli Studi di Pavia, Dipartimento di Scienze della Terra e dell'Ambiente, Via Ferrata 1, 27100 Pavia (Italy)

Ti-chondrodite (Ti-Chn) and Ti-clinohumite (Ti-Chu) assemblages in the eclogitized serpentinites indicate that UHP conditions are attained, in other localities of the Zermatt-Saas Zone (ZSZ) besides Cignana Unit. This finding changes the tectonic scenario of the northwestern portion of the Alpine ophiolites (Luoni et al. 2018). This recognition has been possible by multiscale structural analysis and detailed mapping (1:20 scale) integrated with a petrological investigation of serpentinites at Créton (upper Valtournanche, north-western Italy). Polyphasic ductile deformation transposed original lithostratigraphy of serpentinites comprising magnetite-rich layers, rare veins of Ti-chondrodite + Ti-clinohumite, olivine-rich and pyroxenite layers and lenses. S2 is the dominant fabric in the region and at Créton; it preserves relics of earlier foliation or isoclinal rootless folds (pre-D2) and is crenulated and intersected by shear zones. Pre-D2 mineralogical and textural relicts are preserved regardless of pervasive development of S2 HP-UHP foliation in serpentinites. Pre-D2 mineral assemblages consist of Cpx or Ol + Ti-Chn+ Spl + Atg ±Chl. Ti-Chn+ Ti-Chu polygonal aggregates (with minor Chl + Ilm + Mag + Atg + Cpx or Ol) can be interpreted as either predating S2 or synkinematicwith the early stages of S2 development (pre- to early-D2). The occurrence of Ol + Ti-Chn+ Spl implies recrystallization under UHP conditions (P = 2.8–3.5 GPa, T = 600–670 °C), similarly to those recorded by the nearby Cignana Unit rocks, where coesite and microdiamondhave been found (Reinecke 1991). Furthermore, the P-T conditions for D2 assemblages at Créton are similar to those estimated for D2 in the surrounding serpentinites, which were dated at 65 ±5.6 Ma (Rebay et al. 2012, 2018). These results, coupled with P-T peak condition proposed in this work, lead to consider that the ZSZ was already buried at depth before 70 Ma and dramatically widen the subduction time span under which ZSZ recorded P-T peak conditions. Such observations support the idea that ZSZ is a mosaic of ophiolitic tectono-metamorphic units, which recorded P-peak conditions in different times, and that were coupled during Alpine exhumation, as suggested by quantitative geodynamic modeling (Roda et al. 2012).

References

Luoni P., Rebay G., Spalla M.I. & Zanoni D. (2018). UHP Ti-chondrodite in the Zermatt-Saas serpentinite: Constraints on a new tectonic scenario. American Mineralogist, 103, 1002–1005

Rebay G., Spalla M.I. & Zanoni D. (2012). Interaction of deformation and metamorphism during subduction and exhumation of hydratedoceanic mantle: Insights from the Western Alps. Journal of Metamorphic Geology, 30, 687-702

Rebay G., Zanoni D., Langone A., Luoni P., Tiepolo M., & Spalla M.I. (2018). Dating of ultramafic rocks from the Western Alps ophiolites discloses Late Cretaceous subduction ages in the Zermatt-Saas Zone. Geological Magazine, 155(2), 298-315

Reinecke, T. (1991). Very high pressure metamorphism and uplift of coesite-bearing metasediments from the Zermatt-Saas Zone, Western Alps. European Journal of Mineralogy, 10, 7–17

Roda M., Spalla M.I. & Marotta A.M. (2012). Integration of natural data within a numerical model of ablative subduction: the example of the Austroalpine Domain of the Alps. Journal of Metamorphic Geology, 30, 973-996

Structural and metamorphic evolution of Gias Vej serpentinites (Piemonte Zone, Lanzo Valley, Italian Western Alps)

Assanelli M.*[1], Luoni P.[1], Rebay G.[2] & Spalla M.I.[1]

[1] Dipartimento di Scienze della Terra "A. Desio", Università degli Studi di Milano, Italy.
[2] Dipartimento di Scienze della Terra e dell'Ambiente, Università degli Studi di Pavia, Italy.

Corresponding email: matteo.assanelli@studenti.unimi.it

Keywords: Eclogitized ophiolites, Alpine subduction, multiscale structural analysis.

Thin slivers of metabasites and serpentinites, quartzite, calcschist, fine-grained gneisses (metasediments and metagranitoids) mark the boundary between Piemonte Zone (PZ) metaophiolites and the Sesia-Lanzo Zone (SLZ - Austroalpine Domain), extending from Santanel klippe to Lanzo Massif, over a distance of 50 km. In the upper Tesso valley, in the surroundings of P.ta Gias Vej, numerous slices of serpentinites occur in this subduction-related tectonic mixing. These serpentinites together with the other rocks of SLZ and PZ underwent four episodes of deformation, giving rise to a complex regional tectono-stratigraphy. The earliest deformational structures are represented by up to ten meter-scale isoclinal rootless folds. The metamorphic mineral assemblages marking successive foliations indicate that all rock units (Spalla et al., 1983; Gosso et al., 2015) experienced an early eclogite-facies imprint, followed by re-equilibration under blueschist-facies conditions, and that they were finally widely retrogressed under greenschist-facies conditions during the last two deformation stages (D3 and D4 structures). To refine the tectono-metamorphic history of ultramafites a microstructural and minero-chemical investigation has been performed to integrate the meso-structural analysis, both on Ol-, Ti-Chu- and Di-bearing serpentinites and Di-bearing chloritic schists. Variations in chemical compositions of mineral phases underlying superposed fabrics, developed under different metamorphic environments, will be explored and compared with those from Zermatt-Saas eclogitized serpentinites (Rebay et al., 2012; Luoni et al., 2018).

Gosso G., Rebay G., Roda M., Spalla M.I., Tarallo M., Zanoni D. & Zucali M. (2015) - Taking advantage of petrostructural heterogeneities in subduction-collisional orogens, and effect on the scale of analysis. Per. Mineral., 84, 779-825.

Luoni P., Rebay G., Spalla M.I. & Zanoni D. (2018) - UHP Ti-chondrodite in the Zermatt-Saas serpentinite: Constraints on a new tectonic scenario. Amer. Miner., 103, 1002–1005.

Rebay G., Spalla M.I. & Zanoni D. (2012) - Interaction of deformation and metamorphism during subduction and exhumation of hydrated oceanic mantle: Insights from the Western Alps. J. Metam. Geol., 30, 687-702

Spalla M.I., De Maria L., Gosso G., Miletto M. & Pognante U. (1983) - Deformazione alpina e metamorfismo nel settore esterno della Zona Piemontese e il Massiccio di Lanzo (Alpi Occidentali). Mem. Soc. Geol. Ital., 26, 499-514.

UHP relics in the Zermatt-Saas Zone serpentinites: new puzzle tiles in the geodynamic scenario

Luoni P.*[1], Rebay G.[2], Roda M.[1], Spalla M.I.[1] & Zanoni D.[1]

[1] Università degli Studi di Milano, Dipartimento di Scienze della Terra "A. Desio".
[2] Università degli Studi di Pavia, Dipartimento di Scienze della Terra e dell'Ambiente.

Corresponding email: pietro.luoni@unimi.it

Keywords: Piemonte zone, Ti-chondrodite, numerical modelling.

Ti-chondrodite (Ti-Chn) and Ti-clinohumite (Ti-Chu) assemblages in the eclogitized serpentinites indicate that UHP conditions are attained, in other localities of the Zermatt-Saas Zone (ZSZ) besides Cignana Unit. This finding changes the tectonic scenario of the north-western portion of the Alpine ophiolites. This recognition has been possible by multiscale structural analysis and detailed mapping (1:20 scale) integrated with petrological investigation of serpentinites at Créton (upper Valtournanche, north-western Italy). Polyphasic ductile deformation transposed original lithostratigraphy of serpentinites comprising magnetite-rich layers, rare veins of Ti-chondrodite + Ti-clinohumite, olivine-rich and pyroxenite layers and lenses. S2 is the dominant fabric in the region and at Créton; it preserves relics of earlier foliation or isoclinal rootless folds (pre-D2) and is crenulated and intersected by shear zones. Pre-D2 mineralogical and textural relicts are preserved regardless the pervasive development of S2 HP-UHP foliation in serpentinites. Pre-D2 mineral assemblages consist of Cpx or Ol + Ti-Chn + Spl + Atg ± Chl. Ti-Chn + Ti-Chu polygonal aggregates (with minor Chl + Ilm + Mag + Atg + Cpx or Ol) can be interpreted as either predating S2 or synkinematic with the early stages of S2 development (pre- to early-D2). The occurrence of Ol + Ti-Chn + Spl implies recrystallization under UHP conditions (P = 2.8–3.5 GPa, T = 600–670 °C), similarly to those recorded by the nearby Cignana Unit rocks, where coesite and microdiamond have been found. Furthermore, the P-T conditions for D2 assemblages at Créton are similar to those estimated for D2 in the surrounding serpentinites, which were dated at 65 ± 5.6 Ma. These results, coupled with P-T peak condition proposed in this work, lead to consider that the ZSZ was already buried at depth before 70 Ma and dramatically widen the subduction time span under which ZSZ recorded P-T peak conditions. Such observations support the idea that ZSZ is a mosaic of ophiolitic tectono-metamorphic units, which recorded P-peak conditions in different times, and that were coupled during Alpine exhumation, as suggested by quantitative geodynamic modelling.

Geol. Mag. **155** (*2*), *2018, pp. 298–315. © Cambridge University Press 2017*
doi:10.1017/S0016756817000334

Dating of ultramafic rocks from the Western Alps ophiolites discloses Late Cretaceous subduction ages in the Zermatt-Saas Zone

GISELLA REBAY*†, DAVIDE ZANONI‡, ANTONIO LANGONE§, PIETRO LUONI‡, MASSIMO TIEPOLO‡ & MARIA IOLE SPALLA‡

*Università degli Studi di Pavia, Dipartimento di Scienze della Terra e dell'Ambiente, Via Ferrata, 1 - 27100 Pavia, Italy
‡Università degli Studi di Milano, Dipartimento di Scienze della Terra 'A. Desio', Via Mangiagalli, 34 - 20133 Milano, Italy
§IGG-CNR U.O.S. - Pavia, Via Ferrata, 1 - 27100 Pavia, Italy

(*Received* 28 October 2016; *accepted* 13 March 2017; *first published online* 3 May 2017)

Abstract – The Zermatt-Saas Zone was part of the Middle to Late Jurassic Tethyan lithosphere that underwent oceanic metamorphism during Mesozoic time and subduction during Eocene time (HP to UHP metamorphism). In upper Valtournanche, serpentinite, metarodingite and eclogite record a dominant S2 foliation that developed under 2.5 ± 0.3 GPa and 600 ± 20 °C during Alpine subduction. Serpentinites contain clinopyroxene and rare zircon porphyroclasts. Clinopyroxene porphyroclasts show fringes within S2 with similar compositions to that of grains defining S2. Zircon cores show zoning typical of magmatic growth and thin fringes parallel to the S2 foliation. These features indicate crystallization of clinopyroxene and zircon fringes during HP syn-D2 metamorphism, related to the Alpine subduction. The U–Pb zircon dates for cores and fringes reveal crystallization at 165 ± 3.2 Ma and 65.5 ± 5.6 Ma, respectively. The Middle Jurassic dates are in agreement with the known ages for the oceanic accretion of the Tethyan lithosphere. The Late Cretaceaous - Paleocene dates suggest that the Zermatt-Saas Zone experienced high-pressure to ultra-high-pressure (HP–UHP) metamorphism at *c.* 16 Ma earlier than previously reported. This result is in agreement with the evidence that in the Western Alps the continental Sesia-Lanzo Zone reached the subduction climax at least from 70 Ma and was exhumed during ongoing oceanic subduction. Our results are further evidence that the Zermatt-Saas ophiolites diachronically recorded heterogeneous HP–UHP metamorphism.

Keywords: serpentinites, subduction metamorphism, microstructural analysis, U–Pb dating, Tethys opening

1. Introduction

Ophiolites represent oceanic remnants in mountain chains and their tracking, together with the reconstruction of their structural and metamorphic history, is still one of the basic tools for understanding the dynamics of collisional chain development. In the Alps, the key significance of ophiolites in geodynamics was long understood before the birth of plate tectonics (e.g. Brongniart, 1813; Argand, 1911; Steinmann, 1927). Since the first geological research within the Alps ophiolites from the Piedmont zone have been a favourable investigation object (Dal Piaz, 2010), especially in the exploration of deformation and mineral transformation histories of high-pressure (HP) and ultra-high-pressure (UHP) units of the Zermatt-Saas Zone (ZSZ). In the last years a debate developed on this portion of the Piedmont zone, regarding whether the pressure–temperature (*P–T*) conditions registered by ZSZ rocks are largely uniform or if different portions of ZSZ recorded different *P–T*-peak conditions and underwent different exhumation paths over different time spans (e.g. Lapen *et al.* 2003; Li, Rahn & Bucher, 2004; Angiboust *et al.* 2009; Groppo, Beltrando & Compagnoni, 2009; Angiboust & Agard, 2010; de Meyer *et al.* 2014; Skora *et al.* 2015; Weber & Bucher, 2015; Weber *et al.* 2015). This last view has been recently reinforced by multiscalar structural and petrological analysis supported by detailed field mapping (Rebay, Spalla & Zanoni, 2012; Weber & Bucher, 2015; Zanoni, Rebay & Spalla, 2016). The multiscalar analytical approach could be deeply reinforced by careful geochronological work, and becomes important in understanding the critical size of oceanic units able to record a homogeneous structural and metamorphic evolution during burial and exhumation paths in a subduction system. This means identifying volumes that have completed, remaining intact, their tectonic trajectory during a given time span. In addition, this allows light to be shed on how the coupling and decoupling of tectonic units can occur in the subduction mantle wedge or in the orogenic wedge during continental collision (e.g. Cloos, 1982; Chemenda *et al.* 1995; Stoeckhert & Gerya, 2005; Baumann, Gerya & Connolly, 2010; Roda, Marotta & Spalla, 2010; Gerya, 2011; Malatesta *et al.* 2012, 2016; Roda,

†Author for correspondence: gisella.rebay@unipv.it

American Mineralogist, Volume 103, pages 1002–1005, 2018

LETTER

UHP Ti-chondrodite in the Zermatt-Saas serpentinite: Constraints on a new tectonic scenario

PIETRO LUONI[1,*], GISELLA REBAY[2], MARIA IOLE SPALLA[1], AND DAVIDE ZANONI[1]

[1]Dipartimento di Scienze della Terra 'A. Desio', Università degli Studi di Milano, Via Mangiagalli, 34-20133 Milano, Italy
[2]Dipartimento di Scienze della Terra e dell'Ambiente, Università degli Studi di Pavia, Via Ferrata, 1-27100 Pavia, Italy

ABSTRACT

We focus on the key role of different Ti-humite minerals in subducted serpentinites as possible indicators of extreme pressure conditions. The occurrence of Ti-chondrodite and/or Ti-clinohumite assemblages in the eclogitized serpentinites of the Zermatt-Saas Zone (ZSZ) of the Western Alps allows the recrystallization of such rocks at UHP conditions (P = 2.8–3.5 GPa, T = 600–670 °C) to be determined. Such conditions are similar to those registered by the nearby Cignana unit, a main Alpine area for UHP metamorphism, where coesite and microdiamond have been found. In ZSZ serpentinites, the new UHP assemblage predates the previously recognized HP-UHP paragenesis, which was recently dated at 65 Ma. This finding opens up a new interpretation for the petrologically and structurally well-constrained HP/UHP records, especially because all other ages for HP-UHP metamorphism in the ZSZ are much younger, and for the size of UHP units. Our findings suggest that ophiolites in the axial zone of collisional belts are a mosaic of oceanic lithosphere slices that recorded contrasted thermal and mechanical evolutions during their physical trajectories in the subduction wedge.

Keywords: Ti-clinohumite and Ti-chondrodite assemblages, integrated mineralogical and structural analysis, Alpine subduction, Western Alps

INTRODUCTION

HP-UHP mineral assemblages are the trademark of subduction zones. The most widely known are metamorphic coesite and diamond inclusions in host grains in eclogite-facies crust of the Western Alps, Norway, Central Europe, China, and Kazakhstan and majoritic garnet and Si-bearing spinel in garnet peridotite (e.g., Ernst and Liou 2008; Frezzotti et al. 2011). Recognized as upper mantle minerals from Colorado Plateau kimberlites (Aoki et al. 1976; Smith 1977), Ti-clinohumite and Ti-chondrodite are also part of HP-UHP assemblages in ultramafites from China and the Western Alps (Scambelluri and Rampone 1999; Shen et al. 2015). Shen et al. (2015) proposed conditions of 2.7 GPa and 550–660 °C for the assemblage Ti-chondrodite (Ti-Chn)+Ti-clinohumite (Ti-Chu)+Atg+Chl+Ol+Spl, demonstrating that Ti-Chn+Ti-Chu assemblages are indicators of UHP conditions in serpentinized Ti-rich ultramafites (mineral abbreviations after Whitney and Evans 2010). The experimental demonstration of Ti-humite minerals defining HP-UHP conditions encouraged us to examine in detail fabrics and mineral assemblages in Valtournanche (Rebay et al. 2018 and references therein), to determine the microstructural relationships of Ti-Chu and/or Ti-Chn relics with the dominant HP/UHP foliation (S2) in these rocks. The occurrence of UHP rocks in the axial zones of orogenic belts has fueled debates on geodynamic environment (i.e., subduction, collision, late orogenic extension), exhumation mechanisms, and the timing of exhumation, which strongly influence the preservation of UHP assemblages (Ernst and Liou 2008). In the Alps, findings of UHP phases have led to the identification of hectometer to kilometer UHP tectonic units within HP nappes. Coesite (Reinecke 1991) and microdiamond (Frezzotti et al. 2011) relics occur in the Cignana Lake Unit (CLU) at the tectonic contact between the Zermatt-Saas Zone (ZSZ) and the Combin Zone (CZ). The shape, size, and exhumation environment of these UHP tectonic units are discussed. The occurrence of Ti-humites makes serpentinites a new key target for identification of UHP units.

The ZSZ (Figs. 1a and 1b) was derived from the internal portion of the Piedmont oceanic realm. It was trapped in the suture zone of the Western Alps during Alpine convergence. It comprises serpentinite, meta-gabbro, meta-rodingite, meta-basalt, and various metasediments. The metamorphism of the ZSZ is typical for eclogite facies conditions, locally overprinted by greenschist-facies mineral assemblages (commonly interpreted as exhumation-related). Peak P-T estimates range from 1.9–2.2 GPa and 500–600 °C to 2.3–2.8 GPa and 580–660 °C in different portions of the ZSZ (Bucher et al. 2005; Bucher and Grapes 2009; Zanoni et al. 2016). Such a wide P-T span suggests that different portions of the ZSZ underwent different tectono-metamorphic evolutions. In contrast, a common, and consequently uniform, evolution of the entire ZSZ was proposed by Angiboust and Agard (2010), with metamorphism peaking at 2.3 ± 0.1 GPa and 540 ± 40 °C. UHP conditions of 2.7 to >3.2 GPa and 590–630 °C have been recorded in small slices of oceanic rocks at the boundary between the ZSZ and CZ, at Lago di Cignana (Fig. 1c) (Groppo et al. 2009 and references therein). Protholith U/Pb ages range from 153–164 Ma (metabasites) to 162–168 Ma (serpentinites, Rebay et al. 2018 and references therein). Peak metamorphic ages are 71–38 Ma so that subduction might have been active already at 80 Ma (Table 1 in Rebay et al. 2018), indicating a wide time interval of re-equilibration during subduction and supporting a heterogeneous evolution of ZSZ. In particular, the dominant HP/UHP foliation (S2) of upper Valtournanche has been dated at 65.5 ± 5.6 Ma (Rebay et al. 2018).

* E-mail: pietro.luoni@unimi.it

0003-004X/18/0006–1002$05.00/DOI: http://doi.org/10.2138/am-2018-6460

DEFORMATION HISTORY OF ULTRA HIGH-PRESSURE OPHIOLITIC SERPENTINITES IN THE ZERMATT-SAAS ZONE, CRÉTON, UPPER VALTOURNANCHE (AOSTA VALLEY, WESTERN ALPS)

Pietro Luoni*,✉, **Davide Zanoni***, **Gisella Rebay**** and **Maria Iole Spalla***

* *Dipartimento di Scienze della Terra "A. Desio", Università degli Studi di Milano, Italy.*
** *Dipartimento di Scienze della Terra e dell'Ambiente, Università degli Studi di Pavia, Italy.*
✉ *Corresponding author, e-mail: pietro.luoni@unimi.it*

Keywords: *serpentinites; foliation trajectory map; multi-scale structural analysis; Ti-chondrodite; Ti-clinohumite; subduction tectonics; Western Alps.*

ABSTRACT

Detailed multiscale structural analyses and mapping (1:20 scale) integrated with petrological investigation were used to study a portion of the Zermatt-Saas serpentinites that crop out in upper Valtournanche (north-western Italy). Results are synthesized in a foliation trajectory map that displays the transposed original lithostratigraphy of a serpentinite body exposed at Créton. The serpentinite body comprises magnetite sheets and rare, decimetre-thick, diopsidite layers and lenses. Moreover, veins and aggregates of Ti-chondrodite and Ti-clinohumite, olivine-rich layers and lenses, veinlets of olivine, and layers of dark pyroxenite are embedded in the serpentinites. Serpentinites and associated rocks record three relative age groups of ductile structures: D_1 consists of rare folds and S_1 foliation; D_2 is a group of isoclinal folds and a very pervasive foliation (S_2), which is the dominant structure; D_3 includes a crenulation and shear zones affecting S_2. The detailed meso-structural and microstructural analyses allowed individuating the metamorphic environment of successive deformation stages and correlating the resulting tectono-metamorphic investigation with those already inferred in surrounding areas. In addition, metre- to submillimetre-sized pre-D_2 structural, mineralogical, and textural relics have been clearly identified in spite of the strong transposition imposed during the development of S_2 high pressure - ultra-high pressure foliation.

INTRODUCTION

Serpentinites are ever more considered as key players in processes that involve lithosphere subduction and exhumation. Their structural and metamorphic evolutions are poorly explored with respect to those of crustal rocks due to their extreme plasticity and generally high compositional homogeneity (e.g. Scambelluri et al., 1995; Li et al., 2004; Grigull et al., 2012; Rebay et al., 2012a; 2012b). Because of their low viscosity, the structural overprinting relationships in Alpine serpentinites are often very rich and therefore well-exposed key-outcrops preserving a long tectonic record, such as primary lithological heterogeneities, deserve extreme analytical care. In localities close to Créton, detailed petro-structural analysis (Zanoni et al., 2012; 2016) reconstruct the deformation history of serpentinites and rodingites and allow recognizing primary and metamorphic relic assemblages, often just preserved as single porphyroclasts. Generally during field mapping in the axial portion of orogenic belts, lithostratigraphic, structural and petrological observations are integrated into a modern structural map that reports foliation trajectories over the finite lithostratigraphic framework (Gosso et al., 1983; Passchier, 1990; Johnson and Duncan, 1992; Connors and Lister, 1995; Zucali et al., 2002; Gosso and Spalla, 2009; Baletti et al., 2012; Zanoni et al., 2012). The goal is therefore to collect the full assemblage of details on relative structural chronology, textural types reflecting fabric gradients (Gosso et al., 2010; 2015), and mineral assemblages marking successive foliations. The representation techniques can reveal the sequence of superposed textural and metamorphic imprints and allow following the lateral continuity of information that is the key for evaluating the significance of structural and mineral relics distribution at the regional scale. The integrated interpretation of structural and petrologic data is basic for the reconstruction of the tectonic evolution (e.g. Spalla et al., 2005) and therefore this type of maps permits the recognition of geodynamic settings in which mantle and crust portions of orogenic scars have been forged during mountain building processes.

This approach is here applied to enclose the structures and lithologies within the tectonic framework of the Zermatt-Saas serpentinites in the upper Valtournanche and to separate the Alpine structures and fabrics from pre-Alpine oceanic relics. Finally, mineral assemblages associated with successive foliations are used to constrain the P-T-d-t evolution of the Créton serpentinites adding a new tile to the Zermatt-Saas Zone (ZSZ) tectono-metamorphic puzzle (Luoni et al., 2018).

GEOLOGICAL SETTING

The ZSZ is part of the Piemonte Zone, in the Penninic domain of Western Alps (Fig. 1a, b) (Bigi et al., 1990; Dal Piaz, 1992; Martin et al., 1994 and reference therein), comprising carbonatic and terrigenous metasediments, minor quartzites, metabasites, metagabbros, eclogites, rodingites, serpentinites, and minor ophicalcites. ZSZ is interpreted as a wreckage of the Alpine Tethys that is constituted by an ophiolitic suite typical of a slow-spreading setting (Boudier and Nicolas, 1985; Nicolas and Boudier, 2003) buried at mantle-depths, transposed during Alpine subduction-collision, and at present marking the oceanic scar in the axial zone of Western Alps. ZSZ includes serpentinized peridotites (Li et al., 2004; Rebay et al., 2012a; 2012b), metagabbros and metarodingites (Li et al., 2004; Rebay et al., 2012a; 2012b; Zanoni et al., 2016), N-MORB metabasites (Bucher et al., 2005 and reference therein), and minor metasediments as calcschists and quartzites (Bearth, 1967; Ernst and

Tectono-metamorphic evolution of UHP Zermatt-Saas serpentinites: a tool for vertical paleogeographic restoration

Within the Zermatt-Saas Zone (ZSZ, northwestern Alps), Ti-chondrodite- and Ti-clinohumite-bearing assemblages in serpentinites indicate UHP conditions. Multiscale structural analysis (1:20 scale mapping) and petrological investigation of serpentinites at Créton (upper Valtournanche) evidenced a polyphasic deformation and metamorphic history. In this locality and at regional scale, S2 is the dominant foliation that developed under HP-UHP conditions. Pre-D2 mineral and textural relicts are preserved despite the pervasiveness of S2. Pre-D2 olivine + Ti-chondrodite + spinel assemblage implies re-equilibration at 2.8–3.3 GPa and 600–630 °C, in agreement with conditions recorded by coesite- and microdiamond-bearing rocks in the Cignana Unit. The P-T conditions inferred for syn-D2 assemblages at Créton are similar to those estimated for D2 in the surrounding serpentinites, which were dated at 65 ± 5.6 Ma. These results suggest that portions of ZSZ were subducted at high depth before 70 Ma and widen the time span under which ZSZ recorded P-T peak conditions. The comparison of these data with results of a numerical model of an ocean-continent subduction system gives insights on coupling stages of this UHP unit with the surrounding ZSZ rocks during the Alpine convergence and vertical paleogeography during different time steps.

Keywords: Ti-humites, serpentinite, subduction modelling, Piemonte Zone, Western Alps

Introduction

Emplacement of Ultra High Pressure (UHP) rocks in the axial portion of orogenic chains (Chopin 1984; Smith 1984; Kienast *et al.* 1991; Reinecke 1991; Ernst and Liou 1999) has opened up the need to identify the geodynamic context of their formation and coupling with the surrounding units, apparently free of this metamorphic imprint, and precisely if such formation and/or coupling occurred in a context of subduction, collision or, even, of late orogenic extension. Moreover, the discussion on exhumation mechanisms and timing that are effective for the preservation of UHP assemblages is still open. In the Alps the detection of UHP mineral phases, such as coesite, ellenbergerite, Mg-dumortierite, and microdiamonds, allowed the individuation of hectometre- to kilometre-scale UHP tectonic units enclosed in HP nappes both of oceanic (Zermatt-Saas Zone) and